UNIVERSITÉ DU LUXEMBOURG

PhD-FSTM-2020-33
The Faculty of Sciences, Technology and Medicine

DISSERTATION

Defence held on 15/07/2020 in Esch-sur-Alzette

to obtain the degree of

DOCTEUR DE L'UNIVERSITÉ DU LUXEMBOURG

EN CHIMIE

by

Nicolas GODARD
Born on 17 April 1993 in Virton (Belgium)

INKJET-PRINTED PIEZOELECTRIC FILMS FOR TRANSDUCERS

Dissertation defence committee

Dr Emmanuel Defay, dissertation supervisor
Group Leader, Luxembourg Institute of Science and Technology

Dr Barbara Malič
Professor, Jožef Stefan Institute

Dr Phillip Dale, Chairman
Professor, Université du Luxembourg

Dr Sohini Kar-Narayan
Professor, University of Cambridge

Dr Andrea Picco
Development Engineer, ST Microelectronics

Dr Sebastjan Glinšek
R&T Associate, Luxembourg Institute of Science and Technology

Before printing was discovered, a century was equal to a thousand years.

Henry David Thoreau (1817–1862)
American philosopher, essayist and poet

Inkjet-printed piezoelectric films for transducers

Nicolas Godard, Ferroic Materials for Transducers (FMT) group,
Materials Research and Technology (MRT) department,
Luxembourg Institute of Science and Technology (LIST)

Thesis supervisor: Dr. Emmanuel Defay
Tutors: Dr. Sebastjan Glinšek and Dr. Daniele Sette

Abstract

Lead zirconate titanate (PZT) thin films are a popular choice for piezoelectric devices such as microelectromechanical systems, micro-pumps, micro-mirrors or energy harvesters. Various fabrication techniques exist for the deposition of PZT in the form of thin films. Physical vapor deposition (PVD) methods are particularly cost-intensive, as they require vacuum conditions and expensive infrastructure. Fabrication costs can be decreased by the use of chemical solution deposition (CSD), where the metal precursors are dispersed in a solvent medium and coated onto a substrate. Thermal treatments convert the liquid precursor into a functional solid film.

Spin coating is a conventional coating technique allowing for the deposition of homogeneous layers over large-area substrates. However, it is inherently wasteful, as most of the precursor material is spun off the substrate in the coating process. In addition, as spin coating results in complete coverage of the substrate, layer patterning requires lithography, which adds up extra steps and costs to the overall process. Inkjet printing is an additive manufacturing technique that has the potential to address both of these issues, thus further decreasing manufacturing costs and the associated ecological footprint.

The working principle of inkjet printing can be described as the deposition of individual ink droplets at digitally determined locations on the substrate surface, which then merge into a continuous film. Inkjet printing is compatible with CSD processing of PZT thin films, as demonstrated by the previous works in the field. However, the adaptation of standard CSD processing for inkjet printing comes with several challenges, which have to be considered to obtain state-of-the-art functional PZT layers.

In the present work, we explore several issues related to the processing of PZT thin films by inkjet printing and we provide possible solutions to address them, in a way that had not been described yet by the state of the art. In particular, we describe a novel strategy that uses inkjet-printed alkanethiolate-based self-assembled monolayers for direct patterning of PZT thin films on platinized silicon. Then, we present a systematic study of the pyrolysis step of the process, which enabled us to print dense and textured layers with state-of-the-art electrical properties. We also developed a proof-of-concept piezoelectric energy harvesting device based on inkjet-printed PZT films. Finally, we unveil a comparative study where we identified an alternative solvent for CSD processing of PZT thin films.

Acknowledgements

The Luxembourgish National Research Fund (FNR) is acknowledged for funding this thesis work under project CO-FERMAT (FNR/P12/4853155/Kreisel).

This PhD thesis at the Luxembourg Institute of Science and Technology has been an important experience in my life and I would like to take the time to acknowledge all the people who have helped me in this four-year-long journey and made this work possible.

First of all, I would like to thank my supervisor Dr. Emmanuel Defay for giving me the possibility to carry out this research and for providing me with weekly supervision during four years. His dedication and passion for his work were a source of inspiration for me. I would also like to acknowledge the members of my thesis supervisory committee, Prof. Barbara Malič and Prof. Phillip Dale, for following my work during these four years. I also wish to thank the external members of the jury, Prof. Sohini Kar-Narayan and Dr. Andrea Picco, for their time reading and assessing my manuscript.

Naturally, I would like to thank my tutors Daniele Sette and Sebastjan Glinšek, who took an active part in my training on a daily basis. Daniele ensured my supervision during my internship and at the beginning of my PhD. He gave me the impetus to start working with the printer. Sebastjan took over and helped me until the end, always providing valuable advice and feedback, from my first paper draft to the last lines of this manuscript.

Then, I would like to acknowledge all the co-authors of my publications and the LIST colleagues who contributed to the scientific work presented herein. In particular, I would like to thank Stéphanie Girod for performing the patterning of electrodes on my numerous samples, Jean-Baptiste Chemin for platinum deposition, Benoît Marcolini and Régis Vaudemont for thermal analyses, Maryline Moreno for FTIR spectroscopy, Tony Schenk for X-ray reflectivity, Mathieu Gérard for the design of the test bench for energy harvesters, Nathalie Valle and Brahime El Adib for SIMS analyses, as well as Jérôme Polesel for his help in the development of a proof-of-concept sensing device. I also thank Aleksander Matavž and Prof. Vid Bobnar from the Jožef Stefan Institute for performing the piezoelectric characterization presented in my first article.

It goes without saying that four years of PhD represent a significant amount of time with so many opportunities to meet wonderful people along the way. I would like to thank them all for their presence and the good moments we shared at LIST and outside!

I thank the former and present members of the FMT group with whom I had the chance to work, discuss, have a coffee... or enjoy the traditional Gromperekichelcher at the Schueberfouer and Glühwein at the Christmas market in Luxembourg City! I also thank all the colleagues of the MRT department who helped me in my work, or with whom I had the occasional chat in the kitchen or the corridors of LIST!

I would like to thank Hervé, who started his internship at LIST at the same time as me and with whom I had so many interesting conversations. Thanks also to Lucas, who ended up in a series of side projects with me during his internship. I have to say that our collaboration in the lab was quite fruitful! I also thank the LIST team from Bascharage, who welcomed me during my internship and introduced me to the temple of Croatian gastronomy in Belvaux! Of course, I do not forget my friends from the ERIN department, with whom I spent very nice moments and developed a growing interest for the rivers of South Africa! I also thank my friends from University for their kind invitations to *kitchen meetings*!

I want to thank all the members of the LIST music band I had the chance to play and have fun with: Nicolas B., Katrin, Cédric, Mónica, Enzo, Nicolas R., Franck and Antoine. I am really happy that I could help initiate this project and I wish you all the best! Keep on rockin'! I hope that I can still join you guys from time to time when I am around!

Last but not least in this category, I would like to express my warmest thoughts to my closest friends Antoine and Aymen. We spent so much time together that I believe were qualified as inseparable. The traditional morning coffee was always a great moment to start the day... and having a beer at Coyote was an excellent way to end it! The Belgian-Tunisian friendship is strong and I hope that we will continue to have the best parties altogether (and go skiing in the Alps once in a while)!

Finally, I would like to take a moment to thank my family for supporting me during my studies and my PhD thesis. Even though my field of studies might be quite far from the preoccupations of the environment I was raised in, I would not be where I am now without you and your support! And because a PhD is also a time when unexpected encounters may happen, also known as *beautiful coincidences*, my last thoughts are for you my dear Elena.

List of abbreviations and symbols

ALD	Atomic layer deposition
Bo	Bond number
CAD	Computer-aided design
CIJ	Continuous inkjet
CSD	Chemical solution deposition
CVD	Chemical vapor deposition
DBLI	Double beam laser interferometry
DOD	Drop-on-demand
DTA	Differential thermal analysis
E_c	Coercive field
EH	Energy harvester
FOM	Figure of merit
4PB	Four-point bending
FTIR	Fourier transform infra-red
GHS	Global harmonized system
Hacac	Acetylacetone
IDE	Interdigitated electrodes
IJP	Inkjet printing
IMO	Inverted mixing order
2ME	2-Methoxyethanol

MEMS	Microelectromechanical systems
MIM	Metal–insulator–metal
MOCVD	Metal–organic chemical vapor deposition
MOD	Metal–organic decomposition
1M2P	1-Methoxy-2-propanol
MPB	Morphotropic phase boundary
Oh	Ohnesorge number
P(VDF-TrFE)	Poly(vinylidene fluoride-*co*-trifluoroethylene)
PDMS	Poly(dimethylsiloxane)
PEDOT	Poly(3,4-ethylenedioxythiophene)
PEN	Poly(ethylene 2,6-naphthalate)
PLD	Pulsed laser deposition
P_r	Remanent polarization
PSS	Poly(styrene sulfonate)
PT	Lead titanate
PVDF	Poly(vinylidene fluoride)
PVD	Physical vapor deposition
PZT	Lead zirconate titanate
Re	Reynolds number
RMS	Root mean square
SAM	Self-assembled monolayer
SEM	Scanning electron microscopy
SIMS	Secondary ion mass spectrometry
TGA	Thermogravimetric analysis
We	Weber number
XRD	X-ray diffraction
XRR	X-ray reflectivity

Contents

Introduction

The invention of the printing press in the fifteenth century by Johannes Gutenberg was a turning point in History, as it enabled the dissemination of knowledge and profoundly transformed the European medieval society. Although techniques evolved significantly over the next centuries, the art of printing was still reserved for professional printing workshops. Another revolution took place in the second half of the twentieth century with the invention of computers and spreading of consumer electronics. While early forms of inkjet printing originated in the 1950s, inkjet printers able to reproduce digital images were developed in the 1970s and were made commercially available in the next decade [1]. With further democratization of the technology, inkjet printers have now become ubiquitous in many households, thereby granting the general public access to the reproduction of text and images on paper at low cost.

Modern inkjet printers operate via a simple basic principle: tiny ink droplets are generated either thermally or mechanically and are deposited at digitally determined locations on a substrate. The collection of all deposited droplets recreates the digital image designed by the user. This process can also be implemented at the industrial scale, as professional inkjet printers are now rivalling with offset technology for high-throughput applications [2]. However this technique is not limited to colored inks and paper as a substrate. In fact, inkjet printing recently emerged as a competitive alternative for the deposition of functional materials such as dielectrics, conductors, piezoelectrics, etc.

The current success of 3D printing anticipates enormous potential for inkjet printing as a deposition method for functional layers in the electronics industry. Both techniques are based on additive manufacturing, meaning that an object or a patterned film can be manufactured only by input of material. This makes additive manufacturing inherently cost-efficient compared to subtractive techniques involving lithography or etching commonly used to produce thin-film-based electronics. In addition, a drastic reduction of the amount of generated waste means that additive manufacturing is eco-friendly, which is also a major selling point for this technology.

In this context, it is of particular interest to consider inkjet printing as a fabrication technique for thin-film-based electronic devices such as conductive tracks, capacitors, transistors or diodes. Forecasts predict the market release of inkjet-printed OLED displays in the next years [3]. Another possible field of applications is represented by piezoelectric layers used in microelectromechanical systems (MEMS) and various sensing and actuating devices.

Lead zirconate titanate (PZT) is a metal oxide commonly used for these applications owing to its excellent piezoelectric properties. PZT thin films can be obtained via chemical solution deposition (CSD), where a solution containing the metal precursors is coated onto a substrate and subsequently processed to obtain the final functional oxide. CSD is already considered a low-cost processing method with respect to physical vapor deposition (PVD) techniques, but conventional deposition by spin coating is particularly wasteful due to its low material utilisation rate (~2 %) [4], synonymous with large amounts of precursor material needed and generated waste as a consequence.

The association of CSD and inkjet printing of PZT could therefore combine the best of both worlds: the low cost of PZT solutions and the high material utilization rate of inkjet printing. In turn, this would significantly reduce manufacturing costs and open up opportunities for mass production of piezoelectric devices.

However, several obstacles lie in the way as the adaptation of well-established PZT CSD processing for inkjet printing is not straightforward and poses a series of challenges. This thesis addresses several of these challenges in a way that has not yet been achieved by the state of the art. The present work consists of four main chapters, each of which will address a relevant challenge and attempt to answer a scientific question. After a background chapter explaining the main theoretical concepts and presenting the state of the art, the chapters of this thesis will be articulated as follows.

- Chapter 1 will address the issue of printing on a high surface energy substrate such as platinized silicon. Solutions proposed by the state of the art involve lithography-based steps or prior surface modification. **Can we print well-defined PZT thin-film structures on platinized silicon without lithography?**

- In Chapter 2, we will discuss how standard PZT solutions need to be modified for successful implementation in inkjet printing. We will see that these modifications bring about other process adaptations in order to obtain high-quality films. **How can we obtain PZT thin films with state-of-the art properties via inkjet printing?**

- Chapter 3 will showcase an example of application for inkjet-printed PZT films in the form of energy harvesters. **Can we implement inkjet printing of PZT in the fabrication of functional piezoelectric devices?**

- Finally, in Chapter 4, we will attempt to modify the formulation of PZT solutions based on the carcinogenic solvent 2-methoxyethanol by replacing it with a safe alternative. **Can we use a safe solvent for the preparation of PZT solutions?** We will also show how modified solutions can be used in the inkjet printing process of PZT.

Background

Piezoelectricity

Definition

In 1880, Pierre and Jacques Curie discovered the piezoelectric effect. As they were conducting experiments on crystals, they noticed that the compression of quartz, tourmaline or Rochelle salt (potassium sodium tartrate) resulted in an electric potential across the crystal. This phenomenon became known as the *direct* piezoelectric effect. The *converse* effect was predicted by Gabriel Lippmann and verified experimentally by the Curie brothers one year later: a piezoelectric crystal deforms when an electric field is applied across it (Fig. 1) [5].

The piezoelectric effect is linear, meaning that the deformation of the material and voltage (or electric field) across it are directly proportional.[a] The proportionality constant is the piezoelectric coefficient. Thanks to thermodynamic considerations, both the direct and converse piezoelectric effects are described by the same coefficient. We briefly introduce some notions about piezoelectric formalism here, which will be refined and exploited later.

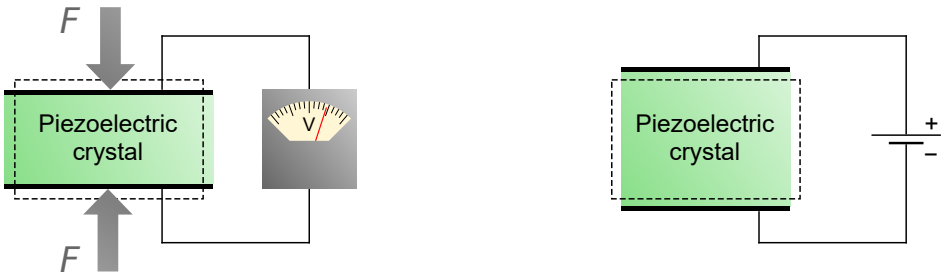

(a) Direct piezoelectric effect (b) Converse piezoelectric effect

Fig. 1. Illustration of the piezoelectric effect. (a) In the direct piezoelectric effect, the application of a force F (represented by the arrows) deforms the material and results in a voltage across it, which can be measured by a voltmeter. (b) In the converse piezoelectric effect, the electric field applied across the material causes a deformation of the latter.

[a] This contrasts with the electrostrictive effect, which applies to any dielectric material and where the deformation under an electric field is proportional to the square of the electric field. The deformation is therefore independent of the sign of the electric field.

Piezoelectricity brings together notions about mechanics and electricity. The general formalism that describes it involves tensor notation and depends on the boundary conditions of the considered system. Let S be the strain experienced by the material (dimensionless), T the stress in Pa, E the electric field in $\mathrm{V\,m^{-1}}$ and D the electric displacement in $\mathrm{C\,m^{-2}}$. The mechanical and electrical properties of the material are described by its compliance s [$\mathrm{Pa^{-1}}$] and permittivity ε [$\mathrm{F\,m^{-1}}$]. The superscript attributed to s or ε indicates the boundary condition.[b] The direct piezoelectric effect can expressed by eq. (1) and the converse effect by eq. (2).

$$D = \varepsilon^T E + dT \tag{1}$$

$$S = s^E T + dE \tag{2}$$

In the absence of an applied electric field, eq. (1) reduces to $D = dT$, which describes the linear relationship between the stress applied to the material and the resulting charge density that appears at its extremities (Fig. 1a). d is the piezoelectric coefficient and is expressed in $\mathrm{m\,V^{-1}}$. Similarly, when no stress is applied to the piezoelectric, eq. (2) becomes $S = dE$ and shows the direct proportionality between the applied electric field and the deformation (Fig. 1b). As stated above, the same coefficient d describes the direct and converse effect. Another formalism invokes the piezoelectric coefficient e,[c] which is expressed in $\mathrm{C\,m^{-2}}$. In this case, stiffness c [Pa] (inverse of compliance) appears in the equation.

$$D = \varepsilon^S E + eS \tag{3}$$

$$T = c^E S - eE \tag{4}$$

Note that we need to take into account the directions along which the electric field or the stress is applied. We will come back to these considerations when discussing the behavior of piezoelectric thin films.

Origin of piezoelectricity

The origin of piezoelectricity in a material is directly linked to the symmetry of its crystalline structure. When a piezoelectric crystal is deformed, the barycenters of positive and negative charges move with respect to each other, resulting in the appearance or variation of an internal dipole moment. As a consequence, the extremities of the crystal become charged. This can only happen if the crystal structure is non-centrosymmetric, i.e. it lacks an inversion center. Of the 32 crystalline classes that exist, 21 are non-centrosymmetric. Crystals that belong to class *432* constitute an exception as they do not exhibit piezoelectric properties. The remaining 20 non-centrosymmetric classes are piezoelectric [6].

[b] Constant S and constant T correspond to situations where the material is mechanically clamped and free, respectively. Likewise, constant E and constant D can refer to short circuit and to open circuit conditions, respectively.

[c] For the sake of completeness, note that there also exist g and h piezoelectric coefficients.

Pyroelectricity and ferroelectricity

In some piezoelectric materials, piezoelectricity is associated with another phenomenon called pyroelectricity. These materials constitute a sub-class of piezoelectrics, as only 10 of the 20 piezoelectric classes exhibit pyroelectricity. As a consequence, a pyroelectric material *is* piezoelectric, while the converse statement is not necessarily true. By definition, a pyroelectric material possesses permanent polarization in the absence of an applied electric field. Polarization is a quantity that describes the amount of dipole moments per unit volume and is expressed in $\mathrm{C\,m^{-2}}$. The macroscopic permanent polarization results from the presence of microscopic dipole moments globally pointing in the same direction.

Some pyroelectric materials possess an additional physical property called ferroelectricity. In these materials, polarization can be reversed or *switched* to another stable polarization state by the application of an external electric field in the opposite direction. As can be seen in Fig. 2a, the curve of polarization versus electric field is a hysteresis loop. In that sense, ferroelectricity can be considered as the electric equivalent of ferromagnetism, where similar hysteresis is observed for magnetization versus magnetic field curves.

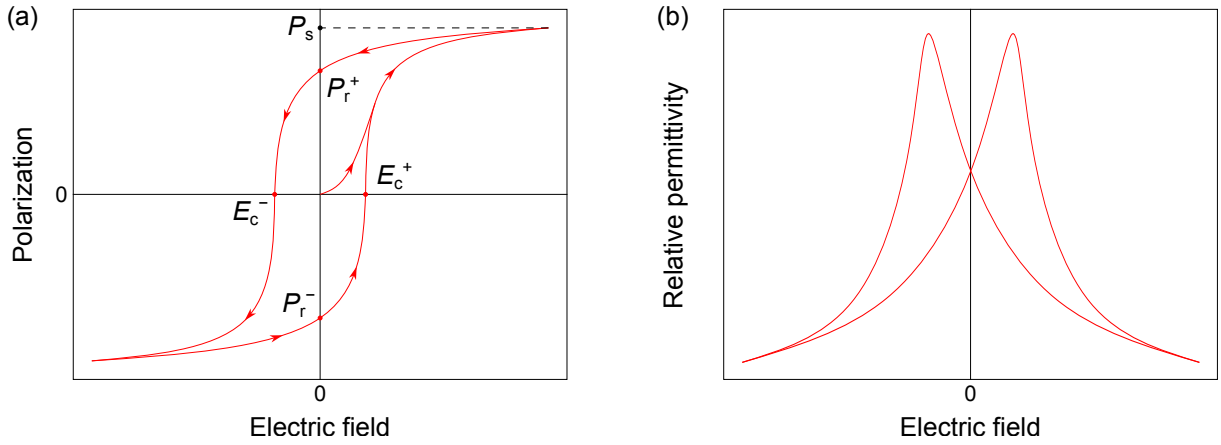

Fig. 2. Electrical properties of ferroelectric materials: (a) polarization–electric field hysteresis loop and (b) relative permittivity–electric field loop.

In the case of the polycrystalline ferroelectric materials that will be presented in this work, a permanent polarization is induced by exposure to an external electric field through a process called *poling*. Indeed, if a polycrystalline ferroelectric material is initially unpoled, the ferroelectric domains are oriented randomly. The macroscopic polarization is therefore zero. As depicted in Fig. 2a, when an electric field is applied, the polarization increases until it reaches a maximal value called the saturation polarization (P_s). Upon removal of the electric field, polarization remains at a non-zero value known as the remanent polarization (P_r). Reversal of the electric field is accompanied by progressive back-switching of the microscopic dipoles and associated ferroelectric domains, resulting in a decrease of polarization until it reaches zero: this electric field is called the coercive field (E_c) of the ferroelectric. Further increase of the

electric field in the negative direction results in an increase of the polarization in the negative direction as well. The rest of the loop is analogous to the positive case. The response of a simple dielectric material would be linear under the same conditions.

Likewise, for a ferroelectric material the evolution of the relative permittivity ε_r with an external applied electric field exhibits unique features. The relative permittivity versus electric field loop has a characteristic butterfly shape with two maxima (Fig. 2b), which correspond to the coercive fields mentioned earlier.

Piezoelectric materials

Quartz and wurtzites

A well-known piezoelectric material is quartz in α phase (low-temperature phase), which is used as a resonator in electronics. Quartz belongs to the trigonal system (point group *32*). A schematic representation of the crystal structure explaining the piezoelectric properties of quartz is shown in Fig. 3a: while the barycenters of positive and negative charges represented by Si^{4+} and O^{2-} ions coincide in the absence of stress, a net dipole moment appears when the crystal is deformed by compression.

Another family of piezoelectric materials are wurtzites, best represented by aluminium nitride (AlN) and zinc oxide (ZnO). The piezoelectric properties and excellent acoustic quality factor of AlN are exploited in acoustic wave filters [6]. ZnO can be grown into nanowires which can be used in piezoelectric nanogenerators [7]. Wurtzites belong to the hexagonal system (point group *6mm*) and can be described as two interpenetrated hexagonal structures offset by $\frac{3}{8}\,c$ along the c direction, as shown in Fig. 3b. These materials are therefore pyroelectric, but they do not usually exhibit ferroelectricity. However, it was recently shown that high levels of scandium doping in AlN resulted in the appearance of a measurable ferroelectric response [8].

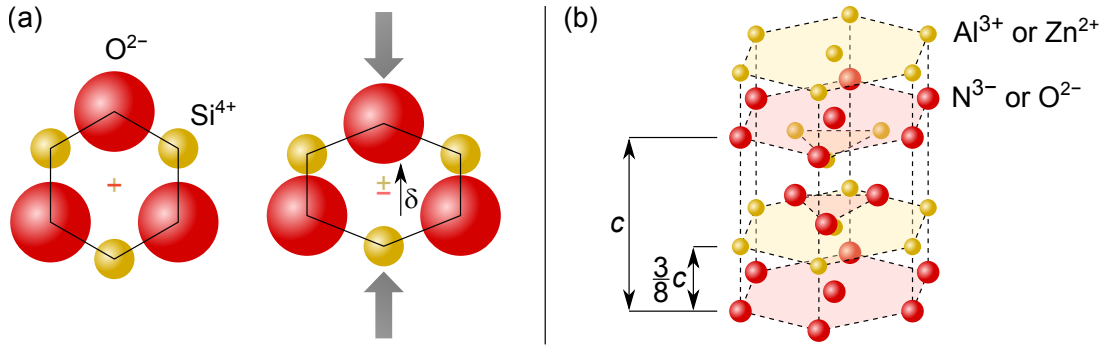

Fig. 3. Representation of the crystal structure of (a) quartz and (b) wurtzites. In (a), when no stress is applied on the crystal structure of quartz, the barycenters of positive and negative charges coincide. As the crystal is deformed by compression, a net dipole moment δ appears. (b) Charge asymmetry in the structures of AlN and ZnO arises from the $\frac{3}{8}c$ offset between the interpenetrated networks of cations and anions.

Perovskites

Alongside these examples exists a family of crystals called *perovskites*, whose name is derived from the naturally occurring mineral $CaTiO_3$. The perovskite structure is described by the general formula ABO_3, where A and B are metal cations with different ionic radii ($r_A > r_B$). The crystal structure can be simply represented as a cube, where A cations occupy the vertices and the B cation lies in the center, surrounded by an octahedron of oxygen anions (Fig. 4a). As such, this *cubic* structure is not piezoelectric and it exists above a temperature known as the Curie temperature (T_C) of the perovskite. Below T_C, distortions of the cubic cell break centrosymmetry, resulting in the appearance of pyroelectricity, as seen in Fig. 4b [6].

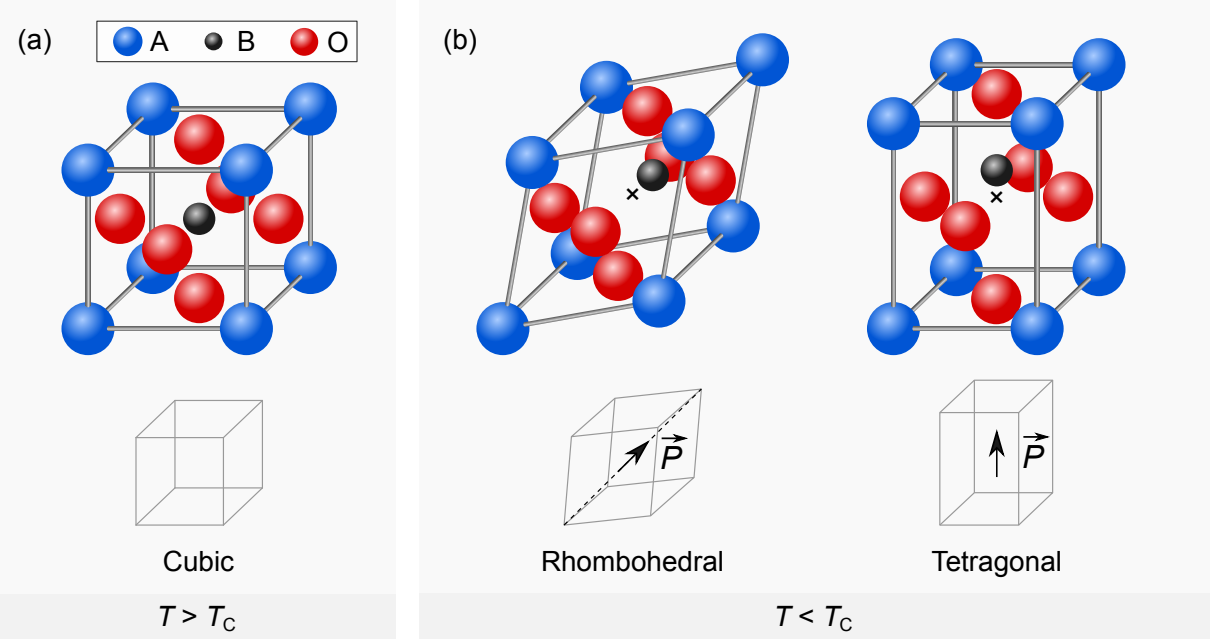

Fig. 4. (a) Cubic perovskite structure and (b) distortions of the cubic cell resulting in a non-centrosymmetric structure below the Curie temperature (T_C). The polarization vector $\vec{P}$ is oriented along the [111] direction in the rhombohedral cell and along the [001] direction in the tetragonal cell.

Lead zirconate titanate ($PbZr_xTi_{1-x}O_3$, abbreviated as PZT) is a well-studied perovskite known for its excellent piezoelectric properties. It is a solid solution of lead zirconate $PbZrO_3$ and lead titanate $PbTiO_3$. In the crystal structure of PZT, Pb^{2+} cations occupy the A sites, while Zr^{4+} and Ti^{4+} cations are on the B sites. The phase diagram of PZT is presented in Fig. 5 [9]. Titanium-rich compositions adopt a tetragonal structure, while zirconium-rich PZT have a rhombohedral structure. A particular feature of this phase diagram is the so-called *morphotropic phase boundary* (MPB) separating the rhombohedral and tetragonal structures below T_C.

PZT at this specific composition displays enhanced piezoelectric properties [10]. In addition, as the MPB is almost vertical, the piezoelectric properties of PZT are remarkably stable with temperature up to its Curie temperature at 350 °C, making it a material of choice for piezoelectric applications.

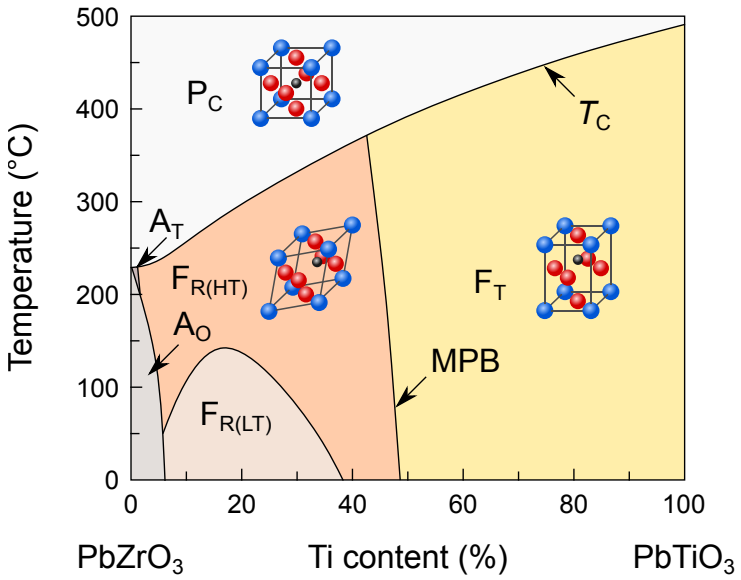

Fig. 5. Phase diagram of PZT, based on Jaffe et al. [9]. The main phases are the paraelectric cubic (P_C), ferroelectric high-temperature and low-temperature rhombohedral phases ($F_{R(HT)}$ and $F_{R(LT)}$, respectively) and ferroelectric tetragonal (F_T) phases. The antiferroelectric orthorhombic (A_O) and antiferroelectric tetragonal (A_T) phases are also represented.

Material geometry and applications

The particular properties of piezoelectric materials allow them to carry out electromechanical transduction, i.e. the direct transformation of mechanical energy into electrical energy and vice versa. Depending on the application, PZT can be found in several forms: bulk (single crystals and ceramics) or thin films. Bulk PZT ceramics are typically found in piezoelectric buzzers, lighters, fuel injectors in diesel engines, ultrasound transducers and electronic components such as capacitors and resonators.

Applications of PZT in the form of thin films (films thinner than 10 µm) include various types of sensors, actuators and energy harvesters. Integration of PZT thin films on silicon-based substrates has been extensively studied in the past decades and constitutes the basis for the development of piezoelectric microelectromechanical systems (MEMS). Notable examples are represented by micro-mirrors, micro-pumps, inkjet nozzles or micro switches [11]. Integration of PZT thin films on other substrates such as metal foils for energy harvesting [12] or glass for haptic applications [13] is also currently gaining attention.

The use of thin films for piezoelectric applications is particularly attractive for two main reasons: (1) they require lower processing temperatures compared to bulk ceramics and (2) the poling process is simpler in the case of thin films with respect to bulk ceramics, as relatively low voltages give rise to high electric fields at the thin-film scale. The present work will focus exclusively on PZT thin films. We now come back to the definition of the piezoelectric coefficients and specify them in the case of thin films.

The characterization of the piezoelectric response of a material depends on the considered direction and configuration of the piezoelectric stack. One possible configuration for thin-film-based piezoelectric devices is the metal–insulator–metal (MIM) structure, where the piezoelectric layer is surrounded by electrodes. If we place this structure in a coordinate system as shown in Fig. 6, the electric field will be applied along direction 3. Measuring the deformation in direction 1 gives access to the transverse e_{31} coefficient (Fig. 6a). Likewise, if we measure the deformation in direction 3, we can determine the longitudinal d_{33} piezoelectric coefficient (Fig. 6b).

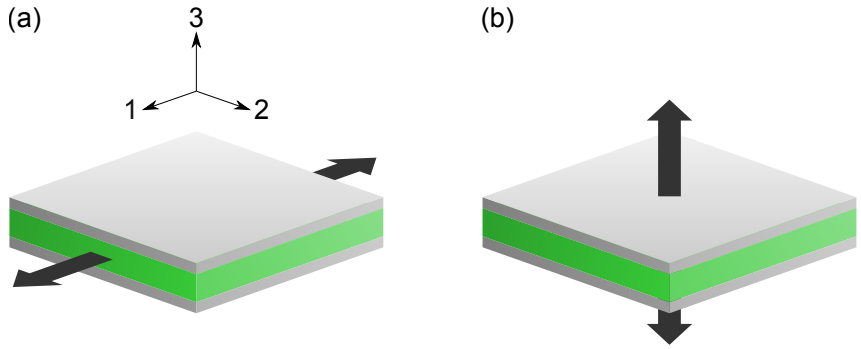

Fig. 6. Electromechanical response of piezoelectric thin films: (a) transverse and (b) longitudinal response.

Strictly speaking, we measure *effective* piezoelectric coefficients in the case of thin films because of the mechanical boundary conditions imposed by the substrate (the piezoelectric film is clamped by the substrate). The effective $e_{31,\mathrm{f}}$ and $d_{33,\mathrm{f}}$ coefficients are related to the in-plane and out-of-plane piezoelectric coefficients, as well as the stiffness (c) or compliance (s) coefficients [6]:

$$e_{31,\mathrm{f}} = e_{31} - \frac{c_{13}^{E}}{c_{33}^{E}} e_{33} \tag{5}$$

$$d_{33,\mathrm{f}} = d_{33} - 2\frac{s_{13}^{E}}{s_{11}^{E} + s_{12}^{E}} d_{31} \tag{6}$$

These piezoelectric coefficients will be measured and discussed in the present work. Details on piezoelectric characterization techniques can be found in Appendix D (please refer to page 139). We will now describe the main methods used for the fabrication of piezoelectric thin films.

Processing of piezoelectric metal oxide thin films

Physical methods

In physical vapor deposition (PVD), thin films are formed out of a vapor phase that is condensed onto a substrate, under vacuum conditions. The vapor phase is created from a condensed phase precursor called *target*, which can be fabricated via the bulk ceramic process. Alternatively, the precursor metals can be supplied via metallic targets. The method by which the vapor is created then depends on the particular PVD technique.

Pulsed laser deposition (PLD) uses a high-power laser to vaporize the target material in the form of a plasma plume, which then deposits onto the substrate mounted on a heating stage (Fig. 7a). This technique is mainly used for research purposes as its large-scale deployment for industrial applications is challenging [14]. Careful tuning of the processing parameters allows for the deposition of high-quality PZT films with well-controlled stoichiometry. For example, PLD was used for the growth epitaxial PZT films [15, 16]. Other examples from the literature include doped PZT films grown on platinized silicon [17] and piezoelectric devices based on PLD-derived PZT films [18].

In **sputtering**, the vapor phase is created by collisions between ions and the target. The ions are generated from an inert gas such as argon introduced into the deposition chamber and ionized. In rf (radiofrequency) sputtering, the plasma is created by an oscillating electric field between the target and the substrate (Fig. 7b). A selection of references from the literature report on sputter-deposited PZT films on platinized silicon [19], on glass [20] or on metal foils for piezoelectric energy harvesting applications [21]. Sputtering can also be used for the deposition of PZT films at fast rates (up to 250 nm min^{-1}), as reported by Jacobsen et al. [22].

While PVD techniques can be used for the fabrication of high-quality PZT thin films, their use in an industrial context can be difficult due to the associated costs. Indeed, they require vacuum conditions, as well as expensive targets and equipment. A cost-efficient alternative to these techniques is represented by chemical deposition methods.

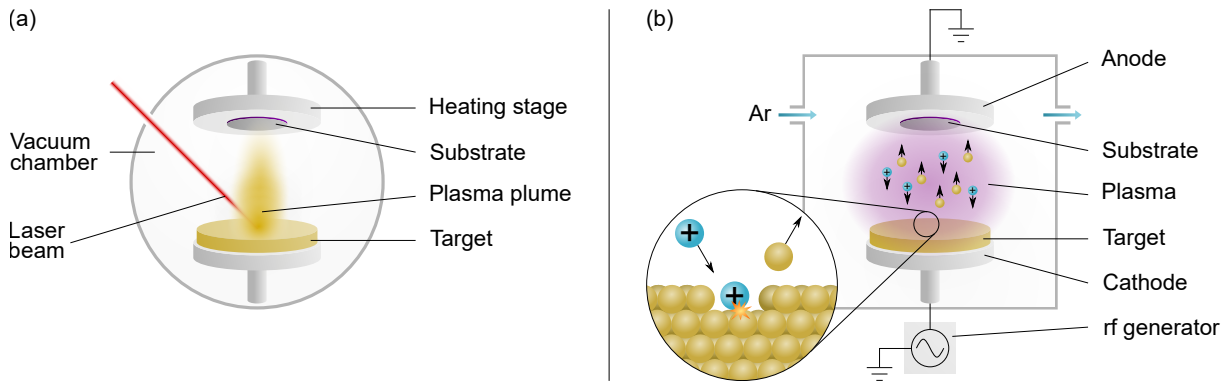

Fig. 7. Working principle of PVD techniques: (a) pulsed laser deposition and (b) sputtering.

Chemical methods

Contrary to physical deposition methods, chemical methods supply the metal precursors in molecular form. Decomposition of the precursors at the substrate surface or in post-deposition annealing steps affords the crystalline metal oxide layer.

Chemical vapor deposition

Chemical vapor deposition (CVD) consists in exposing the substrate to precursors in the vapor phase. Reaction or decomposition of the precursors at the surface results in film growth (Fig. 8a). Of the many variants of this technique, metal–organic CVD (MOCVD) is the most popular for the deposition of metal oxide films such as PZT. Typical precursors are organometals, alkoxides or β-diketonates. In 1990, Okada et al. reported the fabrication of highly oriented PZT films on MgO(100) by MOCVD using tetraethyllead, titanium(IV) isopropoxide and zirconium(IV) dipyvaloylmethane as precursors [23] (Fig. 8b). The main advantage of this method is the fabrication of high-quality films with a fast deposition rate (10 nm min^{-1}). However, organolead compounds are extremely toxic and should be handled with great care. In a recent contribution, Kim et al. reported on the synthesis of Pb(IV) precursors for the deposition of PZT thin films via MOCVD [24].

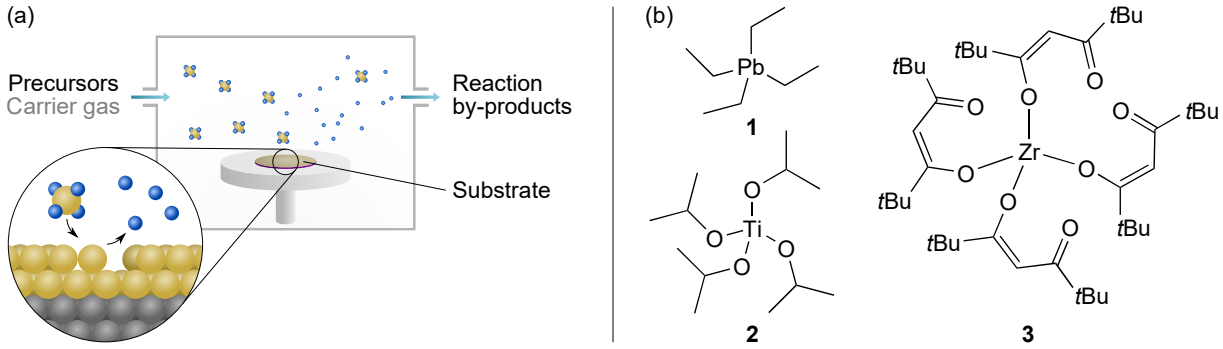

Fig. 8. (a) Working principle of CVD and (b) structures of the precursors used by Okada et al. for the deposition of PZT thin films via MOCVD [23]: tetraethyllead **1**, titanium(IV) isopropoxide **2** and zirconium(IV) dipyvaloylmethane **3**.

Chemical solution deposition

In chemical solution deposition (CSD), the metal precursors are first dispersed in a liquid medium. The resulting solution is then coated onto a substrate to form a layer. A series of thermal steps needs to be subsequently carried out to transform the precursor solution into a solid crystalline film. The main stages of the CSD process are illustrated in Fig. 9 and can be summarized as follows.

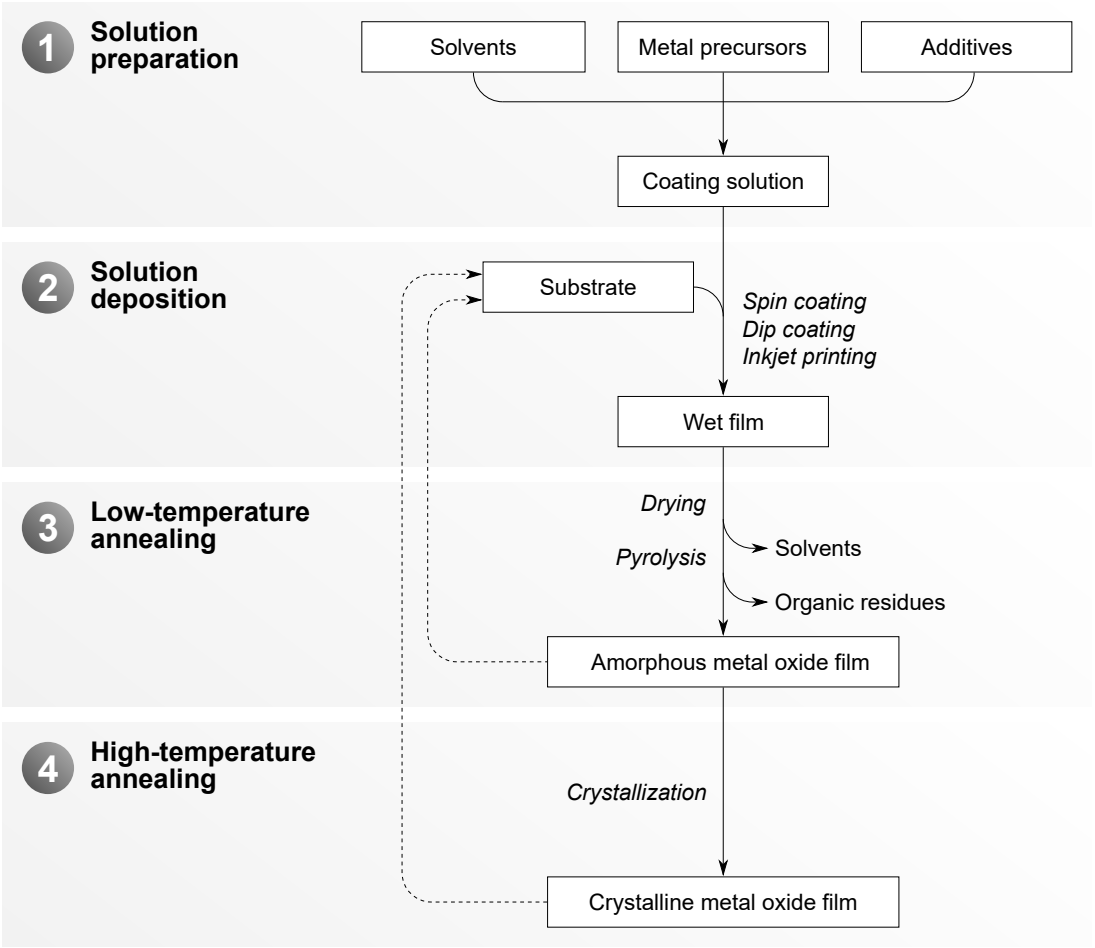

Fig. 9. Flow chart illustrating chemical solution deposition of metal oxide thin films.

1. **Solution preparation.** The solution should be a homogeneous and stable dispersion of metal cations. It is prepared from metal precursors selected for their solubility in the solvent and compatibility with the rest of the process. Importantly, the viscosity of the solution should be adapted to the deposition method by a careful choice of solvents.

2. **Solution deposition.** The solution is deposited onto a substrate via a coating method such as spin coating, dip coating or inkjet printing. This step should apply the solution onto the substrate surface in a homogeneous manner in order to create a liquid film whose thickness can be controlled by tuning the deposition parameters.

3. **Low-temperature annealing.** After deposition, all the organic content must be removed from the film. A drying step (100–200 °C) is usually carried out to evaporate the solvent. The dried film then undergoes a treatment at higher temperature (350–500 °C) called pyrolysis in order to eliminate the residual organic content. This thermal process can also be assisted by light via the incorporation of photoactive species in solution [25]. After pyrolysis, the film should be an amorphous metal oxide. Additional deposition–low-temperature annealing sequences can be performed to increase film thickness.

4. **High-temperature annealing.** Upon completion of pyrolysis, the amorphous film is heated at higher temperature (600–800 °C) to induce the formation of the crystalline phase. The deposition and thermal processing steps are usually repeated to increase film thickness. Indeed, in most cases thick films cannot be grown in a single deposition step because cracks may appear during the thermal treatment. This issue can be addressed by the use of polymer-based solutions, which enable the growth of thicker films in fewer deposition steps [26].

Depending on the type of precursors and chemistry, several terms are often employed to denote CSD, and will be clarified hereafter [27–29]. The so-called **sol–gel process** describes a family of techniques used to prepare inorganic materials from solution-based molecular precursors dissolved in a polar solvent. The starting point is the preparation of a colloidal solution (*sol*), typically based on metal alkoxides, i.e. chemical species of the form $M(OR)_n$, where M is a metal or silicon and R an organic moiety. The two main chemical processes that govern the assembly of these molecular building blocks are hydrolysis and condensation. Hydrolysis occurs in the presence of water, which substitutes alkoxy groups at the metal center, thus forming reactive hydroxy species, eq. (7). These species subsequently react through a condensation reaction, with release of a water (eq. (8)) or an alcohol molecule (eq. (9)), thus forming an oxygen bridge between two metal centers (M−O−M). Another possible reaction is olation, where the metal cations are connected via a hydroxy bridge. The kinetics of these reactions can be controlled by adjusting the solution pH.

$$M(OR)_n + H_2O \longrightarrow M(OH)(OR)_{n-1} + ROH \tag{7}$$

$$2\,M(OH)(OR)_{n-1} \longrightarrow M_2O(OR)_{2n-2} + H_2O \tag{8}$$

$$2\,M(OH)(OR)_{n-1} \longrightarrow M_2O(OH)(OR)_{2n-3} + ROH \tag{9}$$

This process results in the formation of a complex inorganic polymeric network entrapping solvent (*gel*). The transformation from the sol to gel state is known as the sol–gel transition or gelation. Removal of the solvent from the inorganic matrix yields porous materials or powders. The sol can also be coated onto a substrate and processed into a dense solid film. An overview of the sol–gel process is shown in Fig. 10a.

The sol–gel process can be used to fabricate a variety of inorganic materials ranging from silica to complex oxides such as perovskites. Budd et al. first reported sol–gel processing of PZT thin films in 1985 [30]. Their approach consisted in adapting the single-cation sol–gel process to the complex PZT system with three cations. In their original contribution, the authors used lead(II) acetate and zirconium(IV) and titanium(IV) alkoxides as metal precursors. The Pb precursor was reacted separately in 2-methoxyethanol, then combined with the B-site alkoxides. Reflux and distillation steps were carried out to improve solution homogeneity and eliminate reaction by-products. Before deposition, small amounts of water were added to initiate partial hydrolysis (Fig. 10b).

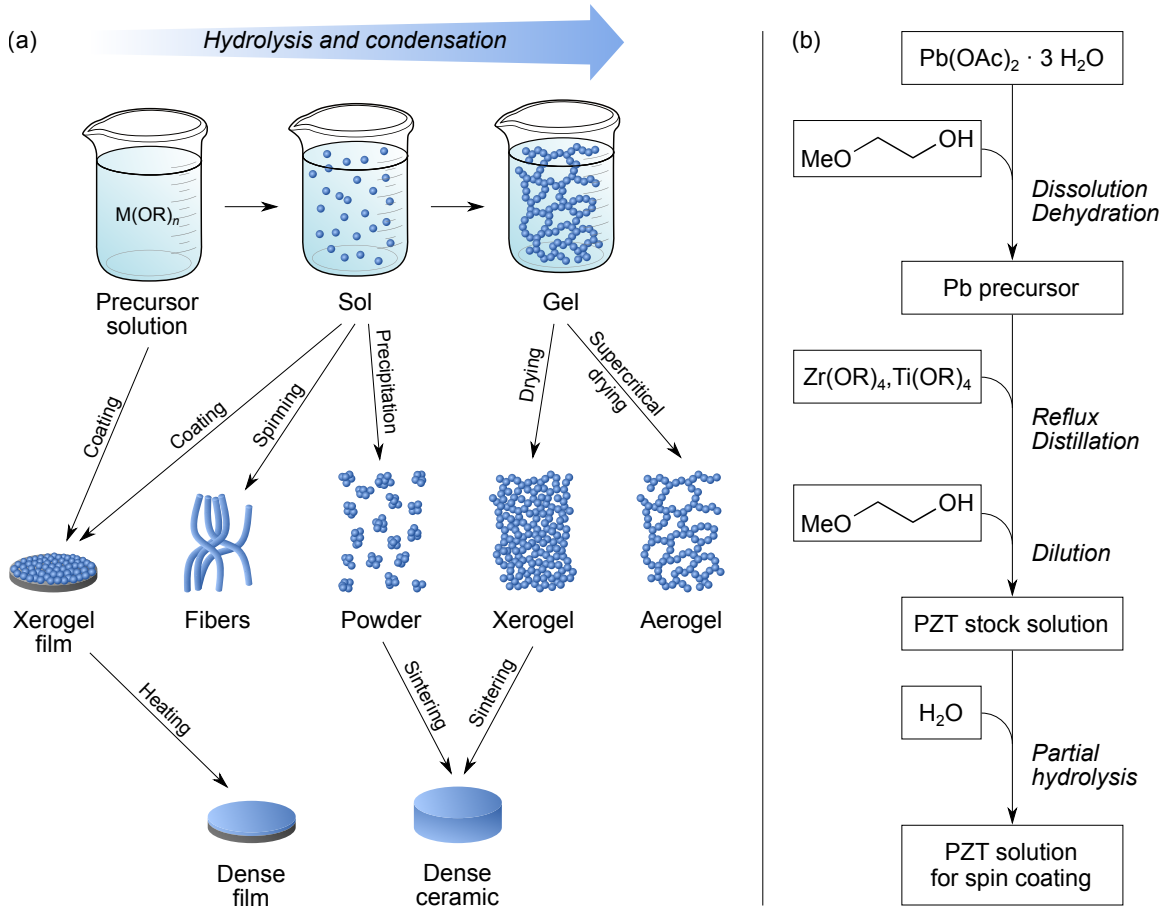

Fig. 10. (a) Overview of the sol–gel process and associated fabrication methods. (b) Original process for the preparation of PZT solutions via the sol–gel process, as described by Budd et al. [30].

From a chemical point of view, only the chemistries of zirconium and titanium alkoxides are that of *true* sol–gel in this system. Indeed, alkoxides of the B-site cations are water-sensitive precursors that can undergo hydrolysis and condensation reactions to form oligo- and polymeric species. The lead cation does not significantly contribute to this main framework and rather occupies random interstitial positions in the gel [31]. Still, the presence of Pb–O–Zr and Pb–O–Ti linkages was evidenced in precursor solutions [32].

This process was found to be remarkably robust and offered good control of the chemical composition of the layers. However, a drawback of the classical sol–gel approach is the long synthesis time and the fact that incomplete reflux or distillation steps may result in premature aging of the solutions [28]. Despite its excellent ability to stabilize alkoxides, the use of the carcinogenic and teratogenic solvent 2-methoxyethanol is also a notable issue. Other solution chemistries were therefore also developed in the wake of the seminal work by Budd et al.

An alternative technique known as **metal–organic decomposition** (MOD) exploits a radically different type of chemistry. Precursors in MOD are typically long-chain carboxylates and β-diketonates and are usually dissolved in an apolar, non-interacting solvent. The precursor species in MOD systems have therefore low reactivity and low sensitivity to water compared

to classical sol–gel systems. Furthermore, the structure of the metal precursors is mostly preserved in solution. A contribution by Fukushima et al. in 1984 already reported the use of lead(II) 2-ethylhexanoate, zirconium(IV) acetylacetonate and titanium(IV) butoxide in butanol as precursor solution for the deposition of PZT films [33]. In 1991, Vest and Zhu described a system that better fits the definition of MOD, with lead(II) 2-ethylhexanoate, zirconium(IV) 2-ethylhexanoate or zirconium(IV) neodecanoate and titanium(IV) dimethoxydineodecanoate in xylene as precursor solution [34] (Fig. 11).

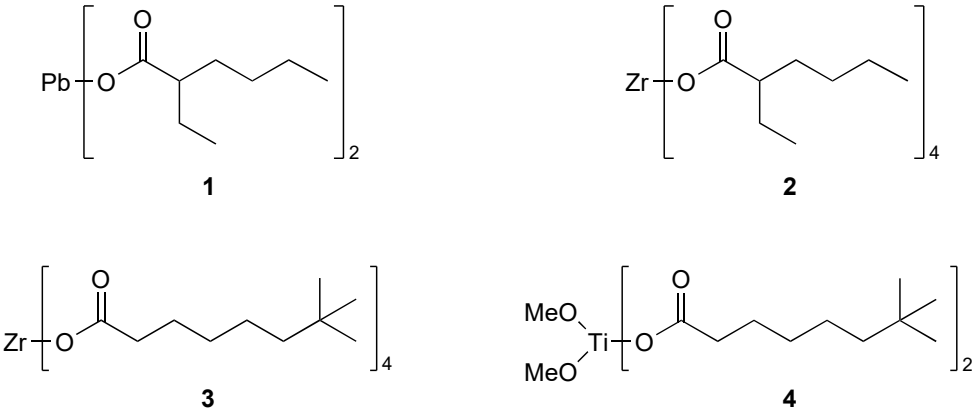

Fig. 11. Structures of precursors employed by Vest and Zhu [34] for the processing of PZT thin films via MOD: lead(II) 2-ethylhexanoate **1**, zirconium(IV) 2-ethylhexanoate **2**, zirconium(IV) neodecanoate **3** and titanium(IV) dimethoxydineodecanoate **4**.

As indicated by the name, **hybrid processes** make use of a combination between sol–gel and MOD in the sense that A-site cations are provided by carboxylate precursors and B-site cations by alkoxides. In addition, chelating agents such as carboxylic acids (e.g. acetic acid) and β-diketonates (e.g. acetylacetone) are often employed in hybrid systems to stabilize the precursors by reducing the sensitivity of alkoxides towards hydrolysis.

The first chelate-based approach for the preparation of PZT solutions was introduced by Yi et al. in 1988 [35], who used acetic acid as a solvent and chelating agent in a sol–gel system based on lead(II) acetate, zirconium(IV) propoxide and titanium(IV) isopropoxide. In 1993, Assink and Schwartz developed a synthesis route known as the 'inverted mixing order' (IMO) process [36], as described in Fig. 12. This fast preparation method is based on prior modification of the B-site alkoxides with a chelating agent (acetic acid) before addition of the lead precursor (lead(IV) acetate in this case). Methanol was used as a co-solvent and a controlled amount of water was added for partial hydrolysis. The IMO process affords stable solutions with better B-site cation homogeneity compared to the standard process and avoids the use of the hazardous solvent 2-methoxyethanol. The downside of this approach is the difficulty to precisely control hydrolysis in solution, as water is also introduced by the hydrated lead precursor and the esterification reactions taking place between acetic acid and alcohols. This irremediably leads to solution aging.

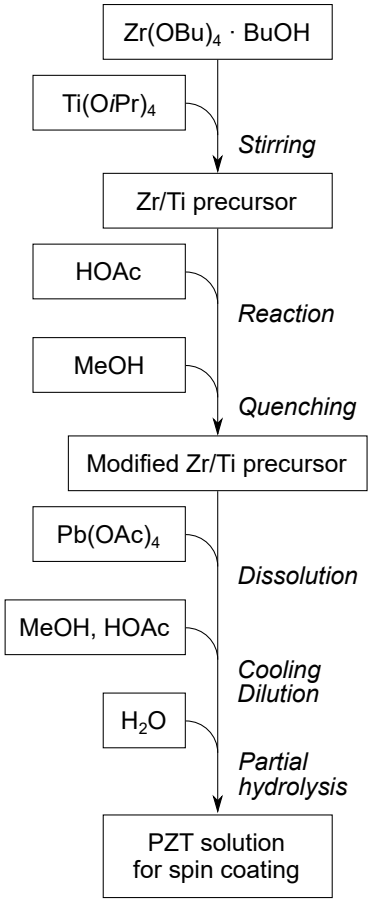

Fig. 12. Hybrid IMO process for PZT solutions developed by Assink and Schwartz [36].

The processing of PZT by CSD also has a series of caveats that need to be considered. Over the last decades, further developments of the original IMO route were made to address these issues. Lead oxide (PbO) has a high vapor pressure at the typical temperatures used for processing of PZT films and spontaneously sublimates. Lead also has the tendency to diffuse in the underlying platinum electrode, which forms transient intermetallic Pt_xPb phases during annealing. Both of these processes result in lead-deficient layers. This is usually addressed by incorporating a superstoichiometric amount of lead precursor in the solution, typically ranging from 5 to 30 % [28]. Lead deficiency is at the origin of the parasitic secondary phases fluorite and pyrochlore[d] that degrade the properties of the PZT films. Since PbO sublimates at a higher rate at the film surface, small amounts of pyrochlore (< 5 %, often not detected by X-ray diffraction) may form on the surface [29]. This surface pyrochlore can be converted into perovskite by coating of a PbO layer over the crystallized film and reannealing.

[d] Both the fluorite ($Pb_2(Zr,Ti)_2O_{7-x}$) and pyrochlore ($Pb_2(Zr,Ti)_2O_7$) have a cubic structure and are formed in lead-deficient environments as they can accommodate larger stoichiometric deviations than the perovskite phase. These phases are also formed transiently during crystallization and are subsequently converted into the perovskite phase, except at the interfaces where Pb volatility is high.

Another particularity of CSD-derived PZT films is related to the crystallization mechanisms. Crystallization of the layer proceeds via nucleation events, which can occur in the bulk of the film in the case of homogeneous nucleation or at interfaces (substrate or film surface) in the case of heterogeneous nucleation (Fig. 13). These two competing mechanisms have an influence on the final film microstructure. In the case of PZT films, heterogeneous nucleation is preferred because it affords textured polycrystalline films with columnar microstructure. It is known that {100}-textured films have a greater piezoelectric response than {111} or randomly oriented films [37]. The type of nucleation process that will occur depends on nucleation kinetics and can be affected by pyrolysis and crystallization conditions (heating profile and atmosphere).

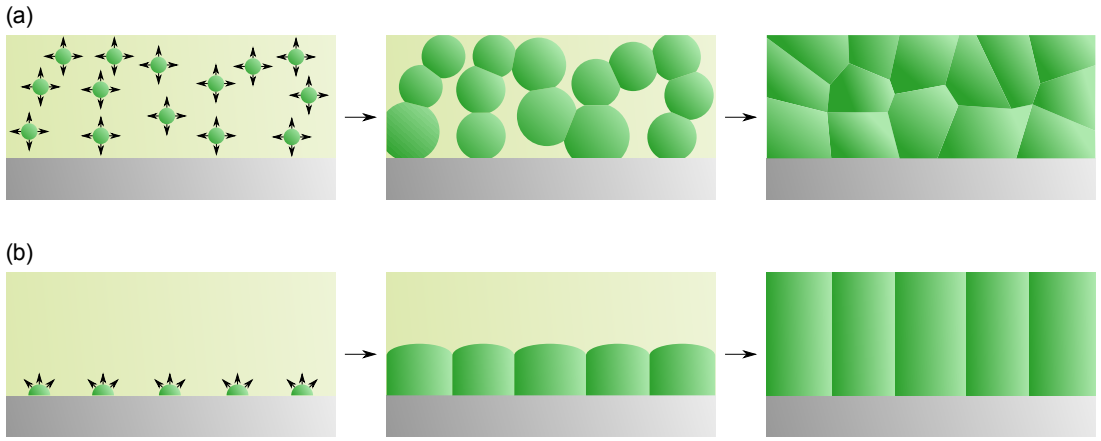

Fig. 13. Nucleation mechanisms occurring in CSD-derived PZT thin films: (a) homogeneous nucleation and (b) heterogeneous nucleation.

The development of texture is also intimately related to the nature and texture of the substrate. Hence a popular approach for texturing PZT thin films is the use of seed layers. PZT films grown on platinized silicon tend to adopt the {111} orientation of platinum. Titanium oxide (TiO_x) seed layers were also shown to favor this orientation. The preferred {100} orientation for piezoelectric applications can be obtained via $PbTiO_3$ or PbO seed layers [38]. In addition, pyrolysis temperature and crystallization conditions also play a major role in the growth of textured layers [28, 39].

Interestingly, in the case of heterogeneous nucleation from the substrate, the crystallization of the layer proceeds via a titanium-rich phase. As the crystallization proceeds from the substrate to the surface, the layer is progressively depleted from titanium, resulting in a chemical gradient of zirconium and titanium cations. When several sets of depositions are carried out with a crystallization step in between, chemical depth analysis reveals a characteristic sawtooth profile [40]. In 2007, Calame and Muralt presented a modification of the sol–gel process to fabricate gradient-free PZT films [41]. Their strategy consisted in using four solutions with different stoichiometries (Zr/Ti ratios) in order to compensate the segregation effect during crystallization. In addition, the authors showed that gradient-free PZT films exhibit enhanced piezoelectric response (up to 20 %) compared to layers with a chemical gradient.

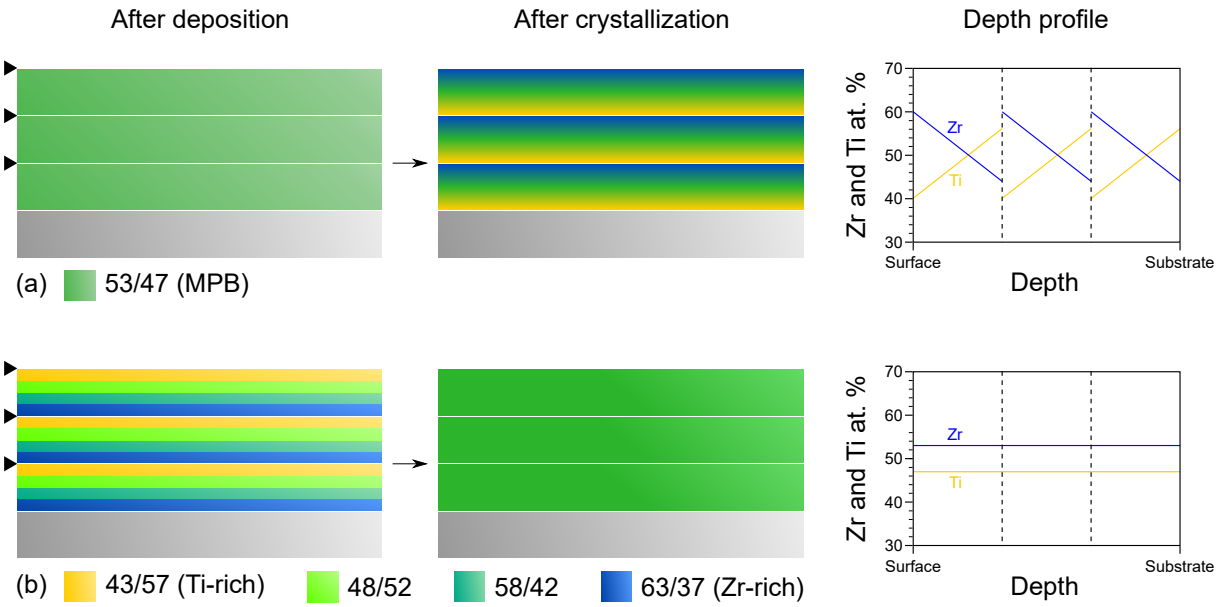

Fig. 14. Illustration of the chemical gradient phenomenon in CSD-derived PZT films. In (a), a single solution with MPB composition was used (Zr/Ti = 53/47). The black triangles (►) indicate the crystallization steps. In the final crystallized film, the Zr and Ti contents follow a sawtooth profile. The strategy of Calame and Muralt [41] shown in (b) makes use of four solutions with different stoichiometries to counterbalance the chemical gradient, resulting in a significant attenuation of the gradient in the final PZT film.

The typical temperatures used for the crystallization of PZT thin films (600–700 °C) are prohibitively high for direct integration on certain substrates such as glass or polymers. In addition, high temperatures are the cause of lead loss and diffusion, as explained earlier. Various strategies have been developed to decrease the crystallization temperature of CSD-derived PZT thin films [25, 42]. Seeding can be used to improve crystallization kinetics by increasing the density of nucleation sites, either via a seed layer grown on the substrate [43] or crystalline seeds incorporated in the solution [44]. Other approaches consisting in tailoring solution chemistry by improving cation homogeneity [45] or extending crystallization time [46] were also reported by Kosec et al. Alternative annealing conditions can also be envisaged, with reports of low-temperature PZT crystallization using laser [47] or microwave annealing [48]. PZT processing temperatures as low as 400–450 °C were achieved via these strategies.

The modification of solution chemistry for low-temperature processing can also be done via the addition of photoactive species. One notable example is represented β-diketonate complexes of titanium or zirconium, which have strong absorption bands in the UV range. Irradiation by UV light during processing was shown to promote the removal of organics from the layers, thereby assisting the pyrolysis step [25]. With this method, Bretos et al. have shown that PZT could be crystallized at 350 °C, enabling its integration on a flexible polyimide substrate [49].

Finally, it was shown that CSD could also be used to grow epitaxial PZT films [50] and a variety of ferroelectric oxide nanostructures [29]. All these examples illustrate the considerable

developments that were achieved during the last decades and the potential of CSD processing with respect to PVD techniques, as CSD gives access to large-area high-quality layers at a reasonable cost without the need for vacuum conditions nor large-scale PVD installations.

Several coating techniques can be used to deposit PZT films from CSD-based solutions. Spin coating is probably the most popular: it consists in applying an excess of solution onto the substrate and then spinning it at high velocity (several thousand rpm). The excess solution is immediately spun off, while a thin homogeneous film forms on the substrate. This coating process is particularly wasteful as the material utilization rate is only about 2 % [4]. In dip coating, the substrate is immersed in the solution, then pulled out of it at a constant speed. Although CSD is considered as a low-cost process, both of these coating techniques require a large excess of precursor solution that is not incorporated into the final product. In addition, the fabrication of patterned layers requires the use of lithography, which adds extra manufacturing costs. Both of these issues can be addressed by the use of inkjet printing as a coating method, as will be discussed in the next section.

Inkjet printing

Principle

Inkjet printing (IJP) is based on the deposition of liquid droplets (V_{droplet} = 1–100 pL) at precise locations on a substrate. Under ideal conditions, these droplets merge together and form a homogeneous continuous layer on the substrate. After deposition, drying and/or other processing steps are required to convert the precursor liquid into the final functional material. IJP is an additive manufacturing technique, meaning that the functional material is only deposited where needed, thus alleviating the need for subtractive steps (lithography or etching). Moreover, it allows for freedom of geometry as the printed structures are first created digitally via computer-aided design (CAD). In the context of low-cost manufacturing, IJP also has the combined advantage of being compatible with CSD and operating under ambient pressure conditions.

Contemporary inkjet printers are based on either continuous inkjet (CIJ) or drop-on-demand (DOD) inkjet printing technologies. In CIJ, a stream of droplets is created from a continuous jet of ink due to the Plateau–Rayleigh instability.[e] As the droplets pass through an electrostatic field, they become electrically charged and can be steered onto a substrate using an electric field. Droplets that were not deflected are collected and recycled. For this reason, CIJ is not used for IJP of functional materials, as the ink recycling process may degrade its quality [51].

In contrast, in DOD systems ink droplets are only generated when needed, which can be done via two mechanisms. Thermal IJP uses a resistive heating element to create a gas bubble in the ink chamber. The rapid expansion of this gas bubble increases the pressure, forcing an ink droplet out of the nozzle (Fig. 15a). In piezoelectric DOD IJP, the pressure increase is caused by the deformation of a piezoelectric element under an applied voltage waveform (Fig. 15b). Piezoelectric inkjet printheads have now become standard for printing functional materials thanks to the decrease of their manufacturing costs and the fact that they do not cause thermal degradation of the ink [51].

In the past decades, IJP was successfully used to deposit a variety of materials including polymers [52], metals [51] and ceramics [53]. These achievements pave the way towards the fabrication of a wide range of devices by inkjet printing, such as organic thin-film transistors, solar cells, light-emitting diodes, memories and sensors [54]. Although conceptually simple, IJP comes with several technical challenges, starting with the formulation an appropriate ink for reliable jetting. After reaching the substrate, the liquid droplets experience interactions with it, as well as subsequent drying, both of which may impact the homogeneity of the final functional layer [55]. These aspects will be covered in the following paragraphs.

[e] The Plateau–Rayleigh instability describes the phenomenon by which a continuous stream of fluid can break up into individual droplets under certain conditions.

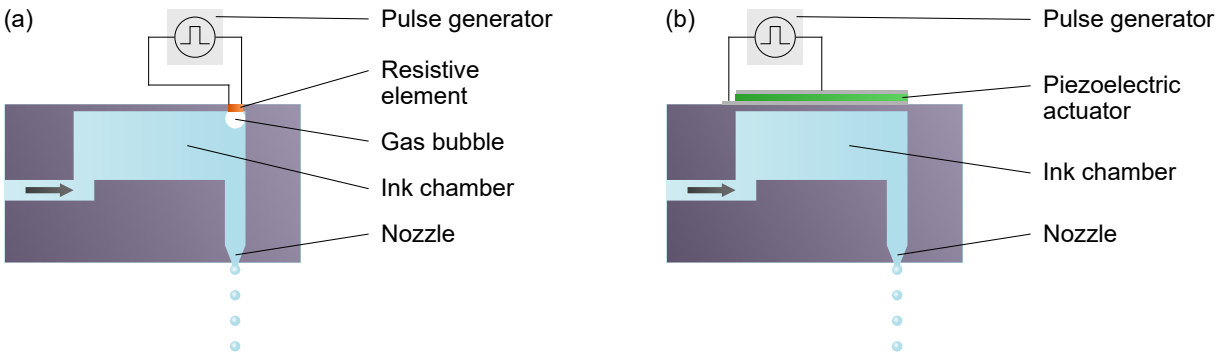

Fig. 15. Drop-on-demand inkjet printing principle: (a) thermal inkjet printing and (b) piezoelectric inkjet printing. Note that the scheme in (b) represents a bend-mode piezoelectric actuator. Other configurations of piezoelectric printheads also exist.

Droplet formation

The formation and stability of droplets is a complex phenomenon governed by fluid mechanics. The behavior of a liquid can be predicted thanks to a series of dimensionless parameters defined by the density ρ, viscosity η, surface tension γ and velocity v of the liquid, as well as the characteristic length a. In the case of inkjet printing, a corresponds to the nozzle size.

The Reynolds number (Re) is the ratio between the inertial and viscous forces of the fluid and characterizes its flow. Systems with a low Reynolds number exhibit laminar flow, while turbulent flow is characterized by a high Reynolds number [56]. The laminar-turbulent transition usually occurs in the 10^3–10^4 range.

$$\mathrm{Re} = \frac{\rho v a}{\eta} \tag{10}$$

The Weber number (We) expresses the ratio between inertial and surface tension forces [56]. The formation of droplets is favored at low Weber numbers, when the system is dominated by surface tension.

$$\mathrm{We} = \frac{\rho v^2 a}{\gamma} \tag{11}$$

In 1984, Fromm found that the $\frac{\mathrm{Re}}{\sqrt{\mathrm{We}}}$ ratio could be used to predict the formation of droplets in inkjet printing [57]. This ratio is the inverse of the Ohnesorge number (Oh) and is known as the Z parameter (eq. (12)).

$$Z = \frac{1}{\mathrm{Oh}} = \frac{\mathrm{Re}}{\sqrt{\mathrm{We}}} = \frac{\sqrt{a\gamma\rho}}{\eta} \tag{12}$$

According to Fromm, the onset of stable jetting occurs for $Z > 2$. This analysis was later refined by Reis and Derby, who identified $1 < Z < 10$ as the range of stable droplet formation [58]. Another study by Jang et al. redefined this range as $4 < Z < 14$ [59]. Low Z values characterize systems where jetting is impossible due to high viscosity. On the contrary, low-viscosity liquids are associated with high Z values, which typically leads to the formation of so-called satellite droplets. Two other constraints on the droplet initial energy set the bounds of the printable range: it has to be high enough to enable droplet formation ($\mathrm{We} > 4$) [60], but

low enough to avoid splashing (i.e. fragmentation into smaller droplets) after impact with the substrate ($We^{1/2}Re^{1/4} < 50$) [61]. A useful visualization of the jettable range was proposed by Derby [55], as illustrated in Fig. 16.

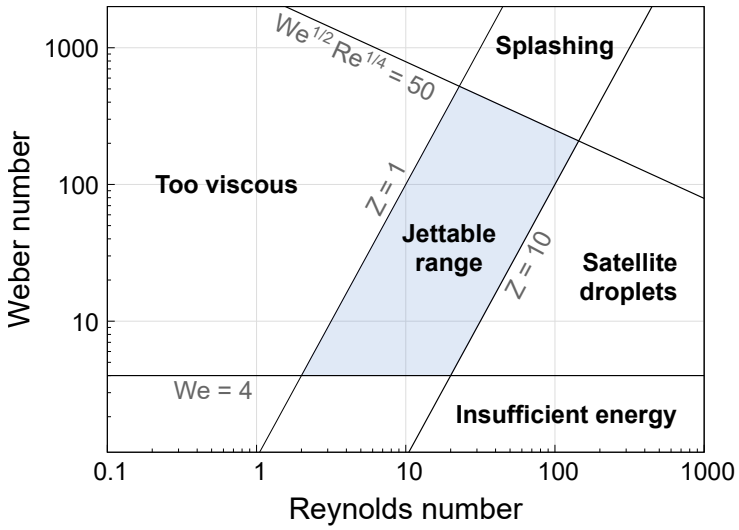

Fig. 16. Representation of the jettable range as function of the Weber and Reynolds numbers, as described by Derby [55].

Ink–substrate interactions

After ejection, droplets travel towards the substrate and collide with it. The nature of the interaction between a droplet and the substrate defines the printing resolution and the minimal feature size that can be achieved. Under normal conditions, the lower bound limit of resolution is set by the droplet size. The generation of 1 pL droplets, which have a diameter of ~12 µm, translates into a printing resolution in the same order of magnitude. However, contrary to the ink–paper system where the ink is mostly absorbed into the porous substrate upon impact, the interaction of a ink droplet with a smooth surface is governed by the dissipation of its kinetic energy and the interfacial energies of the liquid and the substrate.

The Bond number (Bo) is another dimensionless parameter used in fluid mechanics to characterize the balance between gravitational and surface tension forces a liquid is subjected to (eq. (13), where g is the gravitational acceleration constant). Ink droplets are characterized by low values of Bo (10^{-3}–10^{-2}), meaning that the influence of gravitational forces is negligible.

$$\mathrm{Bo} = \frac{\rho g a^2}{\gamma} \tag{13}$$

The impact of the droplet with the substrate can be described in several stages that occur at different timescales. Upon collision ($t < 1$ µs), the droplet undergoes impact-driven spreading, recoil and several oscillations to dissipate its kinetic energy by the viscous forces [62]. At later stages (0.1–1 ms), surface energy takes over and causes ink spreading until equilibrium is

reached. This situation is described by the Young equation (eq. (14)),

$$\cos\theta_c = \frac{\gamma_{sg} - \gamma_{sl}}{\gamma_{lg}}, \tag{14}$$

where θ_c is the contact angle at equilibrium and γ_{sg}, γ_{sl} and γ_{lg} are the interfacial energies between the solid (s), liquid (l) and gas (g) phases (Fig. 17a). Given that the final shape of the droplet can be approximated by a spherical cap, its diameter D_{sub} on the substrate can be expressed as a linear function of its inital diameter D_{drop}, as given by eq. (15) [55].

$$D_{sub} = D_{drop}\left(\frac{8}{\tan\frac{\theta_c}{2}\left(3 + \tan^2\frac{\theta_c}{2}\right)}\right)^{1/3} \tag{15}$$

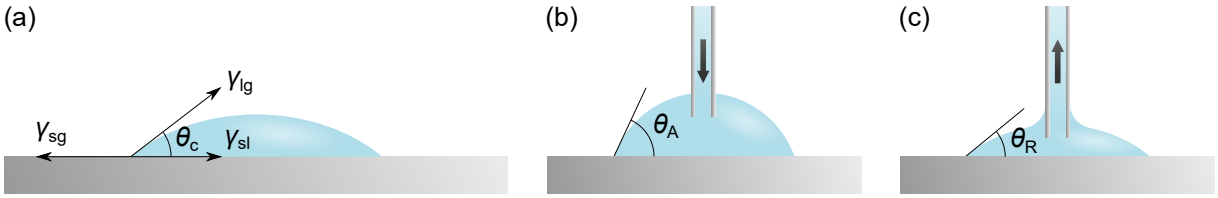

Fig. 17. Contact angles of a drop on a surface: (a) equilibrium contact angle, (b) advancing contact angle and (c) receding contact angle.

In order to form a homogeneous layer, the droplets need to coalesce into a continuous liquid film, which can be achieved by carefully tuning droplet spacing to obtain an ideal overlap of the droplets. This can also prevent jaggedness at the edges of printed structures, as shown by Soltman and Subramanian [63]. Furthermore, it is important that the printed liquid film remains stable on the substrate. In other words, the collection of coalesced droplets should resist the tendency of the liquid to form a circular bead on the surface in order to minimize its surface energy. Duineveld showed that stable patterns can be printed when there exists contact angle hysteresis, i.e. when the advancing contact angle θ_A (Fig. 17b) is significantly different from the receding contact angle θ_R (Fig. 17c) [64], in agreement with previous theoretical and experimental works [65, 66]. The influence of droplet spacing and printing velocity on the stability of printed patterns was also evidenced.

It should be noted that several strategies can be implemented to improve printing resolution beyond what is permitted by *classical* inkjet printing. These methods typically consist in a prior modification of the substrate in order to create a physical feature or a surface energy gradient that can control ink spreading. Such strategies were reported by Sirringhaus et al., enabling them to print structures with a feature size in the sub-100 nm range [67, 68].

Drying and processing into functional layers

After deposition and coalescence of the droplets, the resulting liquid film experiences drying as the ink solvent evaporates. This obviously causes a volume change of the liquid film, but can also lead to a phenomenon known as the coffee ring effect which forms ridge-like deposits at the edges of the printed structures (Fig. 18). This effect is due to the fact that the solvent evaporation rate is greater at the edge of the liquid film as vapor transport is enhanced by the proximity of the dry substrate. Preferential precipitation of the solute therefore occurs at the contact line, which becomes pinned as a result. A capillary-driven outward flow of liquid then takes place in order to replenish the evaporating solvent, thus sustaining the phenomenon [69].

The coffee ring effect is very often undesired and can be counteracted by methods which control the internal flows in the drying liquid film. Strategies such as tuning substrate temperature or exploiting a physical change of the ink upon impact have been reported [55], but a popular approach consists in tailoring the ink composition by using a mixture of solvents with specific properties. In a binary mixture containing solvents of different vapor pressures, the more volatile component will evaporate first. If the second component is chosen such that a surface tension gradient is created at the film edge, the solute will be redistributed towards the center through an inward Marangoni flow [52, 70]. However, depletion of the volatile solvent will eventually stop the inward flow. The use of more complex solvent systems such as ternary solvent mixtures was shown to sustain this phenomenon until late stages of the drying step [71].

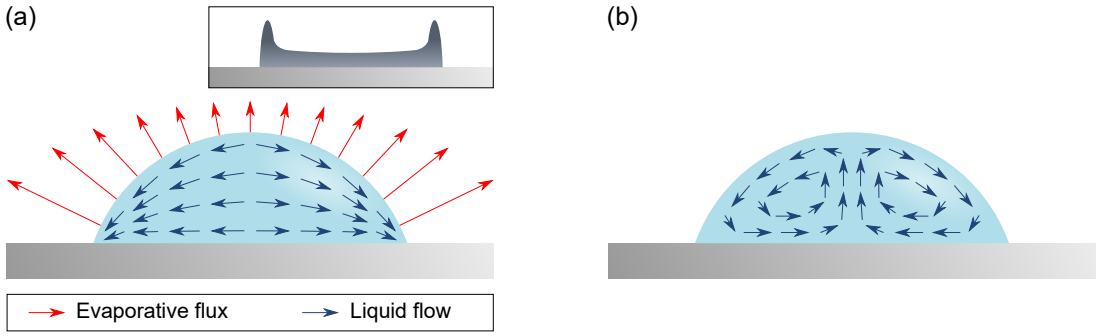

Fig. 18. Illustration of internal flows during drying: (a) evaporation-driven capillary flow resulting in the coffee ring effect (a typical 'coffee ring' profile is shown in the inset) and (b) recirculating inward Marangoni flow.

As the ink is merely a liquid precursor of the final material, post-printing steps are usually required to transform it into the final solid functional material. Thermal treatments are often used for drying, be it on a conventional hot plate, or via infra-red [72] or photonic annealing systems [73]. Curing of inkjet-printed polymers under UV light has also been reported [74]. Iteration of the printing–post-printing process is typically required to increase film thickness, as the thickness per layer is limited by the ink concentration and the volume of ink delivered per unit area on the substrate.

Significant progress was made in the field of inkjet printing of functional materials, as many of the underlying processes have been extensively studied and are supported by theoretical models. Nevertheless, IJP remains largely empirical, as it is very sensitive to the nature of the inks and substrates employed in the process. The particular case of inkjet printing of PZT thin films has been investigated by several groups and will now be presented.

State of the art: inkjet printing of PZT thin films

The earliest reports of PZT printing date back to 1999, where Windle and Derby used aqueous suspensions of PZT powders for the formulation of inks that could be jetted using a commercial inkjet printer [75]. In 2005, Wang and Derby used paraffin suspensions of PZT powders to print centimeter-sized ceramic objects, which could be considered as 3D printing [76]. More recent contributions also feature PZT powder-based ink formulations used for printing thick PZT films [77, 78]. However, since these approaches are not based on CSD, they afford porous materials and require high sintering temperatures, which are incompatible with silicon substrates.

The seminal work in the field of CSD-based inkjet-printed PZT was carried out by Bathurst et al. at MIT from 2008 to 2012 [79, 80]. During this period, Bathurst remarkably addressed several of the challenges related to inkjet printing. The ink formulations he used were based on a commercial CSD precursor, which he modified with co-solvents in order to obtain good jetting using a thermal inkjet printer. He also focused on printing uniform PZT structures. The strategy he adopted to combat the undesired coffee ring effect was to tune the temperature of the substrate during printing in order to balance the competing solute flows inside the drying film.

An important part of Bathurst's work was also dedicated to improving the resolution of PZT patterns printed on platinized silicon, characterized by high surface energy at the origin of ink spreading. His strategy was based on the use of templates to confine the ink and prevent it from spreading. Two original solutions were proposed: (1) hard templates and (2) soft templates. The hard template was a preformed polysilicon mold [81], constituting a physical barrier to the spreading of PZT ink. After printing, the mold was removed by XeF_2 etching. In the case of soft templates, the barrier is of chemical nature. The platinum surface was modified locally by a fluorinated thiol, thus defining ink-repelling areas that would stop the spreading of ink. Thiols ($R-SH$, where R is an organic moiety) have an affinity for noble metals such as platinum and are spontaneously grafted onto the surface in the presence of the metal, forming a so-called self-assembled monolayer (SAM). Microcontact printing was used to deliver a patterned SAM onto the surface, thus defining the areas to be printed in [82]. Note that the fabrication of stamps used in microcontact printing relies on a lithographic process.

The outcomes of this important work were two proof-of-concept devices, namely a ferroelectric capacitor [83] and a piezoelectric micromachined ultrasonic transducer [84]. Although very promising, the electrical properties of the inkjet-printed PZT thin films presented in this

work (P_r = 8.7 µC cm^{-2}) are still relatively modest compared to CSD-derived films deposited by conventional means.

After patenting a series of ink formulations [85], a Japanese research group at Ricoh Co., Ltd. also reported on inkjet-printed PZT in 2012 [86]. The authors printed 2 µm-thick PZT films on platinized silicon via a template-assisted method. Thiol-based SAMs were also used in this case to improve the resolution, though these SAMs were patterned by photolithographic means [87]. An alternative templating strategy was based on the selective formation of SAMs on platinum. A patterned platinum layer was first formed on a conductive oxide, then treated with a thiol. PZT ink was printed on the conductive oxide and remained confined to these areas thanks to the SAM formed on platinum. In both cases, inkjet printing was assisted by a lithographic process to produce a patterned template. In addition, remarkable homogeneity of the printed films was obtained via control of the solvent composition and the heating rate for drying the layers. Electrical characterization revealed a remanent polarization of 10 µC cm^{-2} for these printed PZT films.

In 2017, Matavž et al. developed another method for controlling the surface energy of the substrate prior to printing [88]. Very thin polymeric layers were spin-coated onto platinized silicon. Careful control of the nature of the polymer and the thermal treatment after deposition resulted in surfaces with optimal properties for direct patterning of metal oxide thin films via inkjet printing. Another contribution from this group shed light upon the suppression of the undesired coffee ring effect by the use of a ternary solvent system comprising two high-boiling-point co-solvents that prolong the duration of the inward Marangoni flow during drying, thus resulting in homogeneous layers [71]. In a very recent contribution, Matavž et al. also presented fully inkjet-printed ferroelectric stacks based on PZT and lanthanum nickelate ($LaNiO_3$) electrodes [89].

In the light of the advances made in the field of inkjet-printed PZT thin films, we identified several ideas that could be explored in order to improve the inkjet printing process itself and the quality of the final material. In particular, we will investigate the development of a lithography-free process for direct patterning PZT films on platinized silicon, without prior substrate modification. We will also discuss the required process adaptations to obtain dense layers with state-of-the art electrical properties. We will then present an application of inkjet-printed PZT layers in the form of a proof-of-concept piezoelectric device for energy harvesting. Finally, we will address the issue of toxicity of PZT solutions by investigating an alternative solvent to 2-methoxyethanol.

Chapter 1

Direct patterning of PZT thin films on platinized silicon

1.1. Motivation

Platinized silicon ($Si/SiO_2/TiO_x/Pt$) is commonly used as substrate in piezoelectric devices based on PZT thin films, such as microelectromechanical systems (MEMS). The excellent chemical and thermal stability of platinum makes it a popular choice as bottom electrode in PZT-based piezoelectric stacks. However, as mentioned in the Background chapter, printing structures on platinized silicon represents a challenge due to the high surface energy of platinum ($\sim 2.5\,J\,m^{-2}$) [90]. This high surface energy causes spreading of liquids (Fig. 1.1) and ink droplets deposited by inkjet printing are no exception to this phenomenon. Direct printing on pristine platinized silicon can therefore result in poorly resolved patterned structures.

Fig. 1.1. Demonstration of the wetting properties of a clean platinum surface. A ~1 µL drop of PZT ink was deposited on the surface: complete spreading occurs within seconds after deposition.

Wetting can be controlled by physical or chemical modification of the surface. As such, platinum is prone to contamination through the adsorption of atmospheric organic contaminants [91], effectively lowering its surface energy. Although favorable for inkjet printing, the nature and extent of this contamination can hardly be controlled. A possible solution for precise control of ink-substrate interactions is the modification of the whole platinum surface with thin polymeric layers [88].

Another strategy to limit ink spreading is represented by template-assisted inkjet printing. This solution consists in local surface modification in order to create a mold where the ink can be deposited and constrained by a barrier, be it physical or chemical. A physical mold or *hard*

template can be a preformed polysilicon mold. After printing, the mold can be etched away by a XeF_2 process. The use of such harsh etching steps can be avoided by using chemical molds or *soft templates*.

Thiol-functionalized molecules (R−SH, where R is an organic moiety) can be used for this purpose as they have a strong affinity for noble metal surfaces such as platinum, gold and copper [92, 93]. The thiol moiety acts as an anchoring point on the surface, while the rest of the molecule can be selected based on the desired properties. Alkyl substituents (R = $(CH_2)_nCH_3$) will provide the surface with hydrophobic character, thereby creating an efficient water- and polar-solvent-repelling chemical barrier. The grafting of alkanethiols on platinum is a spontaneous phenomenon, which usually occurs in three steps: (1) the formation of a metal–sulfur covalent bond (chemisorption), (2) the formation of islands with ordered alkyl chains and (3) the full coverage of the surface with chemisorbed species (Fig. 1.2). The resulting ordered molecular monolayer is known as a self-assembled monolayer (SAM). Interestingly, the metal–sulfur bond is labile and desorption of the SAM can be induced thermally, thus making it an excellent reversible surface modifier.

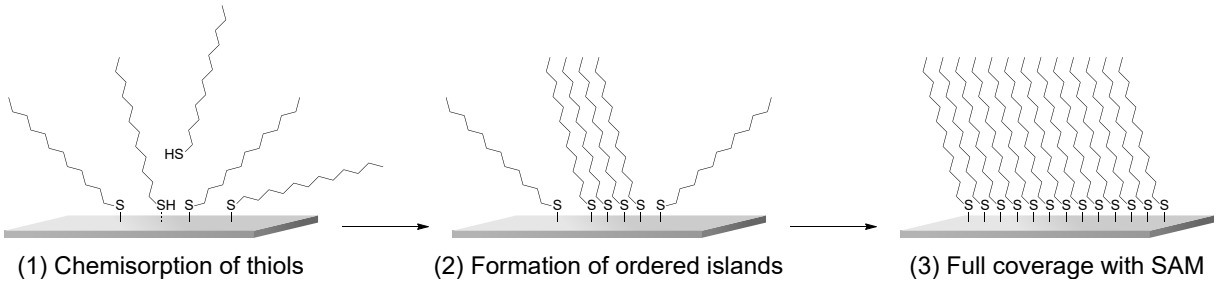

Fig. 1.2. Formation mechanism of a 1-dodecanethiolate-based self-assembled monolayer on a metal surface.

To serve as an IJP-assisting mold, the SAM requires patterning in order to define the areas of the substrate where ink is desired and where it is not. State-of-the art SAM patterning techniques rely on either (1) photolithography, where the SAM is patterned via local oxidation of thiols by UV light [87] or (2) microcontact printing, where thiols are delivered on the surface via a prepatterned PDMS stamp soaked in a solution of the thiols [82]. Both of these methods rely on lithography, which adds complexity and costs to the overall process, partially alleviating the benefits of using inkjet printing in the first place.

In this context, it could be interesting to use inkjet printing as a patterning tool for SAMs to create templates on platinized silicon where PZT ink would be deposited (see Fig. 1.3). We will develop this idea in the present chapter. In particular, we will describe the use of two printheads in the same printing process, where the first printhead defines the template and the second fills it with the functional ink. This strategy will be used for direct patterning of PZT structures on platinized silicon, with no lithographic intervention. A part of the study presented in this chapter was published in *Advanced Materials Technologies* [94].

1.2. Ink formulations

1.2.1. Templating ink

Thiolate-based SAMs are typically formed by the dipping method, where the substrate is directly immersed in a dilute ethanolic solution of the thiol, then rinsed and dried. We therefore used an ethanolic solution of 1-dodecanethiol as basis for the preparation of a templating ink. As can be expected, ethanol has too low viscosity ($\eta_{\mathrm{EtOH}} = 1.074$ mPa s at 25 °C [95]) to be used as such for inkjet printing. We started using a 6:1 ethanol:glycerol (v/v) mixture as solvent for the ink, as reported by Rianasari et al. [96]. The ink was prepared by simply diluting 100× a 0.1 mol L^{-1} ethanolic solution of 1-dodecanethiol with the ethanol:glycerol solvent mixture.

As a proof-of-concept experiment, we printed a single line of this templating ink on platinized silicon without prior treatment of the substrate.[a] The spacing between droplets was 92 µm, so that the droplets touched but did not significantly overlap, as seen in Fig. 1.3a. Evidence for the chemisorption of 1-dodecanethiol is the formation of a ring around the spot where the ink droplet was deposited, as the residual ink is repelled outwards by the SAM (Fig. 1.3b). A drop of PZT ink was then deposited on one side of the printed line using a syringe. Remarkably, the large volume of ink did not cross the SAM barrier, with evident pinning at the base of the drop.

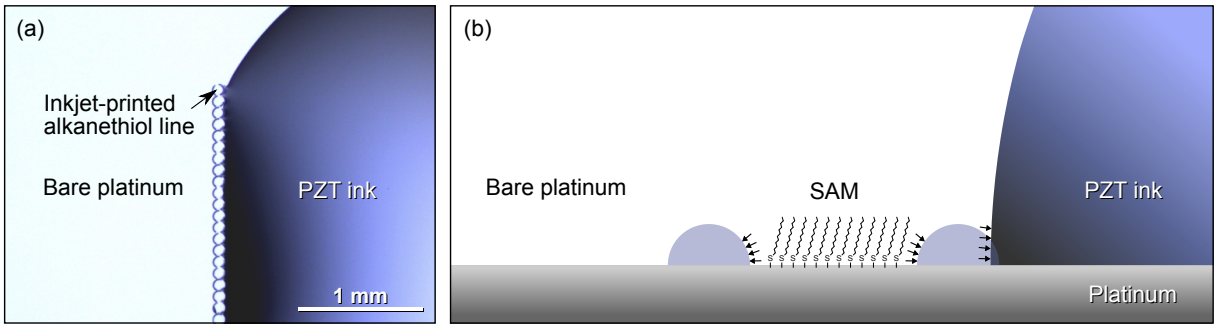

Fig. 1.3. Ink-constraining capabilities of printed 1-dodecanethiol line: (a) optical micrograph of a printed thiol line withholding a large drop of PZT ink on a platinum surface and (b) cross-section scheme of the system. The arrows represent the liquid-repelling action provided by the SAM formed on Pt.

Although stable jetting was achieved with this formulation for a printhead temperature close to room temperature (no heating), we experienced reliability issues as nozzles regularly stopped jetting when the printhead temperature increased during operation ($T_{\mathrm{printer}} \sim 30$ °C). To avoid temperature variations while printing, the substrate and printhead temperatures were set to 30 °C. Due to the high vapor pressure of ethanol at 30 °C (~10 kPa [95]), it is possible that substantial evaporation occurred at the nozzle. The consequence was a significant viscosity increase as the volume fraction of ethanol locally decreased, eventually clogging and deactivating the nozzle.

[a] The chemisorption of thiols on platinum is able to displace surface contamination.

To overcome this issue, we decided to replace ethanol with another solvent. As it constituted the basis of our reliable PZT ink formulation, 2-methoxyethanol appeared as a convenient choice. The new formulation was prepared by a diluting 100× a 0.1 mol L^{-1} ethanolic[b] solution of 1-dodecanethiol with a 3:1 mixture of 2-methoxyethanol:glycerol (v/v). Tolerance towards jetting temperature was considerably improved, with stable jetting possible at 35 °C, while still providing a medium where 1-dodecanethiol is soluble and can be adsorbed onto the surface where the ink is deposited.

1.2.2. PZT ink

Our initial PZT ink formulation was based on a procedure described in a patent [85], where a ternary solvent system based on 2-methoxyethanol, ethylene glycol and bis(2-ethoxyethyl) ether in a 2:2:1 ratio was employed. Although stable jetting was easily achieved at 35 °C, we encountered serious drying issues when the ink was deposited on the substrate, namely important coffee ring effect and high sensitivity towards surface conditions. The following study is based on another PZT ink formulation, inspired from the work of Matavž et al. [71] and based on the ternary solvent system 2-methoxyethanol, glycerol and ethylene glycol in a 65:25:10 ratio (v/v).

The following procedure describes the preparation of 100 mL of PZT spin coating solution (MPB composition, Zr/Ti = 53/47, 10 % lead excess) and its use for the preparation of PZT ink. All the chemicals were purchased from Sigma Aldrich.

A batch of lead(II) acetate trihydrate was freeze-dried overnight. A small quantity of deionized water was added to the compound before freezing it in liquid nitrogen. The addition of water helps in spreading the hydrated lead precursor on the walls of the flask, thus increasing its surface area. The flask containing the frozen solid was then connected to the vacuum manifold of the freeze dryer ($p < 0.05$ mbar). Upon completion of the freeze drying process, lead(II) acetate had the appearance of a fine power and was transferred inside a glovebox for storage.

Zirconium(IV) butoxide (80 wt% in butanol, 7.63 g, 15.9 mmol) was weighed inside a round bottom flask containing 20 mL of anhydrous 2-methoxyethanol. Acetylacetone (99.5 %, 3.28 mL, 31.8 mmol) was added to the solution, which was gently stirred for 15 min. The same procedure was repeated in a separate flask containing 20 mL of 2-methoxyethanol with titanium(IV) isopropoxide (97 %, 4.13 g, 14.1 mmol), to which acetylacetone (2.91 mL, 28.2 mmol) was also added. The two solutions were combined in the first flask and 10 mL of 2-methoxyethanol were used to wash the flask containing the titanium precursor. Freeze-dried lead(II) acetate (99.5 %, 10.79 g, 33.0 mmol) was then added to the resulting mixture of alkoxides. All these operations were performed in a glovebox, where the precursors and solvents were stored.

[b] Due to the poor solubility of 1-dodecanethiol in 2-methoxyethanol, the initial 0.1 mol L^{-1} stock solution had to be ethanol-based.

The flask was connected to a reflux apparatus under argon atmosphere (ARCAL™ Prime, Air Liquide), as illustrated in Fig. 1.4a. An oil bath was used for heating the contents of the flask. Lead(II) acetate was dissolved at 60 °C under stirring (800 rpm). After complete dissolution of the solid, the temperature of the oil bath was raised to 130 °C. The stirring speed was decreased to 300 rpm at the moment of boiling. The solution was maintained at reflux for 2 h. The flask was then transferred to a distillation apparatus (Fig. 1.4b), where 50 mL of the solution were distilled off. The solution was finally diluted to 0.3 mol L^{-1} (V_{final} = 100 mL), affording the PZT solution for spin coating. PZT ink was prepared by mixing 6.7 mL of the spin coating solution with 2.3 mL of glycerol and 0.9 mL of ethylene glycol, thereby diluting the solution to 0.2 mol L^{-1}. PZT solutions and inks were stored in a refrigerator at 4 °C.

The PZT ink can then be injected into the reservoir of a Fujifilm Dimatix DMCLCP cartridge reservoir using a syringe fitted with a 0.2 µm PTFE filter. Note that DMCLCP reservoirs provide chemical resistance, as opposed to standard DMC reservoirs. Indeed, we discovered that the presence of acetylacetone in inks attacks and degrades the O-ring of DMC reservoirs. Both types of reservoirs are compatible with either 1 pL or 10 pL nominal volume printheads.

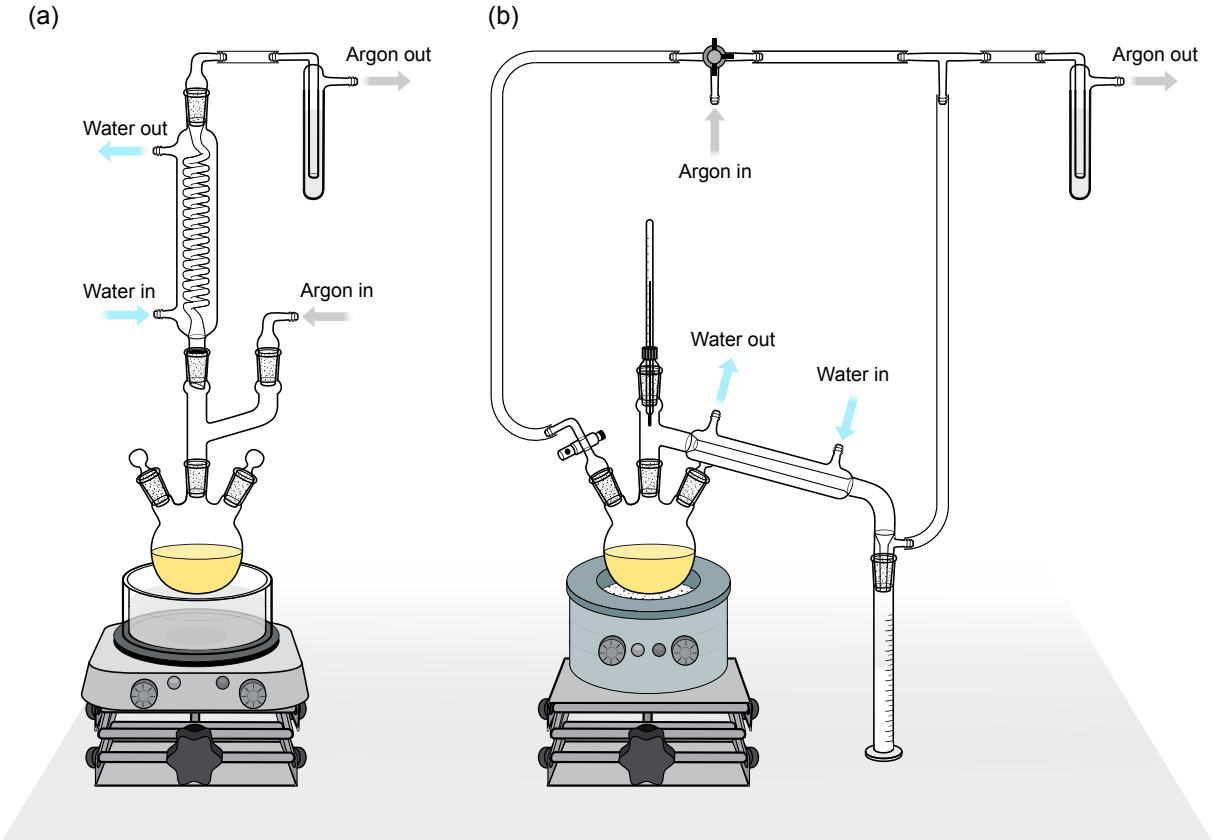

Fig. 1.4. Schemes of the (a) reflux and (b) distillation apparatuses used for the preparation of PZT solutions. In (b), the three-way valve is used to direct the flow of argon to the three-necked round bottom flask for flushing the system or towards the end of the distillation apparatus to provide a small back pressure during distillation. Gentle distillation must be performed, as solution drying over the walls of the flask may result in particles in the final solution.

1.2.3. Jetting behavior

The compositions and room-temperature physicochemical properties of inks are summarized in Table 1.1. The viscosity of the formulations was evaluated by the parallel plate method using an MCR 502 rheometer (Anton Paar, Austria), while surface tension was determined using the pendant drop method (the software OpenDrop was used to process the photographs of droplets and extract surface tension [97]). The density was evaluated by dividing the mass of a 10.0 mL solution sample by its volume. The inverse Ohnesorge number Z, as defined by eq. (12), was evaluated for 1 and 10 pL Fujifilm Dimatix cartridges, whose nozzle sizes are 9.5 and 21 µm, respectively. Z-parameter values of the inks conveniently fall in the 1–10 range for both cartridge types, suggesting that both 1 and 10 pL cartridges can be used for printing with this two-ink system.

		Templating ink	PZT SC solution	PZT ink
Concentration (mol L^{-1})		0.001	0.3	0.2
Solvent composition (vol%)	2-Methoxyethanol	75	100	65
	Glycerol	25	0	25
	Ethylene glycol	0	0	10
Surface tension (mN m^{-1})		35.6	32.5	34.2
Density (g cm^{-3})		1.04	1.05	1.11
Viscosity (mPa s)		7.1	2.0	8.1
Z parameter	1 pL cartridge	2.7	9.2	2.4
	10 pL cartridge	3.9	13.4	3.5

Table 1.1. Room-temperature physicochemical properties of the templating ink, the PZT spin coating (SC) solution and the PZT ink. Viscosity is given for a shear rate of 100 s^{-1}. For the templating ink, concentration is defined as the concentration of 1-dodecanethiol, whereas for PZT solutions, it is defined as $C_{Zr} + C_{Ti}$ in the solution.

As an example, the jetting pulses and corresponding stroboscopic images of PZT ink ejected with 1 and 10 pL Dimatix cartridges are shown in Fig. 1.5. Stable jetting is possible at frequencies in the 10^2–10^4 Hz range with both cartridge types ($T_{printhead}$ = 35 °C). The 1 pL cartridge generates droplets travelling at ~7 m s^{-1}, while the 10 pL cartridge ejects droplets at ~4 m s^{-1}. In Fig. 1.5c, the small tail observed after 25 µs merges into the droplet at the 50 µs timestamp. No satellite droplets nor significant droplet deviations were observed.

The optimized pulse waveform for ejection of the templating ink with the 1 pL is similar to the one presented in Fig. 1.5a, except that the initial voltage is 6 V and the maximum voltage is 12 V. Stable ejection of this ink with the 10 pL cartridge was possible with the pulse waveform represented in Fig. 1.5b.

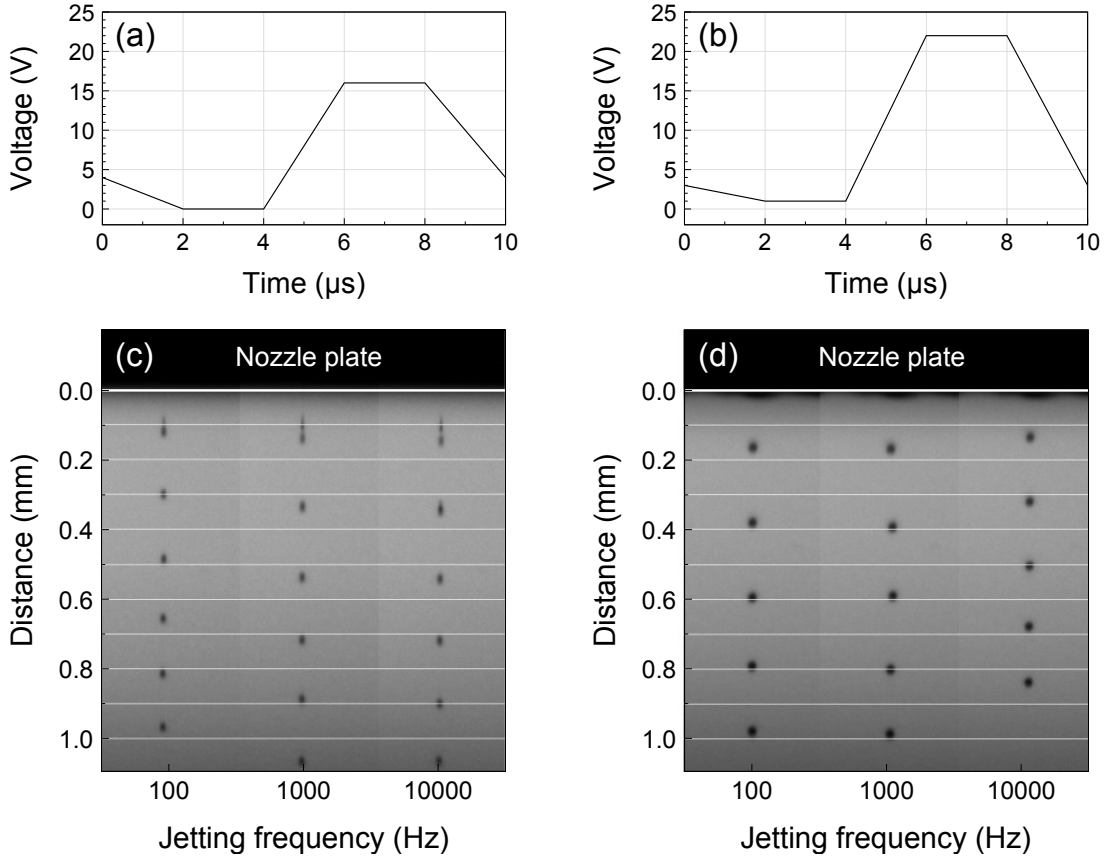

Fig. 1.5. Jetting of PZT ink with 1 and 10 pL Dimatix cartridges. The jetting pulses used for 1 and 10 pL cartridges and are represented in (a) and (b), while the corresponding stroboscopic pictures are shown in (c) and (d), respectively. In (c), the time pitch is 25 µs and it is 50 µs in (d).

1.3. Printing PZT structures on platinized silicon

1.3.1. Process description

Based on the previous considerations, we developed a lithography-free printing strategy for patterning PZT films on platinized silicon, which is described in the scheme of Fig. 1.6. The overall process can be divided in two main parts: inkjet printing and annealing. The starting point is a pristine platinized silicon substrate.[c] The Ceradrop X-Series printer possesses two printheads that can be fitted with Dimatix cartridges.

Printhead 1 is first used to create a SAM template grid by printing lines of templating ink. Printhead 2 then fills the gaps between the templating lines with the functional ink, in this case the PZT ink. After that, the deposited liquid film successively undergoes drying, pyrolysis and crystallization steps, affording a crystalline PZT film, whose thickness can be increased by iteration of the process. As the annealing steps are carried out outside the printer, a

[c] Substrates were degassed on a hot plate at 350 °C for 5 min before printing. This treatment was sufficient to desorb surface contaminants.

realignment step is necessary to deposit the next layers. The templating step has to be performed at every iteration, because the organic SAM is eliminated during the annealing steps. Note that this strategy could be generalized to pattern any CSD-compatible metal oxide on high-surface energy metals such as gold, platinum or copper.

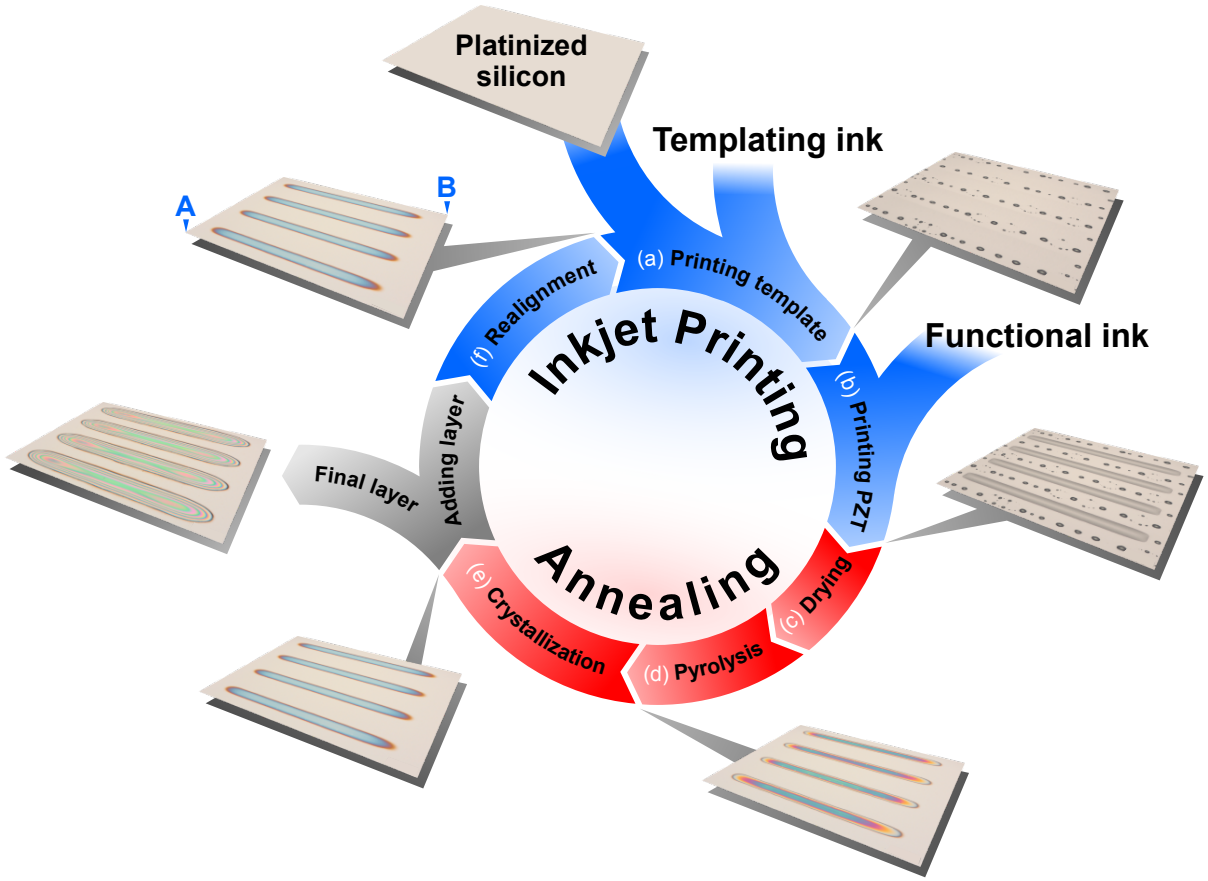

Fig. 1.6. Lithography-free inkjet printing process for patterning PZT films on platinized silicon: (a) a SAM-based template is printed on the substrate and (b) the functional ink is then delivered to the defined areas. An annealing sequence consisting of (c) drying, (d) pyrolysis and (e) crystallization is then performed outside the printer. Film thickness can be increased by iteration of the process, which requires the sample to be (f) placed again in the printer and precisely realigned.

1.3.2. Printing PZT squares

Droplet deposition strategy

Piezoelectric devices based on PZT thin films require a certain film thickness, typically in the order of 1 µm. In conventional CSD processing by spin coating, the film is usually grown by successive thin layers ($d \sim 70$ nm), although there exist solutions enabling the growth of a couple hundred nanometers of PZT in a single deposition step [26]. In the case of inkjet printing, the thickness of a single crystallized layer d_{PZT} will depend on the ink concentration C_{ink}, the

individual droplet volume V_{drop} and the filling density N_{drop} (number of droplets deposited per unit area). It is interesting to get a sense of these values in order to deposit a reasonable amount of material at every printing cycle.

A simple model assuming that the final film is dense, has the correct stoichiometry and is a well-defined cuboid (homogeneous thickness and absence of edge effects) can be derived in a few steps:

$$\begin{aligned} d_{\text{PZT}} &= \frac{V_{\text{PZT}}}{A_{\text{PZT}}} = \frac{m_{\text{PZT}}}{A_{\text{PZT}}\,\rho_{\text{PZT}}} = \frac{M_{\text{PZT}}\,n_{\text{PZT}}}{A_{\text{PZT}}\,\rho_{\text{PZT}}} = \frac{M_{\text{PZT}}\,C_{\text{ink}}\,V_{\text{ink}}}{A_{\text{PZT}}\,\rho_{\text{PZT}}} \\ &= \frac{M_{\text{PZT}}\,C_{\text{ink}}\,V_{\text{drop}}\,N_{\text{drop}}}{\rho_{\text{PZT}}}\,, \end{aligned} \tag{1.1}$$

where M_{PZT} and ρ_{PZT} are the molar mass and the density of PZT, respectively. The molar mass of PZT depends on its composition. For the general formula $PbZr_xTi_{1-x}O_3$, the molar mass is given by eq. (1.2):

$$\begin{aligned} M_{\text{PZT}}(x) &= M_{\text{Pb}} + M_{\text{Zr}}\,x + M_{\text{Ti}}\,(1-x) + 3\,M_{\text{O}} \\ &= 207.20 + 91.22\,x + 47.88\,(1-x) + 3\times 15.999 \\ &= 303.08 + 43.34\,x\,. \end{aligned} \tag{1.2}$$

Therefore, for the MPB composition ($x = 0.53$), the molar mass is $326.05\,\text{g mol}^{-1}$, while its density is $8048\,\text{kg m}^{-3}$ (PDF 01-070-4264). Substituting in eq. (1.1) and solving for N_{drop} yields eq. (1.3) where, for convenience, N_{drop} is expressed in droplets per mm^2, d_{PZT} in nm, C_{ink} in mol L^{-1} and V_{drop} in pL.

$$N_{\text{drop}} = 24.68\,\frac{d_{\text{PZT}}}{C_{\text{ink}}\,V_{\text{drop}}} \tag{1.3}$$

We can estimate that for a final thickness of 70 nm, using 10 pL cartridges (the actual droplet volume was evaluated to be closer to ~13 pL[d]) and 0.2 M ink, the required filling density should be about 660 droplets per mm^2. The other way to act on film thickness for a given amount of delivered ink is the concentration, which is directly proportional to the final thickness. However, we decided to keep this parameter constant for this study as (1) concentrated solutions could be less stable and (2) preparing the PZT ink from a PZT spin coating solution is a convenient approach for practical reasons.

[d] The droplet volume is estimated from the droplet diameter as seen on the live acquisition of the printer stroboscopic camera. The actual ejected volume can differ from the nominal value depending on the jetting pulse.

The Ceradrop printer CAD software (CeraSlice) can fill shapes using different types of lattices. The default one is a simple square lattice (Fig. 1.7a), where the user-defined parameters are the splat diameter D_{splat} and splat overlap O_{splat}. The *no void* setting ensures complete filling of the plane and corresponds to the condition:

$$O_{\text{splat}} = \left(1 - \frac{\sqrt{2}}{2}\right) D_{\text{splat}} \tag{1.4}$$

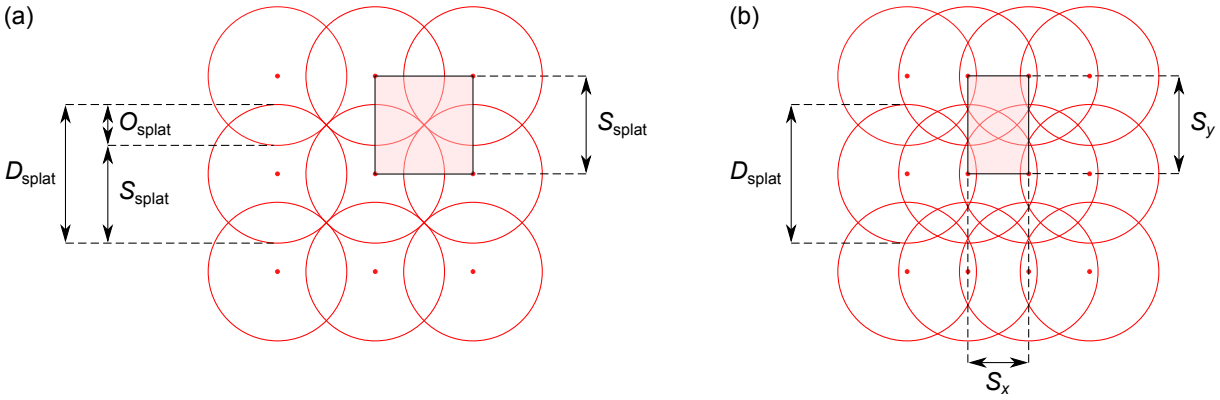

Fig. 1.7. Representation of the (a) square lattice printing strategy in the *no void* condition and (b) the rectangle filling strategy. The colored square and rectangle represent the elementary unit cells which always contain one deposited droplet.

The spacing S_{splat} between two adjacent splats in the x and y directions is identical and is given by $\left(D_{\text{splat}} - O_{\text{splat}}\right)$. The filling density can then be computed by calculating the reciprocal of the square of S_{splat}, which defines the unit cell of this tiling pattern and always contains one droplet.

$$N_{\text{drop}} = \frac{1}{\left(D_{\text{splat}} - O_{\text{splat}}\right)^2} \tag{1.5}$$

Substituting eq. (1.4) in eq. (1.5) gives the filling density in the *no void* condition.

$$N_{\text{drop,nv}} = \frac{1}{\left(D_{\text{splat}} - \left(1 - \frac{\sqrt{2}}{2}\right) D_{\text{splat}}\right)^2} = \frac{2}{\left(D_{\text{splat}}\right)^2} \tag{1.6}$$

The splat diameter of a 13 pL droplet on a clean platinum surface was measured and is in the order of 110 µm. Using the default square filling strategy with the *no void* condition would result in a filling density of only 165 droplets per mm^2, which is four times less than the desired value computed earlier. The expected final film thickness would be ~17 nm. Obviously, a much larger overlap is required to deliver the adequate amount of ink. Alternatively, the ink can be delivered in multiple passes of the printhead.

In order to gain more flexibility over the amount of delivered ink, we decided to use the rectangle filling strategy instead (Fig. 1.7b), which allows for independent control over the droplet spacing along the x and y directions, S_x and S_y, respectively. In the rest of this section, we will discuss patterning of PZT films in the form of $500 \times 500\,\mu m^2$ squares using this deposition strategy.

The droplet deposition strategy is illustrated in Fig. 1.8. The template lines were printed using a single nozzle of a 10 pL cartridge and with a droplet spacing of 75 µm. In these conditions, spreading over the substrate afforded 200 µm-wide templating lines. Lines in the x direction were printed via movement of the printhead, while those in the y direction were printed with the printhead fixed and movement of the substrate. The PZT ink was then delivered into the defined areas using a series of eight consecutive nozzles, with 10 droplets in the x direction and 8 droplets in the y direction. Two depositions of PZT ink were successively carried out,[e] resulting in a grand total of $10 \times 8 \times 2 = 160$ droplets per $500 \times 500\,\mu m^2$ square. This corresponds to a filling density of 640 droplets per mm^2, which is in excellent agreement with the filling density required to achieve ~70 nm-thick PZT layers per deposition step.

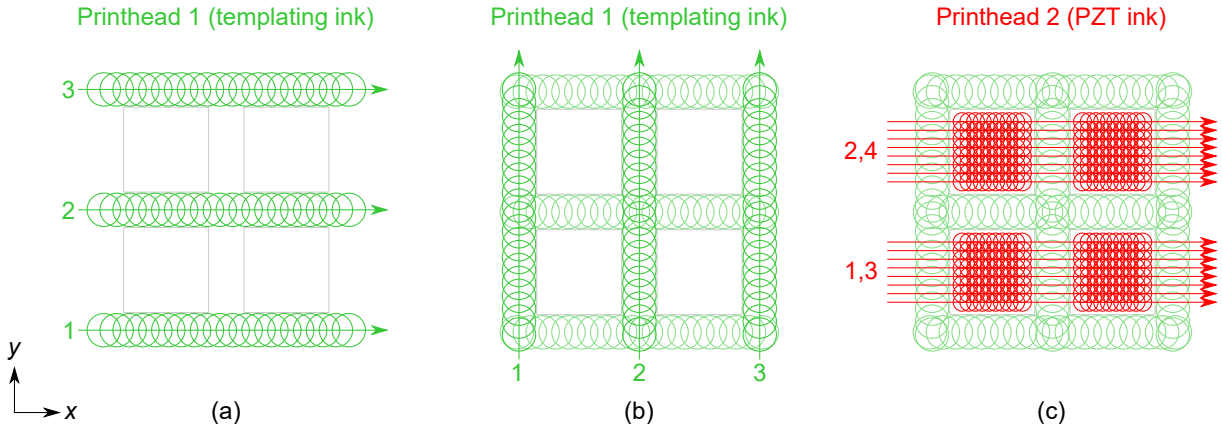

Fig. 1.8. Printing strategy for $500 \times 500\,\mu m^2$ PZT squares. Templating lines are successively printed in the (a) x direction (printhead movement) and in the (b) y direction (substrate movement, fixed printhead) using a single nozzle. (c) The template grid is then filled with PZT ink in two successive passes using eight consecutive nozzles. The numbers represent the different printhead passes.

Layer stacking

The printing strategy described above was implemented in the deposition of an array of $500 \times 500\,\mu m^2$ squares. After printing, the films were dried at 200 °C for 3 min, pyrolyzed at 350 °C for 8 min and finally crystallized at 700 °C for 5 min. This annealing procedure was performed for every printed layer. Here, we show optical micrographs and profilometry measurements for a single printed layer and a succession of two and three printed layers (Fig. 1.9).

[e] Delivering the same amount of ink in a single pass sometimes resulted in ink spilling over the template.

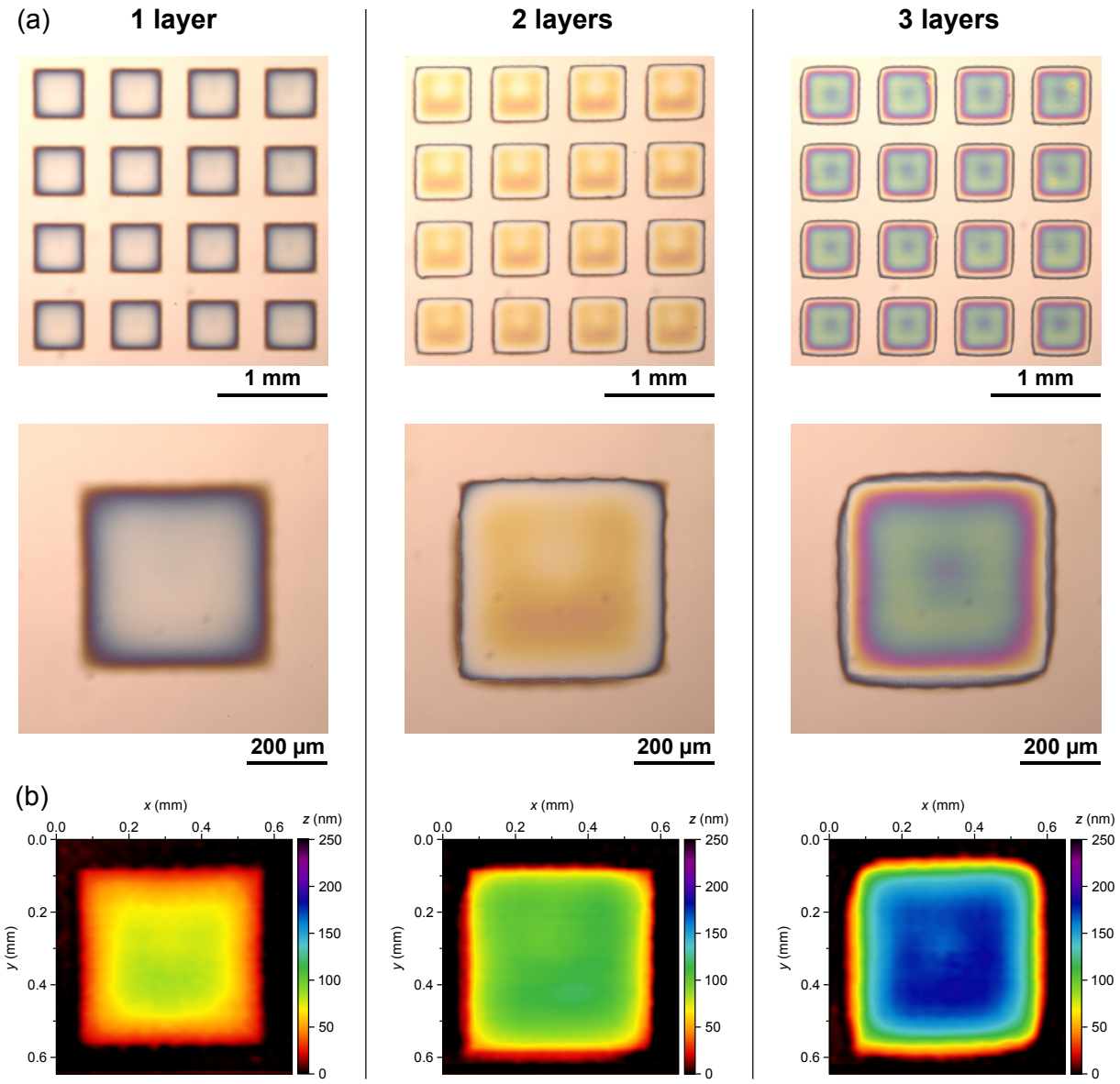

Fig. 1.9. (a) Optical micrographs and (b) profilometry of inkjet-printed $500 \times 500\,\mu m^2$ PZT squares after crystallization. Every layer was dried at 200 °C for 3 min, pyrolyzed at 350 °C for 8 min and crystallized at 700 °C for 5 min.

As explained earlier, the template needs to be reprinted for every layer, as the thermal annealing steps eliminate the organic-based SAM. However, using secondary ion mass spectrometry (SIMS), we evidenced the presence of sulfur at the edge of the printed PZT structures after crystallization, as shown in Fig. 1.10. This sulfur can only originate from the thiol and it is possible that diffusion of 1-dodecanethiol into the PZT ink occurs while both inks coexist at the liquid state on the substrate after printing. This results in a small but detectable amount of sulfur in the film after thermal processing, mostly concentrated in a ~15 µm-wide border at the interface between the substrate and the printed PZT film.

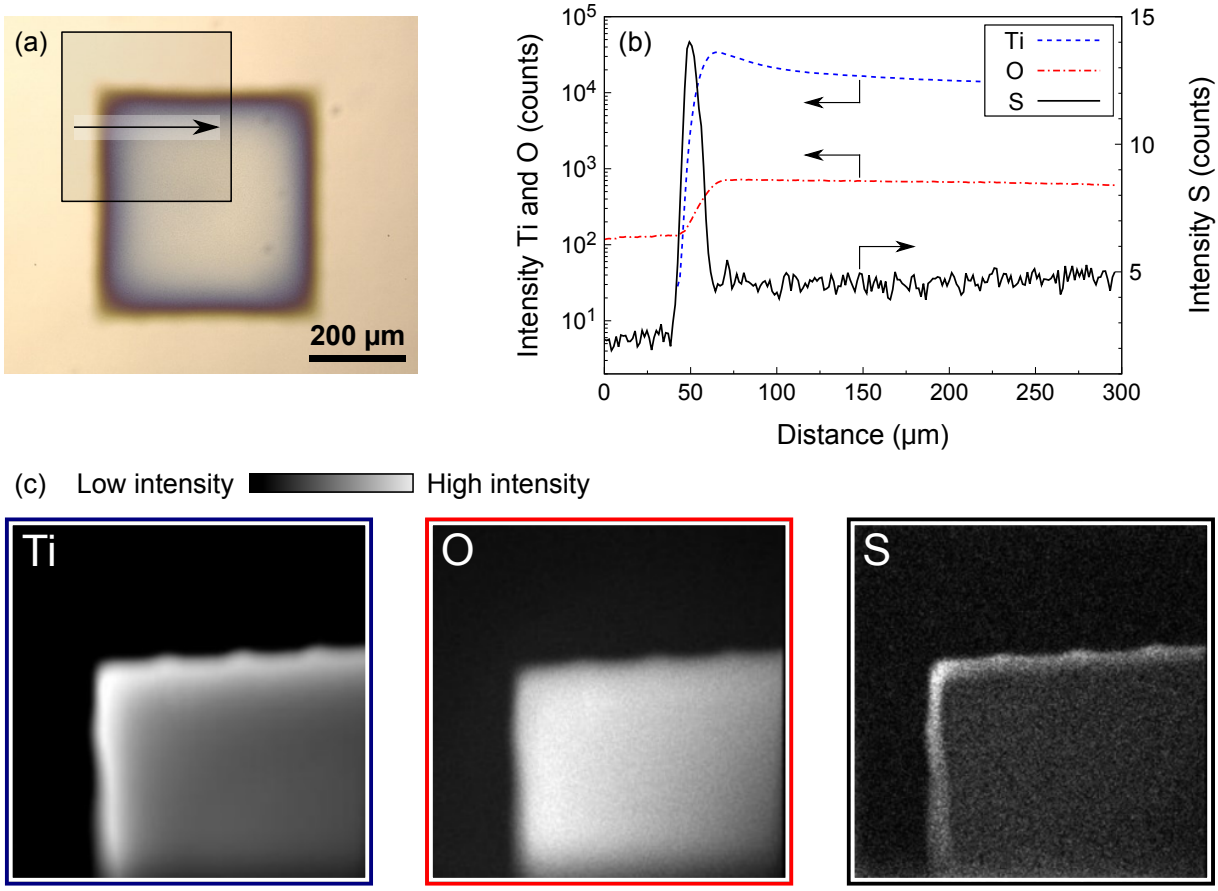

Fig. 1.10. SIMS analysis at the edge of a crystallized $500 \times 500\,\mu m^2$ PZT square: (a) optical micrograph showing the analyzed region, (b) line scan along the arrow shown in (a) and (c) elemental mapping of Ti, O and S in the $350 \times 350\,\mu m^2$ square shown in (a). The primary ions were Cs^+ accelerated at 5.5 keV and positive secondary ions were detected.

Remarkably, our strategy allowed us to pattern PZT films successfully up to a thickness of ~180 nm (3 layers). Spacings between the PZT squares corresponding to where SAM template lines were printed are well-defined, with absence of spilled PZT ink in these areas. The template therefore accomplishes its role for several printed layers of PZT.

The thickness of the printed structures is relatively homogeneous, with absence of coffee ring effect. A slight dimple is nonetheless found in the center of the two-layered and three-layered structures, in accordance with the color differences observed in the optical micrographs.[f] A nonlinearity in the evolution of thickness as function of number of layers is observed and can be explained by a slight enlargement of the square at the second layer.

These findings are very encouraging and suggest that the inkjet templating strategy can still be used as the thickness of PZT increases. Whether the process is robust enough to stack layers until the target thickness of one micron will be discussed in the next paragraphs.

[f] Colors arise from a thin-film interference phenomenon and are a good indicator to estimate film thickness up to ~200 nm.

Micron-thick layers

In order to obtain a micron-thick films, the printing–annealing sequence needs to be performed 15 times ($15 \times 70\,\text{nm} = 1050\,\text{nm} \approx 1\,\mu\text{m}$). The optical micrograph and profilometry characterization are shown in Fig. 1.11. Once again, it appears that the printed template provides an efficient ink-repelling action throughout the process. It is clear that the sample needs precise re-positioning at every iteration of the cycle, which can be carried out thanks to the two-point alignment feature of the printer. For this, the coordinates of only two points are required, which can be easy-to-identify defects on the substrate or, more conveniently, pre-made alignment crosses. The final structure reaches 1 µm at its highest point. The 3D shape of the printed structure can be described as a squared-base truncated pyramid, with the central flat part being a $200 \times 200\,\mu\text{m}^2$ square.

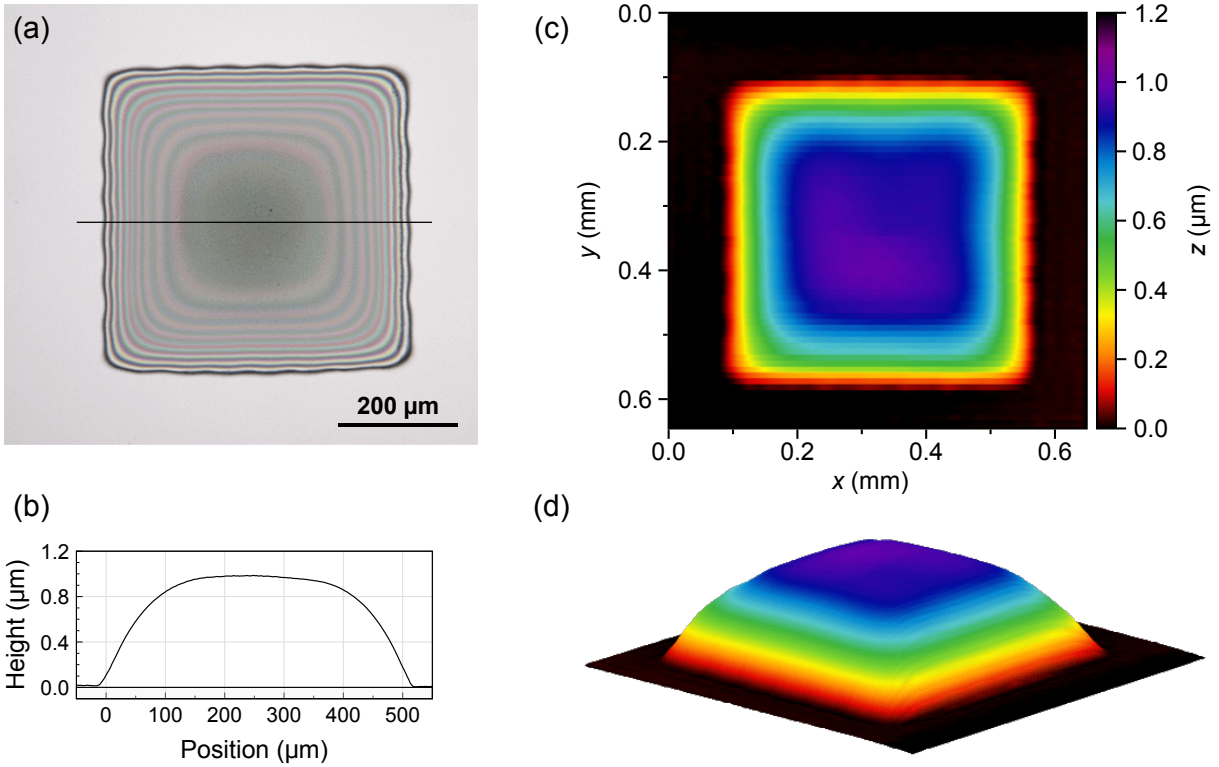

Fig. 1.11. (a) Optical micrograph and (b)–(d) profilometry of an inkjet-printed micron-thick $500 \times 500\,\mu\text{m}^2$ PZT square. The profile shown in (b) corresponds to the line represented in (a).

Based on 3D profilometry, the volume of the printed structure was found to be $1.7 \times 10^5\,\mu\text{m}^3$. If the film were a perfect micron-thick cuboid, the expected volume would be $2.5 \times 10^5\,\mu\text{m}^3$. This large discrepancy could be explained by the error on the measurement of the droplet volume, which is the quantity with the highest uncertainty. Indeed, droplet volume is evaluated by measuring its diameter or radius. A spherical 10 pL droplet has a diameter of 13.4 µm. If the stroboscopic camera is not properly focused and given the small size of the droplets, a ~10 % error on the radius is not unlikely, as the droplet outline is automatically detected by the software. Computing the relative uncertainty shows that a such an error on the measurement of

the radius of the droplet translates into a ~30 % error on measurement of the volume, eq. (1.7). This appears to be the case here and we can work out that the actual droplet volume is 9 pL, which is actually much closer to the nominal value.

$$\frac{\Delta V}{V} \approx 3\frac{\Delta r}{r} \tag{1.7}$$

The patterned array of micron-thick PZT structures was crystallized in the perovskite phase, as shown by the grazing incidence XRD pattern (Fig. 1.12a). However, inspection of the surface by SEM (Fig. 1.12b) reveals the presence of significant inter-granular porosity, along with surface pyrochlore in the form of small bright grains.

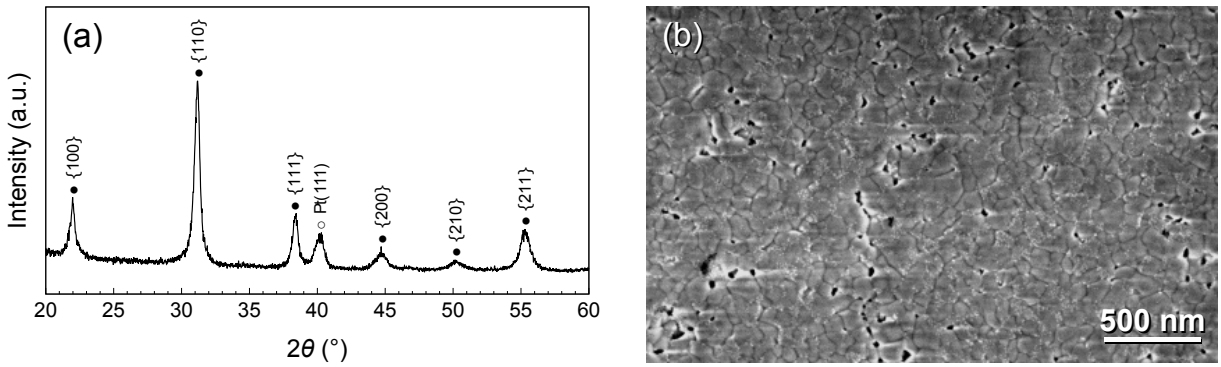

Fig. 1.12. (a) Grazing incidence XRD pattern and (b) surface SEM of inkjet-printed micron-thick PZT structures.

Finally, we performed the electrical characterization after deposition of 100 µm-diameter Cr/Au round top electrodes by evaporation. The polarization–electric field loop is shown in Fig. 1.13a. The inkjet-printed film displays clear ferroelectric behavior, with remanent polarizations $P_r^+ = 19.4\,\mu C\,cm^{-2}$ and $P_r^- = -14.1\,\mu C\,cm^{-2}$. The coercive fields are $E_c^+ = 54\,kV\,cm^{-1}$ and $E_c^- = -63\,kV\,cm^{-1}$. The relative permittivity–electric field loop is represented in Fig. 1.13b, where the relative permittivity at zero bias is ~ 870. The loss tangent is inferior to 0.03. These values are close to the typical values reported for CSD-derived PZT films [98]. The loops are asymmetrical, which is due to the different nature of the electrodes, the bottom electrode being platinum and the top electrode gold with a chromium adhesion layer. Indeed, these metals have different work functions, resulting in different Schottky barriers heights at the interfaces [99].

In this section, we described the different steps that led us to the development of a lithography-free patterning process for $500 \times 500\,\mu m^2$ PZT squares on platinized silicon. The creation of a SAM template on the surface prior to printing PZT was performed in a time- and cost-efficient manner thanks to inkjet-printing itself. Although promising, we have not yet explored the limits of this strategy in terms of spatial resolution. This point will be addressed in the next section, where we will describe inkjet printing of PZT lines using a similar approach.

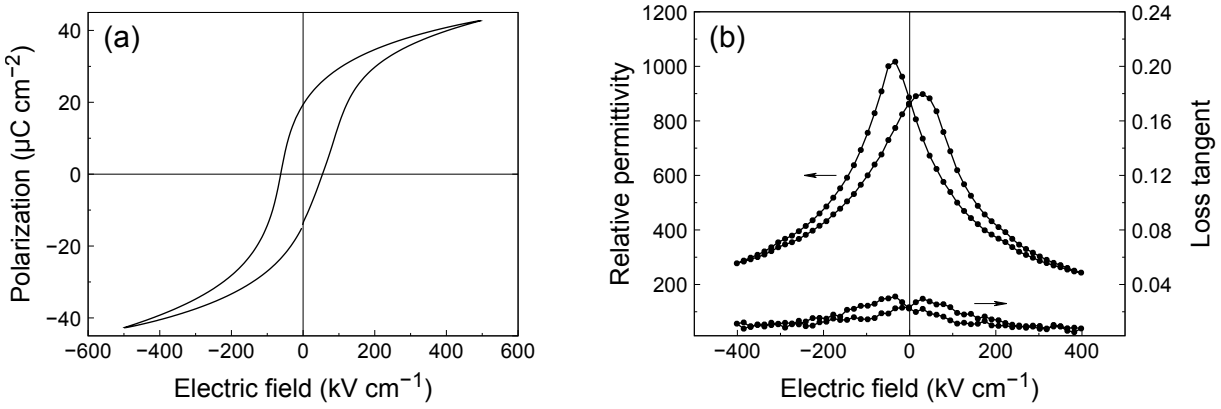

Fig. 1.13. Electrical characterization of inkjet-printed micron-thick $500 \times 500\,\mu m^2$ PZT squares: (a) polarization–electric field loop at 100 Hz and (b) relative permittiviy–electric field loop at 1 kHz (V_{AC} = 100 mV).

1.3.3. Printing PZT lines

In order to achieve a higher resolution, we naturally decided to use 1 pL Dimatix cartridges for both templating ink and PZT ink deposition. The test pattern will be a 50 µm-wide and 1 mm-long PZT line. To begin with, we will present a study of the behavior of the templating lines when printed using a 1 pL cartridge.

Study of templating lines

Unlike *conventional* inks, the templating ink has a surface-modifying behavior. As seen in Fig. 1.3a, dewetting of the residual ink occurs and can form a ring of liquid around the spot where the droplet was deposited. As we will see, under different circumstances (droplet size or surface conditions) the dewetting pattern can take other shapes, making it difficult to visualize where the SAM is formed. Nonetheless, we can use another ink (e.g. the PZT ink) like a 'contrast agent' to reveal the template.

We performed a series of experiments illustrated in Fig. 1.14a. Parallel templating lines were printed along the x axis. While the vertical pitch was kept constant (215 µm), droplet spacing along the x direction (S_x) was varied from 200 to 20 µm. PZT ink was then deposited between the templating lines, thus revealing their position. When S_x = 200 µm, the SAM splats do not influence each other and have a diameter D = 80 µm. We begin to see this influence when S_x = 100 µm, as the droplets start touching each other, resulting in a slight increase of the splat diameter. This trend carries on as the droplet spacing is reduced to 20 µm, then the splat diameter or template linewidth becomes 165 µm.

Interestingly, the residual templating ink is repelled towards the center, forming individual droplets or continuous lines depending on droplet spacing. For the 20 µm spacing, the residual templating ink is even repelled into an irregular pattern. This is not an issue because the residual templating ink is fully removed upon pyrolysis, as seen in Fig. 1.14a (pictures labelled with P).

In addition to template linewidth, tuning droplet spacing also allows control over edge jaggedness of the printed PZT structures. Jagged edges are clearly visible after pyrolysis for droplet spacings down to 60 µm. This effect is significantly less pronounced for $S_x = 40$ µm and non-existent for $S_x = 20$ µm. The latter parameter was adopted in the rest of this study.

In order to stress the importance and effectiveness of the printed template, we attempted to print the test pattern (1×0.05 mm^2 rectangle) without and with the SAM template (Fig. 1.14b). PZT ink droplets were deposited using a single nozzle, in two successive passes and droplet spacing of 10 µm (equivalent to a droplet spacing of 5 µm). In the absence of a template, outward spreading of the ink results in a ~300 µm-wide oval-looking shape. On the other hand, the presence of a template guarantees excellent confinement of the ink into the desired pattern.

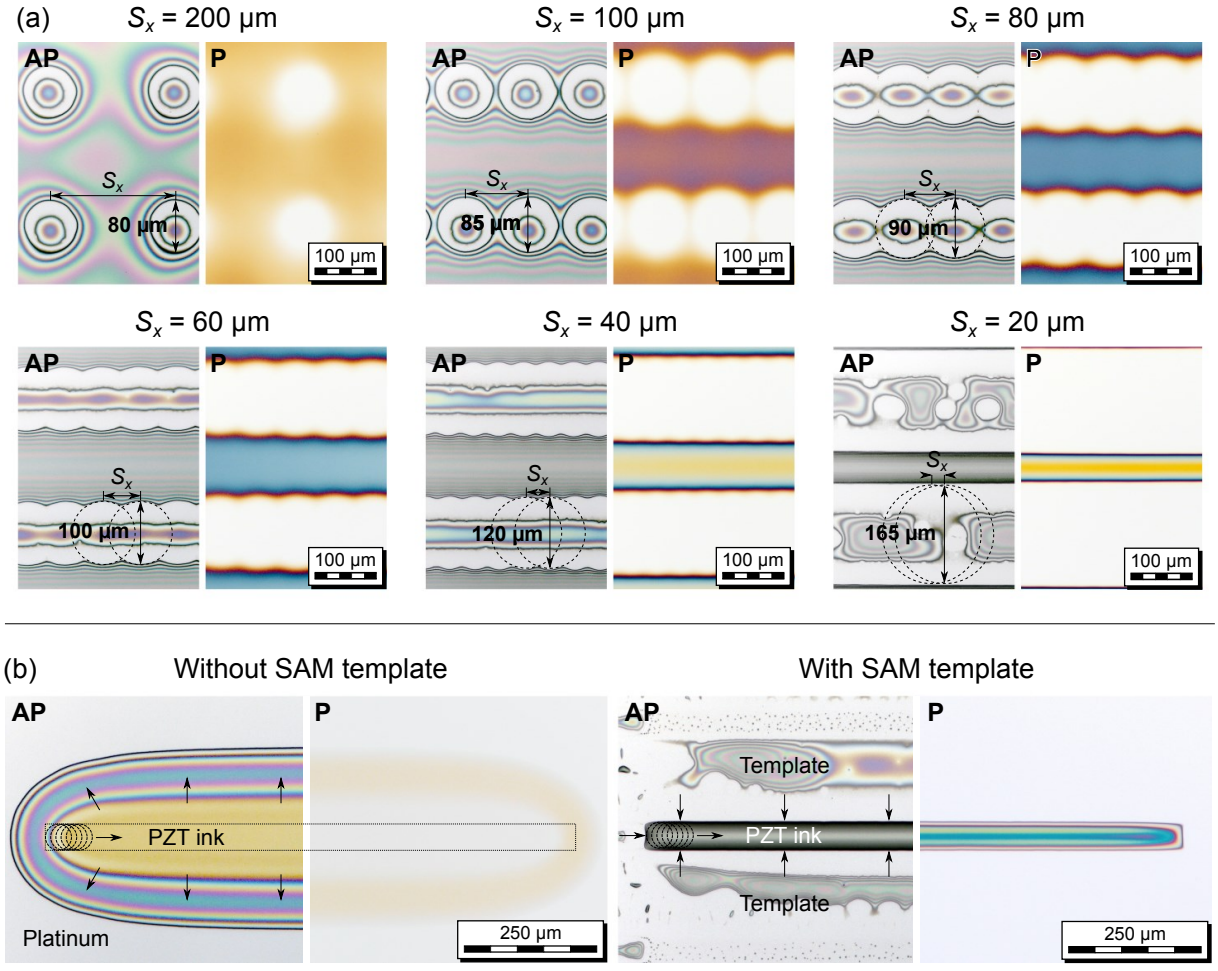

Fig. 1.14. Behavior of the templating ink on platinized silicon for printing PZT lines: (a) influence of droplet spacing on template linewidth and (b) ink-constraining capabilities of printed template lines. The optical micrographs are always presented in pairs, where the left picture shows the films after printing (AP) and the right one after pyrolysis (P).

Structural characterization

We then proceeded with the fabrication of an array of lines, very similarly to what was described before for the $500 \times 500\,\mu m^2$ squares: at every iteration of the process, the films were dried at 200 °C for 3 min, pyrolyzed at 350 °C for 5 min and crystallized at 700 °C for 5 min. However, the main difference in the deposition was the use of a single nozzle for the delivery of PZT ink into the template and the level of precision required to successfully carry out multilayer deposition. Particular attention had to be paid to printhead metrology,[g] fine adjustments of printhead offsets[h] and sample realignment at every deposition.

Optical micrographs of the printed structures are shown in Fig. 1.15a. Monitoring of the visual appearance during ten printing–annealing cycles reveals a series of color changes as film thickness increases. This is also accompanied by widening of the structure from 70 to 150 µm with the number of layers. Nevertheless, edges along the x direction remain straight and the structures stay well-defined throughout the stacking process (no merging between two adjacent lines). No cracking of the films was observed either. Widening of the structures indicates that some degree of spreading of PZT ink over the template can occur, which is probably due to the fact that the structures are especially narrow. Indeed, this was not observed for the $500 \times 500\,\mu m^2$ structures, which conserved the original dimensions throughout the stacking process.

Upon closer examination of the width profiles (Fig. 1.15c), it appears that film thickness measured at the center increases linearly up to eight layers, after which it starts to taper off (Fig. 1.15b). Also note the non-zero intercept of the plot, which is directly linked to the widening of the structures. Importantly, the measured 3D profiles allowed an estimation of the volume of the structures, whose evolution is strictly linear with the number of layers as expected, since the same amount of ink is delivered for each additional printed layer. With the help of eq. (1.1), it is also possible to work out an estimate of the droplet volume, which turns out to be ∼2 pL in this case, i.e. double the nominal value. The 3D profile of the 10-layered structure (Fig. 1.15d) shows that a slight coffee ring-like behavior is observed in the x-section, as the edges are ∼10 % thicker than the center of the structure. Nevertheless, the central area is sufficiently flat, with a thickness of 440 nm. The y-section shows that a width of less than 50 µm at the summit of the structure is flat enough to be exploited for the deposition of top electrodes. We therefore proceeded with the deposition of 20 µm-wide platinum top electrodes.

[g] Printhead metrology is a systematic operation that has to be performed every time a cartridge is changed or removed/reinserted. The body of the cartridge printhead being made of plastic, small offsets in droplet position can be introduced due to mechanical tolerance. The metrology routine allows a precise realignment of the nozzle plate with the coordinate system of the printer.

[h] Despite printhead metrology, offsets can also be introduced by the choice of a particular nozzle (droplet deviation can only be observed along one dimension) or the horizontal component in the droplet trajectory due to the printhead motion.

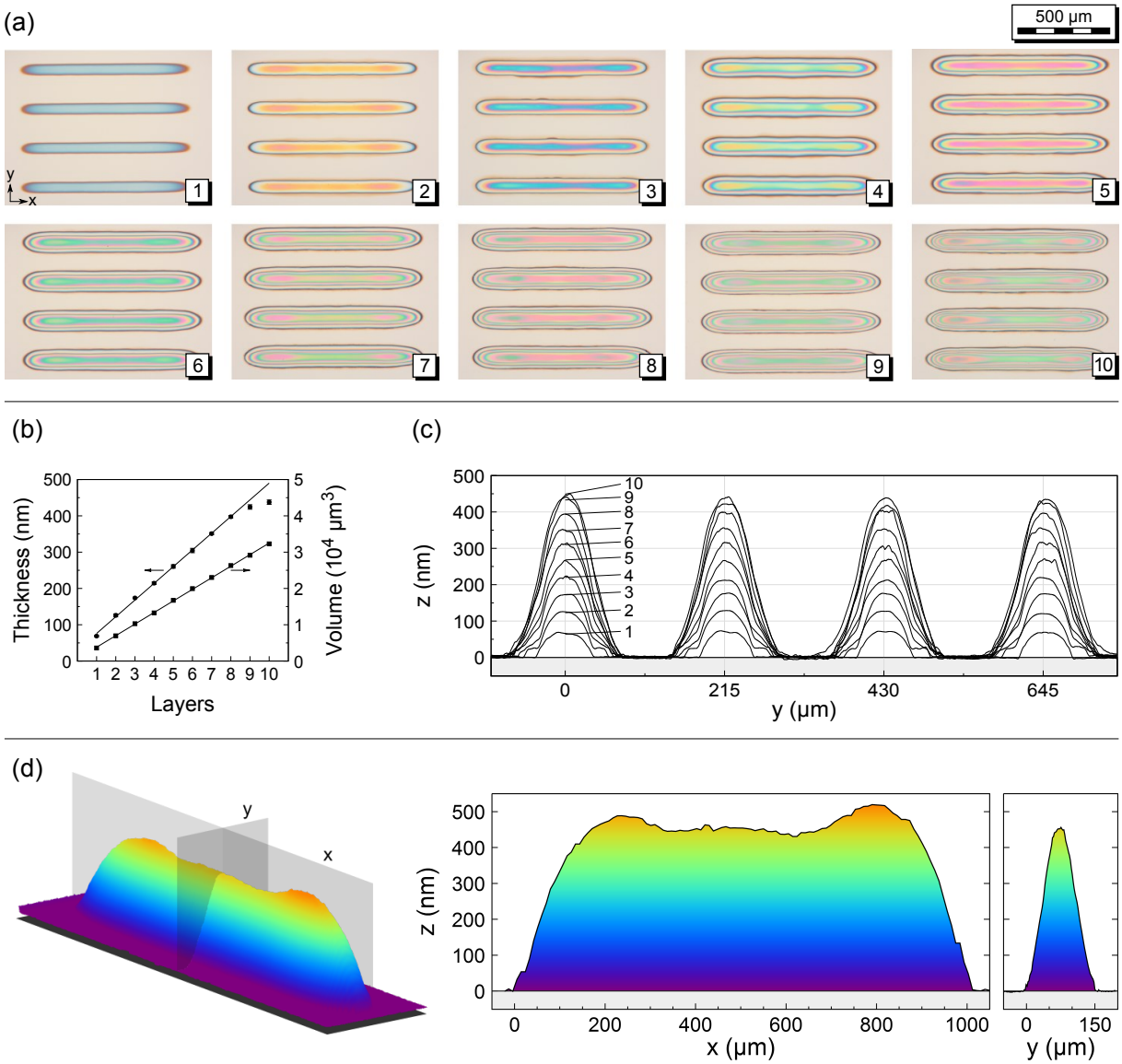

Fig. 1.15. Morphology of inkjet-printed PZT lines: (a) optical micrographs throughout the layer stacking process, (b) evolution of film thickness and volume with the number of deposited layers, (c) thickness profiles measured across the *y* direction for four adjacent lines and (d) 3D profile of the 10-layered PZT structure.

Successful crystallization into the desired perovskite phase is confirmed by grazing incidence XRD (Fig. 1.16a). Observation of the surface by SEM (Fig. 1.16b) reveals hundred-nanometer-sized perovskite grains along with the presence of small quantities of pyrochlore. This parasitic phase is typically present at the surface and accounts for less than 1 % of the volume fraction, hence its absence from the XRD pattern. Pinholes can also be found on the surface, which are believed to be small and shallow enough not to cause short circuits between top and bottom electrodes.

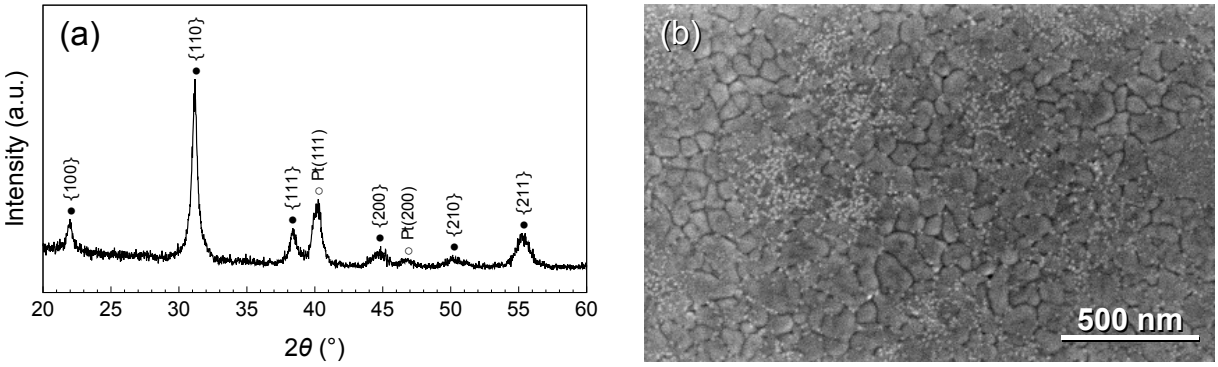

Fig. 1.16. (a) Grazing incidence XRD pattern and (b) surface SEM of inkjet-printed PZT lines.

Electromechanical characterization

Sputtered platinum top electrodes ($300 \times 20\,\mu m^2$) were patterned by photolithography on top of the 440 nm-thick PZT structures for electrical characterization. The polarization–electric field loop shown in Fig. 1.17a exhibits ferroelectric switching with remanent polarization P_r = $13\,\mu C\,cm^{-2}$ and coercive field E_c = $58\,kV\,cm^{-1}$. The relative permittivity–electric field loop (Fig. 1.17b) also displays a typical ferroelectric behavior, with $\varepsilon_r = 900$ and $\tan\delta = 0.07$ at zero electric field bias. These values are in line with what is typically observed for CSD-derived PZT films (Table 1.2) and constitute an improvement with respect to the state of the art of inkjet-printed PZT, taking into account that our process did not involve any lithographic step for patterning the films.

Reference		Year	Process	Substrate	A_{PZT} (mm^2)	d_{PZT} (nm)	$2P_r$ ($\mu C\,cm^{-2}$)	$2E_c$ ($kV\,cm^{-1}$)	ε_r	$\tan\delta$
Bathurst et al.	[83]	2009	IJP	Pt/Si	0.25	400	17	220	–	–
Rho et al.	[100]	2010	SC	Au/Cr/polym.	0.04	360	40	60	1100	–
Pérez et al.	[101]	2010	SC	Pt/Si	–	420	30	100	1000	0.05
Zuo et al.	[102]	2012	PLD	Pt foil	100	200	51	110	2650	–
Machida et al.	[86]	2012	IJP	Pt/Si	0.05	2000	20	46	1700	0.05
Ghoneim et al.	[103]	2015	SC	Pt/Si	0.01	280	25	110	1265	–
This work	[94]	2019	IJP	Pt/Si	0.15	440	26	116	900	0.07

Table 1.2. Inkjet-printed PZT lines: comparison of the electrical properties with literature. The cited references include inkjet-printed (IJP) and spin-coated (SC) layers, as well as PZT films obtained by pulsed laser deposition (PLD).

Piezoelectric characterization was performed using double beam laser interferometry (DBLI). This technique has precise geometry requirements for a quantitative assessment of the effective longitudinal piezoelectric coefficient $d_{33,f}$ of piezoelectric thin films on a substrate. In particular, the ratio between electrode size and substrate thickness needs to be close to unity [104, 105], which is impossible with the PZT line structures. Dedicated samples with large-area PZT films and 700 µm-diameter sputtered platinum top electrodes were therefore fabricated, using

a strategy that will be presented in the next chapter (please refer to page 55). The large-signal displacement and small-signal $d_{33,f}$ coefficient are shown in Figs. 1.17c and 1.17d, respectively. The large-signal displacement characteristic is a typical butterfly-shaped loop. The $d_{33,f}$ coefficient reaches a maximum value 50 pm V^{-1}, which is in good agreement with the one reported by Pérez et al. for 420 nm-thick spin-coated PZT films [101].

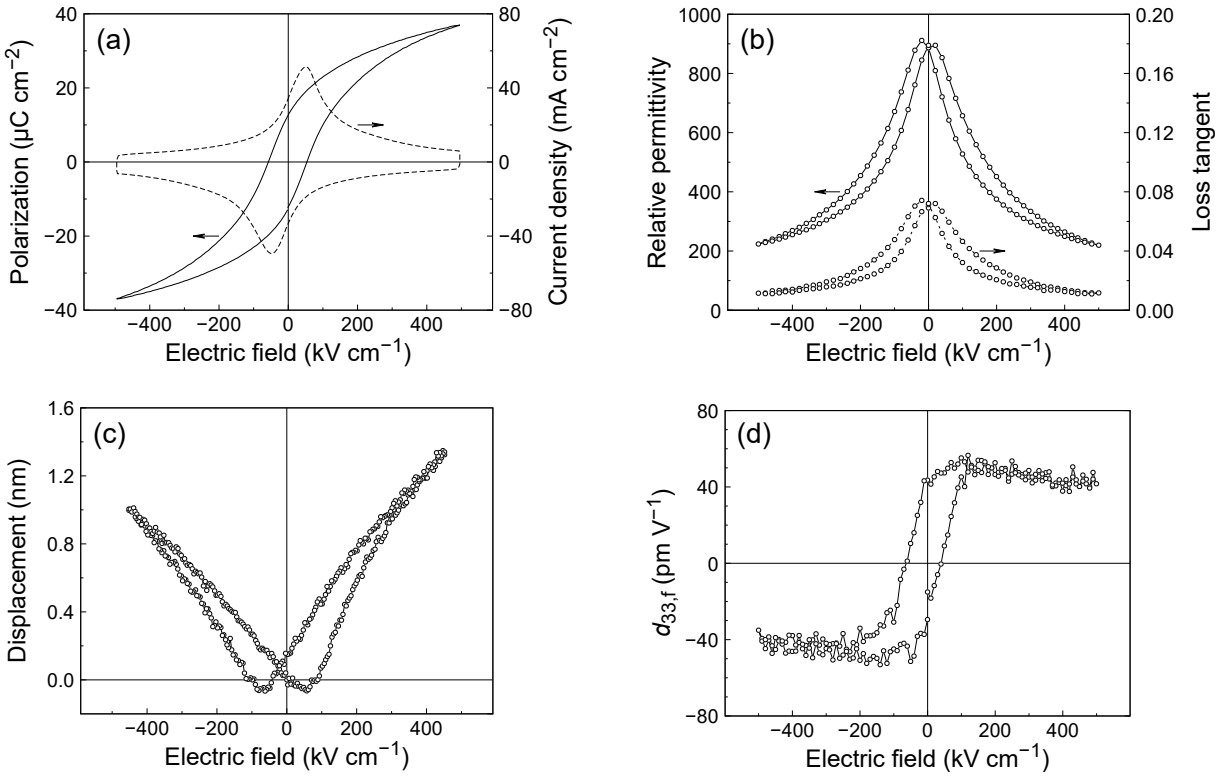

Fig. 1.17. Electrical characterization of 440 nm-thick inkjet-printed PZT lines: (a) *P*–*E* loop measured at 100 Hz and (b) ε–*E* loop measured at 1 kHz (V_{AC} = 1 V). DBLI characterization of inkjet-printed 400 nm-thick PZT films with 700 μm-diameter top electrodes: (c) large-signal displacement at 100 Hz and (d) small-signal $d_{33,f}$ coefficient at 1 kHz.

Discussion and further developments

Thanks to photolithographic techniques, it is possible to achieve resolutions down to the 10–100 nm range [106]. Inkjet printing can realistically achieve resolutions in the 10–100 μm range, due to technical limitations such as droplet size, deviations in the droplet trajectory, accuracy of the printhead and ink-substrate interactions. In our strategy, we need to distinguish the resolution in printing the template and the functional ink. As we have seen, the templating ink displays strong wetting towards the substrate, with a splat size ranging between 80 and 165 μm for ~2 pL droplets (which have an initial diameter of 16 μm) as we go from single splats to continuous lines without jaggedness. This sets the limits for the types of shapes than can be printed with the functional ink via this process and the pitch between the printed patterns.

The procedure is quite straightforward for printing rectangles and squares as the template grid can be printed cleanly. Indeed, the intersections between the template lines form sharp corners and the pitch between them can be tuned down to the desired PZT linewidth (realistically ~30 µm). However, it would be much more challenging to print concave polygons or intricate shapes with sharp inward angles because of the large splat size of the templating ink. Along the same lines, printing a PZT shape with curved edges would also be somewhat challenging as the printer typically operates in a raster fashion along the x or y direction. Some degree of jaggedness in the edges is therefore to be expected. Once again, this raises the importance of carrying out printhead metrology and fine adjustments of the printhead offsets.

A workaround for the line pitch limitation was attempted, as shown in Fig. 1.18. After printing an array of lines as described earlier and performing the drying and pyrolysis steps, the same fabrication file was printed with a vertical offset y_{offset} corresponding to half of the splat diameters of the templating ink (D_{template}) and PZT ink (D_{PZT}) inside the template (eq. (1.8)), effectively printing the same pattern between the previously printed lines.

$$y_{\text{offset}} = \frac{1}{2}\left(D_{\text{template}} + D_{\text{PZT}}\right) = \frac{1}{2}S_{\text{y,template}} \tag{1.8}$$

The vertical offset y_{offset} also corresponds to half of the pitch between the template lines $S_{\text{y,template}}$ as defined in the fabrication file. After this step, the rest of the process is carried out as usual. Although promising, increasing the film thickness by deposition of successive layers was found to be quite challenging due to the widening of PZT lines observed earlier (see Fig. 1.15b).

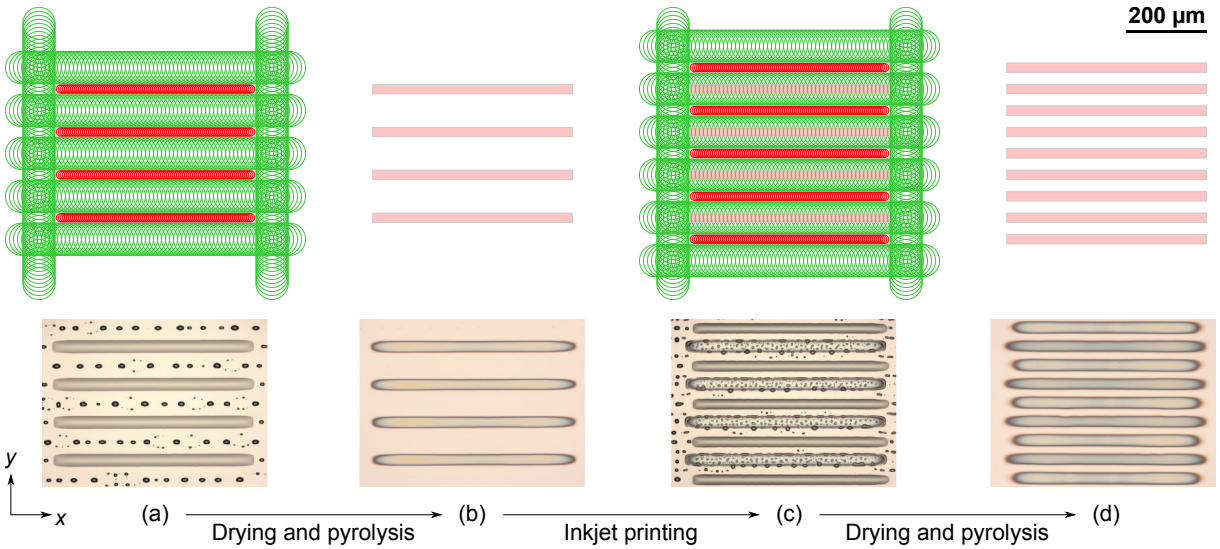

Fig. 1.18. Description of the line intercalation strategy for reducing the pitch between inkjet-printed PZT lines: (a) an array of PZT lines is printed according to the normal strategy, (b) the liquid film is dried and pyrolyzed, (c) a vertical offset is introduced to print the same pattern between the pyrolyzed lines and (d) a final drying–pyrolysis sequence is performed. The array is then ready to be crystallized. Optical micrographs provide a proof of concept of this process.

Another limitation of this process is related to the 3D morphology of the printed structures, which typically display gentle slopes at the edges instead of the desired steep slopes. This in turn limits the area of homogeneous thickness suitable for the deposition of top electrodes and therefore the active area of the final piezoelectric device. Fine tuning of the solvent composition could be envisaged to adjust the balance between the outward capillary and inward Marangoni flows, thus achieving steeper slopes [71]. Two different ink compositions could also be used conjointly and compensate their effects while stacking multiple layers.

Finally, although our inkjet-printed films exhibited an appreciable electrical and piezoelectric response, improvement of the material quality is still possible to match state-of-the-art values. Optimization of the annealing process is the first step to be considered, as the ink chemistry and thermal profile are different from those of the spin coating solution. This topic will be discussed in the next chapter.

1.4. Chapter summary

In this chapter, we addressed the challenge of printing PZT structures on platinized silicon without assistance from lithographic processes. We saw that the high surface energy of platinum at the origin of extreme ink spreading makes direct printing of sub-100 µm patterns impossible. However, thanks to an ink based on 1-dodecanethiol, we were able to print ink-repelling SAM soft templates on the platinum surface. These templates were able to confine PZT ink into well-defined areas, thus enabling patterning of PZT films on platinized silicon using exclusively inkjet printing.

This printing strategy served as basis for the development of an iterative inkjet printing process, where every iteration of the cycle increases the thickness of the printed PZT film. With this process, we were able to print a micron-thick $500 \times 500\,\mu m^2$ PZT square. The SAM-based template proved to be reliable for preventing ink spreading and could very conveniently be integrated in the printing process, making it remarkably time-efficient.

Finally, in order to explore the capabilities of the process in terms of resolution, we attempted to print PZT lines. Although a widening of the line occurred during the layer stacking process due to the narrowness of the pattern, the final $1000 \times 150\,\mu m^2$ and 440 nm-thick PZT structures exhibited typical electrical properties of CSD-derived films, with $P_r = 13\,\mu C\,cm^{-2}$, $E_c = 58\,kV\,cm^{-1}$, $\varepsilon_r = 900$ and $\tan\delta = 0.07$.

Chapter 2

Study of pyrolysis for high-quality inkjet-printed PZT layers

2.1. Motivation

Chemical solution deposition of PZT thin films via spin coating can serve as the basis for the development of the inkjet printing process. The chemistry of solutions and the processing steps remain essentially very similar. However, spin coating solutions cannot be used as such in inkjet printing, for several reasons. First, considerations from fluid dynamics state that the rheological properties (surface tension and viscosity) need to be adjusted for successful droplet formation at the printhead nozzles. This is described by the dimensionless parameter Z as defined by eq. (2.1),

$$Z = \frac{\sqrt{a\gamma\rho}}{\eta}\,, \tag{2.1}$$

where a is the characteristic length (nozzle size) in m, γ is surface tension in $\mathrm{N\,m^{-1}}$, ρ is density in $\mathrm{kg\,m^{-3}}$ and η is viscosity in Pa s. Z describes the balance between surface tension and viscous forces in the liquid and it is accepted that its value should be $1 < Z < 10$ for successful droplet formation [55]. Standard PZT solutions for spin coating are usually based on 2-methoxyethanol (2ME) as a solvent, which is characterized by a relatively low viscosity ($\gamma_{\mathrm{2ME}} = 1.71$ mPa s at 20 °C [107]) resulting in high Z values. A convenient strategy is the modification of such a solution with viscous co-solvents.

The choice of solvents also needs to ensure stability of the CSD precursor solution, which contains highly water-sensitive alkoxide species. An ink that is unstable or consists of a too volatile solvent can result in undesired nozzle clogging, which then requires frequent purging, thereby consuming large amounts of ink and decreasing the printhead lifetime.

In this chapter, we study a PZT ink formulated from a standard solution used for spin coating by addition of high-boiling-point co-solvents. After highlighting the physicochemical differences between these solutions, we will study the influence of solution modification on the processing steps that need to be carried out after deposition. We will show that pyrolysis is a

critical step that directly impacts the quality of the final material. In particular, we will show that inkjet-printed PZT films need to be processed in conditions that differ significantly from the typical ranges of conditions employed in the case of spin-coated PZT thin films. The study presented in this chapter was published in the *Journal of Materials Chemistry C* [108].

2.2. Ink formulation

The PZT ink formulation based on 2-methoxyethanol, glycerol and ethylene glycol was already described in the previous chapter. Please refer to page 30 for a detailed description of the preparation procedure.

2.3. Ink characterization

2.3.1. Physicochemical properties

Viscosity of the solutions was determined via the parallel plate method (50 mm-diameter plate and 1 mm-gap between the plate and the bottom of the steel cup filled with 2 mL of solution) using an MCR 502 rheometer (Anton Paar, Austria). The flow curves are shown in Fig. 2.1a.[a] Surface tension was determined using the pendant drop method. Photographs of 4 µL droplets hanging from a 0.51 mm-diameter needle (treated with a hydrophobization kit) were recorded with an OCA 25 goniometer (DataPhysics, Germany) and processed with the software OpenDrop [97]. Density was determined by a simple gravimetric method: the mass of 10.0 mL of solution was recorded and divided by its volume. The results are presented in Table 2.1 and allowed to evaluate the Z parameter for a nozzle size of 21 µm (10 pL nominal volume Fujifilm Dimatix cartridges), using eq. (2.1).

	PZT SC solution	PZT ink	2-Methoxyethanol	Glycerol	Ethylene glycol
Concentration ($\mathrm{mol\,L^{-1}}$)	0.3	0.2	–	–	–
Surface tension ($\mathrm{mN\,m^{-1}}$)	32.5	34.2	30.84	63.4	47.3
Density ($\mathrm{g\,cm^{-3}}$)	1.05	1.11	0.965	1.26	1.14
Viscosity (mPa s)	2.0	8.1	1.71	1412	16.1
Z parameter	13.4	3.5	14.5	0.03	2.1

Table 2.1. Room-temperature physicochemical properties of the PZT spin coating (SC) solution, the PZT ink and the pure constitutive solvents. The Z parameter was evaluated for a nozzle size of 21 µm and concentration is defined as $C_{Zr} + C_{Ti}$ in the solution.

[a] For the evaluation of Z, we used viscosity values for a shear rate $\dot{\gamma}$ of $100\,\mathrm{s^{-1}}$, as they were consistent with the literature. Note that the actual shear rates experienced during printing are several orders of magnitude higher: for a 10 µs-long pulse, 10 pL droplet and 10 µm-radius, $\dot{\gamma} \approx 10^6\ \mathrm{s^{-1}}$ at the nozzle.

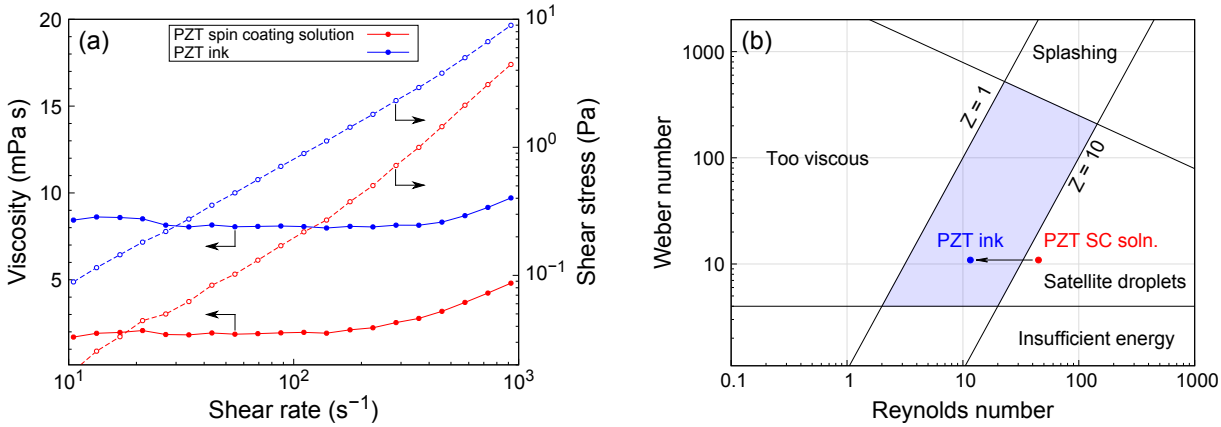

Fig. 2.1. (a) Flow curves of the PZT spin coating solution and PZT ink. Viscosity as function of shear rate is represented by the closed symbols (•), while shear stress as function of shear rate is represented by the open symbols (○). Viscosity values reported in Table 2.1 are the ones obtained for a shear rate of 100 s^{-1}. (b) Representation of the jettable range in terms of Weber and Reynolds numbers (adapted from Derby [55]) and effect of solvent modification on the jettability of PZT CSD precursor solutions.

The addition of glycerol and ethylene glycol to the PZT spin coating solution effectively decreased the Z-value from 13.4 to 3.5, thereby bringing it into the jettable range, as shown in Fig. 2.1b. These Z-values were evaluated at room temperature, whereas the temperature is typically higher during printing ($T_{\text{printhead}}$ = 30 °C). Although Z is expected to increase with increasing temperature because of lower viscosity, its value is assumed to remain within the jettable range. This can be demonstrated by the excellent jetting across a wide range of frequencies, as illustrated in the stroboscopic image of Fig. 1.5d shown in the previous chapter (page 33). Slight deviations in droplet velocity were observed at high jetting frequencies (10 kHz), therefore a frequency of 4 kHz was selected in the rest of the study, as a compromise between printing time and jetting stability.

2.3.2. Thermogravimetric analysis

Thermogravimetric analysis (TGA) coupled with differential thermal analysis (DTA) of the solutions was performed on an STA 409 PC thermal analyzer (Netzsch, Germany), with a heating rate of 10 °C min^{-1} under air atmosphere. The results are presented in Fig. 2.2. For the PZT spin coating solution, drying is characterized by a significant loss of mass and an endothermic signal centered at ~140 °C, which corresponds to the evaporation of 2-methoxyethanol. The addition of high-boiling-point co-solvents shifts the drying step towards higher temperatures in the case of the PZT ink. The initial loss of mass is associated with two endothermic contributions centered at ~155 °C and ~275 °C, which can be ascribed to the evaporation of 2-methoxyethanol and ethylene glycol up to 200 °C and the evaporation of glycerol between 250 and 300 °C, respectively. Glycerol could also decompose at temperatures below 300 °C [109], however the absence of a well-defined exothermic contribution in the DTA signal suggests that

its elimination is mainly dominated by evaporation in this temperature range. The formation of azeotropic mixtures could also account for the absence of three distinct evaporation events associated with each of the solvents.

Above 300 °C, loss of mass is observed until 500 °C for both solutions. The DTA signal shows a broad exothermic contribution which can be ascribed to pyrolysis and crystallization events. A close-up of the normalized mass variation in the 250–500 °C range is shown in the inset of Fig. 2.2. From this representation, it is evident that the proportion of residual organics in the PZT ink is higher than the one in the spin coating solution at any point during the analysis. It has to be noted that the heating rate used for this thermal analysis (10 °C min^{-1}) differs from the actual heating rates employed in the process. Indeed, the latter are much higher due to the use of hot plates for drying and pyrolysis (heating is virtually instantaneous) and rapid thermal annealing (RTA, 50 °C min^{-1}) for crystallization. The thermogravimetric analysis therefore does not properly reflect the kinetics of the process. Nonetheless, it shows that the elimination of organics form the PZT spin coating solution and from the PZT ink is substantially different. A closer examination of the pyrolysis step is the topic of the following section.

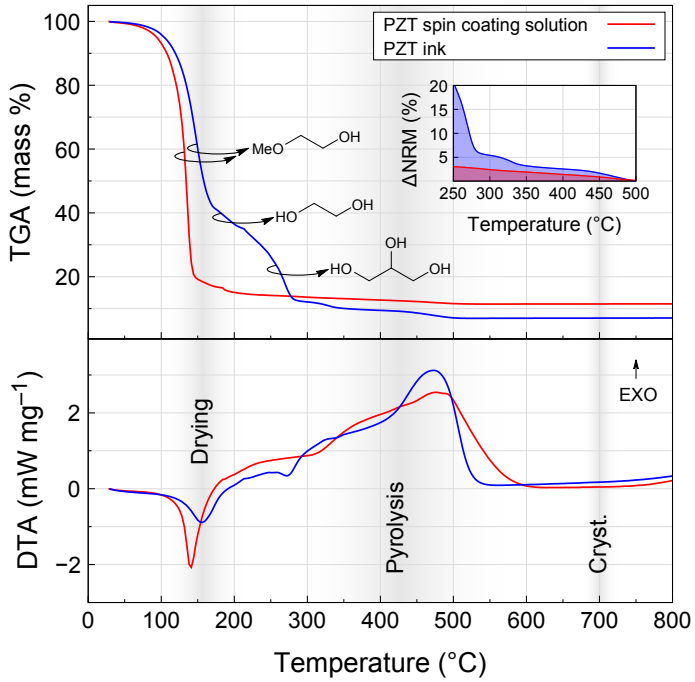

Fig. 2.2. Thermogravimetric analysis (TGA) coupled with differential thermal analysis (DTA) of PZT spin coating solution and PZT ink. The inset of the TGA curve represents the normalized residual mass ($\Delta\text{NRM} = (m - m_{\text{final}})/(100 - m_{\text{final}})$, with m and m_{final} expressed in %, where m_{final} is the mass at 500 °C) in the 250–500 °C temperature range. The highlighted areas denote the temperature ranges used in the deposition process.

2.4. Study of pyrolysis as function of time and temperature

2.4.1. Fourier transform infra-red spectroscopy

As stressed earlier, the purpose of the pyrolysis step is the removal of organic residues from the dried film. We will see later that the completion of pyrolysis is critical, as remaining organics that are carried over to the crystallization step may induce porosity in the final layers. A convenient way to assess the completion of pyrolysis is the analysis of pyrolyzed layers by Fourier transform infra-red (FTIR) spectroscopy.

The FTIR spectrum of PZT ink and its pure constitutive solvents is shown in Fig. 2.3. The typical absorption bands that can be readily identified are the ones corresponding to O–H and C–H stretching, at 3000–3600 cm^{-1} and 2800–3000 cm^{-1}, respectively. The strongest absorption band in the fingerprint region (1000–1100 cm^{-1}) can be attributed to aliphatic alcohol and ether moieties [110]. The FTIR spectrum of the PZT ink is naturally dominated by the absorption bands of 2-methoxyethanol, which is the major constituent of the ink.

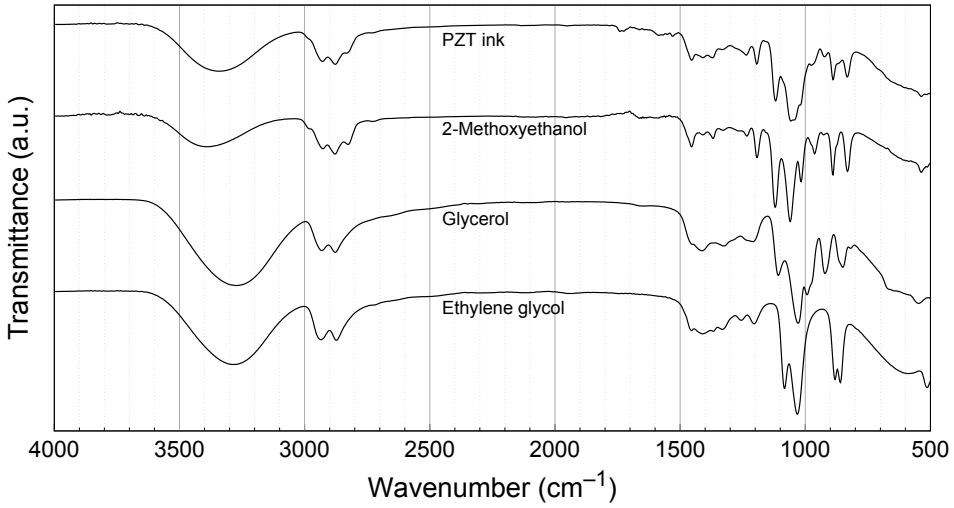

Fig. 2.3. FTIR spectra of PZT ink and its constitutive solvents, measured in ATR mode.

FTIR spectroscopy was then performed on inkjet-printed layers in order to follow the chemical transformations occurring in the films during the annealing process. The analyses were carried out on single layers printed on platinized silicon (degassed at 350 °C for 5 min before printing), resulting from a single pass of the printhead in the x-direction. Droplet spacing was 15 µm along x and 254 µm along y (spacing between consecutive nozzles). This deposition strategy can be used to print 4 mm-wide stripes of PZT with good homogeneity (except at the edges, where a coffee ring-like build up is usually observed). The droplet filling density is such that a homogeneous liquid layer is formed after printing and the thickness of one single layer after processing is $\lesssim$ 20 nm.

The temperatures of the printhead and the substrate were both set to 30 °C during printing. The films were dried on a hot plate at 175 °C for 1 min. Pyrolysis of the films was then performed on hot plates for two sets of parameters: pyrolysis time (t_{pyro} = 0.5, 1, 3, 5 and 10 min) and temperature (T_{pyro} = 350, 375, 400, 425, 450 and 475 °C). Thirty pyrolyzed samples were produced in these conditions. Finally, a pyrolyzed sample was crystallized at 700 °C for 5 min.

FTIR spectra acquired in grazing angle mode of dried, pyrolyzed (extreme conditions: 350 °C for 0.5 min and 475 °C for 10 min) and crystallized films are shown in Fig. 2.4a. The chemical signature of the PZT ink is mostly preserved after drying, as the main absorption bands can still be identified. However, their intensity significantly decreases after pyrolysis. Upon magnification (see the inset of Fig. 2.4b), two groups of absorption bands can be found in the fingerprint region of the spectrum at 1100–1800 cm^{-1} and 600–800 cm^{-1}. These can be attributed to the remaining organics (possibly oxidized species such as carbonates and carboxylates [110]) and to metal–oxygen bonds [111], respectively. The FTIR spectrum of the crystallized film is characterized by the disappearance of the absorption band associated to organics, while that attributed to metal–oxygen bonds becomes sharper and more intense, indicating the transformation from amorphous to crystalline state.

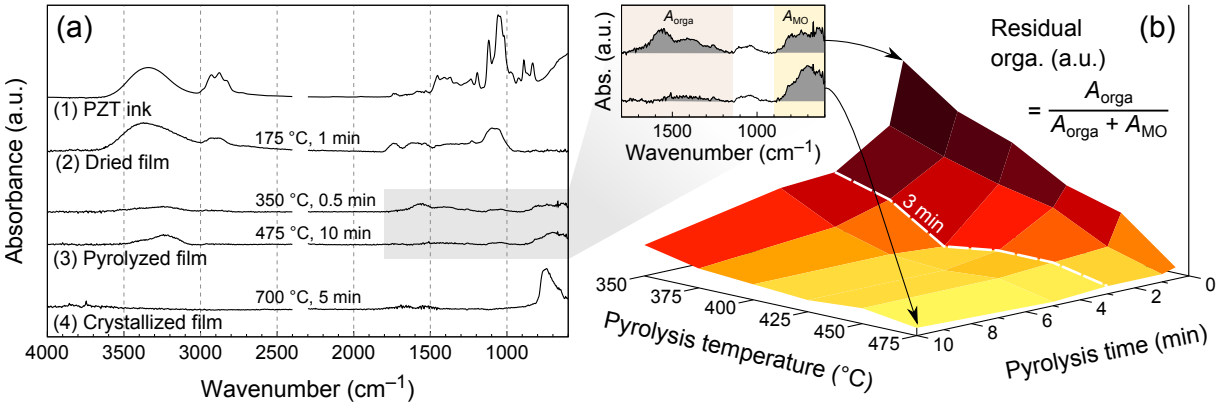

Fig. 2.4. (a) FTIR spectra showing transformations of the PZT ink from liquid to crystallized state: (1) FTIR spectrum of the PZT ink acquired in ATR mode and down-scaled for comparison with FTIR spectra acquired in grazing angle mode, namely a single layer printed on platinized silicon and (2) dried at 175 °C for 1 min, followed by (3) pyrolysis at 350 °C for 0.5 min or 475 °C for 10 min and finally after (4) crystallization at 700 °C for 5 min. (b) The region of interest between 600 and 1800 cm^{-1} in the FTIR spectra of pyrolyzed films was used to draw the correlation between pyrolysis conditions (temperature and time) and amount of residual organics.

The relative amount of residual organics was evaluated from the integrated intensity of the two groups of absorption bands in the region of interest illustrated in the inset of Fig. 2.4b, using eq. (2.2). While this method does not provide an absolute measure of the amount of organic residue, it can very effectively highlight trends in the influence of pyrolysis conditions.

$$\text{Residual organics (a.u.)} = \frac{A_{\text{orga}}}{A_{\text{orga}} + A_{\text{MO}}} \tag{2.2}$$

The results are illustrated in Fig. 2.4b, where the ratio expressed by eq. (2.2) is plotted as a 3D surface, as function of pyrolysis time and temperature. This surface is comparable to a landscape, where the elevated areas are associated with high residual organic content and the bottom flat area represents low organic content, i.e. when pyrolysis tends towards completion. From this representation, it is clear that this flat area is bound by the conditions $T_{\text{pyro}} \geq 400\,^{\circ}\text{C}$ and $t_{\text{pyro}} \geq 3\,\text{min}$. Lower pyrolysis temperatures (350 and 375 °C) appear to be unsuitable for the process as the amount of residual organics is noticeably higher, even when pyrolysis time is extended to 10 min. This observation irrevocably sets the requirement for $T_{\text{pyro}} \geq 400\,^{\circ}\text{C}$ when processing PZT films based on glycerol and ethylene glycol-modified solutions. A qualitative assessment of pyrolysis kinetics can also be drawn from these results. Indeed, for temperatures lower than 450 °C, complete elimination of organics requires at least 3 min, as a significant amount of residual organics is still present after 0.5 and 1 min of pyrolysis.

2.4.2. Microstructural characterization

The previous investigation was carried out on pyrolyzed layers resulting from a single deposition, which are very thin ($\lesssim 20\,\text{nm}$). In this next step of the study, we will focus on 200 nm-thick PZT films prepared by twelve successive printing–drying–pyrolysis cycles and eventually crystallized at 700 °C for 5 min. In particular, we will show how the microstructure of crystallized films is affected by pyrolysis temperature along the 3 min line represented in Fig. 2.4b.

Scanning electron microscopy

Scanning electron microscopy (SEM) observations were performed on a FEI Helios NanoLab 650 microscope. Images of cross sections were obtained with an accelerating voltage of 5 kV (platinum in the substrate stack can evacuate charges), while top views were obtained at 2 kV to avoid charging effects. Cross section micrographs of PZT films pyrolyzed at different temperatures for 3 min and then crystallized at 700 °C for 5 min are shown in Fig. 2.5a. The PZT films pyrolyzed at 350 and 375 °C are clearly porous, as opposed to the comparatively denser rest of the series. SEM top views of the PZT films pyrolyzed at the extreme temperatures of the series are shown in Fig. 2.5b and display a similar trend. Pyrolysis at 350 °C results in significant intergranular porosity, whereas pyrolysis at 475 °C affords dense films with columnar microstructure. A small amount of pyrochlore phase in the form of ~10 nm-sized grains is visible on the surface of these films, however it is not detected in XRD patterns, as seen later (Fig. 2.8).

These observations correlate well with the FTIR study, suggesting a strong influence of residual organics in pyrolyzed films on the development of porosity during crystallization. Indeed, if the elimination of residual organics happens during crystallization, gaseous decomposition products are released rapidly as a result of the high crystallization temperature (700 °C) and fast heating rate ($50\,^{\circ}\text{C}\,\text{s}^{-1}$). This process is believed to hinder film densification, resulting

in a porous granular microstructure. Comparison of cross sections films pyrolyzed at 350 °C and subsequently crystallized at 700 °C (Fig. 2.6) confirms that large pores appear during crystallization. The pyrolyzed films exhibit porosity, which consists of small pores and is evenly distributed throughout the thickness of the layer. This homogeneous distribution of porosity can be explained by the fact that the pyrolyzed layer consists of the twelve thin sublayers that each undergo pyrolysis. In contrast, porosity in the crystallized layer consists of much larger pores mainly located at the PZT/platinum interface.

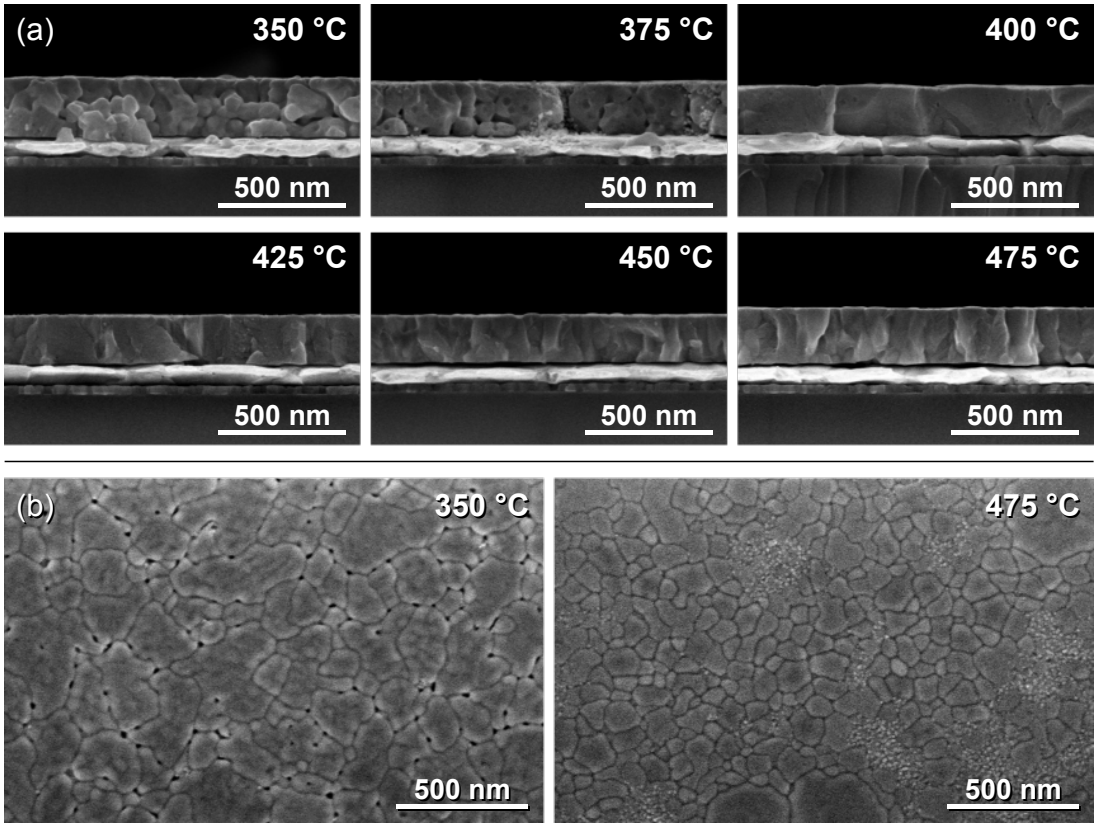

Fig. 2.5. SEM micrographs of crystallized PZT films pyrolyzed at different temperatures for 3 min: (a) cross sections of the complete series and (b) top views of the films pyrolyzed at 350 and 475 °C. The film pyrolyzed at 350 °C clearly exhibits intergranular porosity.

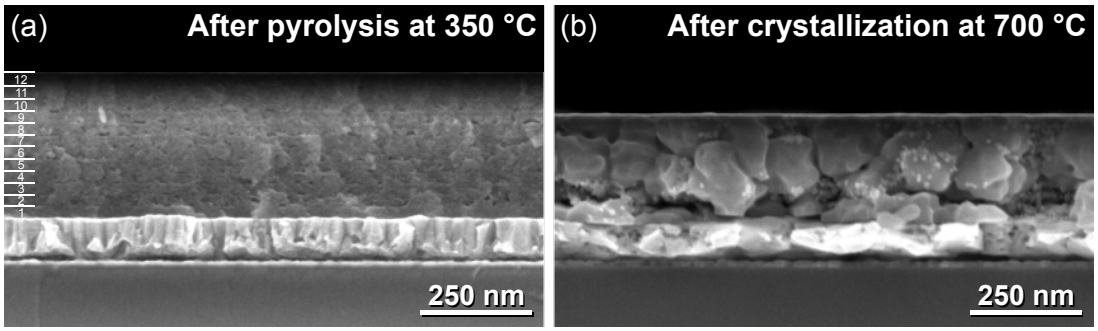

Fig. 2.6. SEM cross sections of an inkjet-printed PZT film (a) pyrolyzed at 350 °C for 3 min (12 layers) and (b) subsequently crystallized at 700 °C.

X-ray reflectivity

X-ray reflectivity (XRR) was used to evaluate the density of the printed layers in order to assess the trend observed in the SEM cross sections presented in Fig. 2.5a. The critical angle of total reflection θ_c can be directly related to the density ρ of the PZT layer and is characterized by an abrupt intensity drop in the plot of the logarithm of intensity as function of 2θ, as shown in Fig. 2.7a (a close-up of the PZT edge is given in Fig. 2.7b). XRR patterns were recorded with a PANalytical X'Pert Pro diffractometer with Cu-K_α radiation (0.154 nm wavelength). The beam width was confined to 4 mm using a mask and the beam footprint was limited with a knife edge collimator. Please refer to page 136 in Appendix D for further details on the technique.

Due to the irregular sample geometry (PZT stripes separated by a gap and presenting thickness variations at the edges), absolute density values could not be reliably extracted. However, we were able to track relative changes in density, as the series of samples was measured in a similar way. The critical angle θ_c was defined as the angle where a 50 % decrease of the maximum recorded intensity found at 2θ = 0.4–0.5° was observed. The density was then calculated from θ_c using atomic scattering factors given in: [112, 113]. The second edge observed at $2\theta \sim 1.1°$ is due to the platinum under the inkjet-printed PZT stripes.

The extracted density values were normalized with respect to the values obtained for the three lowest pyrolysis temperatures and expressed as a percentage variation ($\Delta\rho_{norm}$), representing the improvement of density with pyrolysis temperature. This is illustrated in the inset of Fig. 2.7b, from which we can conclude that density improves by about 9 % above a threshold temperature between 400 and 425 °C.[b] Having determined the link between pyrolysis temperature and porosity, we will now examine the influence of pyrolysis temperature on the crystalline orientation of the inkjet-printed films.

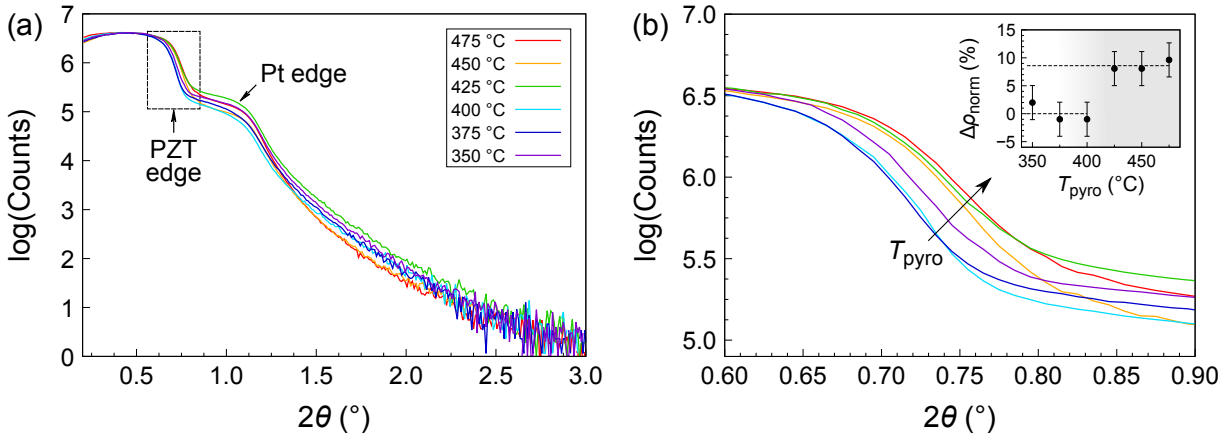

Fig. 2.7. X-ray reflectivity patterns of crystallized inkjet-printed PZT films pyrolyzed for 3 min at temperatures ranging from 350 to 475 °C: (a) full pattern and (b) close-up on the PZT edge. Inset: evolution of normalized density with pyrolysis temperature.

[b] The error bars shown in the plot were derived from: (1) the variation in θ_c obtained from using 0.40, 0.45 or 0.50° as initial intensity and (2) the finite step width of the XRR scan. An uncertainty of ±3 % was estimated.

X-ray diffraction

X-ray diffraction (XRD) patterns of crystallized PZT films recorded in θ-2θ geometry are presented in Fig. 2.8. All the XRD patterns indicate the presence of the desired perovskite phase. Traces of the parasitic pyrochlore phase seen in SEM top views are absent from the XRD pattern (typical signal found at $2\theta \sim 29°$), meaning that this phase represents <1 % of the total volume. Inkjet-printed PZT films pyrolyzed at 350 °C are randomly oriented, as the intensity ratios of the {100} and {110} match those of a powder ({110} is the most intense peak). Interestingly, a noticeable contribution of the {100} orientation is detected in the film pyrolyzed at 375 °C. However, predominance of the {111} orientation is observed for $T_{\text{pyro}} \geq 400$ °C.

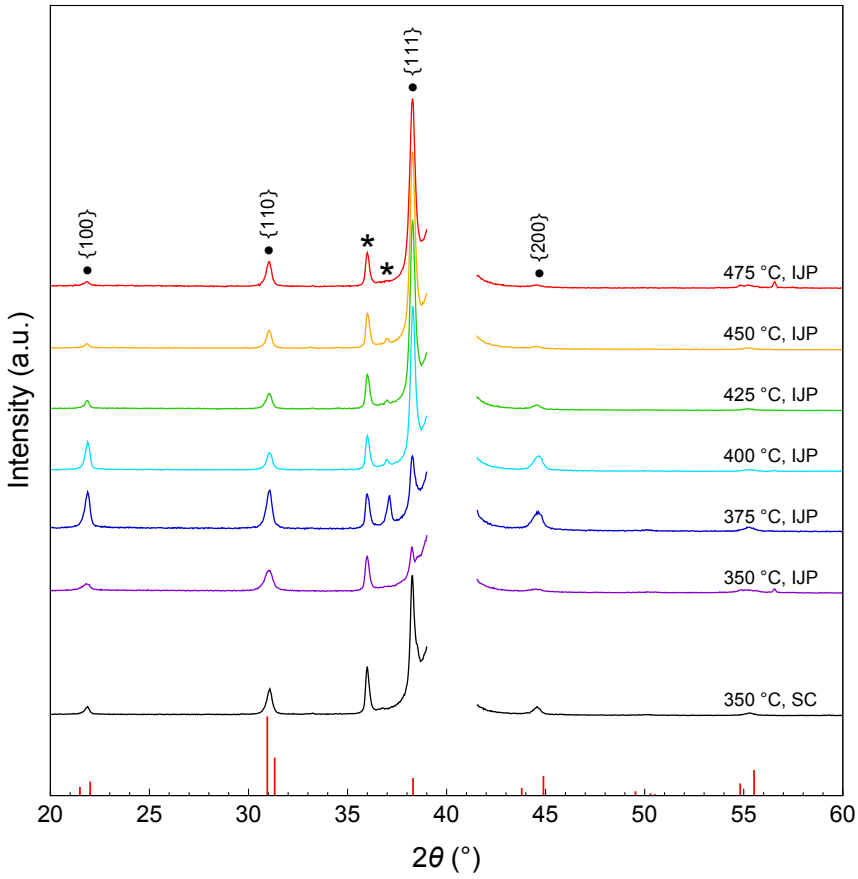

Fig. 2.8. X-ray diffraction patterns of crystallized inkjet-printed (IJP) PZT films pyrolyzed for 3 min at temperatures ranging from 350 to 475 °C. The XRD pattern of a spin-coated (SC) film pyrolyzed at 350 °C for 3 min is given for comparison. Peaks marked with an asterisk (∗) are due to the substrate. The Pt(111) reflection at $2\theta \sim 40°$ was masked for clarity. The red bars represent the intensities for a $Pb(Zr_{0.53}Ti_{0.47})O_3$ powder [PDF 01-070-4264].

It is known that PZT films grown on platinized silicon without a seed layer tend to adopt the texture of the underlying platinum electrode [38]. Studies have also associated the development of {111} orientation with the appearance of a transient Pt_xPb intermetallic phase at the interface between PZT and Pt [114]. This transient phase forms as Pb(II) is reduced to Pb(0) in the reducing environment created by the presence of remaining organics. Pb(0) diffuses into the Pt

electrode, forming a (111)-oriented Pt_xPb phase. Pb(0) is then reoxidized to Pb(II). Whether the {111} orientation in PZT stems from Pt_xPb was questioned by Nittala et al. [39], who also evidenced a strong correlation between texture and heating rate during crystallization.

As the inkjet-printed PZT films pyrolyzed at 350 °C in this study still contained a substantial amount of residual organics, it is probable that the rapid evolution of gases during crystallization disrupted substrate-templated growth of the crystalline phase. Therefore, crystallization proceeded via homogeneous nucleation, resulting in a randomly oriented film. At 375 °C, this effect is less pronounced, as some degree of {100} and {111} textures can be detected. Comparison with a spin-coated PZT film pyrolyzed at 350 °C (also shown in Fig. 2.8) shows that in the absence of high-boiling-point co-solvents and seed layer, {111} texture is predominant, even for pyrolysis at 350 °C, similarly to what is observed for inkjet-printed films pyrolyzed at $T_{\mathrm{pyro}} \geq 400\,°\mathrm{C}$.

2.4.3. Electrical characterization

Sputtered platinum top electrodes (100 µm-diameter) were patterned by lift-off photolithography and reannealed at 400 °C for 10 min. The polarization–electric field (P–E) loops shown in Fig. 2.9a were recorded using an aixACCT TF Analyzer 2000 at a frequency of 100 Hz up to $\pm 500\,\mathrm{kV\,cm^{-1}}$. All the samples of the series exhibit a measurable ferroelectric response in this electric field window, including the porous ones (no significant leakage current contribution). The porous PZT films pyrolyzed at 350 and 375 °C display the lowest remanent polarizations, with 8.0 and $10.2\,\mu\mathrm{C\,cm^{-2}}$, respectively. From 400 to 475 °C, a relatively steady increase of both the remanent polarization P_r and maximum polarization P_{max} can be observed (inset of Fig. 2.9a). The highest value of P_r is observed for the film pyrolyzed at 475 °C ($23.7\,\mu\mathrm{C\,cm^{-2}}$). It should be noted that the measured coercive field is not significantly influenced by the pyrolysis temperature, contrary to what could be expected due to the different levels of porosity. However, the relationship between coercive field and porosity is nontrivial and can be strongly nonlinear as both the distribution and level of porosity come into play [115, 116].

Relative permittivity–electric field (ε_r–E) loops are represented in Fig. 2.9b and were measured at 1 kHz with a small-signal amplitude of 100 mV in the same electric field range as the P–E measurements. The butterfly-shaped loops are characteristic of the ferroelectric response. The relative permittivity at zero bias ($E = 0\,\mathrm{kV\,cm^{-1}}$) increases with increasing pyrolysis temperature until it reaches a plateau at $T_{\mathrm{pyro}} = 400\,°\mathrm{C}$, where $\varepsilon_\mathrm{r} \sim 1000$ (see inset of Fig. 2.9b). An increase of the dielectric losses at zero bias with increasing pyrolysis temperature is also observed. This a typical behavior in ferroelectric thin films and can be ascribed to extrinsic contributions. Interestingly, the loss tangent at high bias fields is higher for the films pyrolyzed at 350 and 375 °C (see magnification in Fig. 2.9d). This could be explained by a higher leakage current at high fields. Indeed, a similar trend is observed in the current–electric field loops corresponding to the P–E loops of Fig. 2.9a and illustrated in Fig. 2.9c.

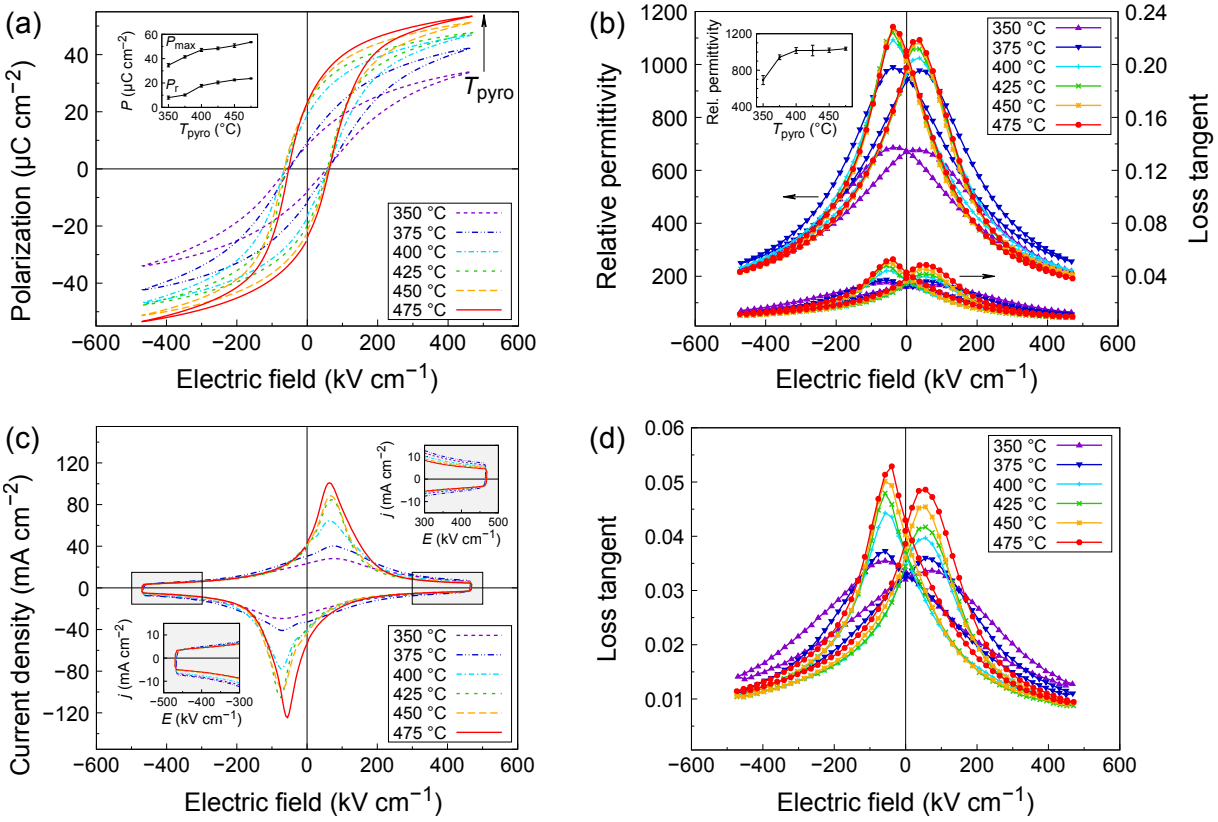

Fig. 2.9. Electrical characterization of 200 nm-thick inkjet-printed PZT films pyrolyzed for 3 min at temperatures ranging from 350 to 475 °C: (a) polarization–electric field loops at 100 Hz and (b) relative permittivity–electric field loops at 1 kHz (V_{AC} = 100 mV). The (c) current–electric field loops (with close up on current at high fields) and (d) close-up on loss tangent are associated with (a) and (b), respectively.

Reference		Year	Process	d (μm)	P_r (μC cm^{-2})	E_c (kV cm^{-1})	ε_r	tan δ
Fang et al.	[117]	2006	Spin coating	1.64	14	30	–	–
Bathurst et al.	[83]	2009	Inkjet printing	0.4	8.5	110	–	–
Morimoto et al.	[118]	2010	Sputtering	2.8	30	50	166	–
Pérez et al.	[98]	2010	Spin coating	0.42	15	50	1000	0.05
Rho et al.	[100]	2010	Spin coating	0.36	20	30	1100	–
Machida et al.	[86]	2012	Inkjet printing	2	10	17	1700	0.05
Zuo et al.	[102]	2012	Pulsed laser depo.	0.2	25	55	2650	–
Borman et al.	[119]	2017	Spin coating	1.5	32	38	1650	0.03
Godard et al.	[94]	2019	Inkjet printing	0.44	13	58	900	0.07
This work	[108]	2020	Inkjet printing	0.2	23	60	1000	0.04

Table 2.2. Comparison of the electrical properties of inkjet-printed PZT presented in this study with the literature.

As could be anticipated, the films pyrolyzed at $T_{\text{pyro}} \geq 400\,°\text{C}$ display the best electrical properties, in good agreement with the observed improvement of the microstructure and development of dense columnar grains. A comparison of the results obtained for the films pyrolyzed at 475 °C with selected works from the literature can be found in Table 2.2. The electrical properties of the films presented in this study are in line with state-of-the art CSD-derived films and show a noticeable improvement compared to previous reports on inkjet-printed PZT films.

The electromechanical response of inkjet-printed films was assessed through the design and testing of a functional device in the form of an energy harvester, which will be fully exposed in the next chapter.

2.5. Chapter summary

In this second chapter, we examined the adaptation of conventional chemical solution deposition processing in order to print PZT thin films. The addition of glycerol and ethylene glycol to a standard 2-methoxyethanol-based PZT precursor solution resulted in a stable PZT precursor ink that exhibited excellent jetting characteristics. As could be expected, the presence of the two high-boiling-point co-solvents shifted the typical processing temperatures higher, which was confirmed by comparing the thermogravimetric profile of the standard PZT solution and the PZT ink.

Then, using a technique based on Fourier transform infra-red spectroscopy, we estimated the amount of residual organics in printed PZT layers after the pyrolysis step, both as function of pyrolysis time and temperature. This study revealed that pyrolysis at 400 °C for at least 3 min was the minimal requirement to achieve what was determined to be the lowest amount of residual organics in the pyrolyzed films. A correlation was also established with the microstructure and texture of the printed PZT films after crystallization at 700 °C: films pyrolyzed at ≥400 °C for 3 min were dense and exhibited clear {111} preferential orientation. The observed trend in the improvement of density was further confirmed by X-ray reflectivity measurements.

Finally, electrical characterization of the series of inkjet-printed PZT pyrolyzed at different temperatures for 3 min showed that films pyrolyzed above 400 °C exhibited the best properties, with $P_{\text{r}} = 23\,\mu\text{C}\,\text{cm}^{-2}$, $E_{\text{c}} = 60\,\text{kV}\,\text{cm}^{-1}$, $\varepsilon_{\text{r}} = 1000$ and $\tan\delta = 0.04$ for the films pyrolyzed at the highest temperature (475 °C), which are in line with properties of state-of-the-art CSD-derived PZT films.

In conclusion, we showed that the pyrolysis step was crucial in the processing of PZT thin films based on a CSD precursor solution modified with high-boiling-point solvents. Careful control of this step enabled high-quality inkjet-printed PZT films with excellent electrical properties.

Chapter 3

Application of inkjet-printed PZT films

As anticipated by the previous chapters, the final purpose of this work is the fabrication of functional piezoelectric devices based on inkjet-printed PZT films. Such applications require PZT films with thicknesses in the order of one micron. For technical reasons, we decided to develop devices that could be fabricated *in-house*, with the available tools and techniques. This chapter will cover the processing of devices based on the direct piezoelectric effect, in the form of energy harvesters. The results presented here were published in our article in the *Journal of Materials Chemistry C* [108]. Another illustrative example exploiting the converse piezoelectric effect can be found in Appendix C (please refer to page 129).

3.1. Energy harvesting

Environments such as cities, industries, infrastructure or engine-powered machines generate mechanical energy in the form of vibrations that eventually dissipate in the surroundings. An energy harvester (EH) is a device capable of tapping this stray mechanical energy and converting it into a usable form of energy (such as electricity) that can be stored and be subsequently used. Among the different types of EHs, piezoelectric devices have the advantage of a relatively simple architecture, as piezoelectric materials readily perform electromechanical conversion. Typical applications of EHs include powering autonomous sensors situated in inaccessible locations or embedded in structures, that collect and transmit data to a remote receiver via a wireless protocol. The concept of energy harvesting is summarized in Fig. 3.1.

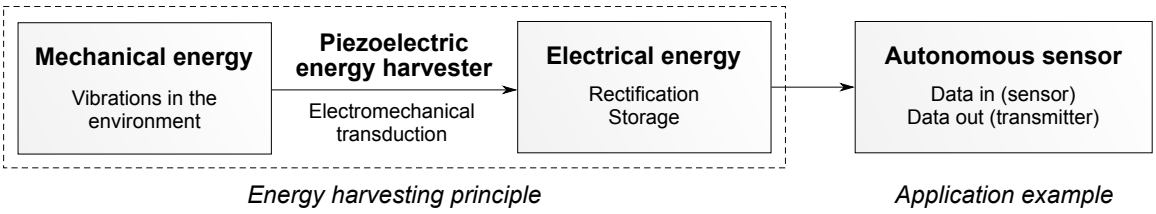

Fig. 3.1. Summary of the energy harvesting concept.

It is commonly accepted that EHs should operate at frequencies in the order of 100 Hz, which are close to the frequencies of vibrations found in the environment [120]. The desired power output usually cited by the literature is 100 µW, but there exist low-power devices with a power consumption of only about 10 µW [121]. The simplest form of piezoelectric EH is called a unimorph and consists of a beam clamped at one end and bearing a piezoelectric stack (piezoelectric film and electrodes) on one side, as illustrated in Fig. 3.2a.

In this chapter, we will describe the different steps in the design, fabrication and characterization of such a device. The substrate will be platinized silicon and a micron-thick active layer of PZT will be printed on it. As a starting point, we will discuss the vibration of cantilever beams, which will help us for the design of our device.

3.2. PZT-based energy harvesters

3.2.1. Euler-Bernoulli beam theory

The Euler-Bernoulli beam theory is one of the simplest models that can describe the physics of vibrating beams [122]. According to this theory, the first resonant frequency f of a cantilever beam is given by:

$$f = \frac{(1.875)^2}{2\pi}\sqrt{\frac{EI}{\lambda L^4}}\,, \tag{3.1}$$

where E is the Young modulus in Pa, I is the moment of inertia about the neutral axis of the beam in m, λ is the mass per unit length in kg m^{-1} and L is the length of the cantilever beam in m. For a cantilever beam with a rectangular cross section, the moment of inertia I is equal to $\frac{bh^3}{12}$. Equation (3.1) can therefore be rewritten as:

$$f = \frac{(1.875)^2}{2\pi}\sqrt{\frac{Eh^2}{12\rho L^4}}\,, \tag{3.2}$$

where b is the cantilever width in m, h is the cantilever thickness in m and ρ is the density in kg m^{-3}. Equation (3.2) needs to be modified when a proof mass M is attached at the end of the cantilever. To derive this expression, let us first consider the case of a massless cantilever with an effective mass m' attached at its free end. This effective mass produces the same resonant frequency as the cantilever without a proof mass (i.e. when the total mass is distributed linearly along the beam). The resonant frequency f' of this massless cantilever corresponds to that of a simple harmonic oscillator and is given by:

$$f' = \frac{1}{2\pi}\sqrt{\frac{k}{m'}}\,, \tag{3.3}$$

where k is the stiffness constant in N m^{-1} of the cantilever beam. In the considered case, $k = \frac{3EI}{L^3}$. Equation (3.3) becomes:

$$f' = \frac{1}{2\pi}\sqrt{\frac{3EI}{m'L^3}}\,. \tag{3.4}$$

Given that $\lambda L^4 = mL^3$, eq. (3.1) can be rewritten as such:

$$f = \frac{(1.875)^2}{2\pi}\sqrt{\frac{EI}{mL^3}}\,, \tag{3.5}$$

where m is the mass of the cantilever beam in kg. Setting eq. (3.4) equal to eq. (3.5) lets us derive an expression for the effective mass m' as function of the mass of the beam m:

$$m' = \frac{3}{(1.875)^4}m\,. \tag{3.6}$$

Finally, with the addition of a real proof mass M, eq. (3.3) needs to be rewritten as such:

$$f_M = \frac{1}{2\pi}\sqrt{\frac{k}{M+m'}}\,, \tag{3.7}$$

where f_M is the resonant frequency of the cantilever beam with a proof mass M attached at this free end. Substituting eq. (3.6) in eq. (3.7) and expressing m as function of the geometrical and physical features of the cantilever beam yields the following expression after simplification:

$$f_M = \frac{1}{2\pi}\sqrt{\frac{Ebh^3}{4L^3\left(M+\frac{3\rho bhL}{(1.875)^4}\right)}}\,. \tag{3.8}$$

We can verify that setting $M = 0$ returns eq. (3.2). In the case of the unimorph energy harvester, we can assume that the influence of the piezoelectric stack (~1 µm-thick) on the mechanical properties of the beam is negligible. The evolution of the resonant frequency f_M as function of beam length L and proof mass M for a 1 cm-wide, 0.7 mm-thick silicon beam ($E = 179$ GPa and $\rho = 2330\,\mathrm{kg\,m^{-3}}$) is represented in Fig. 3.2b.

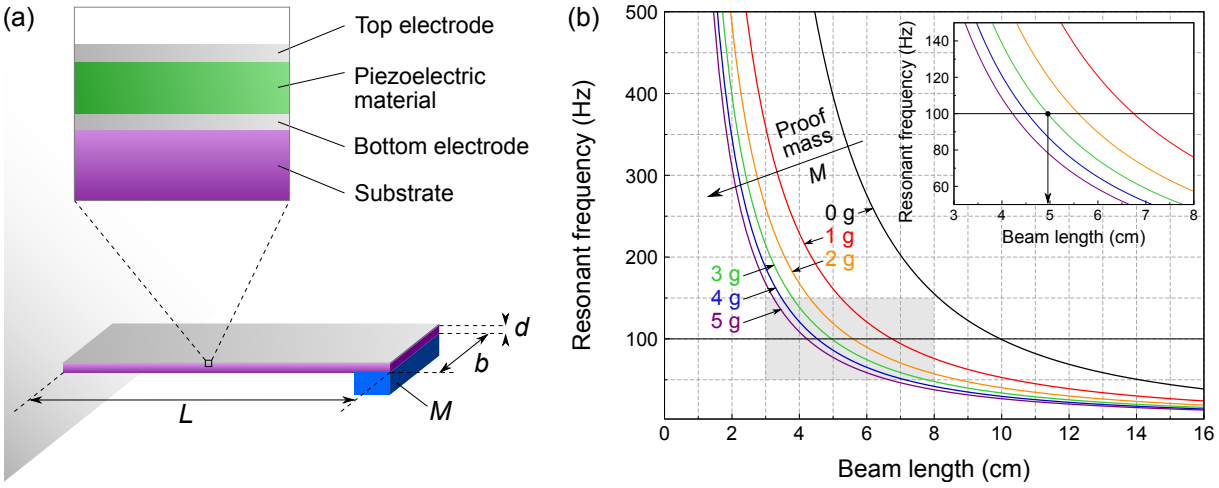

Fig. 3.2. (a) Scheme of a unimorph energy harvester and (b) resonant frequency of a 0.7 mm-thick and 1 cm-wide silicon beam as function of beam length and proof mass at the end. The inset shows a magnification of the shaded area.

3.2.2. Design of the energy harvester

As can be seen in Fig. 3.2b, without a proof mass the beam would have to be 10 cm-long to resonate at 100 Hz. The length can be conveniently decreased by adding a proof mass at the end of the cantilever. In the case of a 3 g proof mass, beam length can be decreased down to 5 cm. These considerations allow us to set the dimensions of the device: it will be a $5 \times 1\,\mathrm{cm}^2$ beam, with one extra cm at the extremity for clamping. A 3 g proof mass will be attached at the other end. The final dimensions of the device are therefore $6 \times 1\,\mathrm{cm}^2$.

The final point to consider in the design is the active area, namely its dimensions and position along the cantilever beam. As our printing process can reliably print 4 mm-wide stripes of PZT, we decided to print two such stripes along the beam (each stripe is $20 \times 4\,\mathrm{mm}^2$) and position them close to the clamping position, which is where strain is the highest during vibration. The top electrodes were chosen to be $18.692 \times 2.675\,\mathrm{mm}^2 = 50\,\mathrm{mm}^2$, so that the total active area of one sample is $1\,\mathrm{cm}^2$. A scheme of the device design is shown in Fig. 3.3a. The structure therefore consists of two piezoelectric stacks connected in series via the common platinum bottom electrode. A series connection rather than parallel was preferred in order to lower the overall capacitance, which in turn enables a higher voltage output.

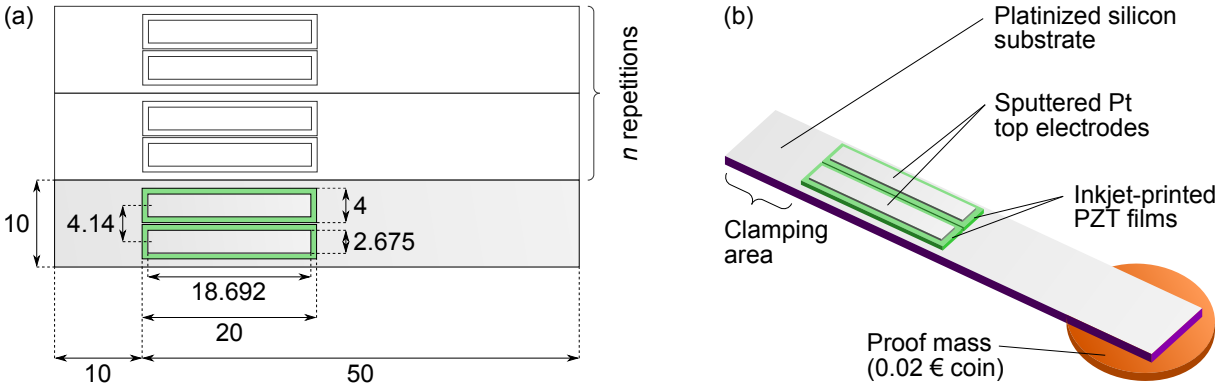

Fig. 3.3. Design of PZT-based energy harvester: n repetitions of the device can be printed on a single substrate. All the dimensions in (a) are given in mm. The scheme in (b) represents the final device.

3.2.3. Fabrication of the energy harvester

PZT rectangles were printed on a platinized silicon substrate according to the design of Fig. 3.3a and the procedure described earlier (page 55). Inkjet printing enables the fabrication of a series of devices in a single printing operation. In order to print n repetitions of the device, the dimensions of the substrate were chosen to be $6 \times (n + 1)$ cm (see Fig. 3.3a). All 16 nozzles of a 10 pL Dimatix cartridge were used and the printing strategy was set such that the droplet spacing was 15 µm in the x direction and 254 µm in the y direction. Five cycles of 12 printing–drying–pyrolysis sequences were performed to deposit 1 µm of PZT. After the printing process, sputtered platinum top electrodes were patterned by lift-off photolithography.

After protection of the surface with S1813 resist (spin coating at 2000 rpm for 30 s, then baking at 115 °C for 10 min), the beams were separated by cutting the sample with a wire saw. Removal of the protection resist was performed by soaking the samples in an acetone bath for 10 min. The beams were then carefully rinsed with isopropanol and deionized water, and finally dried on a hot plate. Reannealing of the devices was performed at 400 °C for 10 min. Contacts on the top electrodes were established by attaching 125 µm-diameter gold wires with two-component conductive epoxy glue. A 0.02 € coin ($M = 3.0$ g) was attached at the end of the beam using a hot-melt adhesive (Fig. 3.3b).

3.3. Characterization of PZT-based energy harvesters

3.3.1. Development of a test bench

In order to test the energy harvesting capabilities of our device, we needed to develop a vibrating characterization platform. Such devices exist on the market, but we decided to opt for a low-cost solution inspired by the following work: [123]. The test bench is based on a modified subwoofer with a fixture to clamp the sample. Our setup uses a Pioneer TS-SW2002D2 subwoofer on which a cylindrical PVC platform was fixed with epoxy glue. A stainless steel circular base and supporting rods were also machined and assembled into a frame for the subwoofer, as illustrated in Fig. 3.4. This subwoofer model is a dual voice coil ($2 \times 2\,\Omega$) and responds in the 20–200 Hz range (which corresponds perfectly to the relevant frequencies in energy harvesting). Its two coils were connected in series, resulting in a total impedance of 4 Ω. The subwoofer was driven by an Agilent 33210A function generator whose sinusoidal output signal was amplified by a Pioneer GM-D8601 amplifier (powered by a 12 V power supply) and then fed into the subwoofer. The signal output of the energy harvester was measured across a variable resistive load (resistance decade box 10^1–10^7 Ω) using a Tektronix TDS2004C oscilloscope.

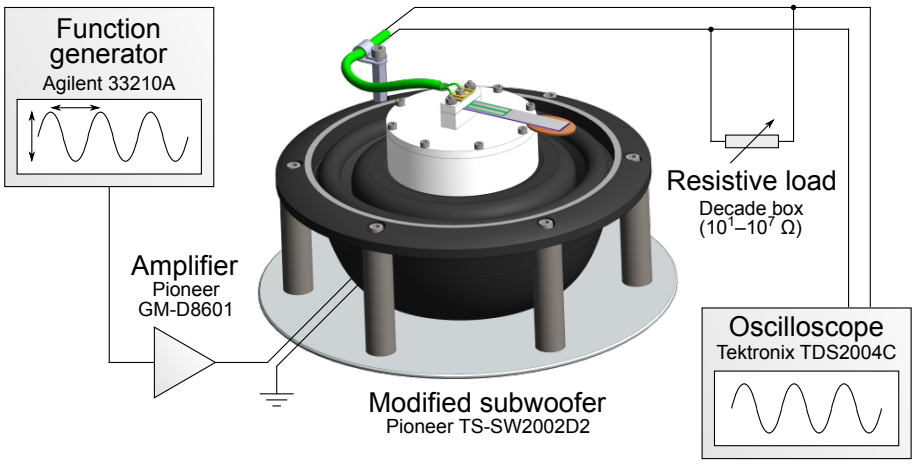

Fig. 3.4. Test bench for the characterization of energy harvesters.

3.3.2. Material characterization

In this study, we fabricated and characterized energy harvesters with both inkjet-printed and spin-coated PZT layers. The devices had the same geometrical features. The inkjet-printed EH was fabricated using the PZT ink formulation described in Chapter 1 (page 30). Pyrolysis was performed at 425 °C for 3 min for each of the 60 individual layers constituting the micron-thick layer. The reference sample for benchmarking was fabricated from a spin-coated PZT film obtained via the standard process and a 2-methoxyethanol-based PZT solution, as will be described in Chapter 4 (page 81).

Examination of the cross sections (Fig. 3.5a) by SEM reveals a certain degree of porosity, but only in the upper part of the films, the first 200 nm being dense, as shown previously in Fig. 2.5 (page 58). It therefore appears that beyond 200 nm, the elimination of residual organics during pyrolysis is less efficient, resulting in porosity after crystallization. This observation is further supported by the XRD pattern (Fig. 3.5c). The inkjet-printed PZT film exhibits a strong {111} textural component, which can be ascribed to the 200 nm-thick dense layer grown on the substrate. As we know from a previous study, pyrolysis at 425 °C results in strong {111} texture (Fig. 2.8, page 60). The rest of the micron-thick film contributes to a randomly textured component that can be identified in the XRD pattern. The spin-coated reference PZT film is dense (Fig. 3.5b) and exhibits {100} texture (Fig. 3.5d), promoted by the use of a $PbTiO_3$ seed layer.

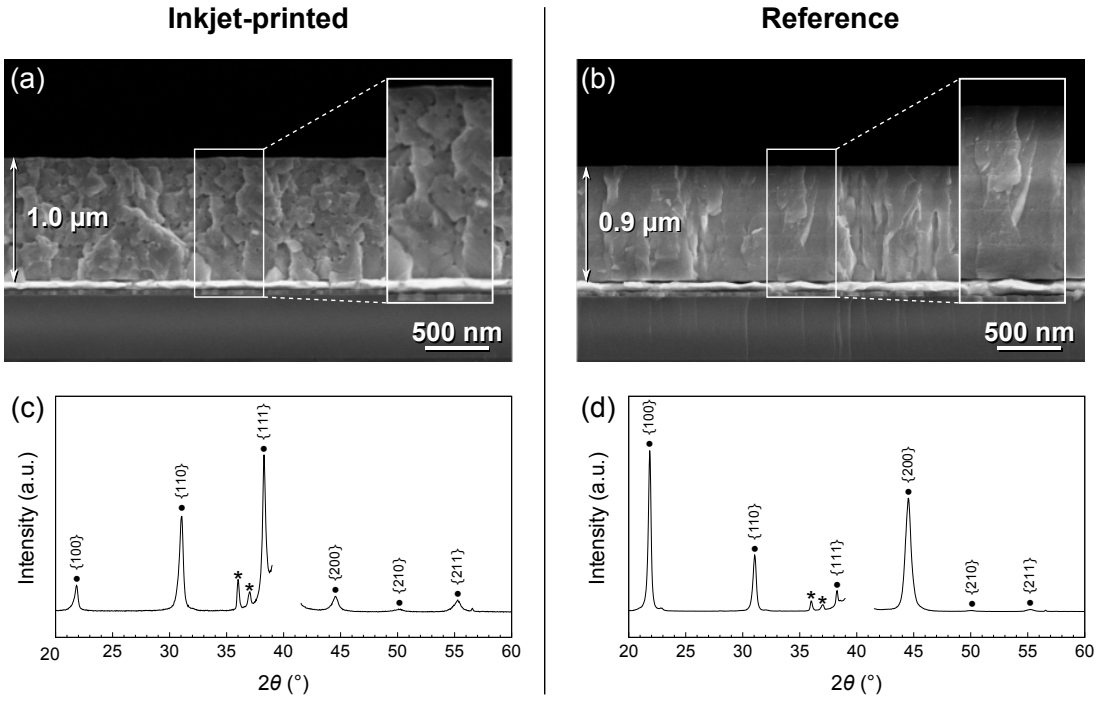

Fig. 3.5. Comparison of inkjet-printed and spin-coated micron-thick PZT films for energy harvesters: (a)–(b) SEM cross sections and (c)–(d) XRD patterns. The Pt(111) peak was omitted for clarity. Peaks due to the substrate are marked with asterisks (∗).

Polarization–electric field loops are presented in Fig. 3.6a. The loops in plain lines were measured for 100 µm-diameter platinum top electrodes. Inkjet-printed and spin-coated PZT films exhibit similar remanent and maximum polarizations with 20 and 50 µC cm^{-2}, respectively. The inkjet-printed PZT film has a slightly higher coercive field (50 kV cm^{-1}) than the spin-coated one (40 kV cm^{-1}). The *P*–*E* loop corresponding to the inkjet-printed film also appears more slanted. While little change is observed for the spin-coated film when the same measurement is performed with a 50 mm^2 top electrode (dashed lines), the inkjet-printed film clearly exhibits lower polarization and higher coercive field. This could be ascribed to the larger amount of defects that the large-area electrode encompasses in the case of the inkjet-printed film. However, no short circuit nor excessive leakage was observed for the IJP device. Relative permittivity–electric field loops shown in Fig. 3.6b reveal similar behavior for both films, with a relative permittivity at zero bias of ~1200.

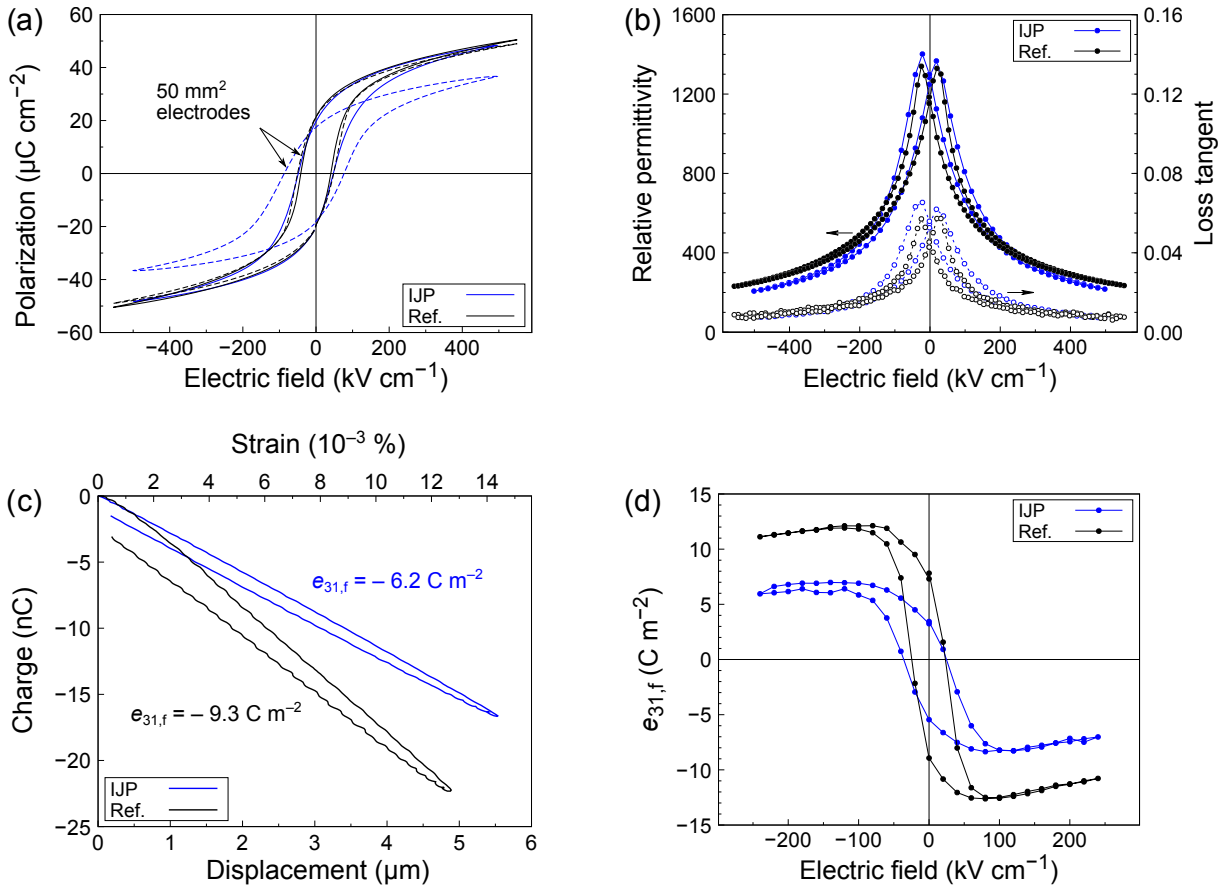

Fig. 3.6. Electrical and piezoelectric characterization of inkjet-printed PZT thin films for energy harvesters. (a) Polarization–electric field loops for the films with (a) 100 µm-diameter (plain lines) and 50 mm^2 (dashed lines) sputtered platinum top electrodes. (b) Relative permittivity–electric field loops (100 µm-diameter sputtered platinum top electrodes, V_{AC} = 1 V). (c) Measurement of the effective transverse piezoelectric coefficient $e_{31,f}$ via the four-point bending method (with prepolarization) and (d) dependence of $e_{31,f}$ with the applied electric field.

The effective transverse piezoelectric coefficient ($e_{31,f}$) was evaluated via the four-point bending (4PB) method. Details on the method can be found in Appendix D (please refer to page 139). From the measurements shown in Fig. 3.6c and eq. (D.7), we can extract values of -6.2 and $-9.3\,\mathrm{C\,m^{-2}}$ for the inkjet-printed and spin-coated films, respectively. Note that the measurements were carried out at zero electric bias, with prepolarization (25 V for 1 s) before the measurement. The electric field-dependence of $e_{31,f}$ is illustrated in Fig. 3.6d. As anticipated, the spin-coated film exhibits higher $e_{31,f}$ values than the inkjet-printed one. The loops are not perfectly symmetrical and the highest values are recorded for a positive bias field, with $e_{31,f} = -8.3$ and $-12.6\,\mathrm{C\,m^{-2}}$ for the inkjet-printed and spin-coated films, respectively. Nevertheless, at zero bias both films retain approximately 70 % of the maximum value of $e_{31,f}$ reaches when the layers are poled with a positive bias field.

3.3.3. Testing the device

Before testing the device, both of its piezoelectric elements had to be poled under a DC electric field. This was performed by heating of the sample at 150 °C and applying an electric field equivalent to approximately three times the coercive field ($200\,\mathrm{kV\,cm^{-1}}$) [124]. The two elements were poled antiparallel to each other. The energy harvester was then mounted on the test bench as shown in Fig. 3.4.

First, we determined the resonant frequency of the beams by monitoring the output voltage of energy harvesters as function of frequency (Fig. 3.7a). The IJP and ref. EHs resonate at 102 and 99 Hz, respectively, in excellent agreement with the value predicted by the Euler-Bernoulli model. Interestingly, a secondary parasitic resonance can be detected at $f < f_{\mathrm{res}}$ and is particularly visible for the ref. EH ($f = 84\,\mathrm{Hz}$). It could be attributed to the clamping of the device or a contribution from the test bench. The mechanical quality factor $Q = \frac{f_{\mathrm{res}}}{\Delta f}$ (with Δf the full width at half maximum of the resonance peak) is 20 for both beams. This value ($Q > \frac{1}{2}$) is characteristic of underdamped mechanical oscillators. The relatively narrow bandwidth (5 Hz) indicates that the EHs need to be excited very close to their resonant frequencies for optimal operation.

We then measured the output peak-to-peak (V_{pp}) voltage at the resonant frequency under an acceleration of 5.0 g ($49\,\mathrm{m\,s^{-2}}$, measured at the clamping position using an accelerometer) as a function of load resistance R. This acceleration value is quite significant, but still in the safe range under the breaking point of the beam. The output power P was calculated using eq. (3.9), where V_{RMS} is the root mean square (RMS) voltage ($V_{\mathrm{RMS}} = \frac{V_{\mathrm{pp}}}{2\sqrt{2}}$). Fig. 3.7b shows the evolution of P and V_{RMS} with R for both devices.

$$P = \frac{V_{\mathrm{RMS}}^2}{R} \tag{3.9}$$

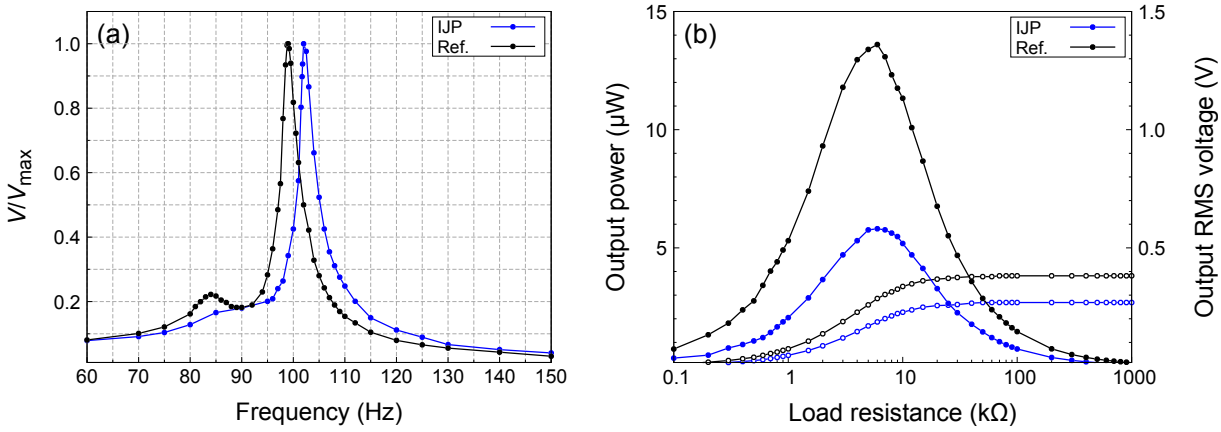

Fig. 3.7. (a) Resonance and (b) power versus load resistance curves for energy harvesters. In (b), power is represented with closed symbols (•) and RMS voltage with open symbols (○).

The power versus resistance curves exhibit a maximum, which corresponds to the situation where the impedance of the resistive load matches that of the capacitor represented by the piezoelectric elements, i.e. $Z_{\max} = \frac{1}{\omega C_{\text{eq}}}$, where C_{eq} is the equivalent series capacitance. Two identical capacitors connected in series (as in the case of our energy harvesters) will have an equivalent capacitance which is half of the capacitance C of a single capacitor, as shown by eq. (3.10).

$$C_{\text{eq}} = \left(\frac{1}{C} + \frac{1}{C}\right)^{-1} = \frac{C}{2} \tag{3.10}$$

Knowing that the capacitance of a parallel plate capacitor is given by eq. (3.11), we can derive an expression for $Z_{\max}$ where d is the thickness of the PZT film, f is the frequency of the output AC signal, ε_{r} is the relative permittivity of PZT and A is the surface area of a single piezoelectric element. Equation (3.12) predicts the values of the optimal resistive loads, which are 5.9 and 5.7 kΩ for the IJP and ref. EHs, respectively. These values are verified experimentally, as shown in Fig. 3.7b.

$$C = \varepsilon_0 \varepsilon_{\text{r}} \frac{A}{d} \tag{3.11}$$

$$Z_{\max} = \frac{d}{\pi f \varepsilon_0 \varepsilon_{\text{r}} A} \tag{3.12}$$

Output power peaks at 5.8 μW for the inkjet-printed EH, while the reference device with spin-coated PZT exhibits a maximum power output of 13.6 μW.

3.3.4. Discussion

A comparison of the relevant properties of both EHs is presented in Table 3.1. The difference in output power (more than a factor of two) can be rationalized using the figure of merit (FOM), as defined for a piezoelectric thin-film based beam [125]. With this definition, the FOM corresponds to the piezoelectric coefficient squared divided by relative permittivity, eq. (3.13). If we take into account the differences in resonant frequency and active volume of the EHs, we can predict that the power output of the inkjet-printed EH should be 5.4 µW, which is in good agreement with the power measured experimentally.

$$\mathrm{FOM} \propto \frac{e_{31}^2}{\varepsilon_\mathrm{r}} \tag{3.13}$$

Device	f_res (Hz)	Z_max kΩ	d (µm)	$e_{31,\mathrm{f}}$ (C m^{-2})	ε_r	FOM	P_meas (µW)	P_model (µW)
IJP	102	5.9	1.0	−6.2	1200	3.3	5.8	5.4
Ref.	99	5.7	0.9	−9.3	1150	8.3	13.6	–

Table 3.1. Comparison of energy harvesters based on inkjet-printed and reference spin-coated PZT layers. The FOM was calculated as $\frac{e_{31,\mathrm{f}}^2 f_\mathrm{res} d}{\varepsilon_\mathrm{r}}$ to account for the differences in resonant frequency and volume of active material. P_model for the IJP device was evaluated by taking the 13.6 µW value for the spin-coated device as a reference.

The performance of our energy harvester based on inkjet-printed PZT is also compared to other works in Table 3.2. Our device stands quite well compared to the literature if we consider the volume of active material, which is 0.1 mm^3. Furthermore, our piezoelectric layers are fully inkjet-printed, whereas the other contributions feature spin-coated [118] or sputtered PZT films [12, 126]. This represents a significant advantage, as we estimate that growing 0.1 mm^3 of PZT for a single energy harvester only requires ∼14 µL of ink. Even if we take into account purging and priming operations, the ink consumption per EH device still remains well below 1 mL for the overall process.

Another advantage of inkjet printing is represented by the simplicity to print repetitions of the device within the same process, in order to fill a wafer for example. Let us consider an 8-inch platinized silicon wafer. As shown in Fig. 3.8, such a substrate can be tiled with 40 devices, resulting in a surface area of 64 cm^2 covered with PZT films (20 % coverage of the whole substrate). The amount of ink required to cover this surface by a 1 µm-thick film is in the order of 560 µL. A 50 % or 100 % coverage of the substrate would require 1.36 mL and 2.72 mL of ink (approximately equal to the capacity of a Dimatix DMCLCP cartridge reservoir), respectively.

These figures can be put into perspective with the amount of PZT solution that would be required to deposit a 1 µm-thick PZT film on an 8-inch wafer by spin coating. In a typical process, 100 mL of solution would be required in total, regardless of the desired substrate coverage. For the fabrication of our EH devices, the spin coating process would require almost 180× more precursor solution than the IJP process.

Reference	Fang et al. [117]	Morimoto et al. [118, 126]	Yeo et al. [12]	This work [108]
Year	2006	2010	2016	2019
Process	Spin coating	Sputtering	Sputtering	Inkjet printing
d (µm)	1.64	2.8	3 (bimorph)	1
Texture	–	(001)	(001)	{111}
P_r (µC cm^{-2})	14	30	40	20
E_c (kV cm^{-1})	30	50	65	48
ε_r	–	166	210	1200
$\tan\delta$	–	–	0.03	0.05
Power (µW)	2.2	5.3	149	5.8
Frequency (Hz)	609	126	6	102
Acceleration (m s^{-2})	10	5	1	50
Active volume (mm^3)	0.78	0.26	1.2	0.1
Power density (µW mm^{-3})	7.6	21	124	58

Table 3.2. Comparison of inkjet-printed energy harvester characteristics with similar works from the literature.

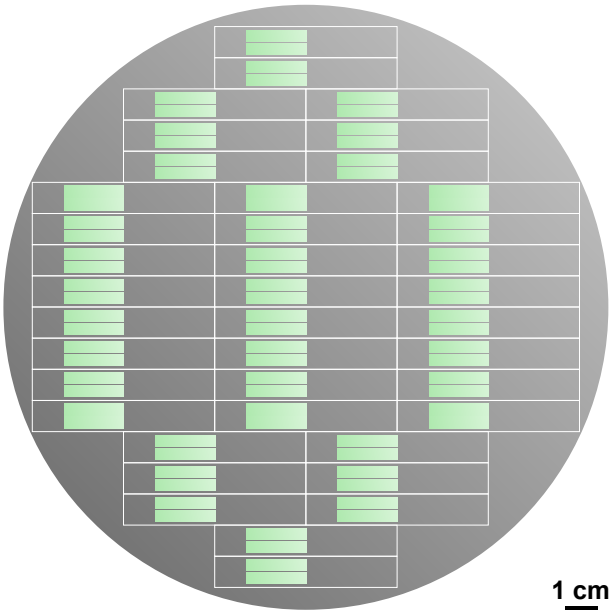

Fig. 3.8. Illustration of an 8-inch platinized silicon wafer covered with EH devices. With the proposed tiling pattern, 40 devices fit on the wafer. 20 % of the total wafer surface is covered with inkjet-printed PZT thin films.

Several points related to both material quality and device design could be addressed to improve its energy output. In addition, we saw that the generated output voltages are quite low (amplitude of ~0.25 V at maximum power). This represents a problem for the rectification of the AC signal into DC for electronic applications, as typical p-n junction semiconductor diodes have a forward threshold voltage of 0.6–0.7 V.

In terms of material quality, the printed layers still contain a significant amount of porosity, as seen in the cross section of Fig. 3.5. Printed micron-thick PZT films also lack the preferable {100} orientation for enhanced piezoelectric response. The next chapter provides possible hints to address this issue (please refer to the discussion at page 93).

Another reason for the low output voltage lies in the fact that silicon is a particularly stiff and fragile substrate. The strain induced in the piezoelectric active layer is therefore relatively modest, as the acceleration needs to be kept below the breaking point of the cantilever beam. The use of a more compliant material as substrate could be envisaged [12].

The high relative permittivity intrinsic to PZT ($\varepsilon_r \sim 1000$) also contributes to lower the output voltage due to the high capacitance of the piezoelectric elements. A possible design modification would be to connect more piezoelectric elements in series in order to lower the equivalent capacitance. With platinized silicon as a substrate, this would require cutting the platinum common bottom electrode in order to isolate electrically each piezoelectric element and perform the connection in series.

Some of these considerations could also be addressed by the use of another piezoelectric material, such as the polymer poly(vinylidene fluoride-*co*-trifluoroethylene) or P(VDF-TrFE). Despite its weaker piezoelectric properties, P(VDF-TrFE) has a much lower relative permittivity than PZT and can be easily integrated on a compliant substrate such as a polymer sheet. A study on P(VDF-TrFE)-based energy harvesters can be found in Appendix B (please refer to page 117).

3.4. Chapter summary

In this chapter, we presented an application of inkjet-printed PZT films. We described the fabrication of simple energy harvesting devices consisting of micron-thick PZT films printed on platinized silicon beams. The energy harvesters were tested using a home-made test bench. Under 5.0 *g* acceleration, the device could output 5.8 µW of power across a 6 kΩ resistive load at its resonant frequency (102 Hz). This example shows that it is possible to fabricate functional devices based on inkjet-printed piezoelectric layers and demonstrates the potential of inkjet printing for low-cost fabrication of piezoelectric sensors or actuators.

Chapter 4

Development of safer solutions

4.1. Motivation

Safety is a critical aspect in industry, as well as in research. Chronic exposure to harmful chemical substances can have long-term effects on a person's health and should not be considered lightly. Typical precursor solutions for PZT films pose a series of health hazards due to the combined presence of lead and 2-methoxyethanol.

Lead is a neurotoxic and nephrotoxic metal that can bioaccumulate in case of prolonged exposure. It can cause cognitive decline and a whole range of other symptoms. Its concentration in homogeneous materials used in electronics is restricted to a maximum level of 1000 ppm by the RoHS (restriction of hazardous substances) European directive EU 2015/863. This is a strong incentive for the development of lead-free piezoelectrics. Although significant progress has been made in this field in the past decades for specific applications [127, 128], PZT still remains the battle horse of the piezoceramics industry owing to its excellent properties, low manufacturing costs and ease of processing. Replacing lead by another element is therefore not straightforward and is still an active research topic.

The solvent 2-methoxyethanol is a known carcinogenic and teratogenic substance. Exposure issues can be mitigated quite efficiently at the laboratory scale by the use of protective equipment and due to the small quantities involved. However, one can imagine that industrial-scale processes require an additional level of safety measures. As described in the Background section, 2-methoxyethanol-free solutions for the processing of PZT thin films have been developed, but they can be prone to aging and have therefore a limited shelf life [27]. The 2-methoxyethanol-based route remains popular owing to its simplicity and reliability. The work presented in this chapter was initially motivated by the replacement of 2-methoxyethanol by a safer solvent in our process for the deposition of PZT thin films by spin coating.

4.2. Role of the solvent

As we have discussed in the previous chapters, the solvent is an important element of the solution as it is a carrier medium for the metal precursors of PZT. It needs to have the adequate rheological properties depending on the deposition method. In addition, the solvent stabilizes the metal precursors via ligand exchange.

The molecule of 2-methoxyethanol possesses two functional groups: a primary alcohol and a methyl ether. Both oxygen atoms of the molecule can interact with a metallic center, conferring it a chelating character. Chelation greatly stabilizes alkoxide precursors [27], which are very sensitive to water and react readily with air moisture. This stabilizing effect makes it an ideal solvent for PZT solutions, as zirconium and titanium are introduced in the form of alkoxides. The stability of these precursors in solution is primordial for process reproducibility and allows the preparation of solutions with a long shelf life.

Despite its multiple advantages for CSD, 2-methoxyethanol has adverse biological effects in the body as a result of its metabolism (Fig. 4.1). One of the main metabolic pathways degrades 2-methoxyethanol into 2-methoxycitrate and interferes with the natural metabolite citrate [129, 130]. This is a key metabolite of the Krebs cycle, which occupies a central part in metabolism and is connected to a series of other metabolic pathways involved in cell development. As can be anticipated, this results in abnormal cell growth, which in turn translates into the carcinogenic and teratogenic effects mentioned earlier.

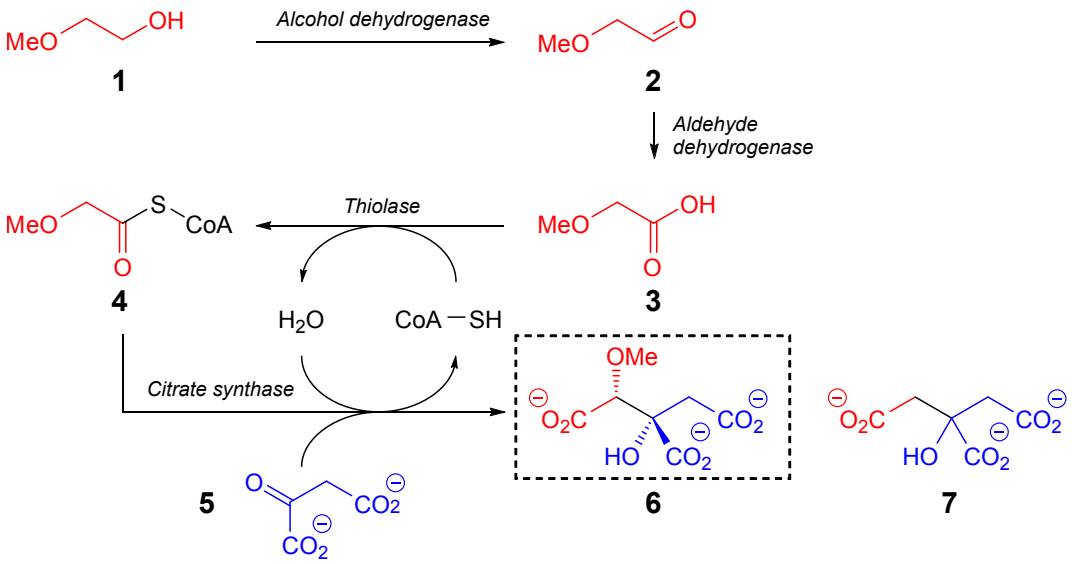

Fig. 4.1. Metabolism of 2-methoxyethanol. In the body, 2-methoxyethanol **1** undergoes two successive oxidations of the primary alcohol moiety, yielding methoxyacetaldehyde **2** and methoxyacetic acid **3**. A thioesterification then takes place, where the methoxyacetyl moiety is grafted to the coenzyme A (CoA), yielding methoxyacetyl-CoA **4**. The subsequent reaction with oxaloacetate **5** releases the coenzyme A and yields 2-methoxycitrate **6** as a final product, which interferes with metabolic pathways involving the natural metabolite citrate **7**.

In the quest for an alternative solvent with low toxicity, our intuition was guided by both (1) chemical (reactivity and functional groups) and (2) physical (surface tension, viscosity, boiling point) considerations. The solvent should also be commercially available and ideally at a reasonable cost. From a chemical point of view, the molecule should be an oxygenated bidentate ligand. Diols such as ethylene glycol and propylene glycol could be suitable candidates (Fig. 4.2). However, their viscosities and boiling points are relatively high compared to 2-methoxyethanol (Table 4.1). If we choose to preserve the main scaffold of the molecule and both chemical functions (alcohol and ether), we could also change the alkyl chain of the ether. However, 2-ethoxyethanol follows the same metabolic pathway as 2-methoxyethanol and therefore leads to similar ill biological effects [131].

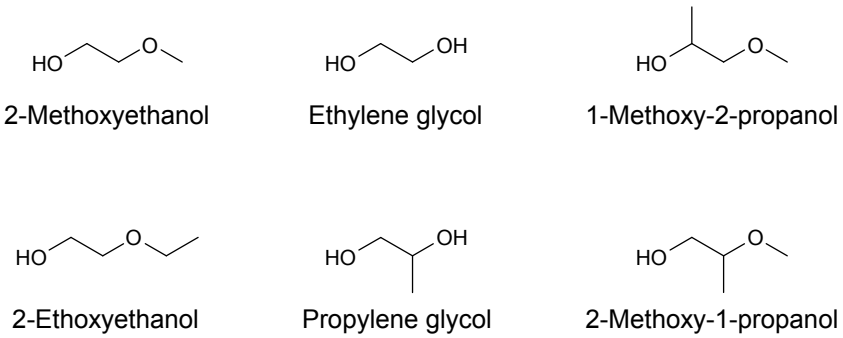

Fig. 4.2. Structures of the solvents listed in Table 4.1. All these compounds contain a similar backbone structure (alcohol, two-carbon chain, oxygen) and can act as bidentate ligands for metal cations.

Solvent	Molar mass ($g\,mol^{-1}$)	Surface tension ($mN\,m^{-1}$)	Density ($g\,cm^{-3}$)	Viscosity (mPa s)	Boiling pt. (°C)	GHS
2-Methoxyethanol	76.09	30.84	0.965	1.72	124	
2-Ethoxyethanol	90.12	28.2	0.930	1.84	135	
Ethylene glycol	62.07	47.99	1.113	16.1	197	
Propylene glycol	76.09	40.1	1.036	56.0	188	–
2-Methoxy-1-propanol	90.12	N/A	0.938	N/A	130	
1-Methoxy-2-propanol	90.12	27.7	0.916	1.7	118	

Table 4.1. Room-temperature physicochemical properties of 2-methoxyethanol and potential candidates for its replacement in PZT CSD processing. Global harmonized system (GHS) pictograms indicate the hazards associated with each substance.

1-Methoxy-2-propanol appears to stand out from this simple screening and importantly, it has very favorable toxicological properties when compared to 2-methoxyethanol. The metabolic pathway shown in Fig. 4.3 reveals that the degradation products of 1-methoxy-2-propanol are lactate and pyruvate [132]. These are natural metabolites involved in the energy-producing metabolic pathways and are therefore of little concern if an individual is exposed to low doses. 1-Methoxy-2-propanol can therefore be considered as a relatively safe solvent.

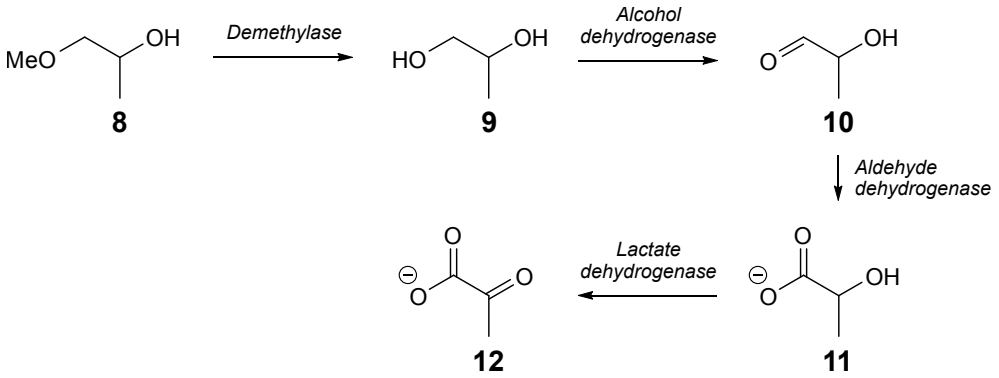

Fig. 4.3. Metabolism of 1-methoxy-2-propanol **8**. After demethylation of the methyl ether moiety, the resulting propylene glycol **9** is oxidized to lactaldehyde **10**. Subsequent oxidations yield lactate **11** and pyruvate **12**, which are natural metabolites.

In this chapter, we will attempt to replace 2-methoxyethanol (2ME) by 1-methoxy-2-propanol (1M2P) in the processing of PZT films. Our starting point will be standard deposition of PZT thin films via spin coating.

4.3. Study of solvent influence

4.3.1. Preparation of 1-methoxy-2-propanol-based solutions

The preparation procedure for the PZT spin coating solution is identical to the one presented in Chapter 1 (please refer to page 30), except that 2ME was replaced by 1M2P. Unfortunately, anhydrous 1M2P was not commercially available at the time of the experiments. The use of anhydrous solvents is advised for the preparation of PZT solutions, as traces of water can react with titanium and zirconium alkoxides. We used 3 Å zeolite molecular sieves for drying the solvent. Molecular sieves are aluminosilicate beads that have the property of trapping water molecules inside their porous structure, and are therefore ideal for drying organic solvents. After thermal activation (300 °C for 24 h inside a furnace), the molecular sieves were transferred and stored inside a glovebox. A 20% mass-to-volume ratio of activated molecular sieves was used for drying 1M2P [133], which were simply placed in a bottle containing the solvent.

The solvent change did not affect much the preparation of the PZT spin coating solution as all reagents were miscible with and soluble in 1M2P at these concentrations. In addition to the PZT solution, a lead titanate (PT) solution was prepared. Lead titanate is commonly used as a seed layer for growing PZT films by CSD as it favors the {100} orientation. The PT solution was prepared according to a similar procedure as the PZT solution, as detailed in Fig. 4.4. The differences between both solutions are summarized in Table 4.2.

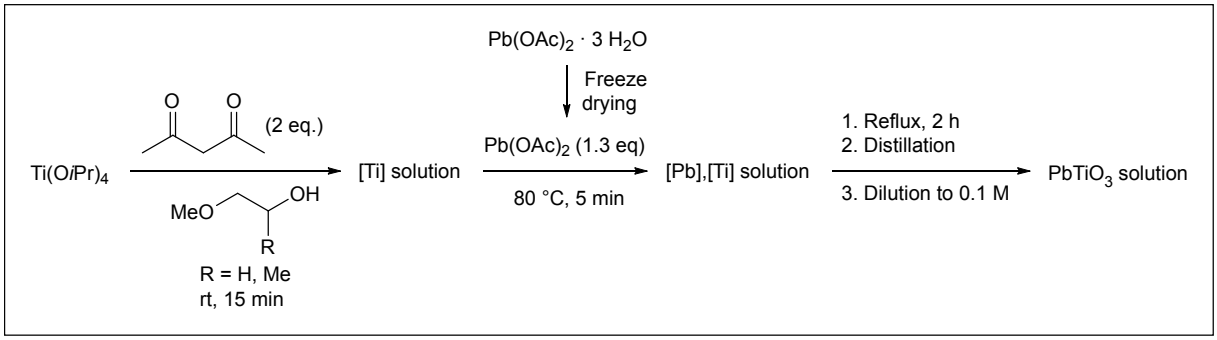

Fig. 4.4. Preparation procedure for PT solutions: freeze-dried lead(II) acetate ($Pb(OAc)_2$) and titanium(IV) isopropoxide ($Ti(OiPr)_4$) are used as metal precursors.

Solution	PT	PZT
Concentration (mol L^{-1})	0.1	0.3
Pb excess (%)	30	10
Zr:Ti ratio	0:100	53:47
Spinning	3000 rpm, 30 s	3000 rpm, 30 s
Drying	130 °C, 3 min	130 °C, 3 min
Pyrolysis	350 °C, 3 min	350 °C, 3 min
Crystallization	700 °C, 1 min	700 °C, 5 min

Table 4.2. Summary of solution characteristics and deposition conditions for the fabrication of PT seed layers and PZT films.

4.3.2. Deposition of PZT films by spin coating

The deposition process starts with the deposition of the PT seed layer on platinized silicon. The substrates are $1.5 \times 1.5\,cm^2$ squares obtained by manual cleavage of a 6-inch platinized silicon wafer supplied by Sintef, Norway. Substrates are always degassed on a hot plate at 350 °C for 5 min before deposition. Solutions are deposited onto the substrate using 3 mL syringes fitted with 0.2 µm PTFE filters (13 mm diameter). The spin coating program has two steps: (1) 50 rpm for 10 s, which ensures homogeneous spreading of the deposited solution and (2) 3000 rpm for 30 s to spin the excess solution off the substrate and reach the final thickness. A couple drops of solution (~0.1 mL) are enough to cover the substrate surface.

After spinning the PT solution, the film is dried at 130 °C for 3 min and pyrolyzed at 350 °C for 3 min on hot plates, then crystallized in an RTA furnace at at 700 °C for 1 min (heating ramp 50 °C s^{-1}, air atmosphere). This affords a thin seed layer of lead titanate, on top of which the PZT film will be grown. Deposition of the PZT film proceeds via the same scheme, except that the spinning–drying–pyrolysis sequence is performed several times (five times for 2ME-based solutions) before the final crystallization at 700 °C for 5 min (heating ramp 50 °C s^{-1}, air atmosphere). The resulting crystallized PZT film has a thickness of 200 nm. The PZT deposition procedure is then iterated to obtain thicker films, as illustrated in Fig. 4.5.

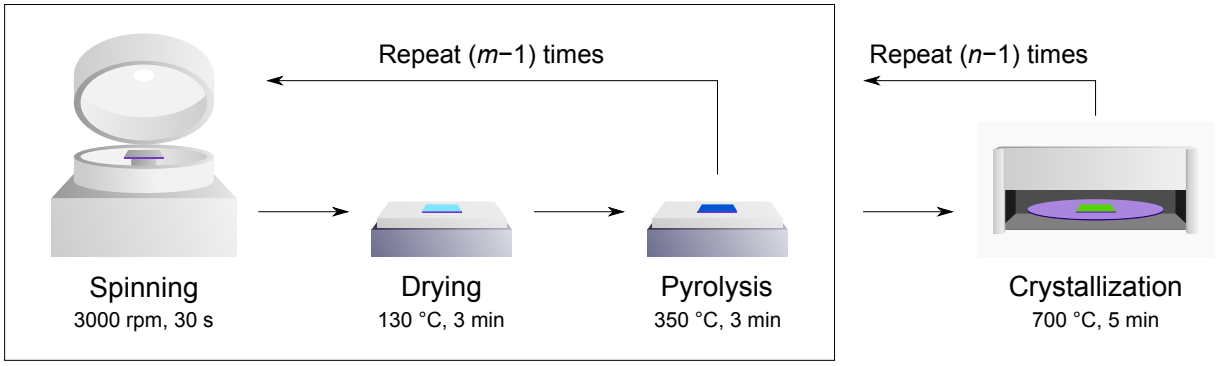

Fig. 4.5. Spin coating of PZT thin films: workflow of the overall process. For the deposition of a micron-thick film using a 0.3 M 2ME-based solution, $m = 5$ and $n = 5$.

4.3.3. Influence on film thickness

The thickness of a spin-coated film depends on the spinning rate. It is commonly accepted that the thickness h of the liquid film is proportional to $\frac{1}{\sqrt{\omega}}$, where ω is the angular velocity. However, the thickness of the film also depends on the rheological properties of the spinned liquid. According to Emslie, Bonner and Peck's model, h is a function of the intial thickness of the liquid h_0, its density ρ and viscosity η. Its evolution with time t is given by eq. (4.1) [134].

$$h = \frac{h_0}{\sqrt{1 + \frac{4\rho\omega^2}{3\eta} h_0^2 t}} \tag{4.1}$$

For a given spinning rate and time, the resulting film will be thicker if the liquid is less dense and/or more viscous. It is therefore expected that performing the process with 2ME and 1M2P-based solutions will yield films of different thicknesses. In order to provide meaningful comparisons in this study, we decided to first evaluate the impact of the solvent on the thickness of the final crystallized film for one series of depositions. The 1M2P process would then be adapted to comply with the 2ME process.

When processed in the same conditions, the 1M2P-derived PZT film has a thickness of 260 nm (Fig. 4.6b), which is approximately $\frac{5}{4}\times$ thicker than its 200 nm-thick 2ME-derived counterpart (Fig. 4.6a). We therefore decided to deposit only four layers in the 1M2P process, which should result in a final thickness close to 200 nm. Performing this sequence five times yields 950 nm-thick films (≈1 µm), as shown in Figs. 4.6c and 4.6d. This initial study therefore shows that 1M2P-based PZT solutions can afford dense films with columnar microstructure. Implementing slight adaptations in the number of depositions enabled us to fabricate micron-thick PZT films, allowing us to carry out a meaningful comparison of the two solvents.

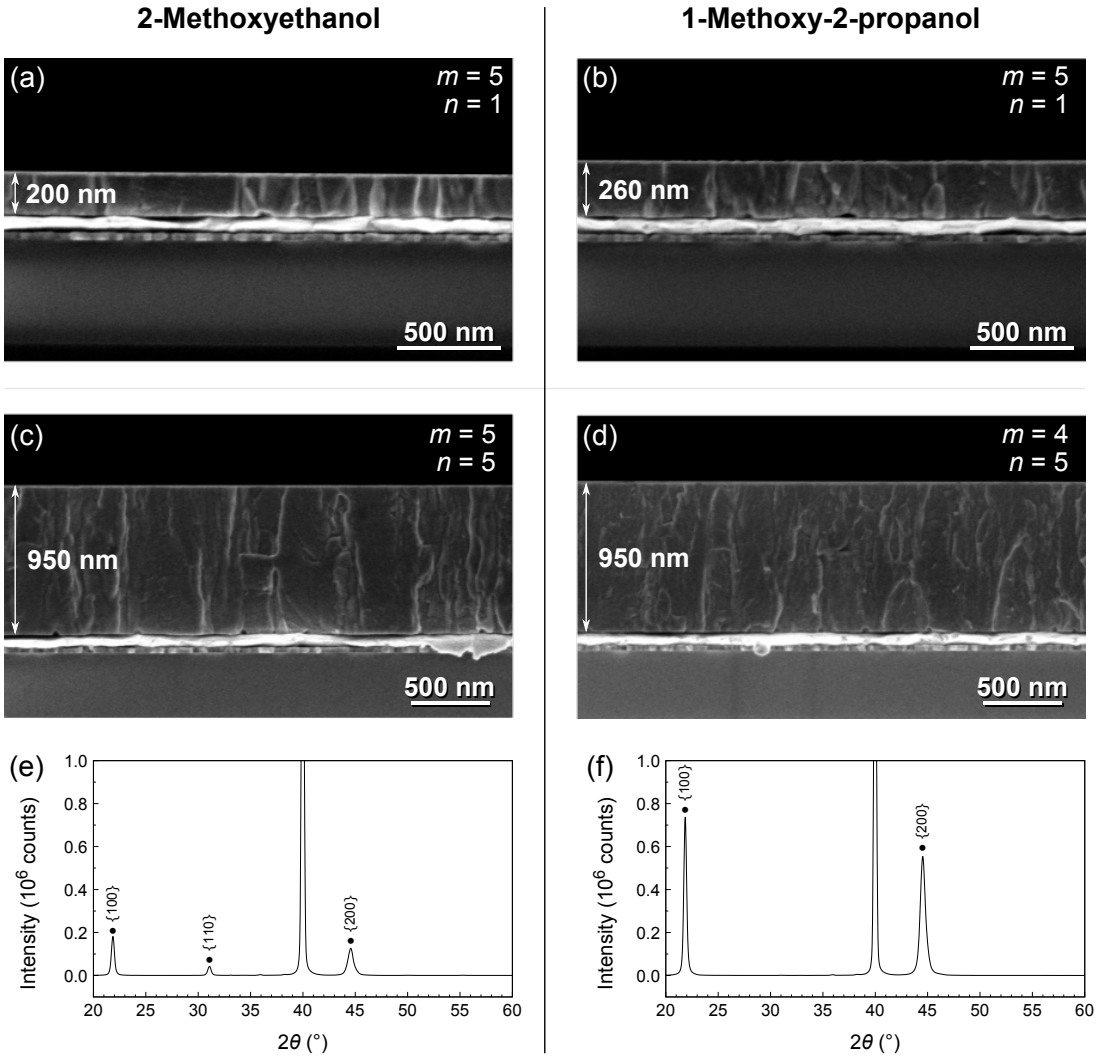

Fig. 4.6. SEM cross sections of PZT films deposited using (a),(c) 2ME and (b),(d) 1M2P-based solutions. The values of *m* and *n* correspond to the number of steps, according to the sequence represented in Fig. 4.5. A simple adjustment of *m* allowed deposition of films of the same thickness with both 2ME and 1M2P-based solutions. XRD patterns of micron-thick (e) 2ME and (f) 1M2P-derived PZT films. The peak at $2\theta \sim 40°$ corresponds to Pt(111). Note that the intensities are expressed in absolute units (number of counts) and the scale is identical for both XRD patterns.

4.3.4. Influence on film orientation

Since we used a $PbTiO_3$ seed layer, we anticipate {100} preferential orientation of the micron-thick PZT films. That is indeed the case, as seen in the XRD patterns of Figs. 4.6e and 4.6f, performed in θ-2θ geometry. However, there is a striking difference in the intensities of the signals: the 1M2P-derived film appears to be exclusively {100}-oriented, whereas the PZT obtained from the 2ME-based solutions has a noticeable contribution from the {110} plane. This surprising observation raises the question of the origin of this strong orientation in the 1M2P-derived films.

A possible explanation is that the strong orientation is induced by the $PbTiO_3$ seed layer. In order to confirm this hypothesis, we performed a 'cross-check' experiment, whose results are summarized in Fig. 4.7. The experiment was performed as follows: $PbTiO_3$ seed layers were first grown on platinized silicon substrates, then 200 nm-thick films were grown on top, with every solvent combination. As expected, fully 2ME and 1M2P-derived films exhibited the same behavior as the micron-thick films. Interestingly, the 1M2P-derived PZT film grown on the 2ME-derived PT seed layer exhibited the same type of orientation as the fully 2ME-derived one. Likewise, 2ME-derived PZT crystallized on the 1M2P-derived seed layer exhibits strong {100} orientation. These findings strongly suggest that the nature of the seed layer influences the growth of the PZT film.

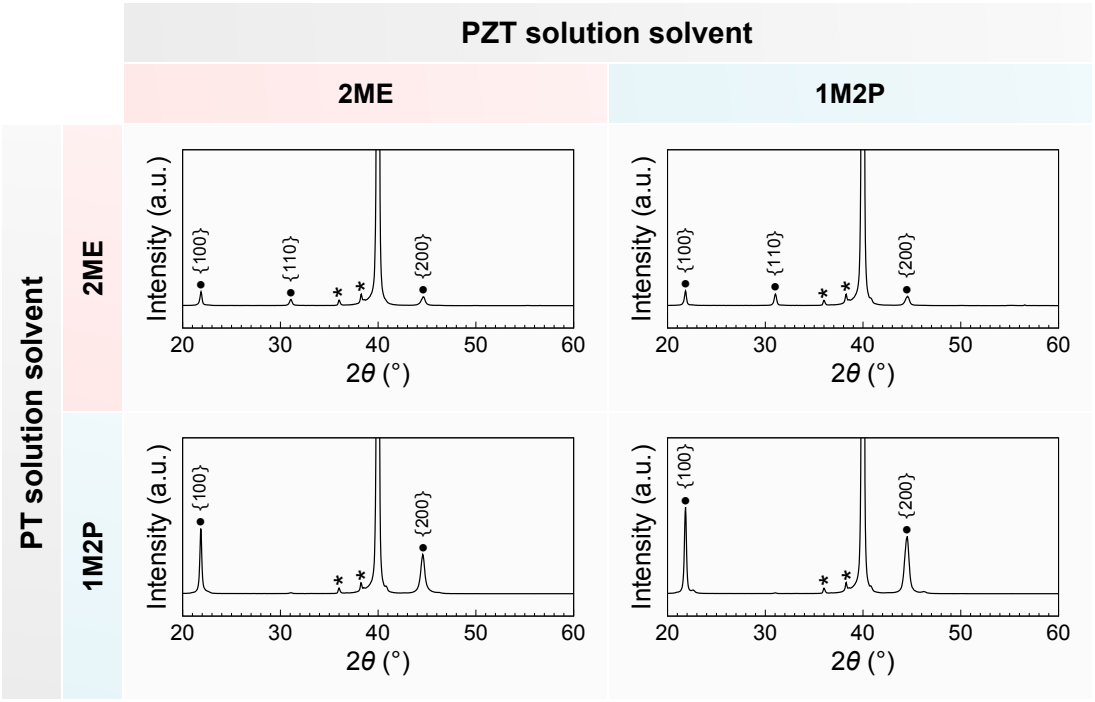

Fig. 4.7. XRD patterns of 200 nm-thick PZT films as function of PT and PZT solution solvent. The peaks marked with asterisks (∗) are attributed to the substrate. The scale is identical for all XRD patterns.

We then naturally went on to investigate the structure of seed layers. The XRD patterns shown in Fig. 4.8a reveal a clear difference between the seed layers: the 2ME-derived PT seed layer exhibits modest (001)/(100) orientation, with noticeable (101)/(110) contributions. On the other hand, strong (001)/(100) texture is detected in the 1M2P-derived seed layer. These two reflections could even be very well resolved in the XRD pattern (Fig. 4.8b). The strong orientation was also assessed by performing a rocking curve around the (100) reflection (Fig. 4.8c): the curve corresponding to the 1M2P-derived $PbTiO_3$ seed layer exhibits a distinct peak with a full width at half maximum of ~4°. This is not the case for the 2ME-derived sample, which only displays a broad low-intensity peak under the same measurement conditions.

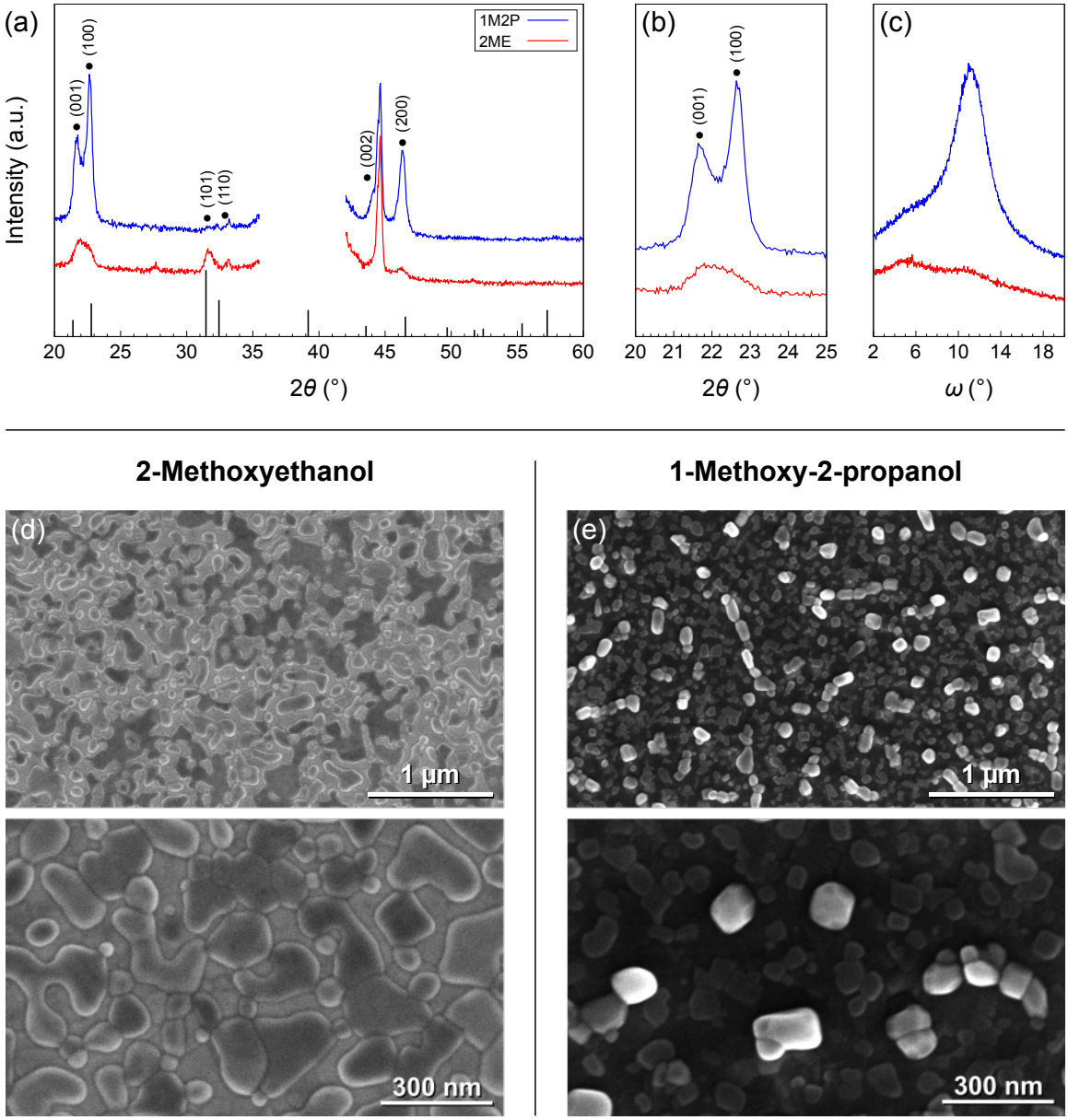

Fig. 4.8. (a)–(c) XRD patterns and (d),(e) surface SEM micrographs of 2ME and 1M2P-derived seed layers. In (a), the black bars represent the intensities for a $PbTiO_3$ powder [PDF 00-006-0452]. The Pt(111) reflection at $2\theta \sim 40°$ is masked for clarity and the parasitic peak at 44.7° could be attributed to the diffractometer aluminium stage (Al(200)). A close-up view of the 20–25° range is given in (b) and the rocking curve around the (100) reflection ($2\theta = 22.68°$) is shown in (c).

This difference is further emphasized upon examination of the surface by SEM. When 2ME is employed as solvent for the PT solution, the resulting seed layer consists of $PbTiO_3$ nanoislands distributed across the Pt surface. These nanoislands have complex curved shapes and only partially cover the surface (Fig. 4.8d). However, the 1M2P-based PT solution affords $PbTiO_3$ nanocrystals with well-defined facets (Fig. 4.8e). Based on these observations, it is reasonable to assume that the strong orientation in the PZT layer stems from the quality of the orientation of the seed layer.

Coming back to the discussion of section 4.3.3, we could hypothesize that the solvent plays a role in the amount of precursor material deposited on the surface and that is then available for the growth of the $PbTiO_3$ crystalline phase. We have seen that 1M2P-based solutions afford thicker films as compared to 2ME-based solutions under identical spinning conditions, due to the nature of the solvent. If we assume that the thickness of the liquid film is proportional to $\frac{1}{\sqrt{\omega}}$, we can postulate that for a given solvent i, the thickness d_i is equal to $\frac{c_i}{\sqrt{\omega}}$, where c_i is a constant depending on the nature of the solvent. From the previous experiments with PZT films (where the solution concentration was 0.3 M), we know that $\frac{d_{1M2P}}{d_{2ME}} \approx \frac{5}{4}$, which infers that $\frac{c_{1M2P}}{c_{2ME}} \approx \frac{5}{4}$.

Based on this simple model, we can work out that spinning the 2ME-based PT solution at 1900 rpm should result in a liquid film having a similar thickness as the one obtained from the 1M2P-based PT solution spun at 3000 rpm. Conversely, spinning the 1M2P-based solution at 4700 rpm would result in a layer thickness similar to the one of the 2ME-based solution spun at 3000 rpm. Therefore in both cases, a comparable amount of precursor material would be available on the surface for crystallization of the seed layer.

The results are presented and compared in Fig. 4.9. It appears that the spinning rate has no significant influence on the observed phenomenon at the selected spinning rates. The *thicker* 2ME-derived PT seed layer exhibits a similar microstructure as the one spun at 3000 rpm. There only appears to be a higher amount of small-sized $PbTiO_3$ nanoislands on the *thicker* sample, possibly due to an increased number of nucleation sites. Likewise, the two 1M2P-derived seed layers share similar features. The *thinner* sample exhibits a greater amount of well-defined single nanocrystals (in the shape of truncated pyramids), whereas the *thicker* one mainly consists of nanocrystal clusters.

With the influence of the amount of precursor material in the orientation effect ruled out, we could reasonably invoke a role from the solution chemistry. As mentioned earlier, the solvent interacts with the metal cations in solution via substitution reactions. The nature of the metal–organic species in a PT solution is typically quite complex, with polynuclear heterometallic complexes (or oligomers) [135]. Based on the structural difference between 2ME and 1M2P, it can be hypothesized that the reactivity of these two solvents towards alkoxides is different, with 1M2P being less reactive than 2ME (due to the steric hindrance of the methyl moiety on the alpha carbon relative to the alcohol). The structures of the metal oligomers obtained upon reaction with the Pb and Ti precursors should therefore be different. This structure and distribution of metal cations is expected to be preserved in the dried and amorphous pyrolyzed layers. This in turn can affect the growth of the crystalline phase.

In a contribution from 2006, P. Muralt attributed the nucleation of the (100) orientation in sputter-deposited $PbTiO_3$ seed layers to a high PbO partial pressure in the system [136]. In the case of our solution-based spin-coated seed layers, we can further hypothesize that the nature of the metal species formed in solution upon reaction with 1-methoxy-2-propanol provides a lead-rich environment during crystallization that favors the formation of (100)-oriented crystallites.

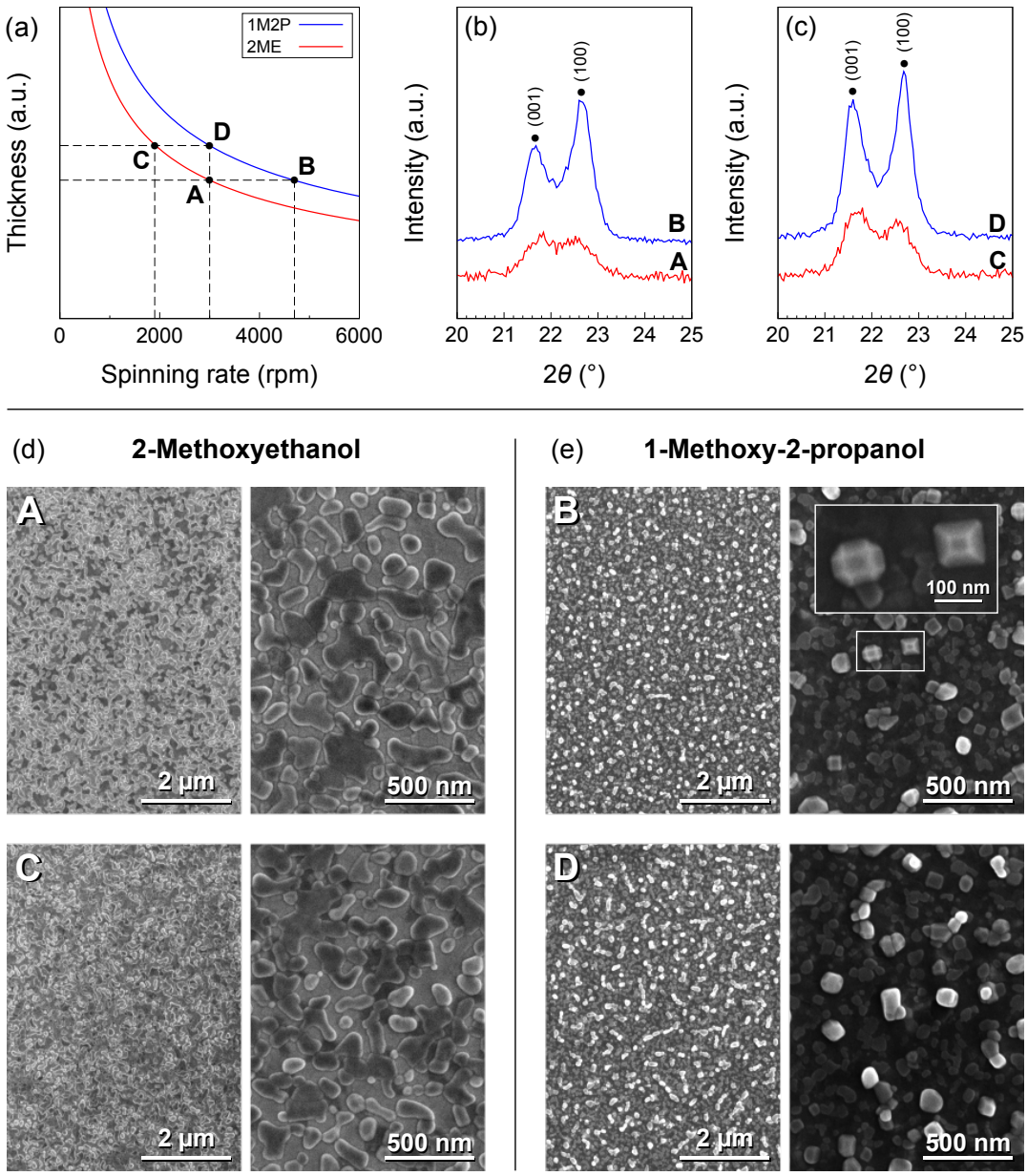

Fig. 4.9. Influence of the spinning rate on the microstructure of PT seed layers: (a) evolution of the thickness of the liquid film based on the $\propto \frac{1}{\sqrt{\omega}}$ model, (b),(c) XRD patterns of the (001)/(100) reflection and (d),(e) surface SEM micrographs.

Studying the structure of the solution precursors could help us understand the mechanism of the observed phenomenon. Probing the lead environment by the means of liquid state ^{207}Pb nuclear magnetic resonance (NMR) spectroscopy was attempted. However, our investigations were not conclusive, probably due to the complexity of the lead-containing species and the existence of exchange phenomena in solution, both of which cause signal broadening and intensity decrease. The wide spectral window of ^{207}Pb is an additional difficulty.

Nevertheless, we also discovered that the presence of acetylacetone (Hacac) in the solution was required for the orientation effect to be observed, as illustrated in Fig. 4.10. Acetylacetone is used as an *additive* as it has strong chelating properties, in particular with titanium alkoxides. Its reaction with Ti(O*i*Pr)$_4$ is fast and yields a yellow-colored complex. It appears that the structure of the metal species in solution is both mediated by the solvent and Hacac. We can therefore conclude that the strong orientation in 1M2P-derived seed layers results from a synergistic effect between 1M2P and Hacac.

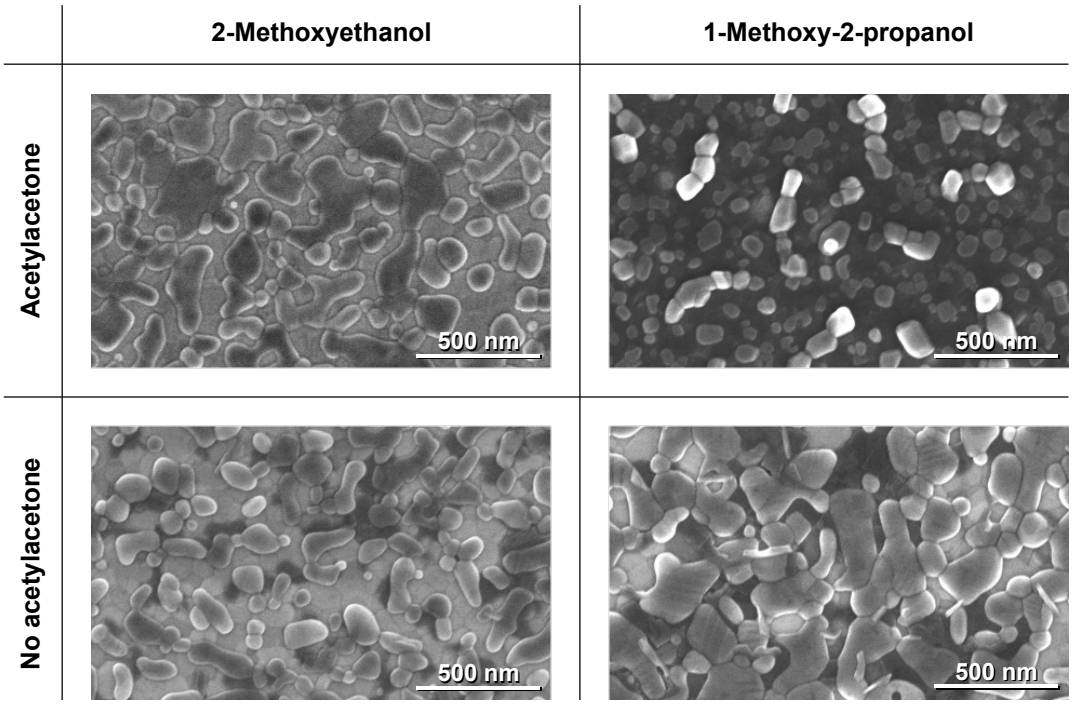

Fig. 4.10. Influence of the presence of acetylacetone on the microstructure of PT seed layers (surface SEM). Note the presence of visible ferroelectric domains in the $PbTiO_3$ seed layer prepared from a 1M2P-based solution without Hacac.

4.3.5. Influence on electrical and piezoelectric properties

After examination of the structural features of micron-thick PZT films deposited from 2ME and 1M2P-based solutions, we went on to assess their respective performances in terms of functional properties. We could expect that the strong {100} orientation in 1-methoxy-2-propanol-derived films results in an enhanced piezoelectric response [38].

Polarization–electric field loops are presented in Fig. 4.11a and were measured at 100 Hz for 100 µm-diameter sputtered platinum top electrodes. Under normal conditions (bipolar measurement up to ±500 kV cm^{-1}), the loops appear relatively similar, with $P_r \sim 18\,\mu C\,cm^{-2}$ and $E_c \sim 35\,kV\,cm^{-1}$. However, for some electrodes or when the field was initially increased up to 0.7–1 MV cm^{-1}, we could measure a significantly higher response, with remanent polarization reaching as high as 30 and 37 µC cm^{-2} for 2ME and 1M2P-derived films, respectively. The coercive field is close to 55 kV cm^{-1} for both samples. Remarkably, the *P*–*E* loop measured for the 1M2P-derived films displays a square shape which reminds that of a single crystal. This 'wake up' effect could be attributed to interface defects that can occasionally be eliminated by applying a high enough electric field. Further investigations would be required to verify this hypothesis.

The relative permittivity–electric field loops measured at 1 kHz (Fig. 4.11b) do not appear to be significantly affected by the nature of the solvent used for processing, with $\varepsilon_r \sim 1300$ and $\tan\delta \sim 0.04$.

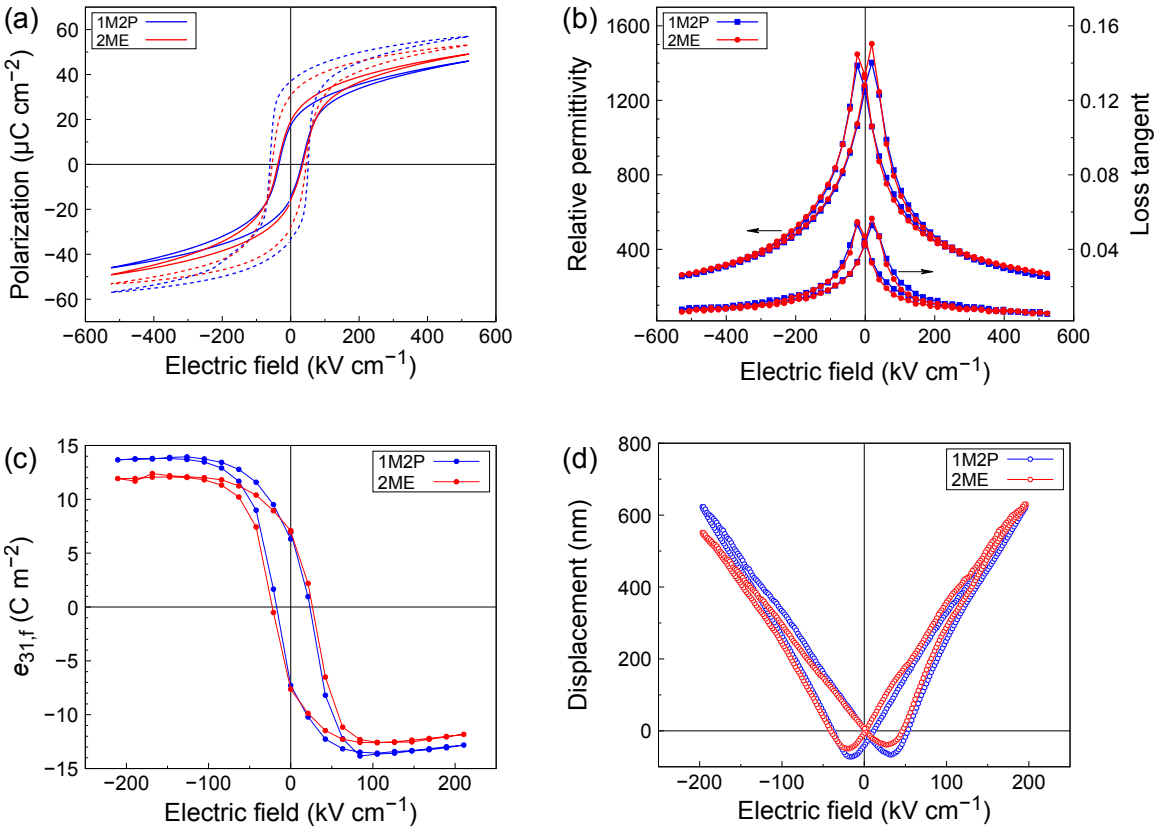

Fig. 4.11. Electrical and piezoelectric characterization of micron-thick 2ME and 1M2P-derived PZT films. (a) Polarization–electric field loops measured at 100 Hz. The loops measured as a result of the observed 'wake up' effect are shown in dashed lines. (b) Relative permittivity–electric field loops measured at 1 kHz (V_{AC} = 500 mV). (c) Effective transverse piezoelectric coefficient as function of electric field measured via the direct 4PB method (measurement at 10 Hz). (d) Displacement–electric field characteristic used for the evaluation of $e_{31,f}$ via the converse method (measurement at 20 Hz).

To complete the electromechanical characterization, we measured the effective transverse piezoelectric coefficient $e_{31,f}$ by the direct and converse methods (see description in Appendix D, page 139). The electric field-dependence of $e_{31,f}$ measured via the direct 4PB method is shown in Fig. 4.11c. The 1M2P-derived PZT film displays slightly higher $e_{31,f}$, reaching $\pm 13.8\,\mathrm{C\,m^{-2}}$. However, the remanent values (at zero electric field) are similar for both layers, with $\sim 7\,\mathrm{C\,m^{-2}}$. We then measured the large-signal displacement as function of the applied electric field (converse method), as shown in Fig. 4.11d. We estimated the piezoelectric coefficient by applying eq. (D.8) to the slope of the displacement curve (linear fittings in the -100–$0\,\mathrm{kV\,cm^{-1}}$ and 0–$100\,\mathrm{kV\,cm^{-1}}$ ranges were performed to extract the slope). The values are compiled in Table 4.3 for comparison with the ones obtained via the direct measurements. Despite some differences in the absolute values, the piezoelectric coefficients measured via the two methods are in good agreement, with a similar observed trend.

	Direct measurement		Converse measurement	
	$e^{+}_{31,f}$	$e^{-}_{31,f}$	$e^{+}_{31,f}$	$e^{-}_{31,f}$
2-Methoxyethanol	−12.6	12.1	−13.9	11.3
1-Methoxy-2-propanol	−13.8	13.8	−14.6	13.1

Table 4.3. Effective transverse piezoelectric coefficients of micron-thick 2ME and 1M2P-derived PZT films. We report here the maximum $e_{31,f}$ values extracted form direct and converse measurements, for positive ($e^{+}_{31,f}$) and negative ($e^{-}_{31,f}$) electric bias. The values are expressed in $\mathrm{C\,m^{-2}}$.

As the PZT films processed using 1M2P-based solutions exhibit stronger {100} orientation than the 2ME-derived films, we could have expected to measure a higher remanent $e_{31,f}$ for these layers. Since both PZT films were grown via a conventional CSD method where a single solution with MPB composition was employed, chemical gradients should exist across the layers, as explained in the Background section (page 17). A more pronounced chemical gradient in the case of 1M2P-derived films could account for these observations. To verify this hypothesis, a depth profiling of the PZT films was performed by dynamic secondary ion mass spectrometry (D-SIMS). The results of the analyses are presented in Fig. 4.12. Five oscillations in the zirconium and titanium signals associated with the five deposition cycles ($n = 5$, see Fig. 4.5) can be clearly distinguished. Interestingly, the chemical profiles of lead and oxygen in the PZT films are correlated with zirconium signals and display a higher concentration at the film surface. Nonetheless, similar trends in the chemical profiles are observed for both samples.

We can therefore conclude that the nature of the solvent does not have a significant influence on the development of chemical gradients during crystallization. The ‘wake up’ effect observed for polarization loops could perhaps be invoked here, as it could play a similar role in the piezoelectric characterization. Again, the verification of this hypothesis would require further investigations.

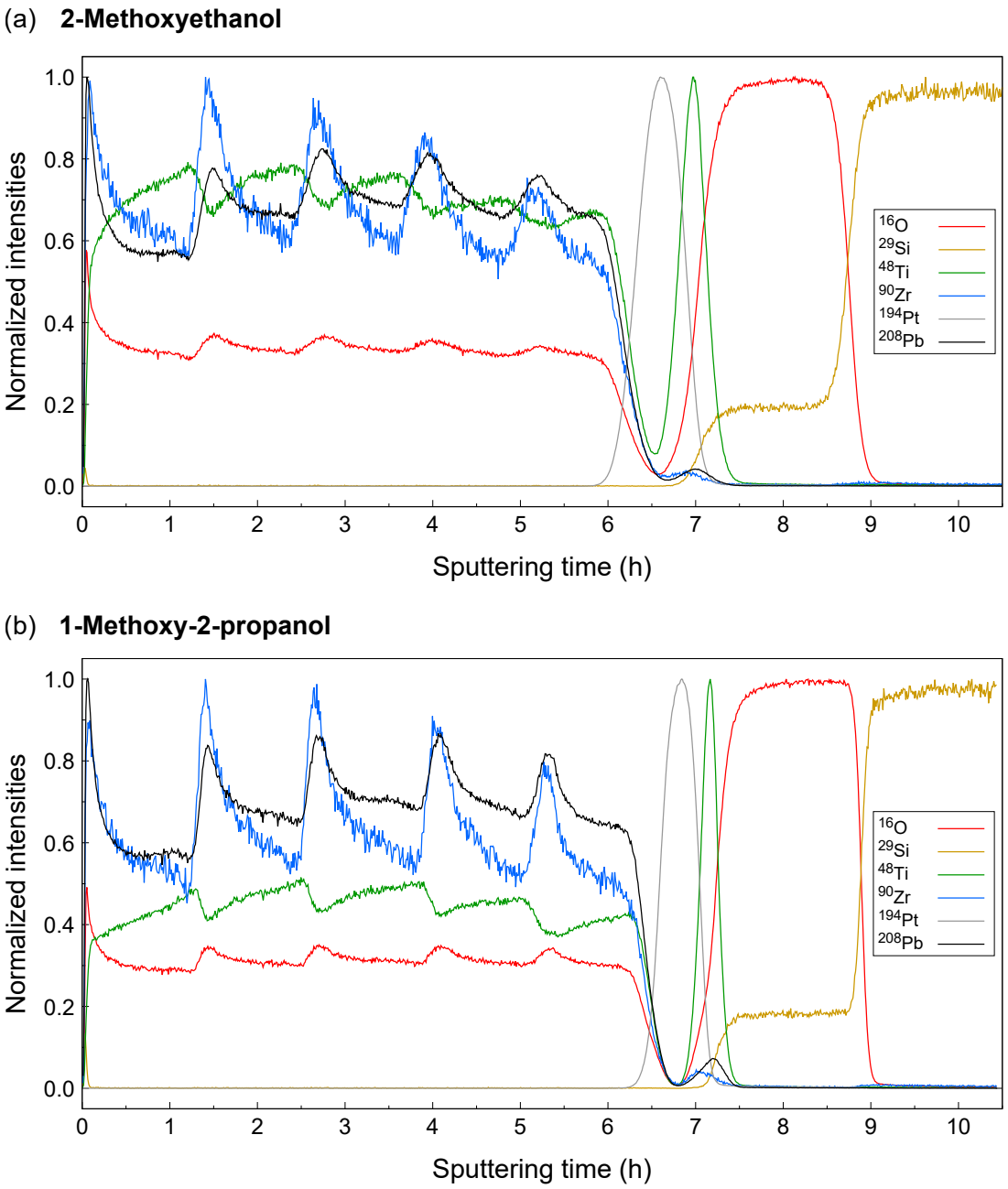

Fig. 4.12. D-SIMS depth profiling of (a) 2ME and (b) 1M2P-derived micron-thick PZT films. The primary ion beam consisted of Cs^+ ions accelerated at 1 keV and positive secondary ions were detected in a 60 µm-diameter spot. The structure of the platinized silicon substrate is clearly represented for sputtering times $\gtrsim$ 6.5 h, with the succession of Pt, TiO_x, SiO_2 and bulk Si. Note the presence of Pb in the TiO_x layer.

From this study, we can conclude that 1-methoxy-2-propanol is a suitable solvent for the preparation of PZT solutions and the deposition of high-quality films via spin coating. These layers exhibit electrical and piezoelectric properties which are comparable to the ones obtained for 2-methoxyethanol-derived layers, with even a noticeable improvement that could be ascribed to the strong {100} orientation induced by 1M2P-derived $PbTiO_3$ seed layers.

4.4. Implementation of 1-methoxy-2-propanol in the inkjet printing process

We have seen that 1-methoxy-2-propanol is a promising alternative to 2-methoxyethanol for chemical solution deposition of PZT films via spin coating. In order to make a link with the main topic of this work, we will now come back to inkjet printing and discuss how our process can be improved thanks to 1M2P.

4.4.1. Simplification of the printing process

A downside of our printing process is the number of individual steps that need to be performed to deposit large-area micron-thick films. The original procedure described in Chapter 2 (page 55) involves 60 individual printing–drying–pyrolysis sequences for printing a micron-thick film, which represents 10 h of work at the laboratory scale. In order to make this process more time-efficient, we would need to increase the thickness per deposition step. Referring back to eq. (1.1) in Chapter 1, this can be done in two ways: (1) by increasing the amount of deposited ink or (2) by increasing the ink concentration. The first approach could lead to spreading and inhomogeneity issues, whereas the second one appears more straightforward to test. In the rest of this chapter, we will attempt to double the ink concentration, i.e. shifting from 0.2 to 0.4 M inks. This should decrease the number of individual deposition steps to 30, making it comparable to conventional spin coating in terms of processing time.

As a starting point, we tested our original ink formulation (based on the 2-methoxyethanol, glycerol and ethylene glycol solvent mixture in 65:25:10 ratio) at a concentration of 0.4 M. The process was carried out as usual, with only six depositions done by inkjet printing. Drying was carried out at 175 °C for 1 min and pyrolysis was performed at 475 °C for 3 min after each deposition. The cross section of the film crystallized at 700 °C for 5 min (Fig. 4.13a) reveals significant porosity across the whole ~200 nm-thick layer. This contrasts strongly with the study presented in Chapter 2. As we have discussed in that chapter, the elimination of organic residues due to the presence of high-boiling point solvents is a crucial factor for the growth of dense films. The present study suggests that the original formulation is not suitable for this modified process due to incomplete elimination of organic residues (even at 475 °C), which are assumed to mainly come from glycerol (Fig. 4.13c). The six individual layers are probably too thick to ensure efficient transport of the pyrolysis by-products out of the layer.

Likewise, porosity was also observed in the top part of micron-thick films printed according to the original procedure with 0.2 M glycerol-based ink (the SEM cross section can be found in Chapter 3, page 70), further suggesting that glycerol might be at the origin of porosity. Despite its beneficial influence for the jetting and drying behavior, glycerol may not be the ideal solvent for printing thick layers due to all the considerations described above. In the next test, we will attempt to phase it out from the formulation, while replacing it with another viscous solvent.

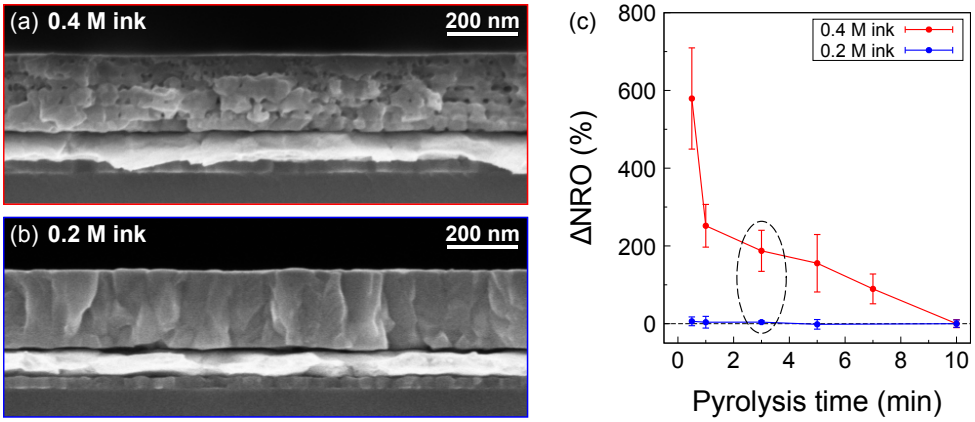

Fig. 4.13. SEM cross sections of inkjet-printed PZT film printed using (a) a 0.4 M glycerol-containing ink formulation (6 deposition steps) and (b) the original 0.2 M glycerol-containing ink formulation. Both films were pyrolyzed at 475 °C for 3 min. Porosity in (a) can be correlated with a significant amount of residual organics in the film (c). The variation of normalized residual organics (ΔNRO) after pyrolysis at 475 °C was obtained from the FTIR study of the films (see Chapter 2). The data were normalized with respect to the point at 10 min and expressed as a percentage variation.

A promising formulation was prepared as follows. A 1 M PZT stock solution in 2-methoxyethanol was initially prepared according to the protocol detailed at page 30. This solution was then diluted down to 0.4 M with 1,3-propanediol. The addition of this viscous solvent resulted in a stable ink, that exhibited no precipitation, even after several months of storage in a refrigerator. This ink displayed good jetting characteristics too, and only slight adjustments of the waveform illustrated in Fig. 1.5b (V_0 = 5 V and V_{max} = 30 V) were required for optimal jetting with 10 pL Fujifilm Dimatix cartridges at $T_{printhead}$ = 32 °C.

4.4.2. Highly oriented seed layers for {100}-textured inkjet-printed PZT

The new 0.4 M ink formulation was used to print 200 nm-thick films with only six deposition cycles. After printing, each layer was dried at 175 °C for 1 min and pyrolyzed at 475 °C for 3 min. In addition, the films were printed on $PbTiO_3$ seed layers obtained via spin coating of 2ME and 1M2P-based solutions, as described earlier. XRD patterns of the inkjet-printed PZT films are presented in Fig. 4.14a. Without a seed layer, the films exhibit a {111} texture, similarly to what was observed for the 0.2 M glycerol-containing formulation. The presence of $PbTiO_3$ induces {100} orientation as expected and the influence of the solvent is comparable to the case of spin-coated films, with the strongest orientation associated with the 1M2P-derived seed layer.

In all cases, the films exhibit a dense microstructure, as can be seen in the cross sections shown in Figs. 4.14b to 4.14d. The inkjet-printed PZT film printed without a seed layer is 200 nm-thick, which is the expected thickness for this process. In contrast, the PZT films printed on 2ME and 1M2P-derived seed layers have respective thicknesses of 230 and 245 nm.

The thickness difference could be ascribed to the presence of the seed layer. The visual appearance of the layers also suggested thickness variations across each respective sample. In the following electrical characterization, we used these values for the thicknesses of the films and performed the measurements using electrodes in the vicinity of the region where the cross section cut was made.

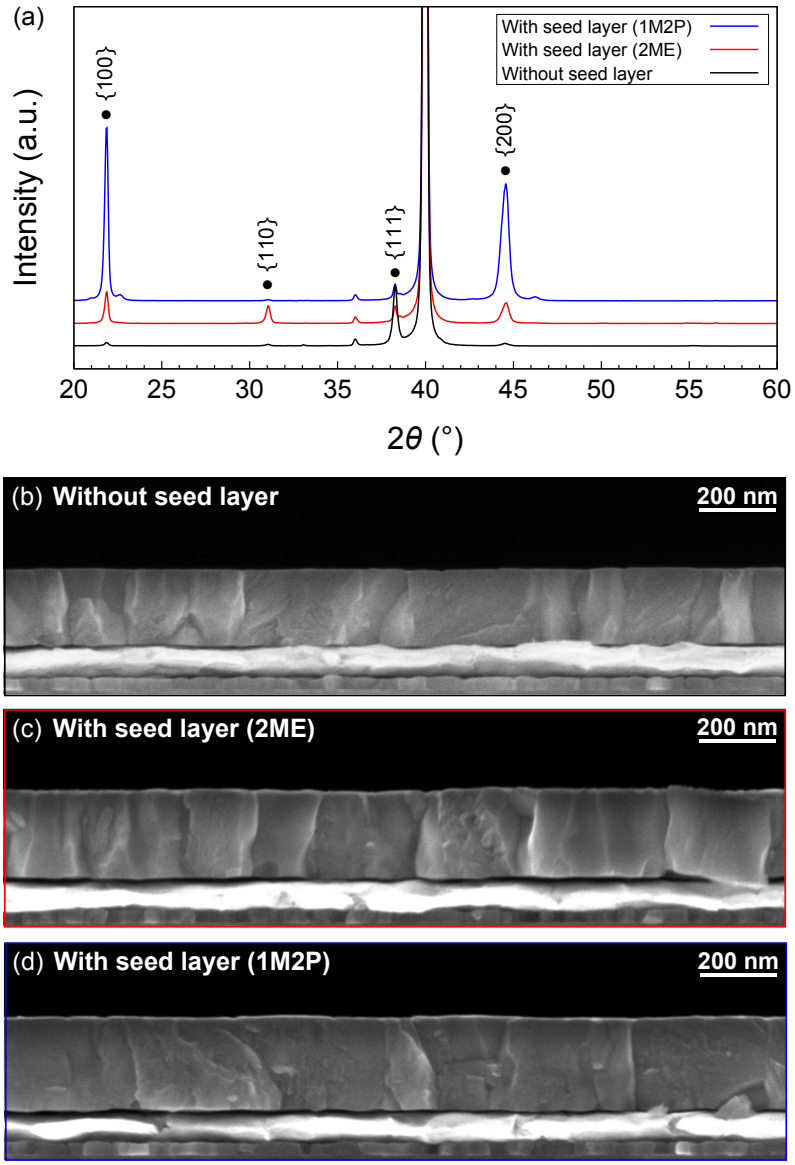

Fig. 4.14. (a) XRD patterns and (b)–(d) SEM cross sections of PZT films printed using the 0.4 M glycerol-free ink formulation.

The polarization–electric field loops are shown in Fig. 4.15a. The unseeded {111}-textured PZT film displays a remanent polarization of 24 µC cm^{-2} and a coercive field of 60 kV cm^{-1}, which are in excellent agreement with the properties of the layer printed using the glycerol-based ink formulation and pyrolyzed at 475 °C (please refer back to Fig. 2.9a, page 62). A decrease of P_r, P_{max} and E_c is observed for the printed films grown on $PbTiO_3$ seed layers and can be attributed to the {100} texture [137].

In the relative permittivity–electric field loops represented in Fig. 4.15b, we can observe that the unseeded film has a relative permittivity of 950 at zero bias, while its seeded counterparts reach a value close to 1100. The loss tangent remains at 0.04 for all the inkjet-printed PZT films.

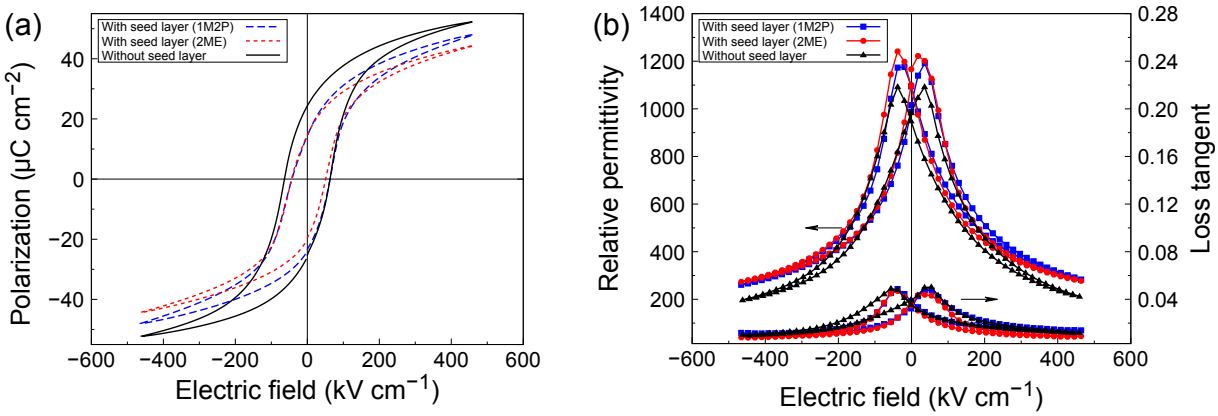

Fig. 4.15. Electrical characterization of PZT films printed using the glycerol-free ink formulation: (a) polarization–electric field loops measured at 100 Hz and (b) relative permittivity–electric field loops measured at 1 kHz.

We have therefore shown that it is possible to control the texture of PZT films printed using the modified glycerol-free ink formulation. For pyrolysis performed at 475 °C, printing on pristine platinized silicon results in {111} texture, while the use of a 1-methoxy-2-propanol-derived $PbTiO_3$ seed layer affords strong {100} texture.

4.4.3. Towards 2-methoxyethanol-free ink

The natural question that now comes to mind is whether 2ME can also be replaced by 1M2P in PZT inks. When we tried to prepare a 1 M PZT stock solution in 1M2P (as described in the modified procedure for the preparation of 0.4 M ink), we encountered an issue: the solubility of lead(II) acetate in 1M2P is too low to obtain directly a solution at this concentration. Even upon prolonged heating and vigorous stirring, a significant amount of undissolved lead precursor remained in the flask. Nevertheless, it was possible to prepare a 1 M solution by first preparing a dilute solution (~0.3 M) via the usual route and then concentrating it by distillation. The stock solution could then be diluted to 0.4 M with 1,3-propanediol as described before.

PZT stripes were printed onto a fused silica substrate using this ink formulation. The substrate was coated with a 24 nm-thick buffer layer of HfO_2 (deposited by ALD) and a 1M2P-derived spin-coated $PbTiO_3$ seed layer prior to printing. The XRD pattern shown in Fig. 4.16 indicates clear {100} texture of the printed layer. This final example demonstrates that it is possible to use the safe solvent 1-methoxy-2-propanol as basis for the preparation of PZT inks and that the printed layers exhibit the desired {100} orientation for piezoelectric applications.

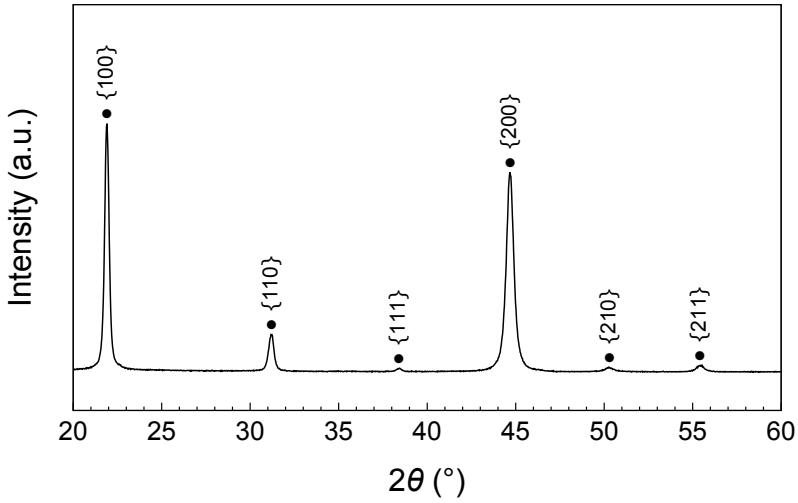

Fig. 4.16. XRD pattern of a PZT film printed on fused silica using a 1-methoxy-2-propanol-based ink formulation.

4.5. Chapter summary

In this chapter, we addressed the issue of the toxicity of PZT solutions based on 2-methoxyethanol. After a screening of potential candidates based on structure and physicochemical properties, we selected 1-methoxy-2-propanol as a replacement. This experiment was successful in the sense that we could obtain dense PZT films with excellent ferroelectric and piezoelectric properties through the 1-methoxy-2-propanol route.

Furthermore, we found out that lead titanate seed layers derived from 1-methoxy-2-propanol-based solutions had a strong (100)/(001) orientation, which in turn induced a strong {100} orientation in PZT films grown on top of them. These $PbTiO_3$ seed layers can also be used for the {100} orientation in inkjet-printed PZT films. To conclude this study, we also showed that 1-methoxy-2-propanol could be used as basis of the preparation of PZT inks.

Summary and conclusions

In this work, we have studied different aspects related to inkjet printing and solution processing of lead zirconate titanate thin films. This section provides a summary of the four chapters of this thesis and presents the conclusions we can draw from the present work.

Chapter 1 was dedicated to the study of inkjet-printed PZT structures on platinized silicon. PZT was prepared from a CSD solution suitable for spin coating by addition of viscous high-boiling-point co-solvents. To overcome the issue of ink spreading due to the high surface energy of the substrate, we developed a novel printing strategy based on inkjet-printed soft templates. In our process, an ink-repelling self-assembled monolayer was selectively formed on the surface by direct printing of an ink containing 1-dodecanethiol. State-of-the-art methods using a similar strategy involved a lithographic step in order to pattern the template.

Several PZT structures were printed using this strategy, namely 1 µm-thick $500 \times 500\,\mu m^2$ squares and 440 nm-thick $1000 \times 150\,\mu m^2$ rectangles. These thicknesses were achieved by iteration of the printing process. Inkjet-printed templates were shown to provide an efficient ink-repelling action, in addition to being fabricated in a time-efficient manner. In the case of the printed squares, the initial dimensions were preserved throughout the stacking process, while a gradual widening of the rectangles occurred with each additional deposited layer. Nevertheless, the electrical properties of the inkjet-printed PZT films were in line with those of typical CSD-derived layers with $P_r = 13\,\mu C\,cm^{-2}$, $E_c = 58\,kV\,cm^{-1}$, $\varepsilon_r = 900$ and $\tan\delta = 0.07$.

We conclude that it is possible to perform a direct patterning of metal oxide structures with a feature size in the ~100 µm range on platinized silicon without the assistance of a lithography-based templating method or prior surface modification. Inkjet printing itself can be used for the fabrication of a patterned ink-repelling soft template.

In **Chapter 2**, we studied the transformation of the ink formulation developed in the previous chapter into a functional layer. The modification of the 2-methoxyethanol-based CSD solution with viscous high-boiling-point co-solvents (glycerol and ethylene glycol) required adaptations of the standard processing route in order to obtain dense layers. In particular, we examined the pyrolysis step of the process, required for the elimination of the residual organic content before crystallization at 700 °C.

First, comparison of the thermogravimetric profiles of the CSD solution and the ink confirmed the expected shift of processing temperatures. We then used Fourier transform infra-red spectroscopy to estimate the amount of residual organics in inkjet-printed pyrolyzed layers as function of pyrolysis temperature and time. We showed that pyrolysis at 400 °C for at least 3 min was a minimal requirement for effective elimination of organic residues. Indeed, the presence of residual organics was associated with porosity and degradation of the electrical properties in the crystallized films. The implementation of optimal processing conditions afforded dense {111}-textured 200 nm-thick PZT layers on platinized silicon, with $P_r = 23\,\mu C\,cm^{-2}$, $E_c = 60\,kV\,cm^{-1}$, $\varepsilon_r = 1000$ and $\tan\delta = 0.04$. This represents a significant improvement with respect to the previous chapter and the current state of the art.

It can be concluded that pyrolysis is the crucial step in the processing of inkjet-printed PZT thin films. The introduction of glycerol, though beneficial for the jetting behavior, required the use of higher temperatures than the ones used in conventional processing. A systematic investigation of the completion of pyrolysis as function of temperature and time was shown to be a valuable tool for obtaining dense and textured layers.

In **Chapter 3**, we examined a possible application of inkjet-printed PZT layers in silicon-based unimorph energy harvesters. The devices were designed to have their resonant frequency close to 100 Hz. A power output of 5.8 µW was measured across a 6 kΩ resistive load under 5.0 *g* acceleration. It is therefore possible to implement inkjet printing as a manufacturing step in the fabrication of piezoelectric devices based on PZT thin films.

Finally, in **Chapter 4** we proposed to use 1-methoxy-2-propanol as an alternative solvent to 2-methoxyethanol in order to mitigate the toxicity issues associated with PZT processing. The solvent was selected based on its structure and physicochemical properties. We showed that this safe solvent could be used to grow dense layers via the conventional spin coating process. Interestingly, we identified an unexpected characteristic of 1-methoxy-2-propanol: its presence in precursor solutions for the deposition of lead titanate seed layers was shown to induce a strong (100)/(001) orientation in the latter. Although the underlying mechanism of this phenomenon is still not fully understood, we showed that 1-methoxy-2-propanol-derived seed layers could be used for the growth of strongly {100}-textured PZT layers on platinized silicon, be it via spin coating or inkjet printing.

Here, we conclude that 2-methoxyethanol can be replaced by 1-methoxy-2-propanol for the processing of PZT thin films. In addition to its low toxicity, 1-methoxy-2-propanol has a beneficial effect on the orientation of PZT films, thus representing a double advantage compared to 2-methoxyethanol.

Outlooks

The present work attempted to answer a series of questions about inkjet printing and CSD processing of PZT thin films. Our investigations lead us to new questions and let us now formulate several outlooks, which we will examine chapter by chapter.

From **Chapter 1**, we learnt that the lithography-free technique we developed to pattern PZT films could be used for patterning 440 nm-thick $1000 \times 150\,\mu m^2$ rectangles. Nevertheless, profilometry measurements of these structures revealed a relatively limited area of constant thickness in the central part as a result of the gradual slopes. It would be interesting to improve the profile of these structures in order to increase the usable surface area. A possible solution would be to tune the solvent composition to induce a coffee-ring-like redistribution of solute at the edges of the structures. In addition, limitations of the ink-constraining capabilities provided by the thiol ink were demonstrated by the widening of the printed lines, which had a nominal width of 50 µm in the fabrication file but became 150 µm-wide after ten depositions. A fluorinated thiol could provide a more efficient templating action. However, the ink formulation might have to be revised to dissolve this compound and preserve good jetting characteristics.

In **Chapter 2**, we saw that a PZT ink based on a solvent composition containing 25 % of glycerol by volume required a pyrolysis temperature of at least 400 °C for 3 min for efficient removal of organic residues from the layer and subsequent consolidation into a dense layer during the crystallization step at 700 °C. These findings could naturally be implemented for processing the patterned structures described in Chapter 1, thus combining lithography-free patterning of PZT films on platinized silicon with optimized processing conditions.

As seen in **Chapter 3**, inkjet-printed PZT films on platinized silicon can be used for energy harvesting. We discussed the reasons behind the modest voltage output of our devices, even those based on {100}-textured spin-coated PZT films. Other applications of inkjet-printed PZT films could therefore be explored and extended to substrates such as glass. An example is provided in Appendix C (please refer to page 129), where transducers based on inkjet-printed PZT films were used to induce a Lamb wave in a glass plate. After implementing the processing conditions determined in Chapter 2, we observed that micron-thick inkjet-printed PZT films still exhibit porosity and lack the preferred {100} orientation for enhanced piezoelectric response.

Chapter 4 provided valuable insights on the influence that solvents could play in a CSD formulation. We saw that the presence of glycerol was an obstacle to the growth of films in fewer deposition steps, as its removal during pyrolysis was incomplete. The alternative formulation based on 2-methoxyethanol and 1,3-propanediol showed promising results, as we were able to print {100}-textured 200 nm-thick PZT films on platinized silicon in six deposition steps, when a spin-coated $PbTiO_3$ seed layer derived from a 1-methoxy-2-propanol-based solution was used. Further developments of this ink formulation could be considered (including the replacement of 2-methoxyethanol by 1-methoxy-2-propanol), in order to improve its reliability and behavior on the substrate. This naturally poses the question of whether $PbTiO_3$ seed layers could be deposited by inkjet printing and used for the subsequent growth of {100}-textured inkjet-printed PZT layers.

Finally, it would be interesting to elucidate the mechanism by which 1-methoxy-2-propanol induces strong (100) orientation in $PbTiO_3$ seed layers. As discussed in the corresponding section, the solvent can influence the local coordination environment around the metal centers, resulting in a different structure of the precursors in solution and in the as-deposited layers as a consequence. We attempted to probe lead in solution by the means of liquid state ^{207}Pb NMR spectroscopy, which was not conclusive. The same experiments could be attempted using solid state NMR to analyze powders obtained after drying of the solutions. Alternatively, a technique of choice to probe the local environment of lead would be EXAFS (extended X-ray absorption fine structure) spectroscopy.

The present work could also inspire broader perspectives that would make use of the potential of inkjet printing for the fabrication of low-cost piezoelectric stacks. The development of inkjet-printed electrodes could be envisaged, thereby enabling fully printed piezoelectric transducers. In Appendix A we present a study on inkjet-printed silver top electrodes. However, it could be interesting to extend our printing expertise to transparent indium tin oxide (ITO) electrodes, which are particularly relevant for applications on glass substrates.

We could also think about the improvement of technical aspects of the process that would facilitate its industrialization. For example, automation of the printing process could be achieved by performing the annealing steps inside the printer thanks to an integrated annealing system (e.g. photonic annealing). The implementation of low-temperature processing strategies for inkjet-printed ceramic layers could be an asset in this context, as it would also expand the compatibility of our process to other substrates such as standard glass.

Ultimately, we could consider the integration of our lithography-free patterning process in the microfabrication workflow of silicon-based piezoelectric devices such as MEMS. As an example, an array of narrow inkjet-printed PZT structures such as the ones presented in Chapter 1 could be used to manufacture inkjet printheads. This would illustrate quite remarkably the role inkjet printing technology can play in its own development.

Alongside these *technical* outlooks, we can also think of other aspects more oriented towards material science. Understanding drying phenomena in our layers could help us improve the thickness homogeneity of our films. In turn, this would enable inkjet printing of homogeneous layers at different length scales – from sub-100 µm structures to the coverage of entire wafers.

Fine tuning of solution and ink chemistry could also be considered to further improve the quality of our material. For example, similarly to what was achieved in spin-coated films, we could use several inks with different stoichiometries to fabricate gradient-free PZT films. Our study on highly oriented $PbTiO_3$ seed layers could also inspire the development and study of inkjet-printed epitaxial layers.

Finally, this work could also serve as basis for the development of printing processes for other ferroic materials. Solution chemistry is specific to each CSD system and its adaptation for inkjet printing is therefore not necessarily straightforward. The present work can provide guidelines and insights for the formulation and processing of inks into high-quality materials. In order to go one step beyond the issue we addressed in Chapter 4, we could envisage the development of inkjet-printed lead-free piezoelectric thin films.

Publications, conferences and activities

Articles in peer-reviewed journals

As first author

1. Nicolas Godard, Sebastjan Glinšek, Aleksander Matavž, Vid Bobnar and Emmanuel Defay, 'Direct patterning of piezoelectric thin films by inkjet printing', *Advanced Materials Technologies* **2019**, *4*, 1800168.

2. Nicolas Godard, Sebastjan Glinšek and Emmanuel Defay, 'Inkjet-printed silver as alternative top electrode for lead zirconate titanate thin films', *Journal of Alloys and Compounds* **2019**, *783*, 801–805.

3. Nicolas Godard, Mohamed Aymen Mahjoub, Stéphanie Girod, Tony Schenk, Sebastjan Glinšek and Emmanuel Defay, 'On the importance of pyrolysis for inkjet-printed oxide piezoelectric thin films', *Journal of Materials Chemistry C* **2020**, *8*, 3740–3747.

4. Nicolas Godard, Lucas Allirol, Antoine Latour, Sebastjan Glinšek, Mathieu Gérard, Jérôme Polesel, Fabrice Domingues Dos Santos and Emmanuel Defay, '1-mW vibration energy harvester based on cantilever with printed polymer multilayers', *Cell Reports Physical Science* **2020**, 100068.

As co-author

1. Daniele Sette, Stéphanie Girod, Nicolas Godard, Noureddine Adjeroud, Jean-Baptiste Chemin, Renaud Leturcq and Emmanuel Defay, 'Transparent piezoelectric transducers for large area ultrasonic actuators' *2017 IEEE 30th International Conference on Micro Electro Mechanical Systems* **2017**.

2. Tony Schenk, Nicolas Godard, Aymen Mahjoub, Stéphanie Girod, Aleksander Matavž, Vid Bobnar, Emmanuel Defay and Sebastjan Glinšek, 'Toward thick piezoelectric HfO_2-based films', *Physica Status Solidi RRL* **2020**, *14*, 1900626.

3. Sebastjan Glinšek, Mohamed Aymen Mahjoub, Matthieu Rupin, Tony Schenk, Nicolas Godard, Stéphanie Girod, Jean-Baptiste Chemin, Renaud Leturcq, Nathalie Valle, Sébastien Klein, Cédrick Chappaz and Emmanuel Defay, 'Fully transparent friction-modulation haptic device based on piezoelectric thin film', *Advanced Functional Materials* **2020**, accepted manuscript.

Patents

1. Nicolas Godard, Daniele Sette, Sebastjan Glinšek and Emmanuel Defay, 'Inkjet printing process', LU100270 B1 (2017), WO2018202576 A1 (2018).

2. Nicolas Godard, Daniele Sette, Sebastjan Glinšek and Emmanuel Defay, 'Inkjet printing process', WO2020084066 A1 (2020).

3. Nicolas Godard, Sebastjan Glinšek and Emmanuel Defay, 'Seed layer to optimize crystalline orientation of piezoelectric films', in the process of filing (2020).

Conferences

Oral presentations

1. Nicolas Godard, Daniele Sette, Sebastjan Glinšek and Emmanuel Defay, 'Self-assembled monolayer-assisted inkjet printing of PZT films on platinized silicon', COST TO-BE Spring Meeting, 3–5 April 2017, Luxembourg City, Luxembourg.

2. Nicolas Godard, Daniele Sette, Sebastjan Glinšek and Emmanuel Defay, 'Self-assembled monolayer-assisted inkjet printing of PZT films on platinized silicon', IEEE International Symposium on Applications of Ferroelectrics (ISAF), 7–11 May 2017, Atlanta, United States of America.

3. Nicolas Godard, Sebastjan Glinšek and Emmanuel Defay, 'Self-assembled monolayer-assisted inkjet printing of PZT films on platinized silicon', E-MRS Spring Meeting, 18–22 June 2018, Strasbourg, France.

4. Nicolas Godard, Sebastjan Glinšek and Emmanuel Defay, 'Inkjet-printed PZT films for energy harvesting', IEEE International Symposium on Applications of Ferroelectrics (ISAF), 14–19 July 2019, Lausanne, Switzerland.

Poster presentations

1. Nicolas Godard, Daniele Sette, Sebastjan Glinšek and Emmanuel Defay, 'Self-assembled monolayer-assisted inkjet printing of PZT films on platinized silicon', IEEE International Symposium on Applications of Ferroelectrics (ISAF), 7–11 May 2017, Atlanta, United States of America.

2. Nicolas Godard, Sebastjan Glinšek, Daniele Sette, Stéphanie Girod and Emmanuel Defay, 'Self-assembled monolayer-assisted inkjet printing of PZT films on platinized silicon', 19th International Sol-Gel Conference, 3–8 September 2017, Liège, Belgium.

Awards

1. **Nomination for the student poster competition**, IEEE International Symposium on Applications of Ferroelectrics (ISAF), 7–11 May 2017, Atlanta, United States of America.

2. **Best pitch award at student pitch contest**, IEEE International Symposium on Applications of Ferroelectrics (ISAF), 14–19 July 2019, Lausanne, Switzerland.

Summer schools

1. 4th International School of Oxide Electronics (ISOE), 11–21 April 2017, Cargèse, France.

2. Electroceramics XVI Summer School, 6–7 July 2018, Hasselt, Belgium.

3. 2nd International Summer School on Knowledge-Driven Innovation and Entrepreneurship, 1–5 July 2019, Marienthal, Luxembourg.

Teaching

1. 'Travaux pratiques de Physique', University of Luxembourg (Campus Limpertsberg), winter semester 2016/2017.

2. 'Travaux pratiques de Physique', University of Luxembourg (Campus Limpertsberg), winter semester 2017/2018.

Appendix A

Inkjet-printed silver top electrodes

A.1. Motivation

In the main part of this work, we presented and discussed inkjet printing of PZT thin films. Piezoelectric transducers also consist of electrodes, which brings the question of whether it is possible to print these components of the piezoelectric stack as well. The typical electrode materials used in PZT-based piezoelectric stack are noble metals and conductive metal oxides such as $LaNiO_3$, RuO_2, $SrRuO_3$ or IrO_2 [138–141]. Metal oxide electrodes were shown to improve the fatigue characteristics of PZT thin films and enable the growth of epitaxial perovskite layers. However, platinum remains a popular choice owing to its low-leakage characteristics. Its deposition on piezoelectric films is usually performed via cost-intensive PVD methods and therefore requires lithography for patterning.

Inkjet printing of metal layers can be done using nanoparticle-based inks. Colloidal suspensions of nanoparticles are typically used, as they can be prepared in bulk quantities, remain stable over time and afford layers with good electrical conductivity [51]. Although many metals can be dispersed in a liquid medium as nanoparticles, silver is particularly interesting thanks to its relative low cost and chemical stability towards oxidation. Silver inks have therefore become standard for printing of conductive layers and are widely available from chemical suppliers. Nanoparticle colloids usually contain stabilizing agents to prevent the aggregation of particles, which is of crucial importance for inks as aggregates can precipitate out, clog the nozzles and result in inhomogeneous layers. Appropriate annealing conditions need to be applied after printing in order to eliminate the stabilizing agent and allow the growth of metal grains.

In this section, we will assess inkjet-printed silver as an electrode for CSD-derived PZT thin films deposited by spin coating. After optimizing the printing strategy and annealing process to obtain good-quality silver layers, the inkjet-printed silver electrodes will be compared with sputtered platinum top electrodes patterned by lift-off photolithography. This work is published in the *Journal of Alloys and Compounds* [142].

A.2. Inkjet printing of silver ink

A.2.1. Substrate preparation

For this study, we selected as substrate {100}-textured polycrystalline PZT films deposited on platinized silicon via spin coating. The PZT spin coating solution was prepared according to the standard procedure described at page 30. In addition, a $PbTiO_3$ seed layer was used to promote the growth of the {100} orientation. The solution concentration, stoichiometries and processing parameters can be found in Table 4.2 (page 81). The process was used to grow 170 nm and 750 nm-thick PZT films, for electrical and piezoelectric characterization, respectively.

A.2.2. Printing strategy

SunTronic nanosilver EMD5730 ink was purchased from SunChemical. The ink was stored in a refrigerator at 4 °C and was shaken for 1 min before introduction into a Fujifilm Dimatix DMC-11610 cartridge (10 pL nominal volume) through a 5 µm PTFE filter. The printhead and substrate temperatures were set to 30 °C. The actuation pulse is shown in the inset of Fig. A.2. It consists of a trapezoidal pulse with a rise and decay time of 2 µs. The maximum voltage V_{max} is maintained for 3 µs at a value in the range 30–50 V. The jetting frequency was 500 Hz. A single nozzle was used for printing an array of 10×10 circular electrodes with 200 µm horizontal and vertical pitch, each droplet of nanosilver ink forming a single electrode. The velocity of the printhead v_{PH} was 10 cm s^{-1}.

The delivery of the droplets onto the surface was performed in two ways. A 10 mm-long priming line was always printed 20 mm away from the electrode array before printing the latter. The distance between the end of the priming line and the first electrode of the array is referred to as the priming distance d_{prim}.

- In the first deposition method, a line of electrodes was printed in a single pass of the printhead, meaning that consecutive electrodes were printed at intervals of 2 ms (except for the first one in the line).

- In the second strategy, a priming line was printed for each electrode. Each electrode was therefore printed at an interval of at least $\frac{d_{prim}}{v_{PH}} = 200$ ms after printing the priming line. This interval will be referred to as jetting dwell time, as jetting was systematically paused during the displacement of the printhead from the end of the priming line to the electrode to be printed.

After printing, the electrodes were dried at 200 °C for 10 min and sintered between 250 and 350 °C for 30 min (the sintering temperature range recommended by the ink manufacturer is 150–250 °C). These annealing steps were performed on hot plates.

As a starting point, we studied the influence of the maximum actuation voltage V_{max} and jetting dwell time on the size and morphology of the printed electrodes after annealing. As can be seen in Fig. A.1, the top electrode diameter can be controlled from 75 to 93 ± 1 µm by varying V_{max} from 30 to 50 V. The 50 V actuation pulse was selected for further investigations, as it produced electrodes with a size similar to the reference sputtered platinum ones. In addition, the selection of lower voltages sometimes lead to nozzle deactivation during printing.

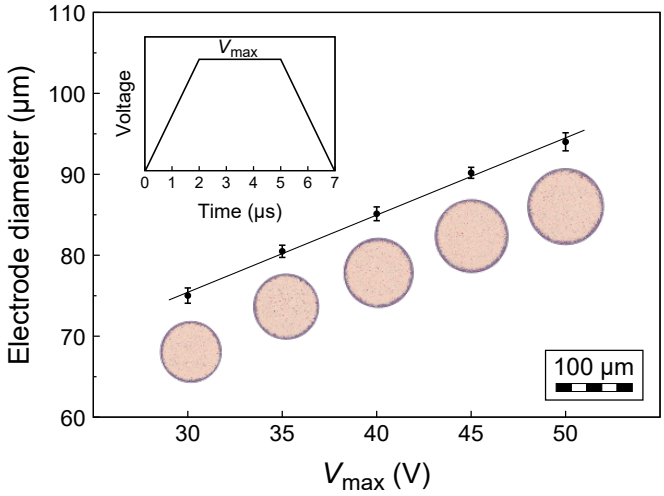

Fig. A.1. Diameter of inkjet-printed silver electrodes as function of the actuation pulse voltage V_{max}. Optical micrographs of the sintered electrodes are shown below the data points. Inset: waveform of the actuation pulse.

Interestingly, we found that jetting dwell time had a considerable effect of the morphology of the electrodes after sintering. On the optical micrograph shown in Fig. A.2a, we observe that without jetting dwell time, only the first electrode of each line has a consistent and homogeneous appearance. All the other electrodes in the line are surrounded by a dark rim that consists of sparsely distributed silver nanoparticles. This undesired effect was accentuated for each consecutive electrode in the line. The introduction of jetting dwell time resolved this issue, as shown in Fig. A.2b. With this printing strategy, all the electrodes in the array were homogeneous and could be printed with excellent repeatability.

SEM observations of the two types of electrodes revealed a difference in the microstructure, as electrodes printed without jetting dwell time were highly porous and did not cover the substrate completely: in Fig. A.2a the underlying PZT film can be seen through the electrode. Coverage was much improved after the implementation of jetting dwell time. A possible explanation is that this time is required to allow the cartridge ink chamber to replenish itself and be reset to its initial state, enabling droplet formation in a reproducible manner. Indeed, slight variations in droplet volume or velocity could result in the observed effect. In the following studies, we naturally used jetting dwell time in the printing of electrode arrays.

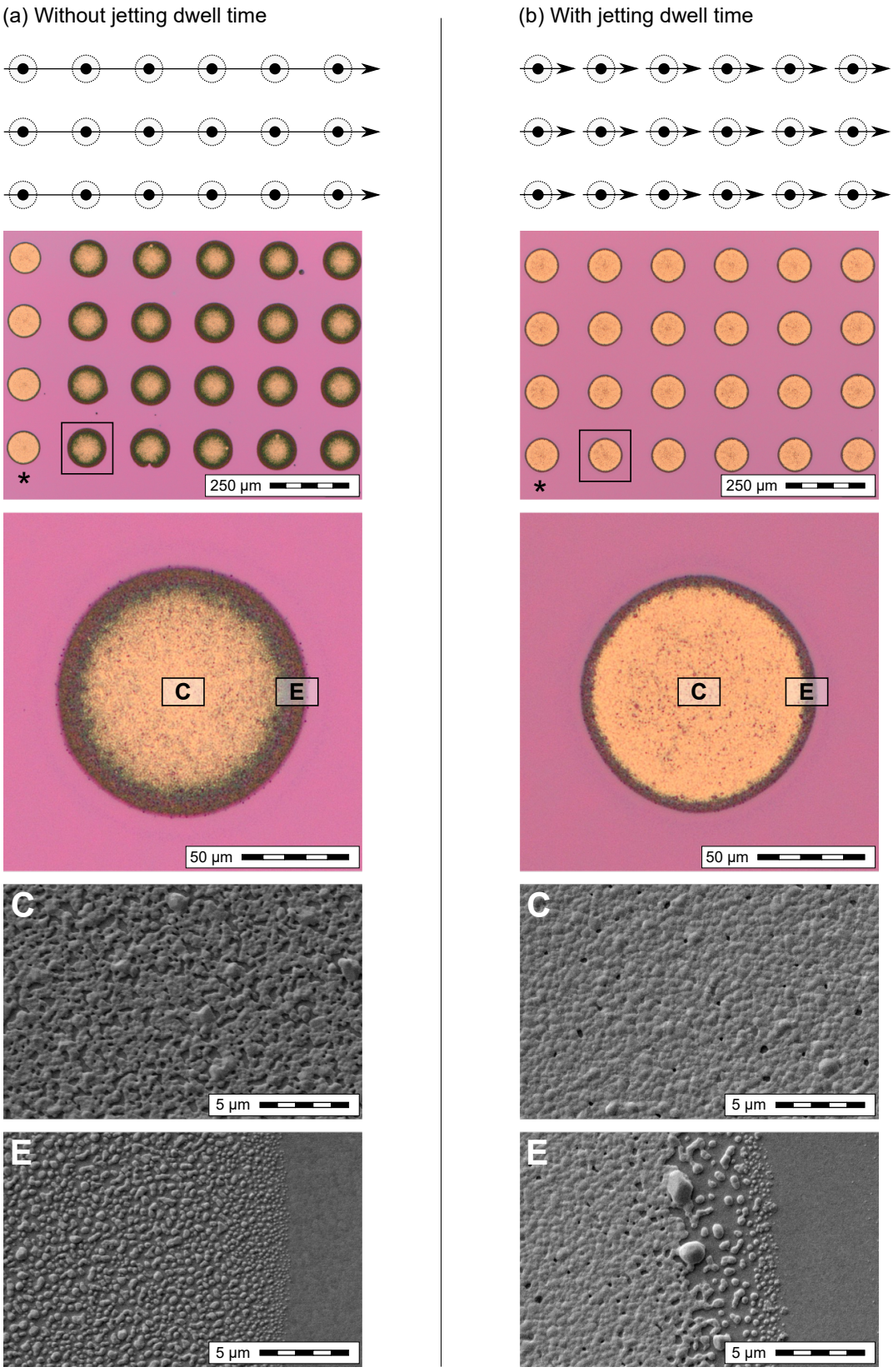

Fig. A.2. Printing strategy for silver top electrodes: influence of jetting dwell time on morphology. In (a), the electrodes in a row were printed in a single pass of the printhead (represented by an arrow on the scheme), whereas in (b) every electrode was printed during its own printhead pass. Optical micrographs and surface SEM pictures show the different structures at the center (C) and edge (E) of the printed electrodes. The asterisks ($*$) represent the origin of the electrode array on the optical micrographs.

A.2.3. Effect of sintering temperature

The microstructure of the inkjet-printed silver electrodes is significantly impacted by the sintering temperature. Fig. A.3 illustrates the evolution of the microstructure as function of temperature for dried inkjet-printed layers. After drying at 200 °C, the silver top electrode is highly porous as it consists on silver nanoparticles with a size in the order of 100 nm. Nanoparticle aggregates can also be distinguished on the surface (marked with an arrow in Fig. A.3a). The onset of sintering is observed when annealing is performed at 250 °C for 30 min. A gradual decrease of porosity is associated with the growth of silver grains as the sintering temperature is increased to 300 and 350 °C. A small quantity of pinholes can still be found on the surface after sintering at 350 °C. Examination of the cross section reveals a ~200 nm-thick dense silver layer that provides good coverage of the underlying PZT film. The presence of silver grains is responsible for the observed surface roughness.

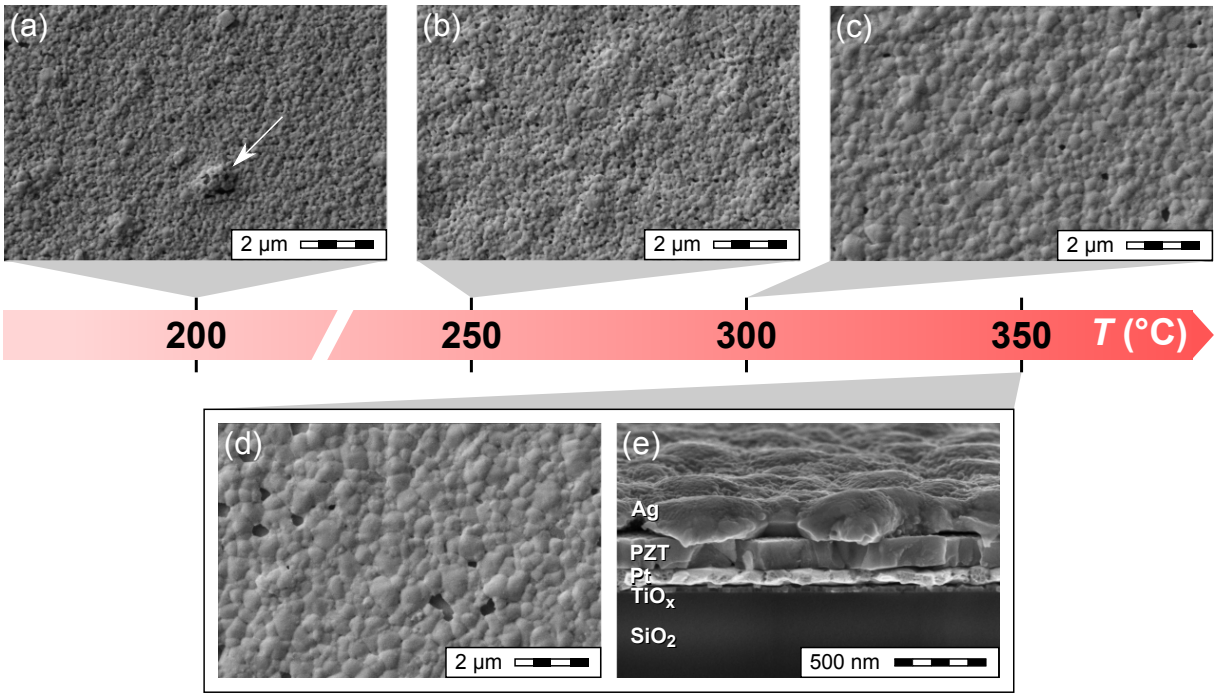

Fig. A.3. Surface SEM micrographs of inkjet-printed silver electrodes dried at 200 °C as function of sintering temperature: (a) no sintering (as dried), (b) 250 °C, (c) 300 °C and (d) 350 °C for 30 min. (e) Cross-section SEM micrograph of the platinized silicon substrate/PZT thin film/silver top electrode stack. The top electrode was sintered at 350 °C (sample tilted by 10°).

A.3. Comparison with sputtered platinum

A.3.1. Ferroelectric properties

The ferroelectric stacks constituted by inkjet-printed silver top electrodes, 170 nm-thick spin-coated PZT film and platinum bottom electrode were characterized to assess the measured ferroelectric properties and compare them with a stack where sputtered platinum top electrodes (100 µm-diameter) were patterned by lift-off photolithography and reannealed at 400 °C for 10 min before characterization.

The electrical characterization was performed using an aixACCT TF Analyser 2000. As can be seen in Fig. A.4a, the *P*–*E* loop measured at 100 Hz with silver top electrodes only dried at 200 °C reveals high coercive field ($E_c \sim 190\,\mathrm{kV\,cm^{-1}}$). E_c was found to be highly frequency dependent, decreasing to $110\,\mathrm{kV\,cm^{-1}}$ at 1 Hz. PZT films with dried silver electrodes are also characterized by a low relative permittivity ($\varepsilon_r \sim 115$) and high losses ($\tan\delta \sim 0.20$). Only slight improvement of the properties occurs when the layers are sintered at 250 °C for 30 min after the drying step. However, sintering at 300 °C results in significant improvement of the measured ferroelectric properties, with $P_r^- = -22.5\,\mu\mathrm{C\,cm^{-2}}$, $P_r^+ = 19.5\,\mu\mathrm{C\,cm^{-2}}$, $E_c^- = -50\,\mathrm{kV\,cm^{-1}}$, $E_c^+ = 60\,\mathrm{kV\,cm^{-1}}$, $\varepsilon_r = 920$ and $\tan\delta = 0.08$. The *P*–*E* loop is almost symmetrical, does not exhibit significant frequency dependence in the 10–1000 Hz range and clearly evidences ferroelectric switching of the PZT layer.

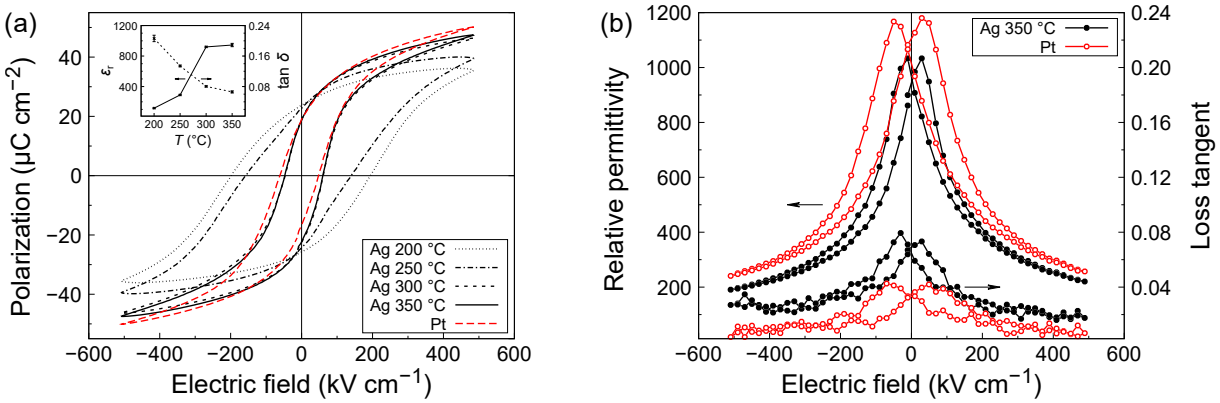

Fig. A.4. Electrical properties of PZT films with inkjet-printed silver top electrodes as function of sintering temperature and comparison with sputtered platinum top electrodes. (a) Polarization loops of 170 nm-thick PZT films measured at 100 Hz. Inset: evolution of relative permittivity and loss tangent at 1 kHz ($V_{AC} = 100$ mV). (b) Relative permittivity and loss tangent as function of electric field of 170 nm-thick PZT films with inkjet-printed silver top electrodes sintered at 350 °C and sputtered platinum top electrodes, both measured at 1 kHz ($V_{AC} = 100$ mV).

Further increase of the sintering temperature to 350 °C yields a very similar result, which can be compared with the reference sputtered platinum top electrodes. The shape of the P–E loop and the measured values for P_r and E_c are similar, although in the case of the inkjet-printed electrodes, the loop is slightly shifted towards positive fields. The ε_r–E loop measured with the silver top electrode sintered at 350 °C displays $\varepsilon_r = 940$ and $\tan\delta = 0.07$ at zero bias, which are comparable to the values obtained for the reference platinum top electrode ($\varepsilon_r = 1080$ and $\tan\delta = 0.04$), as shown in Fig. A.4b. The loop is also slimmer and slightly shifted towards positive fields.

However, significant leakage was observed in the case of inkjet-printed silver top electrodes, with 0.29 µA cm^{-2} at 120 kV cm^{-1}, i.e. two orders of magnitude higher than the current density measured at the same field with the platinum top electrode (0.0026 µA cm^{-2}). Nevertheless, the ferroelectric stacks can withstand a poling electric field higher than the coercive field of PZT (measurement of a P–E loop up to ±500 kV cm^{-1}), which will enable the assessment of piezoelectric properties.

The effect of sintering temperature on the measured ferroelectric properties can be ascribed to the enhancement of the electrical conductivity of the printed silver electrodes as sintering tends toward completion at temperatures ≥ 300 °C. Indeed, the silver electrodes that were only dried and sintered at 250 °C display a particle-like microstructure and a significant amount of inter-particle porosity, which increases the electrical resistance of the electrode. The electrical conductivity of electrodes sintered at temperatures ≥ 300 °C should be strongly enhanced, as could be expected from the observed dense and large-grained microstructures (Fig. A.3) [143]. As a result, the measured ferroelectric response of the PZT thin film is much improved and becomes comparable to the reference platinum-based stack (Fig. A.4a).

However, higher dielectric losses, higher leakage current and lower breakdown field were observed in the case of inkjet-printed silver electrodes. The PZT film being identical in both cases, it is reasonable to assume that the difference with the sputtered platinum top electrodes is related to the nature of the electrode/film interface. A possible explanation is that the work function of silver (4.3 eV) is smaller than the one of platinum (5.7 eV), resulting in a lower Schottky barrier at the metal/PZT interface. However, a study by Pintilie et al. shows that leakage current cannot be simply correlated with the electrode metal work function in (001)-oriented epitaxial PZT films [140]. In addition, the authors showed that evaporated silver electrodes exhibited lower leakage currents than sputtered platinum electrodes. Nevertheless, it is known that the metal/PZT interface can be strongly processing dependent [144]. Furthermore, the presence of pinholes in our inkjet-printed silver electrodes could also decrease the effective electrode area, while giving rise to high local electric fields at the origin of dielectric breakdown of the PZT film.

A.3.2. Piezoelectric properties

The electromechanical response of a 750 nm-thick PZT film spin-coated on platinized silicon was performed via the four-point bending (4PB) method, which enables the extraction of the effective transverse piezoelectric coefficient $e_{31,f}$. The sample was designed according to the specifications of Prume et al. [145], as described in Appendix D.10 (page 139). $10 \times 2\,\mathrm{mm}^2$ silver top electrodes were printed on the PZT film with a droplet spacing of 70 µm (equivalent to 360 dpi). As in the previous case, reference samples were fabricated with a 100 nm-thick sputtered platinum top electrode.

Fig. A.5 shows the charge measured on the electrodes of the sample subjected to a 10 Hz mechanical bending excitation as function of the induced deformation or strain. A prepolarization pulse of 10 V was applied during 1 s before the measurement. While the reference sample with the Pt top electrode exhibited an $e_{31,f}$ value of $5.1\,\mathrm{C\,m^{-2}}$, the sample with the large-area inkjet-printed silver top electrode still displayed an appreciable response in the same measurement conditions, with $4.1\,\mathrm{C\,m^{-2}}$. The discrepancy could be partly ascribed to the slight porosity of the printed silver electrode. It is noteworthy that the unfavorable leakage characteristics of inkjet-printed electrodes did not prevent the poling of the sample and the measurement a piezoelectric coefficient comparable to the sputtered platinum reference.

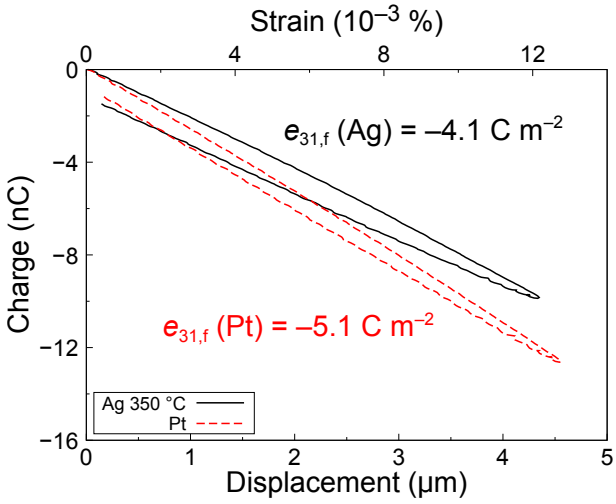

Fig. A.5. Four-point bending characterization of PZT devices with inkjet-printed silver top electrode sintered at 350 °C and sputtered platinum top electrode, measured at 10 Hz.

A.4. Summary

In this study, we investigated inkjet printing of silver top electrodes on CSD-derived PZT thin films deposited on platinized silicon via spin coating. Optimization of the printing and processing parameters was necessary to obtain functional homogeneous top electrodes in a reproducible manner. These conditions were related to the nature of the ink, which required the introduction of a systematic jetting dwell time in the printing sequence for printing each single electrode as well as the use of a sintering temperature of at least 300 °C.

Inkjet-printed silver top electrodes allowed the measurement of polarization–electric field loops for 170 nm-thick PZT films. The obtained values for remanent polarization and coercive field were comparable to the ones measured in the same conditions with sputtered platinum top electrodes, with $P_r \sim 20\,\mu C\,cm^{-2}$ and $E_c \sim 55\,kV\,cm^{-1}$. We could also evaluate the effective transverse piezoelectric coefficient $e_{31,f}$ of a sample with a $20\,mm^2$ silver top electrode printed on a 750 nm-thick PZT film. The value of $4.1\,C\,m^{-2}$ was comparable to the reference sample with a platinum top electrode.

Thanks to this inkjet printing process, the deposition of top electrodes can be performed in a time-efficient manner, without lithography nor the vacuum conditions otherwise required by PVD. It could therefore be a promising alternative to PVD, enabling low-cost characterization of piezoelectric thin films and the fabrication of devices where the piezoelectric layer is not exposed to high electric fields, such as energy harvesters.

Appendix B

P(VDF-TrFE)-based energy harvesters

B.1. Acknowledgements

This part of the work results from a collaboration which I would like to acknowledge at the beginning of this chapter. The P(VDF-TrFE) multilayer devices were fabricated by Antoine Latour (Liten, CEA, France) using polymers provided by Fabrice Domingues Dos Santos (Piezotech, Arkema, France). Antoine Latour also performed the SEM cross section. Mathieu Gérard designed the energy harvesting test bench. Jérôme Polesel helped in the design of the final proof-of-concept device. Sebastjan Glinšek and Lucas Allirol helped perform the characterization of the device. Finally, I would like to acknowledge the contribution of my supervisor Emmanuel Defay, who suggested the idea and took an active part in the theoretical and experimental work presented here. This study was published in *Cell Reports Physical Science* [146].

B.2. Motivation

In Chapter 3, we discussed the fabrication and characterization of silicon-based piezoelectric energy harvesters (EHs) using inkjet-printed PZT thin films as active layers. The energy output of 5.8 µW was promising, as devices with an energy consumption in this range have already been described [121]. However, the output voltage of the PZT-based device remained quite low (below the threshold voltage of a diode). We identified the stiffness of the silicon substrate and the high relative permittivity of PZT as main causes for the low output voltage.

The importance of these two parameters can be highlighted via the derivation of a simplified one-dimensional model [120, 147]. A piezoelectric material subjected to a variation of longitudinal strain from 0 to S can store energy in the form of mechanical elastic energy. Assuming that S is homogeneous all over the volume $\mathcal{V}$ of the material, the mechanical energy density E_m [J m^{-3}] can be expressed by Hooke's law:

$$E_\mathrm{m} = \frac{1}{2}\, c_\mathrm{f}\, S^2, \tag{B.1}$$

where c_f is the effective stiffness of the piezoelectric material in Pa. As the material is piezoelectric, mechanical energy is coupled to electrical work W_e (expressed here per unit volume) via the square of effective electromechanical coupling factor k_f in transverse mode (in-plane deformation, out-of-plane generation of charges):

$$W_\mathrm{e} = k_\mathrm{f}^2 \, E_\mathrm{m} = \frac{e_{31,\mathrm{f}}^2}{c_\mathrm{f} \, \varepsilon} \, E_\mathrm{m} = \frac{e_{31,\mathrm{f}}^2}{2\varepsilon} \, S^2 \tag{B.2}$$

where $e_{31,\mathrm{f}}$ is the effective transverse piezoelectric coefficient in $\mathrm{C\,m^{-2}}$ and ε is permittivity in $\mathrm{F\,m^{-1}}$. If the EH is driven by a sinusoidal mechanical excitation of frequency f [Hz], the output power in W will be given by [147]:

$$P_\mathrm{H} = \frac{e_{31,\mathrm{f}}^2}{2\varepsilon} \, \pi \, f \, S^2 \, \mathcal{V} \tag{B.3}$$

Note that this model is based on the assumption that S is imposed to the piezoelectric material (which is the case when a thin piezoelectric layer is integrated on an elastic substrate). The output power P_H is therefore independent from the stiffness of the piezoelectric material. We also assumed an ideal case where the strain distribution is homogeneous.

Nevertheless, it is obvious from eq. (B.3) that strain should be maximized, while the piezoelectric material should have low permittivity in order to increase the output power. Both of these conditions can be fulfilled by the use of polymers. A polymer sheet used as substrate can undergo significant deformation and induce higher strain in the piezoelectric layer. Poly(vinylidene fluoride) (PVDF) is a piezoelectric and ferroelectric polymer characterized by a relative permittivity in the order of 10, which is two orders of magnitude lower than that of PZT films. Its modest piezoelectric coefficient ($\sim$0.1 $\mathrm{C\,m^{-2}}$) compared to the one of PZT ($\sim$10 $\mathrm{C\,m^{-2}}$) can be compensated by its low permittivity and the high strain that can be applied to it, thus making it a solid competitor for PZT. The added value of PVDF lies in its low processing temperature compared to PZT, which does not exceed 150 °C. This enables simple integration on flexible substrates and implementation into wearable devices.

From eq. (B.3), we also see that power is proportional to the volume of piezoelectric material. In the context of device integration, it is of interest to maximize the power output per unit area. In other words, the footprint of the device should be minimized. Increasing the thickness of the piezoelectric layers is a possibility, but it has a limit as the layers require poling by an external electric field. As the coercive field of PVDF is rather high (0.5–1 $\mathrm{MV\,cm^{-1}}$), the very high voltages are required for poling thick films could result in dielectric breakdown of the material. This issue can be addressed by processing the piezoelectric polymer into multilayers, thereby decreasing the poling voltage by a factor equal to the number of individual layers.

Several works have demonstrated the use of PVDF layers for energy harvesting applications. In 1998, Kymissis et al. integrated PVDF layers in a shoe sole and were able to harvest 1.1 mW at a 1 Hz walking pace, for an active area of 65 $\mathrm{cm^2}$ [148]. A very recent contribution by Yuan et al. reported a rugby ball-shaped device based on 3D-printed P(VDF-TrFE) multilayers that could collect 11 mW for an active area of 1.89 $\mathrm{cm^2}$ [149].

B.3. Piezoelectric polymers

Poly(vinylidene fluoride) (PVDF) is a thermoplastic polymer obtained via the polymerization of the monomer vinylidene fluoride ($F_2C{=}CH_2$). The polymer chain of PVDF therefore consists of repeating $-CF_2-CH_2-$ units. As carbon–fluorine bonds are highly polarized due to the electronegativity difference ($\chi_F - \chi_C = 1.4$), local dipoles exist along the polymer chain and different interactions between these dipoles are possible depending on its conformation. In the *TGTG'* conformation (*T* = *trans* and *G* = *gauche*), the dipoles compensate each other resulting in zero macroscopic polarization. This type of conformation is found in the non-piezoelectric α crystalline phase (Fig. B.1). On the other hand, in the all-trans conformation (*TTTT*), dipole moments point in the same direction and add up as a result. This structure is the one present in the piezoelectric β phase. Note that polar γ and δ have also been identified, but are not as abundant as the main phases we have just described [150].

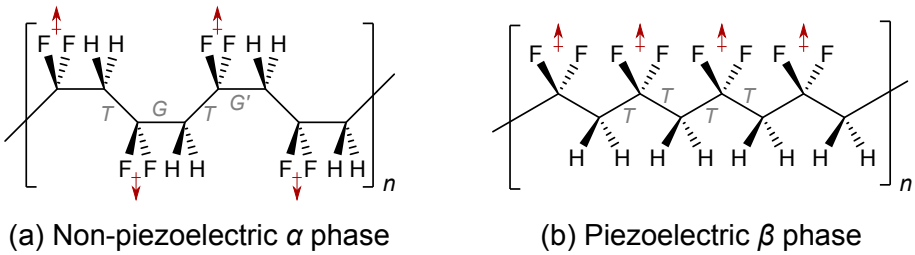

(a) Non-piezoelectric α phase (b) Piezoelectric β phase

Fig. B.1. Conformations of PVDF and associated crystalline phases: (a) *TGTG'* conformation (α phase) and (b) *TTTT* conformation (β phase). Dipole moments are indicated by the arrows (chemist convention).

It follows that the β phase needs to be present and stabilized to obtain a piezoelectric response. This can be performed by mechanical orientation of the polymer chains (stretching of the material) or by incorporating trifluoroethylene (TrFE) as a co-monomer. The typical blend consists of 75 % vinylidene fluoride and 25 % trifluoroethylene. The resulting copolymer is known as poly(vinylidene fluoride-*co*-trifluoroethylene) or P(VDF-TrFE).

B.4. Energy harvester fabrication

The P(VDF-TrFE) copolymer formulation used in this study consisted of 75 % vinylidene fluoride and 25 % trifluoroethylene (supplied by Arkema, France). The P(VDF-TrFE) powder was dissolved in cyclopentanone at a concentration of 15 wt%. The fabrication of the device is entirely based on screen printing (EKRA X5 screen printing apparatus). P(VDF-TrFE) multilayers were screen-printed on a 150 µm-thick poly(ethylene naphthalate) (PEN) sheet, with intercalated screen-printed poly(3,4-ethylenedioxythiophene) poly(styrene sulfonate) (PEDOT:PSS) electrodes (Clevios™ S V4, Heraeus, Germany). The structures of PEDOT:PSS and PEN are shown in Fig. B.2.

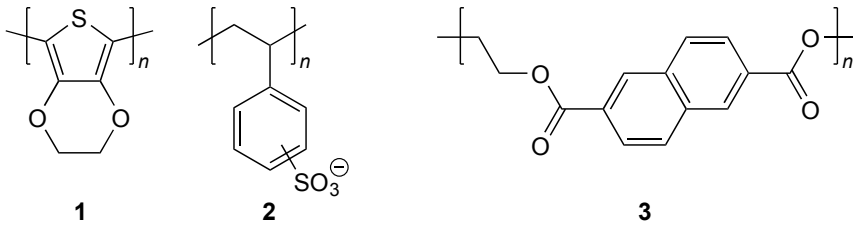

Fig. B.2. Structures of electrode and substrate polymers: poly(3,4-ethylenedioxythiophene) (PEDOT) **1**, poly(styrene sulfonate) (PSS) **2** and poly(ethylene naphthalate) (PEN) **3**. PEDOT:PSS is a mixture between **1** and **2**.

As illustrated in Fig. B.3a, the final multilayer stack consists of a succession of 0.8 µm-thick PEDOT:PSS electrodes intercalated between 2.5 µm-thick P(VDF-TrFE) layers. Every second electrode is electrically connected, resulting in stack of ten round-shaped 1.95 cm-diameter capacitors connected in parallel, as explained in Fig. B.3b.

After the screen printing process, the multilayer was annealed in air at 150 °C for 30 min. The SEM cross section presented in Fig. B.3c shows the succession of layers. As can be seen in Fig. B.3d where three devices are illustrated, silver traces (dark lines) were also printed on PEDOT:PSS to increase the conductivity and protect the contacts. A final 3 µm-thick layer of P(VDF-TrFE) was printed over the multilayer stack to act as a passivation layer.

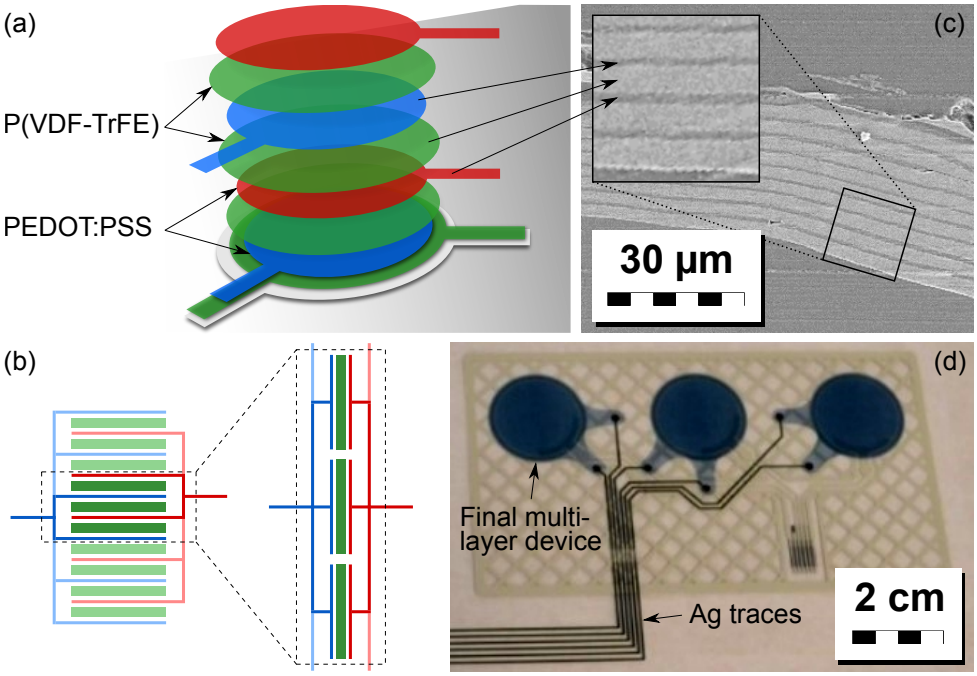

Fig. B.3. Design of P(VDF-TrFE) multilayer energy harvesters: (a) scheme of the multilayer stack, (b) representation of the parallel connection of the piezoelectric elements, (c) SEM cross section and (d) photograph of the final devices.

B.5. Material characterization

The XRD pattern of the P(VDF-TrFE) multilayer shown in Fig. B.4a exhibits clear evidence of β phase (reflection at $2\theta = 20.1°$). The intense signal at $2\theta = 26.8°$ can be ascribed to the PEN substrate. The relative permittivity–electric field characteristic (Fig. B.4b) displays typical ferroelectric behavior with a sudden change at the coercive fields, $E_c^- = -500\,\mathrm{kV\,cm^{-1}}$ and $E_c^+ = 450\,\mathrm{kV\,cm^{-1}}$. Relative permittivity has a value of 7.3 at zero bias and peaks at 9.3 at the coercive fields, in accordance with typical values reported in the literature [151]. The loss tangent follows similar dependency with the electric field, with 0.5 at the coercive fields and 0.13 at high fields.

The polarization–electric field loop shown in Fig. B.4c also exhibits a clear ferroelectric signature. Note that the measurement was carried out at low frequency (0.2 Hz) due to the low conductivity of the PEDOT:PSS electrodes and the slow switching dynamics of P(VDF-TrFE). The values of the coercive fields are in agreement with the ones from the relative permittivity–electric field loop. The remanent polarization is $8\,\mu\mathrm{C\,cm^{-2}}$. The P–E loops displays saturation at high electric fields (pinched shape in upper right and lower left quadrants of the plot).

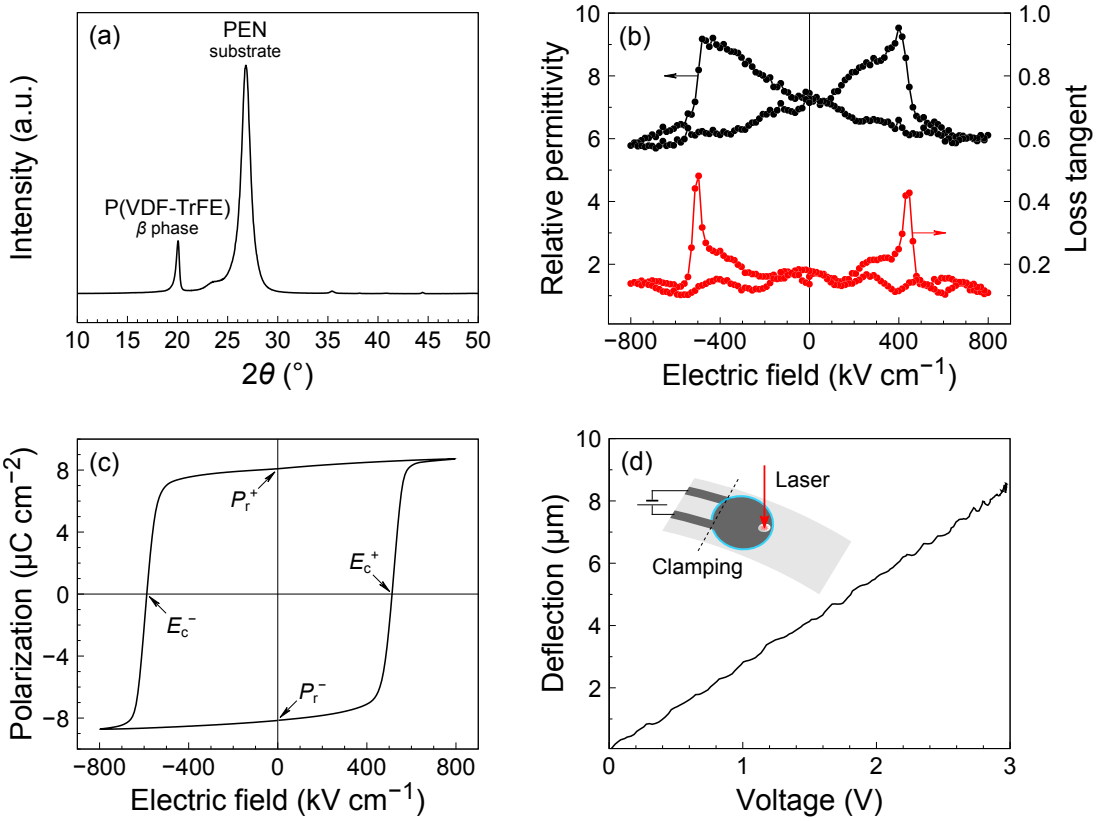

Fig. B.4. Structural, electrical and piezoelectric characterization of P(VDF-TrFE) multilayers: (a) XRD pattern, (b) relative permittivity–electric field loop at 100 Hz and $V_{AC} = 50\,\mathrm{mV}$, (c) polarization–electric field loop at 0.2 Hz and (d) deflection of the beam as function of applied voltage used to evaluate the piezoelectric coefficient.

In order to evaluate the effective transverse piezoelectric coefficient $e_{31,f}$, we measured the deflection of the multilayer P(VDF-TrFE) device under an applied voltage (actuator mode), as illustrated in Fig. B.4d. The value of $e_{31,f}$ was extracted form the displacement d versus voltage V plot thanks to eq. (B.4), adapted from Defay [6],

$$e_{31,f} \simeq \frac{Y_{PEN}\, t_{PEN}^2}{3L^2}\, \frac{d}{V}, \tag{B.4}$$

where Y_{PEN} and t_{PEN} are the Young modulus and the thickness of the PEN substrate, i.e. 5 GPa and 150 µm, respectively. L is the distance between the clamping line and the spot of the interferometer (11.5 mm). Note that the influence of the 30 µm-thick P(VDF-TrFE) multilayer was neglected in this simplified model (the Young modulus of P(VDF-TrFE) is at least three times smaller than the one of PEN). The extracted piezoelectric coefficient $e_{31,f}$ is 0.038 C m^{-2}.

B.6. Energy harvester characterization

B.6.1. Experimental setup

The test bench presented in Chapter 3 (page 69) was used for the characterization of the P(VDF-TrFE)-based EHs. The tested cantilevers were cut out from the PEN sheets with scissors and made stiffer by doubling the thickness of the substrate, i.e. a layer of substrate was glued to the one bearing the active layers using adhesive tape. Two metal nuts (1.3 g each) were used as a proof mass and were attached at the end of the cantilevers to decrease the resonant frequency and increase the amount of harvested energy.

Electrical contacts were established by gluing metallic wires onto the silver traces of the samples using a two-component conductive epoxy adhesive (MG Chemicals 8331). Poling of the multilayer stack was performed by applying a unipolar sine voltage with an amplitude of 300 V at 1 Hz and room temperature. Samples were then mounted on the test bench and were clamped along the active part diameter perpendicular to the length of the cantilever. This was done to maximize the strain in the piezoelectric multilayer. The EH characterization setup is illustrated in Fig. B.5a.

B.6.2. Harvested power

The output voltage of the EH was monitored as function of frequency in the 15–80 Hz range (Fig. B.5b). Resonance of the cantilever occurs at 33.5 Hz and the cantilever beam has a mechanical quality factor of $\frac{f_{res}}{\Delta f} = 4.5$, ($f_{res}$ is the resonant frequency and Δf the full width at half maximum). We then followed the output peak-to-peak voltage V_{pp} as function of load resistance R at the resonant frequency, as shown in Fig. B.5c.

The output power P was evaluated as $P = \frac{V_{pp}^2}{8R}$. It reaches a maximum value of 0.97 mW for a load resistance of 60 kΩ, which corresponds to the capacitance impedance of the multilayer

at 33.5 Hz ($Z_C = \frac{1}{\omega C}$, with $C = 90$ nF). In these conditions, the peak-to-peak voltage V_{pp} and current I_{pp} are 21.6 V and 0.36 mA, respectively. In open circuit conditions ($R \rightarrow \infty$), V_{pp} reaches as high as 34 V. These voltages are significantly higher than the ones measured for PZT-based EHs in Chapter 3 thanks to the lower permittivity of the piezoelectric and the much higher strain applied to the piezoelectric layer. Such output voltage values represent a double advantage: they are high enough for rectification and low enough for a voltage regulator to handle. Indeed, the voltage regulator (LTC3588-1, Linear Technology) used later in the study discards parts of the rectified waveform with an amplitude above 20 V. This point further highlights the importance of multilayers for this EH device. A single 30 µm-thick piezoelectric layer would yield output voltages over 100 V, thus reducing the overall efficiency of the EH–voltage regulator system.

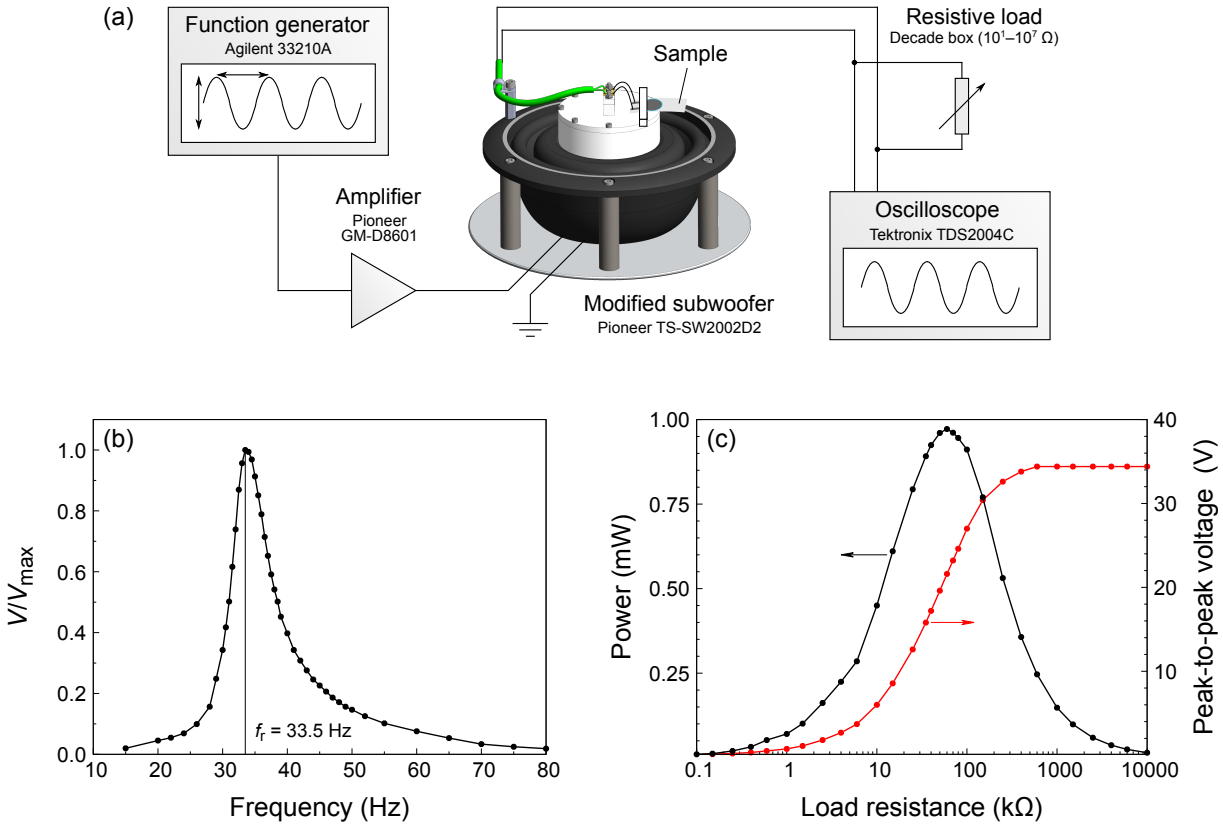

Fig. B.5. Characterization of P(VDF-TrFE)-based energy harvester: (a) vibrating test bench used for the characterization, (b) resonance curve and (c) power versus load resistance curve.

B.6.3. Discussion

Comparison with model

The harvested energy can be compared with the predictions of the model presented earlier (eq. (B.3)). Strain S in the P(VDF-TrFE) layers can be evaluated using eq. (B.5):

$$S(x) = \frac{3d(L-x)\,t_{\mathrm{PEN}}}{2L^3}, \tag{B.5}$$

where x is the coordinate along the beam, d is the deflection of the beam measured via interferometry and L is the total length of the beam. In our experiment, $L = 22\,\mathrm{mm}$, $t_{\mathrm{PEN}} = 310\,\mu\mathrm{m}$ (thickness doubled) and d measured at the tip of the cantilever was 20 mm. Taking into account the length of the electrode with respect to the total length of the cantilever and the fact that 80 % of the multilayer area was used, we can estimate an average S value of 1.44 %.

The acceleration was evaluated by vibrometry, which enables the direct measurement of velocity. Since the mechanical excitation is sinusoidal and velocity v can be expressed as $v(t) = v_0 \sin(\omega t)$, acceleration a is simply $a(t) = \frac{\mathrm{d}v(t)}{\mathrm{d}t} = v_0\omega\cos(\omega t)$. The amplitude of acceleration can therefore be derived from $a_0 = v_0\omega$ and was found to be $57\,\mathrm{m\,s^{-2}}$ or 5.8 g.

Using eq. (B.3) and the values of the parameters found experimentally, the model predicts a value of 1.41 mW. This is 45 % higher than our experimental value (0.97 mW), but still a reasonable estimation of the power that can be harvested with our device. The discrepancy can be ascribed to the assumptions of the model, such as a uniform strain distribution in the cantilever. This analysis further highlights the crucial role of strain in the amount of harvested energy, as flexible polymer layers can withstand higher levels of strain than stiff substrates such as silicon.

Power density

A primordial feature for device integration is the amount of collected power for a given footprint of the energy harvester. We can define this footprint as being the area of the piezoelectric layer. In Table B.1, we have compiled examples of EHs with an output power higher than 100 µW at a frequency lower than 150 Hz. For the sake of comparison, we also report the power density (power per unit area). The majority of the cited examples are based on bulk PZT ceramics, which can achieve power densities as high as $1.56\,\mathrm{mW\,cm^{-2}}$ [152, 153]. The remaining examples feature PZT films on nickel foil [12], AlN films [154] or P(VDF-TrFE)-derived layers [155].

Our energy harvester achieved a power density of $0.405\,\mathrm{mW\,cm^{-2}}$. By assembling two of our devices into a bimorph, we could potentially reach $0.81\,\mathrm{mW\,cm^{-2}}$, i.e. more than half the power density obtained using PZT ceramics. This further illustrates the influence of the volume of piezoelectric material on the harvested power (eq. (B.3)). As thickness stands for the smallest dimension ($t \leq 1\,\mathrm{mm}$ in the provided examples), it can be augmented to increase the active volume of the piezoelectric device without significant impact on its footprint. The correlation

between power density and thickness of the piezoelectric layer (up to thicknesses of 200 µm) is illustrated in the inset of Fig. B.6. In this context, it is of particular interest to use multilayers: the thickness of the active layer can be increased, while the poling process remains simple (use of lower voltage for poling).

Ref.	Year	Material and config.	$T_{process}$ (°C)	f (Hz)	t (µm)	P (mW)	A (cm^2)	P/A ($mW\,cm^{-2}$)
[156]	2012	PZT, ceramic	900	150	200	28	19.6	1.4
[157]	2004	PZT, ceramic	900	120	280	0.375	0.35	1.06
[158]	2016	Bulk PZT on phosphor bronze	900	101	57	0.321	0.55	0.58
[159]	2009	Terfenol-D/PZT bulk composite	900	51	1000	1.055	1.2	0.88
[160]	2010	PZT bulk	900	42	500	2.5	11.8	0.21
[161]	2011	PZT bulk	900	20	1000	1.08	1.7	0.325
[162]	2012	PZT bulk fiber composite on Al	900	28	300	1.43	2.0	0.73
[163]	2015	PZT bulk with with nonlinear circuit	900	90	200	0.385	6.0	0.065
[164]	2016	PZN-PT single crystals	1350	38	400	0.43	0.72	0.60
[165]	2017	PZT bulk bimorph on Be-bronze	900	77	129	0.979	0.48	1.0
[152]	2017	PZT bulk in compression	900	20	1000	15	4.8	1.56
[153]	2017	PZT bulk	900	67	200	2.35	1.5	1.56
[12]	2016	PZT films on Ni foils	650	6	6	0.284	2	0.14
[154]	2011	AlN thin film	400	143	5	0.134	1.3	0.1
[155]	2010	P(VDF-TrFE-CFE) thick layer	150	100	50	0.415	5	0.083
This work [146]	2020	P(VDF-TrFE) multilayer	150	33	30	0.972	2.4	0.405

Table B.1. Comparison of our P(VDF-TrFE) energy harvester with selected works from the literature (power output P higher than 100 µW and frequency f lower than 150 Hz). For the sake of comparison, P was normalized with respect to the active surface area A of the piezoelectric layer.

Processing temperature

In Table B.1, we also reported the maximum processing temperature used for the fabrication of piezoelectric layers. We assumed that unless specified, all the devices based on bulk PZT should require a processing temperature of at least 900 °C [166]. The energy density of the EH devices is represented as function of processing temperature in Fig. B.6. From this representation, it is clear that our device provides an appreciable power output, even when compared with the best bulk PZT-based EHs, with a processing temperature limited to 150 °C. This represents a considerable advantage, as our lead-free device is fully compatible with flexible electronics.

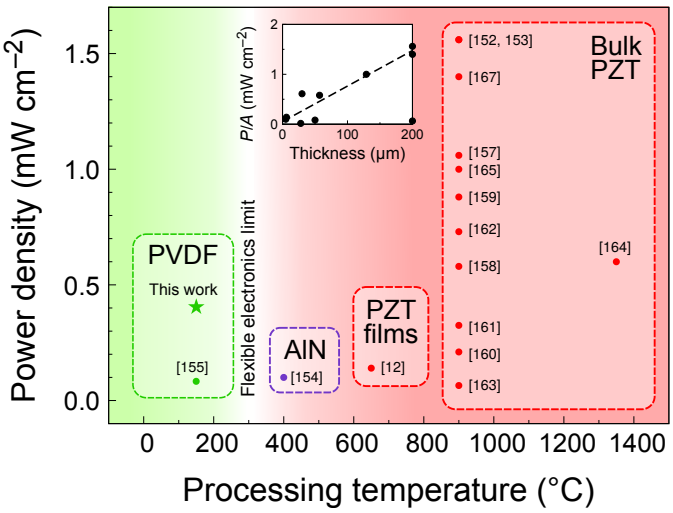

Fig. B.6. Comparison of power density of vibrating energy harvesters based on bulk PZT ceramics, PZT films, AlN films, PVDF foils and P(VDF-TrFE) multilayers (this work). The vertical boundary at 300 °C defines the temperature limit beyond which technology is not compatible with flexible electronics. Inset: power density as function of the piezoelectric layer thickness.

B.7. Development of a proof-of-concept device

To conclude this study, we developed a proof-of-concept device consisting of the P(VDF-TrFE)-based energy harvester described earlier and an Arduino-based temperature sensor, as illustrated in Fig. B.7. Two EHs were assembled together back-to-back with adhesive tape and were wired in parallel. The resulting energy harvesting device was mounted on the test bench. In this case the resonant frequency was 36 Hz and the acceleration was kept at $\sim 2\ g$ in order to prevent premature aging of the polymer layers. The AC output of the EH was directly fed into a voltage rectifier and regulator (LTC3588-1, Linear Technology). In the first phase of the experiment, the DC output of the voltage regulator was used to charge a 0.4 F supercapacitor (CAP-XX HA230). This was done by continuous shaking of the device during 5 h, until the voltage at the terminals of the supercapacitor reached 3.3 V.

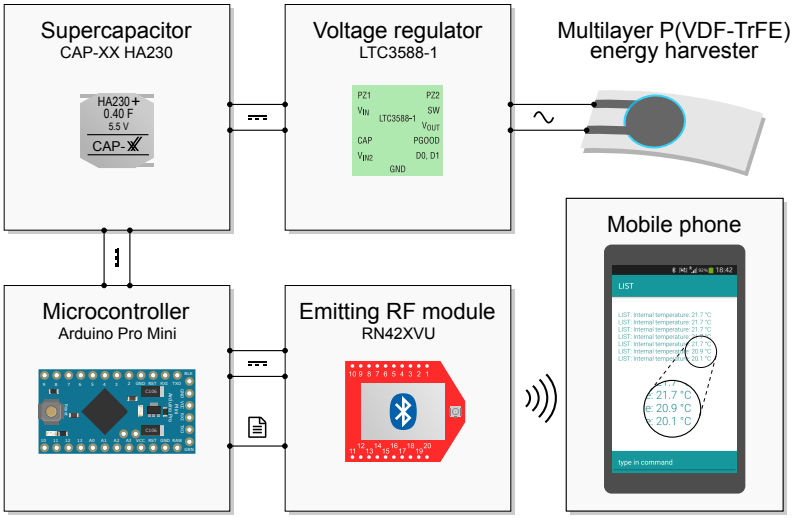

Fig. B.7. Block diagram description of a proof-of-concept device powered by a P(VDF-TrFE)-based energy harvester. The AC output of the EH is rectified and used to charge a supercapacitor. The energy stored in the supercapacitor is then used to power a microcontroller equipped with a temperature sensor. The recorded temperature values are transmitted to a mobile phone via a Bluetooth emitter.

In the second phase of the experiment, the supercapacitor was used to power an Arduino Pro Mini microcontroller connected to a radio frequency emitter (RN-42 Bluetooth module, Microchip). The microcontroller has an integrated temperature sensor, whose reading was transmitted via Bluetooth to a mobile phone for approximately 10 s. Through this experiment, we show that it is possible to use the electrical energy harvested by a P(VDF-TrFE)-based device to power a sensor and transmit data via a wireless protocol to a receiver device.

Over the course of 5 h, the EH collected approximately 2.2 J of electrical energy. This corresponds to a continuous power output of 120 µW. This is significantly lower than the value of 0.97 mW reported earlier due to (1) the much lower strain applied in this case in order to prevent aging and (2) the losses due to the voltage regulator. The microcontroller module could be powered for 10 s during the discharge of the supercapacitor, at which point the voltage at the supercapacitor terminals dropped to 2 V, causing the microcontroller to turn off. The amount of energy consumed is approximately 1.4 J, meaning that the sensor had a power consumption in the order of 140 mW during data transmission. Note that exist optimized transmitting devices with a simpler architecture and design than an Arduino microcontroller. Their power consumption is therefore significantly lower.

B.8. Summary

In this study, we demonstrated the potential of screen-printed P(VDF-TrFE) multilayers for energy harvesting. A device consisting of ten 3 µm-thick P(VDF-TrFE) layers separated by PEDOT:PSS electrodes was fabricated on a flexible PEN sheet as a substrate. The piezoelectric elements of the stack were connected in parallel, which simplified the poling process. Under a 5.8 *g* mechanical excitation at a frequency of 33.5 Hz, the device had an output of 0.97 mW of electrical power, for an active area of 2.4 cm^2.

This represents a rather high power density, even when compared to similar devices based on bulk PZT ceramics. However, the processing of P(VDF-TrFE) is lead-free and only requires temperatures up to 150 °C. It is therefore readily compatible for integration with flexible electronics. Furthermore, the compliant nature of polymers allows the application of large strain levels in the piezoelectric layers. Their active volume was increased with no impact on the device footprint thanks to the multilayer structure. Strain and active volume were shown to be critical parameters influencing the power output, with quadratic and linear contributions, respectively.

Although the high power output of 0.97 mW could only be sustained for a limited period due to material fatigue and mechanical deterioration, we showed that useful amounts of energy could be harvested over the course of several hours under moderate conditions of mechanical excitation. Thanks to two devices connected in parallel, we were able to harvest 120 µW of continuous power for 5 h in order to charge a supercapacitor. The collected energy was then used to power a microcontroller-based sensor that successfully transmitted temperature data to a mobile phone through a wireless protocol.

The fabrication of the P(VDF-TrFE)-based devices presented in this section is low-cost, involves low temperatures and can be deployed for large-scale production. Piezoelectric polymers are therefore promising candidates for high-power-density energy harvesting applications, such as human body-related autonomous sensors.

Appendix C

Haptic devices

C.1. Acknowledgements

The work presented in this part results from a collaboration with co-workers and external partners. It is only shown here for illustrative purposes, as an addition to Chapter 3. The inkjet-printed piezoelectric layers featured in this example of application were developed in the framework of this PhD thesis. I would like to acknowledge Aymen Mahjoub and Stéphanie Girod for performing most of the experimental work presented in this section (processing and characterization). The design of the haptic device was developed by the company Hap2U (France). Emmanuel Defay and Sebastjan Glinšek managed the project.

C.2. Haptic technology

User experience has now become a major selling point for consumer electronics. In particular, mobile devices such as smartphones and tablets interact with the user via tactile screens. Haptic technology has the potential to 'bring life' to these otherwise inert surfaces by recreating the sensation of touch at the surface of the screen. Combining visual and tactile sensory inputs can therefore make the user experience richer. Textures can be rendered by a solid surface such as the glass plate of a screen by inducing a stationary acoustic wave in it. This type of acoustic wave is known as a Lamb wave [168]. The induction of the Lamb wave in the plate can be achieved via piezoelectric actuators placed at specific locations along its surface corresponding to anti-nodes of the stationary vibration mode. The frequency of this vibration mode should be in the ultrasonic range (>20 kHz) in order to be inaudible. Furthermore, the amplitude of the displacement has to be greater than one micron and the wavelength of the acoustic wave in the order of one centimeter. Under these conditions, the vibration of the surface can be sensed by dragging a finger across it, as the air pressure locally increases between the epidermal ridges of the fingertip and the surface (Fig. C.1). Different textures can be simulated by modulating the frequency and amplitude of the vibration.

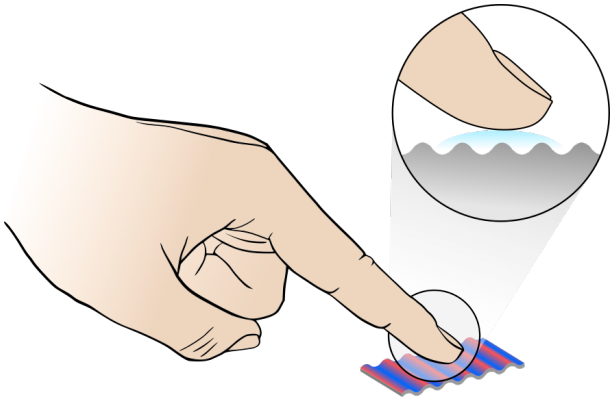

Fig. C.1. Illustration of the haptic force feedback principle.

C.3. Design and fabrication of a haptic device

The haptic device is a $47 \times 17\,\mathrm{mm}^2$ fused silica plate with four piezoelectric actuators at its surface. The actuators are located at the anti-nodes of the Lamb wave and consist of a micron-thick PZT film on top of which interdigitated electrodes (IDE) are deposited. These IDEs consist of comb-like structures whose fingers are separated by a 10 µm gap. A schematic description of the device is shown in Fig. C.2.

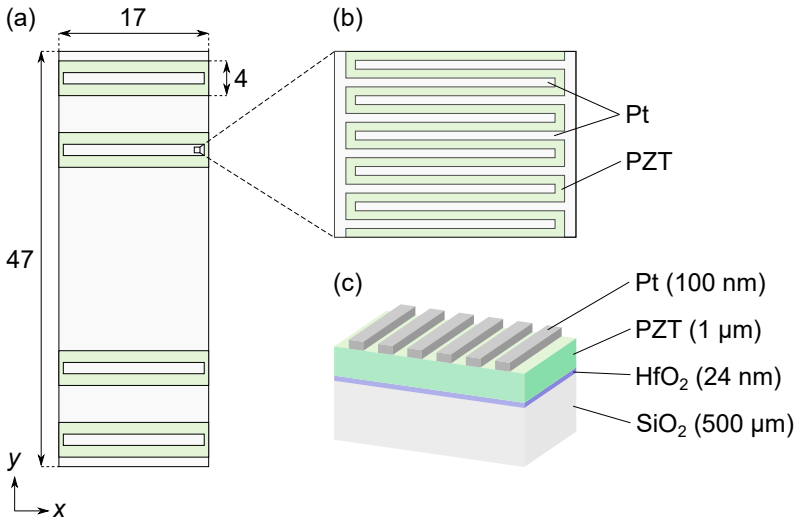

Fig. C.2. Design of the haptic device based on inkjet-printed PZT films: (a) top view of the device (all dimensions are given in mm), (b) close-up view of the IDE structure (proportions are not respected) and (c) cross section of the piezoelectric actuator stack.

For the fabrication of the device, a two-inch fused silica wafer was used as substrate. A buffer layer of HfO_2 (24 nm) was deposited by atomic layer deposition (ALD). PZT stripes were then printed on the substrate according to the design shown in Fig. C.2a and the printing strategy described in Chapter 2 (please refer to page 55). After every printing step, the films were dried at 175 °C for 1 min and pyrolyzed at 450 °C for 3 min. Crystallization at 700 °C for 5 min was

performed after the deposition of 12 layers. This process was carried out four more times to afford micron-thick PZT layers.

Sputtered platinum IDEs were patterned on the printed PZT films via lift-off photolithography. After protection with photoresist, the sample was cut according to the design dimensions using a wire saw. The final device was passivated with a layer of resist to prevent electrical arcing between the fingers. Electrical connections were established via metal wires glued on IDE pads with a two-component conductive epoxy adhesive.

C.4. Characterization of the haptic device

Observation of the PZT film cross section by SEM (Fig. C.3a) reveals the presence of porosity in the 1.1 µm-thick layer. The amount of porosity appears to be greater than in the case of the film printed on platinized silicon (see Fig. 3.5a, page 70). A possible explanation could be the difference in thermal conductivity between the two substrates: the thermal conductivity of silicon is a hundred times greater than that of fused silica. This in turn can have an impact on the completion of the pyrolysis process. As can be anticipated from the microstructure, the XRD pattern of the PZT film (Fig. C.3b) indicates random orientation of the printed layer.

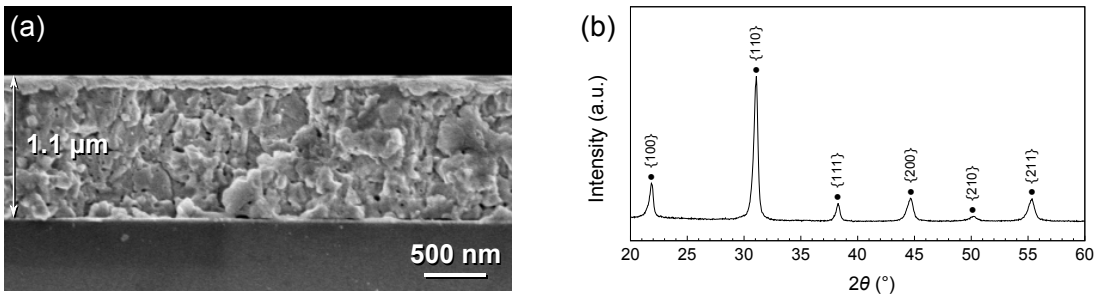

Fig. C.3. (a) SEM cross section and (b) XRD pattern of PZT inkjet-printed on fused silica for the fabrication of a haptic device.

Electrical properties of the inkjet-printed PZT film on fused silica were measured in the IDE configuration. The polarization–electric field loop (Fig. C.4a) displays properties comparable with the ones of CSD-derived PZT films, with $P_r \sim 17\,\mu C\,cm^{-2}$ and $E_c \sim 40\,kV\,cm^{-1}$. The relative permittivity–bias voltage loop (Fig. C.4b) shows a typical ferroelectric behavior with a value of ε_r close to 950 at zero bias. Note that the relationship between the electric field E and the voltage V in the case of interdigitated electrodes is given by eq. (C.1), where a is the IDE gap width and Δa a correction term depending on film thickness t_f, $\Delta a \approx 1.324\ t_f$ [169].

$$E = \frac{V}{a + \Delta a} \tag{C.1}$$

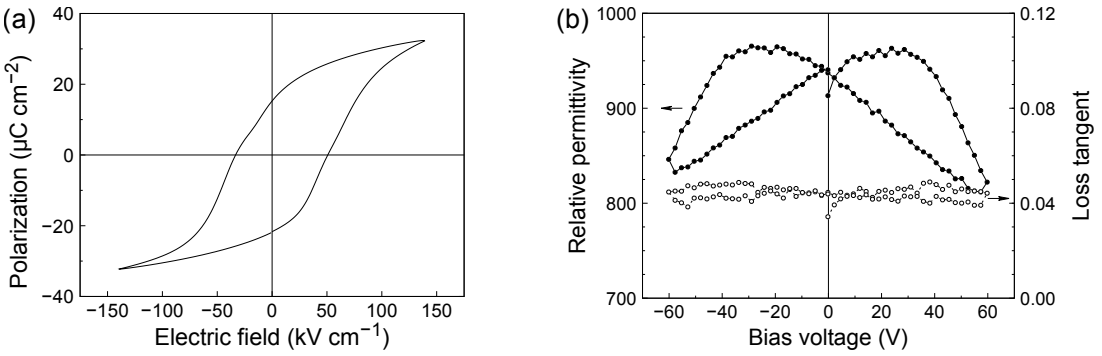

Fig. C.4. Electrical characterization of haptic device based on inkjet-printed PZT films: (a) polarization–electric field loop (100 Hz) and (b) relative permittivity–bias voltage loop (1 kHz).

Finally, the acoustic properties of the devices were investigated. A sinusoidal electrical excitation was applied to the piezoelectric actuators and the displacement of the plate was measured using a laser Doppler vibrometer. For a given amplitude of the driving signal (50 V_{pp}), the displacement was measured at an anti-node and a frequency scan was performed across the ultrasonic range (20–100 kHz). As seen in Fig. C.5a, the main resonance of the plate occurs at 80 kHz. The vibrometer sample stage is motorized and allows for 1D and 2D scans of the device. A line scan in the *y* direction was performed for different driving voltages, as shown in Fig. C.5b. A Lamb wave was successfully induced in the plate and the amplitude of the displacement at the anti-nodes increases almost linearly as the driving voltage is raised from 50 to 150 V_{pp}. To complete the analysis, a 2D map of the device under a 100 V_{pp} driving signal was performed. The map presented in Fig. C.5c reveals the pattern of the Lamb wave. A displacement amplitude of one micron was measured at the anti-nodes, which corresponds to the target value. A final test was performed by dragging a fingertip across the device surface: it was indeed possible to feel the vibration of the plate.

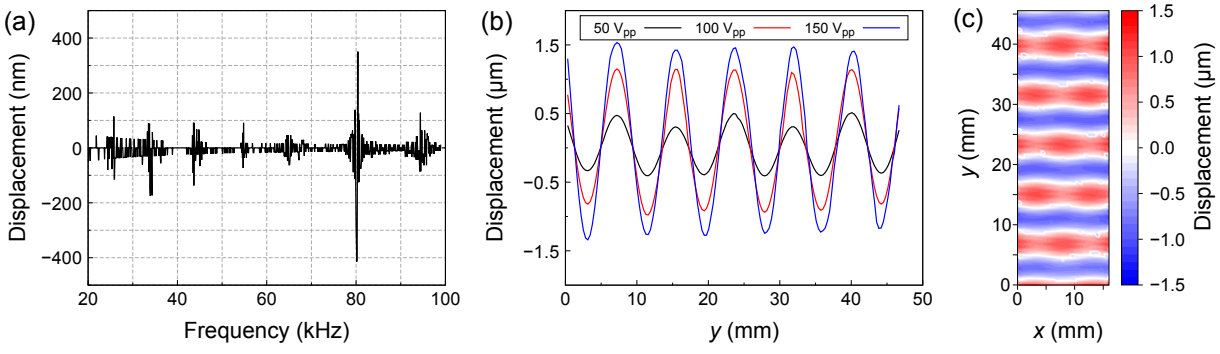

Fig. C.5. Acoustic characterization of haptic device based on inkjet-printed PZT films: (a) resonance curve and (b) displacement in the *y* direction as function of driving voltage. (c) 2D mapping of the Lamb wave induced in the glass plate.

Appendix D

Processing and characterization techniques

D.1. Lift-off photolithography

In this work, the patterning of platinum top electrodes on PZT films was performed by lift-off photolithography. An overview of the process is shown in Fig. D.1. After thermal dehydration of the sample, two layers of photoresist are successively spin coated onto the sample: (1) a resist based on polydimethylglutarimide (LOR3A, MicroChem™) and (2) a cresol formaldehyde resin (S1813, Microposit™). After exposure of the resist using a direct laser exposure aligner (MLA 150, Heidelberg Instruments), the development is performed using a tetramethylammonium hydroxide-based developer (MF-319, Microposit™). This process creates an undercut in the resist layers. Platinum is then deposited by sputtering. The lift-off step is performed using a resist remover based on *N*-methyl-2-pyrrolidone (Remover PG, MicroChem™) in which the sample is immersed. The sample is finally rinsed with solvents and dried under nitrogen.

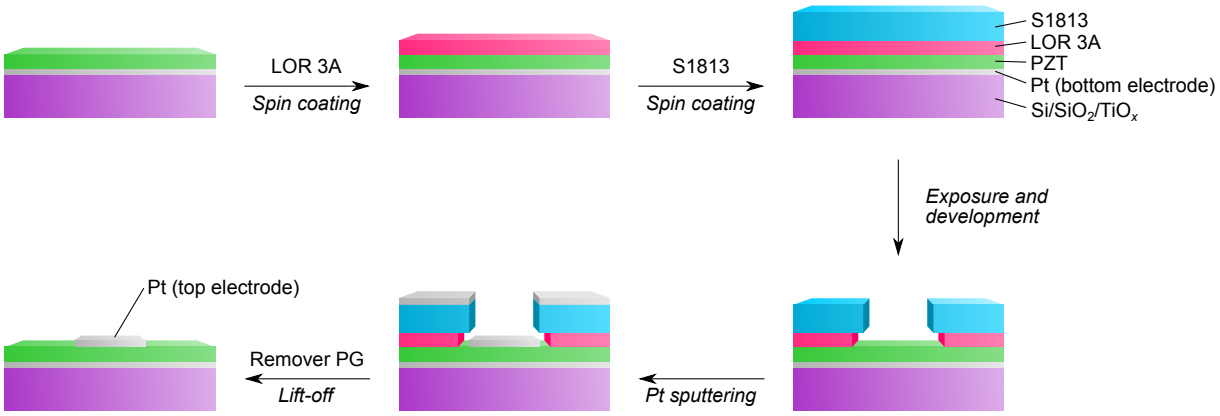

Fig. D.1. Overview of the lift-off photolithography process for patterning platinum top electrodes.

D.2. Freeze drying

Freeze drying is a technique for the dehydration of samples at low temperatures and is particularly useful for the dehydration of temperature-sensitive compounds. It is based on the fact that below the triple point of water ($T < 0\,°C$ and $p < 6.12\,mbar$) ice sublimates, i.e. it transitions directly from the solid to the gas state.

In order to freeze dry a solid sample (e.g. a hydrated salt such as lead(II) acetate trihydrate), the sample is first frozen inside a flask. A small amount of water is typically added to help freeze the compound and spread it on the walls of the flask to increase its surface area. The sample is then put under reduced pressure by connecting the flask to the freeze dryer manifold, causing ice in the sample to sublimate. The generated water vapor is condensed back into ice on a plate condenser, whose temperature is lower than that of the sample.

D.3. Fourier transform infra-red (FTIR) spectroscopy

Fourier transform infra-red (FTIR) spectroscopy is a vibrational spectroscopy technique used for chemical characterization. Structural information can be extracted from the position and intensity of absorption bands, which can be used to identify functional groups. In FTIR the final spectrum is obtained by performing a Fourier transform of the raw acquisition data.

Several geometries can be used for the measurement. In attenuated total reflectance (ATR), the sample (liquid or solid) is deposited onto a crystal through which an infra-red beam is passed at an angle such that total internal reflection occurs. The beam interacts with the sample at the interface with the crystal via evanescent waves. The exiting beam is then analyzed and processed into a spectrum. Thin films on a metallic substrate can be analyzed using a grazing angle objective (GAO), where the infra-red light is directed onto the sample at an angle. The optical path is such that the beam interacts twice with the sample, which increases the signal intensity. This setup is coupled with an optical microscope that enables localized analysis on a sample.

D.4. Secondary ion mass spectrometry (SIMS)

Secondary ion mass spectrometry (SIMS) is a surface chemical characterization technique where a primary ion beam is used to sputter the sample surface. The generated secondary ions are collected and analyzed by a mass spectrometer, which allows their identification based on their mass/charge ratio. It is therefore a destructive characterization technique. SIMS can be used to perform chemical imaging a the sample surface (see page 39) or depth profiling (see page 91).

D.5. Scanning electron microscopy (SEM)

Electron microscopy allows the observation of features that cannot be resolved by optical microscopy due to the use of visible light. In virtue of the wave-particle duality, electrons possess wave-like properties. Their associated wavelength is shorter than that of visible light, allowing for much higher resolutions. In a scanning electron microscope, electrons are accelerated down a column and focused onto the sample. Several types of interactions can take place between the incident electrons and the sample such as the emission of secondary electrons, back-scattered electrons, Auger electrons and X-rays, all of which can be detected. The detection of secondary electrons is used to recreate a magnified topographical image of the sample.

D.6. Thermogravimetric analysis (TGA)

Thermogravimetric analysis consists in measuring the mass of a sample as function of temperature, thereby providing information about the physical or chemical changes the sample undergoes with temperature. This information can be coupled with differential thermal analysis (DTA), where the temperature of the holder containing the analyzed sample is compared with the temperature of a reference holder during the thermal analysis. Temperature variations can be linked with exothermic or endothermic processes taking place in the sample.

D.7. X-ray diffraction (XRD)

X-ray diffraction is an analysis technique for crystalline materials. Electronic densities of the atoms constituting the crystal lattice can diffract an incident X-ray beam in various directions, which correspond to conditions where constructive interference occurs. These conditions are expressed by Bragg's law eq. (D.1),

$$2d \sin\theta = n\lambda, \tag{D.1}$$

where d is the interplanar spacing, θ is the incident angle, n is an integer and λ is the wavelength of the incident X-ray radiation. Diffractometers typically use copper K_α radiation ($\lambda = 1.54$ Å). Configurations where the condition for constructive interference is met results in peaks in a plot of intensity of X-rays as function of the deviation angle 2θ. The intensity of these peaks depends on the chemical composition at the crystal planes.

Two common setup configurations for XRD measurements are illustrated in Fig. D.2. In the θ-2θ configuration, the X-ray tube and the detector move at the same rate, thereby only probing crystal planes that are parallel to the sample surface. In the grazing incidence setup, the position of the X-ray source is fixed at a small angle ($\omega \sim 1°$) and only the detector moves. Due to its particular geometry, this configuration is particularly sensitive to the sample surface.

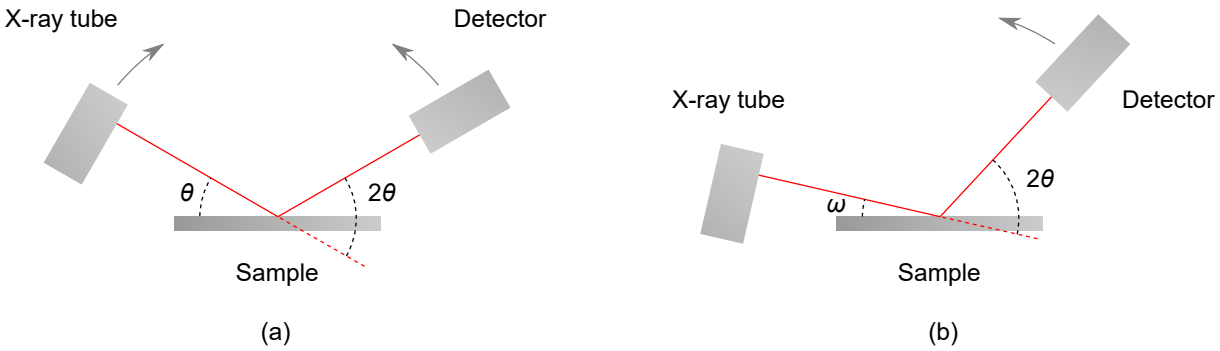

Fig. D.2. Setup configurations for X-ray diffraction: (a) θ-2θ configuration and (b) grazing angle configuration.

D.8. X-ray reflectivity (XRR)

X-ray reflectivity is a technique used for the characterization of the density, thickness and roughness of thin films by analyzing X-rays reflected from the surface as function of the incidence angle. XRR operates at shallow angles, which are close to the critical angle of total reflection θ_c. The position of θ_c corresponds to a significant intensity drop of the reflected X-rays in a plot of log(intensity) as function of 2θ and can be used to determine the density ρ of the material using eq. (D.2):

$$\rho = \theta_c^2 \frac{\pi}{r_e \lambda^2 N_A} \frac{\sum_i x_i}{\sum_i x_i \frac{f_i}{M_i}} \tag{D.2}$$

where r_e is the classical electron radius (2.818×10^{-5} Å), λ the X-ray wavelength, N_A the Avogadro constant (6.626×10^{23} mol^{-1}), x_i the stoichiometric coefficients, M_i the molar masses of the elements and f_i the real part of the atomic scattering factors [170].

D.9. Electrical characterization

Electrical characterization is performed to assess the ferroelectric properties of thin-film ceramic piezoelectrics such as PZT, namely the response of polarization and relative permittivity as function of the applied electric field. For thin films grown on platinized silicon, metal electrodes are deposited on top the film, thus forming a metal–insulator–metal (MIM) structure. This parallel plate capacitor can be electrically contacted through the top and bottom electrodes for characterization of the ferroelectric thin film, which can be performed using a measurement station as the aixACCT TF Analyzer 2000 used in this work. Here, we present the basic principle of these measurements.

D.9.1. Polarization–electric field

The polarization–electric field (P–E) loop is obtained by applying a bipolar voltage waveform with frequency f (here triangle, Fig. D.3a) to the sample and measuring the current $i(t)$ (Fig. D.3b). In an ideal ferroelectric, this current corresponds to the switching current, i.e. the movement of charges due to the switching of the polarization. Since $i(t) = \frac{\mathrm{d}Q(t)}{\mathrm{d}t}$, the charge Q can be obtained by integration of the current. The polarization P can be then be calculated by dividing this charge by the surface area A of the capacitor (eq. (D.3)).

$$P(t) = \frac{Q(t)}{A} = \frac{1}{A}\int i(t)\mathrm{d}t \tag{D.3}$$

The hysteresis loop is then simply constructed by representing P as a function of the electric field E. Note that this measurement does not provide an absolute measure of polarization. The P–E loop is therefore represented such that $P^{+}_{\mathrm{max}} = \left|P^{-}_{\mathrm{max}}\right| = P_{\mathrm{max}}$, as shown in Fig. D.3c.

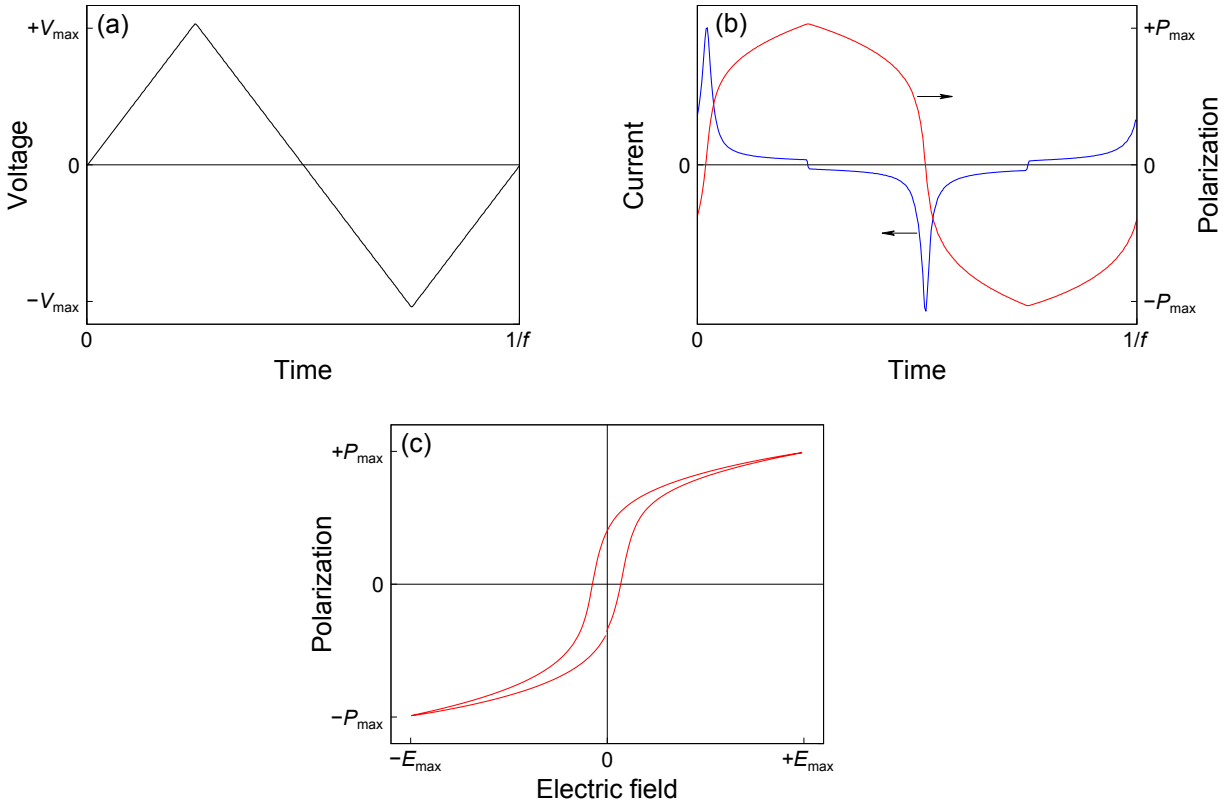

Fig. D.3. Measurement principle of polarization–electric field loops: (a) a bipolar triangle waveform applied to the sample and (b) current is measured as function of time (blue curve). Polarization is obtained using eq. (D.3) (red curve) and (c) represented as function of electric field.

D.9.2. Relative permittivity–electric field

The measurement of the relative permittivity–electric field loop is done by measuring the capacitance of the MIM structure as function of a DC bias electric field on which a low-amplitude AC excitation is superimposed. This electrical excitation applied to the sample is represented in Fig. D.4a.

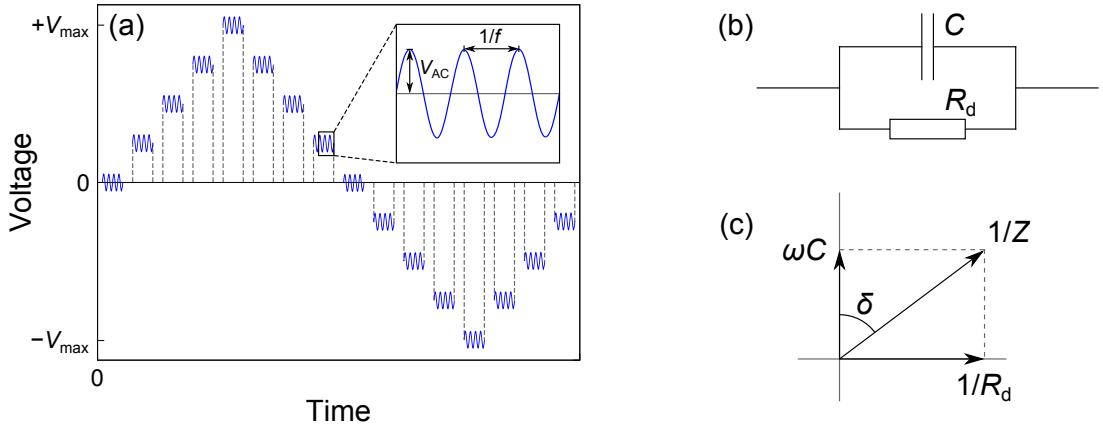

Fig. D.4. Measurement principle of relative permittivity–electric field loops. (a) Electrical signal applied to the sample. The small signal has an amplitude V_{AC} and a frequency f. It is superimposed to a staircase DC bias voltage. (b) Modelling of a real capacitor by an RC parallel circuit and (c) representation of the components inverse impedance in the complex plane.

In AC regime, a real ferroelectric capacitor can be modelled as an RC parallel circuit, where the resistance R_d represents the losses (Fig. D.4b). Note that in this model, we assume that the conduction current is negligible, i.e. there are no free charges flowing through the capacitor. Relative permittivity ε_r can be expressed as a complex quantity, where the real part ε' corresponds to the electrical energy stored in the material and the imaginary part ε'' to the energy dissipated by the dielectric losses, as described by eq. (D.4) (j is the imaginary unit).

$$\varepsilon_r = \varepsilon' - j\varepsilon'' \tag{D.4}$$

The inverse of the equivalent impedance of the RC circuit is given by $\frac{1}{Z} = \frac{1}{R_d} + j\omega C$. Dielectric losses are usually expressed by the loss tangent, $\tan\delta$, which corresponds to:

$$\tan\delta = \frac{\varepsilon''}{\varepsilon'} = \frac{1}{\omega C R_d} \,. \tag{D.5}$$

The angle δ is the angle between the vectors associated to $\frac{1}{Z}$ and $j\omega C$ in the complex plane (Fig. D.4c). Its value decreases as the resistive contribution $\frac{1}{R_d}$ of the dielectric losses decreases. Since the capacitance C of a capacitor can be defined as the variation of charge with respect to the voltage applied across it $\left(\frac{\partial Q}{\partial V}\right)$, measuring the capacitance gives access to the relative permittivity of the material via the expression of capacitance for a parallel plate capacitor:

$$\varepsilon_r \cong \frac{Cd}{\varepsilon_0 A} \,, \tag{D.6}$$

where d is the thickness of the film and A the capacitor area.

D.10. Piezoelectric characterization

The piezoelectric properties of thin films on a substrate can be evaluated by several methods. We present here the techniques used in this work to evaluate effective piezoelectric coefficients, namely $e_{31,f}$ and $d_{33,f}$. As for electrical measurements, piezoelectric characterization can be performed using equipment from aixACCT Systems.

D.10.1. Direct measurement

The so-called *direct* measurement is based on the direct piezoelectric effect and uses the four-point bending (4PB) method. A sample with precise geometric features first needs to be fabricated, as shown in Fig. D.5a.[a] The sample is then mounted on the measuring stage and pressed between four metallic rods: two from the bottom of the sample and two from the top, which also make electrical contact with the electrodes. A mechanical excitation is applied to the sample via actuation of the metallic rods, causing the sample to bend (Fig. D.5b). The charge Q on the electrodes and the displacement at the center of the sample u are measured during bending. If the mechanical properties of the substrate are known, it is possible to extract the piezoelectric coefficient thanks to eq. (D.7),

$$e_{31,f} \simeq \frac{l^2}{4\,A\,t_{sub}\,(1-\nu_{sub})}\frac{Q}{u}\,, \tag{D.7}$$

where l is the distance between the bottom rods, A is the electrode surface area, t_{sub} and ν_{sub} are the substrate thickness and Poisson's ratio, respectively [145]. The relationship between the displacement (or strain in the substrate) and the measured charge should be linear. Note that the measurement can be carried out with prior prepolarization of the sample or with a bias voltage to observe the dependence of $e_{31,f}$ with the electric field.

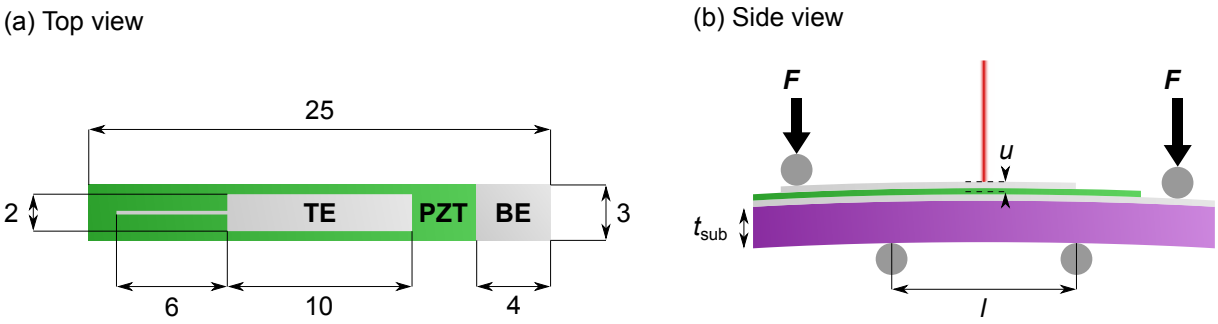

Fig. D.5. Principle of the 4PB technique. (a) Description of the sample for testing. TE and BE stand for top and bottom electrodes, respectively. All dimensions are given in mm. (b) Representation of the sample under test: the sample is bent, while its displacement and charge on the electrodes are measured.

[a] In our case the samples were cut using a wire saw. Note that for spin-coated layers which cover the whole sample area, etching of the piezoelectric film is required for access to the platinum bottom electrode. An etching solution for PZT can be prepared by adding 5 mL of concentrated HCl (37 %) and a couple drops of concentrated HF (40 %) to 30 mL of deionized water. The etching solution can be applied on the PZT film using a swab.

D.10.2. Converse measurement

The $e_{31,f}$ coefficient can also be evaluated via the converse piezoelectric effect. The sample described in Fig. D.5a can be clamped at its extremity. The cantilever beam is then actuated by an electrical signal applied across its electrodes and its deflection u is measured by laser interferometry. If the deflection is measured at the extremity of the electrode, i.e. at a distance d from the clamping point, the $e_{31,f}$ coefficient can be evaluated by eq. (D.8):

$$e_{31,f} \simeq -\frac{1}{3}\frac{Y_{sub}}{(1-\nu_{sub})\,c_f}\left[c_f + (1-c_f)\,(1-\nu_{sub})\right]\frac{t_{sub}^2}{d^2}\frac{u}{V}\,, \tag{D.8}$$

where Y_{sub}, ν_{sub} and t_{sub} are the Young modulus, Poisson's ratio and thickness of the substrate, respectively. The parameter c_f is the coverage factor and corresponds to the ratio between the electrode width and the substrate width [126, 171].

The converse measurement can be associated with the electrical characterization techniques described earlier. The electrical signal used to measure polarization hysteresis loops (Fig. D.3a) gives the large-signal displacement curve of the cantilever. The staircase waveform shown in Fig. D.4a can be used to derive the electric field dependence of the small-signal $e_{31,f}$ coefficient.

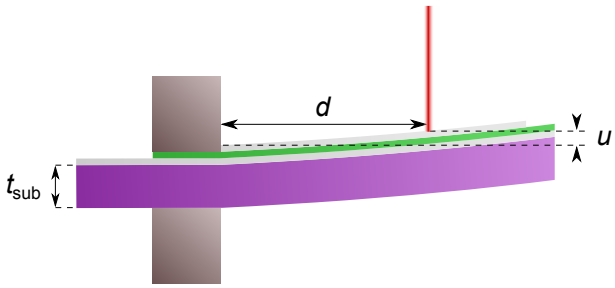

Fig. D.6. Principle of piezoelectric characterization in converse mode: an electrical signal is applied across the electrodes and the displacement of the clamped cantilever is measured by laser interferometry.

D.10.3. Double beam laser interferometry

Double beam laser interferometry (DBLI) can be used to measure the out-of-plane piezoelectric coefficient ($d_{33,f}$) of a piezoelectric film on a wafer in MIM configuration. This represents a challenge for the measurement as wafer bending occurs, which introduces large measuring errors. Wafer bending effects can be suppressed by gluing the wafer onto a rigid surface or by using a dual interferometric setup, which performs a differential measurement of the displacement and can achieve resolutions < 1 pm [172]. Still, thickness expansion or compression of the substrate can hamper the derivation of meaningful $d_{33,f}$ values, which vary with electrode size. Sivaramakrishnan et al. showed that the ratio between the electrode size and substrate thickness should be close to unity for the extraction of reliable $d_{33,f}$ values [104].

D.11. Laser Doppler vibrometry

Laser Doppler vibrometry is a non-contact technique that can be used to measure the vibrations of a surface. A laser beam is directed onto the surface and the reflected beam is analyzed. The motion of the surface causes a Doppler shift, which is used to extract the vibration amplitude and frequency. Coupling the vibrometer with a positioning stage can be used for two-dimensional mapping of the vibrations at the surface.

List of figures

List of tables

Bibliography

[1] S. Magdassi, *The Chemistry of Inkjet Inks*, World Scientific Publishing, Singapore, **2009**.

[2] A guide to industrial inkjet, Xaar, **2018**, https://www.xaar.com/en/resource-centre/xaar-guide-to-industrial-inkjet.

[3] C. Li, Inkjet printing for AMOLED technology & market report 2019, IHS Markit, **2019**.

[4] Toray Research Group, *Printing Technology for Flexible Substrates*, InterLingua Publishing, Redondo Beach (CA), **2006**.

[5] S. Katzir, 'The discovery of the piezoelectric effect' in *The Beginnings of Piezoelectricity*, Springer Netherlands, Dordrecht, **2006**, pp. 15–64.

[6] E. Defay, *Integration of Ferroelectric and Piezoelectric Thin Films*, John Wiley & Sons, Inc., Hoboken (NJ), **2011**.

[7] Z. L. Wang, J. Song, 'Piezoelectric nanogenerators based on zinc oxide nanowire arrays', *Science* **2006**, *312*, 242–246.

[8] S. Fichtner, N. Wolff, F. Lofink, L. Kienle, B. Wagner, 'AlScN: A III-V semiconductor based ferroelectric', *Journal of Applied Physics* **2019**, *125*, 114103.

[9] B. Jaffe, W. R. Cook, H. Jaffe, 'Solid solutions of $Pb(Ti, Zr, Sn, Hf)O_3$' in *Piezoelectric Ceramics*, Academic Press, London, **1971**, pp. 135–183.

[10] B. Jaffe, R. S. Roth, S. Marzullo, 'Piezoelectric properties of lead zirconate-lead titanate solid-solution ceramics', *Journal of Applied Physics* **1954**, *25*, 809–810.

[11] P. Muralt, 'Recent progress in materials issues for piezoelectric MEMS', *Journal of the American Ceramic Society* **2008**, *91*, 1385–1396.

[12] H. G. Yeo, X. Ma, C. Rahn, S. Trolier-McKinstry, 'Efficient piezoelectric energy harvesters utilizing (001) textured bimorph PZT films on flexible metal foils', *Advanced Functional Materials* **2016**, *26*, 5940–5946.

[13] D. Sette, S. Glinšek, S. Girod, N. Godard, E. Defay in 2017 Joint Conference of the European Frequency and Time Forum and IEEE International Frequency Control Symposium (EFTF/IFCS), IEEE, **2017**, pp. 514–515.

[14] J. Schwarzkopf, R. Fornari, 'Epitaxial growth of ferroelectric oxide films', *Progress in Crystal Growth and Characterization of Materials* **2006**, *52*, 159–212.

[15] J. S. Horwitz, K. S. Grabowski, D. B. Chrisey, R. E. Leuchtner, 'In situ deposition of epitaxial $PbZr_xTi_{1-x}O_3$ thin films by pulsed laser deposition', *Applied Physics Letters* **1991**, *59*, 1565–1567.

[16] M. D. Nguyen et al., 'Misfit strain dependence of ferroelectric and piezoelectric properties of clamped (001) epitaxial $Pb(Zr_{0.52}, Ti_{0.48})O_3$ thin films', *Applied Physics Letters* **2011**, *99*, 252904.

[17] M. D. Nguyen et al., 'Effect of dopants on ferroelectric and piezoelectric properties of lead zirconate titanate thin films on Si substrates', *Ceramics International* **2014**, *40*, 1013–1018.

[18] M. Jambunathan et al. in Proceedings of ISAF-ECAPD-PFM 2012, IEEE, **2012**.

[19] E. Defay, B. Semmache, C. Dubois, M. Leberre, D. Barbier, 'Compositional gradient in and mechanical stability of RF-sputtered and RTA annealed $Pb(Zr, Ti)O_3$ thin films', *Sensors and Actuators A: Physical* **1999**, *74*, 77–80.

[20] R. H. Wilke et al., 'Sputter deposition of PZT piezoelectric films on thin glass substrates for adjustable X-ray optics', *Applied Optics* **2013**, *52*, 3412–3419.

[21] H. G. Yeo et al., 'Strongly (001) oriented bimorph PZT film on metal foils grown by rf-sputtering for wrist-worn piezoelectric energy harvesters', *Advanced Functional Materials* **2018**, *28*, 1801327.

[22] H. Jacobsen, K. Prume, B. Wagner, K. Ortner, T. Jung, 'High-rate sputtering of thick PZT thin films for MEMS', *Journal of Electroceramics* **2010**, *25*, 198–202.

[23] M. Okada, K. Tominaga, T. Araki, S. Katayama, Y. Sakashita, 'Metalorganic chemical vapor deposition of *c*-axis oriented PZT thin films', *Japanese Journal of Applied Physics* **1990**, *29*, 718–722.

[24] E. H. Kim, C. W. Moon, J. G. Lee, M. S. Lah, S. M. Koo, 'Synthesis and characterization of lead(IV) precursors and their conversion to PZT materials through a CVD process', *Polyhedron* **2020**, *177*, 114270.

[25] I. Bretos, R. Jiménez, J. Ricote, M. L. Calzada, 'Low-temperature crystallization of solution-derived metal oxide thin films assisted by chemical processes', *Chemical Society Reviews* **2018**, *47*, 291–308.

[26] H. Kozuka, S. Takenaka, H. Tokita, M. Okubayashi, 'PVP-assisted sol-gel deposition of single layer ferroelectric thin films over submicron or micron in thickness', *Journal of the European Ceramic Society* **2004**, *24*, 1585–1588.

[27] R. W. Schwartz, T. Schneller, R. Waser, 'Chemical solution deposition of electronic oxide films', *Comptes Rendus Chimie* **2004**, *7*, 433–461.

[28] G. L. Brennecka, J. F. Ihlefeld, J.-P. Maria, B. A. Tuttle, P. G. Clem, 'Processing technologies for high-permittivity thin films in capacitor applications', *Journal of the American Ceramic Society* **2010**, *93*, 3935–3954.

[29] N. Bassiri-Gharb, Y. Bastani, A. Bernal, 'Chemical solution growth of ferroelectric oxide thin films and nanostructures', *Chemical Society Reviews* **2014**, *43*, 2125–2140.

[30] K. D. Budd, S. Y. Dey, D. A. Payne, 'Sol-gel processing of $PbTiO_3$, $PbZrO_3$, PZT, and PLZT thin films', *British Ceramic Society Proceedings* **1985**, *36*, 107–121.

[31] S. Sengupta, L. Ma, D. Adler, D. Payne, 'Extended X-ray absorption fine structure determination of local structure in sol-gel-derived lead titanate, lead zirconate, and lead zirconate titanate', *Journal of Materials Research* **1995**, *10*, 1345–1348.

[32] I. Arčon, B. Malič, M. Kosec, A. Kodre, 'Study of the lead environment in liquid and as-dried precursors of PZ, PT and PZT thin films', *Journal of Sol-Gel Science and Technology* **1998**, *13*, 861–864.

[33] J. Fukushima, K. Kodaira, T. Matsushita, 'Preparation of ferroelectric PZT films by thermal decomposition of organometallic compounds', *Journal of Materials Science* **1984**, *19*, 595–598.

[34] R. W. Vest, W. Zhu, 'Films of 60/40 PZT by the MOD process for memory applications', *Ferroelectrics* **1991**, *119*, 61–75.

[35] G. Yi, Z. Wu, M. Sayer, 'Preparation of $Pb(Zr, Ti)O_3$ thin films by sol gel processing: Electrical, optical, and electro-optic properties', *Journal of Applied Physics* **1988**, *64*, 2717–2724.

[36] R. A. Assink, R. W. Schwartz, 'Proton and carbon-13 NMR investigations of lead zirconate titanate ($Pb(Zr, Ti)O_3$) thin-film precursor solutions', *Chemistry of Materials* **1993**, *5*, 511–517.

[37] N. Ledermann et al., '100-Textured, piezoelectric $Pb(Zr_x, Ti_{1-x})O_3$ thin films for MEMS: integration, deposition and properties', *Sensors and Actuators A: Physical* **2003**, *105*, 162–170.

[38] S. Trolier-McKinstry, P. Muralt, 'Thin film piezoelectrics for MEMS', *Journal of Electroceramics* **2004**, *12*, 7–17.

[39] K. Nittala et al., 'Phase and texture evolution in solution deposited lead zirconate titanate thin films: formation and role of the Pt_3Pb intermetallic phase', *Journal of Applied Physics* **2013**, *113*, 244101.

[40] Y. Bastani, N. Bassiri-Gharb, 'Enhanced dielectric and piezoelectric response in PZT superlattice-like films by leveraging spontaneous Zr/Ti gradient formation', *Acta Materialia* **2012**, *60*, 1346–1352.

[41] F. Calame, P. Muralt, 'Growth and properties of gradient free sol-gel lead zirconate titanate thin films', *Applied Physics Letters* **2007**, *90*, 062907.

[42] B. Malič, H. Suzuki, 'Low-temperature processing of solution-derived ferroelectric thin films', *Journal of the Ceramic Society of Japan* **2014**, *122*, 1–8.

[43] C. K. Kwok, S. B. Desu, 'Low temperature perovskite formation of lead zirconate titanate thin films by a seeding process', *Journal of Materials Research* **1993**, *8*, 339–344.

[44] A. Wu, P. M. Vilarinho, I. Reaney, I. M. Miranda Salvado, 'Early stages of crystallization of sol-gel-derived lead zirconate titanate thin films', *Chemistry of Materials* **2003**, *15*, 1147–1155.

[45] M. Kosec, B. Malič, M. Mandeljc, 'Chemical solution deposition of PZT thin films for microelectronics', *Materials Science in Semiconductor Processing* **2002**, *5*, 97–103.

[46] M. Mandeljc, B. Malič, M. Kosec, G. Dražič, 'Crystallization of zirconium-rich PLZT thin films below 500 °C', *Integrated Ferroelectrics* **2002**, *46*, 329–338.

[47] T. Miyazaki et al., 'Low-temperature crystallization of CSD-derived PZT thin film with laser annealing', *Materials Science and Engineering: B* **2010**, *173*, 89–93.

[48] A. Bhaskar, H. Y. Chang, T. H. Chang, S. Y. Cheng, 'Effect of microwave annealing temperatures on lead zirconate titanate thin films', *Nanotechnology* **2007**, *18*, 395704.

[49] I. Bretos et al., 'Activated solutions enabling low-temperature processing of functional ferroelectric oxides for flexible electronics', *Advanced Materials* **2014**, *26*, 1405–1409.

[50] C. T. Shelton, B. J. Gibbons, 'Epitaxial $Pb(Zr, Ti)O_3$ thin films on flexible substrates', *Journal of the American Ceramic Society* **2011**, *94*, 3223–3226.

[51] G. Cummins, M. P. Desmulliez, 'Inkjet printing of conductive materials: a review', *Circuit World* **2012**, *38*, 193–213.

[52] B.-J. de Gans, P. C. Duineveld, U. S. Schubert, 'Inkjet printing of polymers: state of the art and future developments', *Advanced Materials* **2004**, *16*, 203–213.

[53] A. Matavž, B. Malič, 'Inkjet printing of functional oxide nanostructures from solution-based inks', *Journal of Sol-Gel Science and Technology* **2018**, *87*.

[54] M. Singh, H. M. Haverinen, P. Dhagat, G. E. Jabbour, 'Inkjet printing – Process and its applications', *Advanced Materials* **2010**, *22*, 673–685.

[55] B. Derby, 'Inkjet printing of functional and structural materials: fluid property requirements, feature stability, and resolution', *Annual Review of Materials Research* **2010**, *40*, 395–414.

[56] B. E. Rapp, 'Fluids' in *Microfluidics: Modelling, Mechanics and Mathematics*, Elsevier, Oxford, **2017**, pp. 243–263.

[57] J. E. Fromm, 'Numerical calculation of the fluid dynamics of drop-on-demand jets', *IBM Journal of Research and Development* **1984**, *28*, 322–333.

[58] N. Reis, B. Derby, 'Ink jet deposition of ceramic suspensions: modeling and experiments of droplet formation', *Material Research Society Symposium Proceedings* **2000**, *625*, 117–122.

[59] D. Jang, D. Kim, J. Moon, 'Influence of fluid physical properties on ink-jet printability', *Langmuir* **2009**, *25*, 2629–2635.

[60] P. C. Duineveld et al. in Proceedings SPIE 4464, Organic Light-Emitting Materials and Devices V, **2002**, pp. 59–67.

[61] R. Bhola, S. Chandra, 'Parameters controlling solidification of molten wax droplets falling on a solid surface', *Journal of Materials Science* **1999**, *34*, 4883–4894.

[62] R. Rioboo, M. Marengo, C. Tropea, 'Time evolution of liquid drop impact onto solid, dry surfaces', *Experiments in Fluids* **2002**, *33*, 112–124.

[63] D. Soltman, V. Subramanian, 'Inkjet-printed line morphologies and temperature control of the coffee ring effect', *Langmuir* **2008**, *24*, 2224–2231.

[64] P. C. Duineveld, 'The stability of ink-jet printed lines of liquid with zero receding contact angle on a homogeneous substrate', *Journal of Fluid Mechanics* **2003**, *477*, 175–200.

[65] S. H. Davis, 'Moving contact lines and rivulet instabilities. Part 1. The static rivulet', *Journal of Fluid Mechanics* **1980**, *98*, 225–242.

[66] S. Schiaffino, A. A. Sonin, 'Formation and stability of liquid and molten beads on a solid surface', *Journal of Fluid Mechanics* **1997**, *343*, 95–110.

[67] H. Sirringhaus et al., 'High-resolution inkjet printing of all-polymer transistor circuits', *Science* **2000**, *290*, 2123–2126.

[68] C. W. Sele, T. von Werne, R. H. Friend, H. Sirringhaus, 'Lithography-free, self-aligned inkjet printing with sub-hundred-nanometer resolution', *Advanced Materials* **2005**, *17*, 997–1001.

[69] R. D. Deegan et al., 'Capillary flow as the cause of ring stains from dried liquid drops', *Nature* **1997**, *389*, 827–829.

[70] Y. Zhang, S. Yang, L. Chen, J. R. G. Evans, 'Shape changes during the drying of droplets of suspensions', *Langmuir* **2008**, *24*, 3752–3758.

[71] A. Matavž, R. C. Frunza, A. Drnovšek, V. Bobnar, B. Malič, 'Inkjet printing of uniform dielectric oxide structures from sol–gel inks by adjusting the solvent composition', *Journal of Materials Chemistry C* **2016**, *4*, 5634–5641.

[72] E. Sowade et al., 'Roll-to-roll infrared (IR) drying and sintering of an inkjet-printed silver nanoparticle ink within 1 second', *Journal of Materials Chemistry C* **2015**, *3*, 11815–11826.

[73] D. Angmo, T. T. Larsen-Olsen, M. Jørgensen, R. R. Søndergaard, F. C. Krebs, 'Roll-to-roll inkjet printing and photonic sintering of electrodes for ITO free polymer solar cell modules and facile product integration', *Advanced Energy Materials* **2013**, *3*, 172–175.

[74] N. B. Cho, T. H. Lim, Y. M. Jeon, M. S. Gong, 'Inkjet printing of polymeric resistance humidity sensor using UV-curable electrolyte inks', *Macromolecular Research* **2008**, *16*, 149–154.

[75] J. Windle, B. Derby, 'Ink jet printing of PZT aqueous ceramic suspensions', *Journal of Materials Science Letters* **1999**, *18*, 87–90.

[76] T. Wang, B. Derby, 'Ink-jet printing and sintering of PZT', *Journal of the American Ceramic Society* **2005**, *88*, 2053–2058.

[77] D. Kuscer, O. Noshchenko, H. Uršič, B. Malič, 'Piezoelectric properties of ink-jet-printed lead zirconate titanate thick films confirmed by piezoresponse force microscopy', *Journal of the American Ceramic Society* **2013**, *96*, 2714–2717.

[78] T. Bakarič, B. Malič, D. Kuscer, 'Lead-zirconate-titanate-based thick-film structures prepared by piezoelectric inkjet printing of aqueous suspensions', *Journal of the European Ceramic Society* **2016**, *36*, 4031–4037.

[79] S. P. Bathurst, Master thesis, Massachusetts Institute of Technology, **2008**.

[80] S. P. Bathurst, PhD thesis, Massachusetts Institute of Technology, **2012**.

[81] S. P. Bathurst, H. W. Lee, S. G. Kim in 2008 IEEE 21st International Conference on Micro Electro Mechanical Systems, IEEE, **2008**, pp. 391–394.

[82] H. J. Lee, S. Bathurst, H. Lee, S. G. Kim, 'Templated inkjet printing for MEMS', *Microsystems Technology Laboratories Annual Research Report* **2009**, 15.

[83] S. P. Bathurst, S. G. Kim, 'Designing direct printing process for improved piezoelectric micro-devices', *CIRP Annals – Manufacturing Technology* **2009**, *58*, 193–196.

[84] S. P. Bathurst, S. G. Kim, 'Printing of uniform PZT thin films for MEMS applications', *CIRP Annals – Manufacturing Technology* **2013**, *62*, 227–230.

[85] K. Ueda, Y. Akiyama, O. Machida, A. Shimofuku, T. Kihira, US 8,690,297 B2, **2011**.

[86] O. Machida et al., 'Fabrication of lead zirconate titanate films by inkjet printing', *Japanese Journal of Applied Physics* **2012**, *51*, 09LA11.

[87] O. Machida, A. Takeuchi, D. Jang, R. Tashiro, US 8,888,253 B2, **2014**.

[88] A. Matavž, V. Bobnar, B. Malič, 'Tailoring ink-substrate interactions via thin polymeric layers for high-resolution printing', *Langmuir* **2017**, *33*, 11893–11900.

[89] A. Matavž et al., 'Additive manufacturing of ferroelectric-oxide thin-film multilayer devices', *ACS Applied Materials & Interfaces* **2019**, *11*, 45155–45160.

[90] L. Vitos, A. Ruban, H. Skriver, J. Kollár, 'The surface energy of metals', *Surface Science* **1998**, *411*, 186–202.

[91] K. W. Bewig, W. A. Zisman, 'The wetting of gold and platinum by water', *The Journal of Physical Chemistry* **1965**, *69*, 4238–4242.

[92] J. C. Love, L. A. Estroff, J. K. Kriebel, R. G. Nuzzo, G. M. Whitesides, 'Self-assembled monolayers of thiolates on metals as a form of nanotechnology', *Chemical Reviews* **2005**, *105*, 1103–1170.

[93] Z. Li, S.-C. Chang, R. S. Williams, 'Self-assembly of alkanethiol molecules onto platinum and platinum oxide surfaces', *Langmuir* **2003**, *19*, 6744–6749.

[94] N. Godard, S. Glinšek, A. Matavž, V. Bobnar, E. Defay, 'Direct patterning of piezoelectric thin films by inkjet printing', *Advanced Materials Technologies* **2019**, *4*, 1800168.

[95] D. R. Lide, *CRC Handbook of Chemistry and Physics (89th edition)*, CRC Press, Boca Raton (FL), **2008**.

[96] I. Rianasari, L. Walder, M. Burchardt, I. Zawisza, G. Wittstock, 'Inkjet-printed thiol self-assembled monolayer structures on gold: quality control and microarray electrode fabrication', *Langmuir* **2008**, *24*, 9110–9117.

[97] J. D. Berry, M. J. Neeson, R. R. Dagastine, D. Y. Chan, R. F. Tabor, 'Measurement of surface and interfacial tension using pendant drop tensiometry', *Journal of Colloid and Interface Science* **2015**, *454*, 226–237.

[98] J. Pérez de la Cruz, E. Joanni, P. M. Vilarinho, A. L. Kholkin, 'Thickness effect on the dielectric, ferroelectric, and piezoelectric properties of ferroelectric lead zirconate titanate thin films', *Journal of Applied Physics* **2010**, *108*, 114106.

[99] F. Chen et al., 'Barrier heights, polarization switching, and electrical fatigue in Pb(Zr, Ti)O_3 ceramics with different electrodes', *Journal of Applied Physics* **2010**, *108*, 104106.

[100] J. Rho et al., '$PbZr_xTi_{1-x}O_3$ ferroelectric thin-film capacitors for flexible nonvolatile memory applications', *IEEE Electron Device Letters* **2010**, *31*, 1017–1019.

[101] J. Pérez, P. M. Vilarinho, A. L. Kholkin, J. M. Herrero, C. Zaldo, 'Effect of processing conditions on the piezoelectric properties of sol-gel derived Pb(Zr, Ti)O_3 films for micromechanical applications', *Journal of Materials Research* **2005**, *20*, 1428–1435.

[102] Z. Zuo et al., 'Preparation and ferroelectric properties of freestanding Pb(Zr, Ti)O_3 thin membranes', *Journal of Physics D: Applied Physics* **2012**, *45*.

[103] M. T. Ghoneim et al., 'Thin PZT-based ferroelectric capacitors on flexible silicon for nonvolatile memory applications', *Advanced Electronic Materials* **2015**, *1*, 1–10.

[104] S. Sivaramakrishnan et al., 'Electrode size dependence of piezoelectric response of lead zirconate titanate thin films measured by double beam laser interferometry', *Applied Physics Letters* **2013**, *103*, 132904.

[105] S. Sivaramakrishnan, P. Mardilovich, T. Schmitz-Kempen, S. Tiedke, 'Concurrent wafer-level measurement of longitudinal and transverse effective piezoelectric coefficients ($d_{33,f}$ and $e_{31,f}$) by double beam laser interferometry', *Journal of Applied Physics* **2018**, *123*, 014103.

[106] A. Pimpin, W. Srituravanich, 'Reviews on micro- and nanolithography techniques and their applications', *Engineering Journal* **2012**, *16*, 37–55.

[107] C. Wohlfarth, 'Viscosity of 2-methoxyethanol' in *Landolt-Börnstein – Group IV Physical Chemistry*, Springer Materials, Berlin, Heidelberg, **2008**, pp. 179–181.

[108] N. Godard et al., 'On the importance of pyrolysis for inkjet-printed oxide piezoelectric thin films', *Journal of Materials Chemistry C* **2020**, *8*, 3740–3747.

[109] B. Dou, V. Dupont, P. T. Williams, H. Chen, Y. Ding, 'Thermogravimetric kinetics of crude glycerol', *Bioresource Technology* **2009**, *100*, 2613–2620.

[110] R. M. Silverstein, F. X. Webster, D. J. Kiemle, D. L. Bryce, *Spectrometric Identification of Organic Compounds*, 8th ed., John Wiley & Sons, Inc., Hoboken, NJ, **2014**.

[111] Y. Wang, J. J. Santiago-Avilés, 'Synthesis of lead zirconate titanate nanofibres and the Fourier-transform infrared characterization of their metallo-organic decomposition process', *Nanotechnology* **2004**, *15*, 32–36.

[112] B. L. Henke, E. M. Gullikson, J. C. Davis, 'X-ray interactions: photoabsorption, scattering, transmission and reflection at E = 50–30,000 eV, Z = 1–92', *Atomic Data and Nuclear Data Tables* **1993**, *54*, 181–342.

[113] Lawrence Berkeley National Laboratory, The atomic scattering factor files, **2020**, http://henke.lbl.gov/optical_constants/asf.html.

[114] S.-Y. Chen, I.-W. Chen, 'Texture development, microstructure evolution, and crystallization of chemically derived PZT thin films', *Journal of the American Ceramic Society* **2005**, *81*, 97–105.

[115] V. Stancu, M. Lisca, I. Boerasu, L. Pintilie, M. Kosec, 'Effects of porosity on ferroelectric properties of $Pb(Zr_{0.2}Ti_{0.8})O_3$ films', *Thin Solid Films* **2007**, *515*, 6557–6561.

[116] Y. Zhang et al., 'Understanding the effect of porosity on the polarisation-field response of ferroelectric materials', *Acta Materialia* **2018**, *154*, 100–112.

[117] H.-B. Fang et al., 'Fabrication and performance of MEMS-based piezoelectric power generator for vibration energy harvesting', *Microelectronics Journal* **2006**, *37*, 1280–1284.

[118] K. Morimoto, I. Kanno, K. Wasa, H. Kotera, 'High-efficiency piezoelectric energy harvesters of *c*-axis-oriented epitaxial PZT films transferred onto stainless steel cantilevers', *Sensors and Actuators A: Physical* **2010**, *163*, 428–432.

[119] T. M. Borman et al., 'Effect of lead content on the performance of niobium-doped {100} textured lead zirconate titanate films', *Journal of the American Ceramic Society* **2017**, *100*, 3558–3567.

[120] S.-G. Kim, S. Priya, I. Kanno, 'Piezoelectric MEMS for energy harvesting', *MRS Bulletin* **2012**, *37*, 1039–1050.

[121] L. Wong et al., 'A very low-power CMOS mixed-signal IC for implantable pacemaker applications', *IEEE Journal of Solid-State Circuits* **2004**, *39*, 2446–2456.

[122] W. Weaver Jr., S. P. Timoshenko, D. H. Young, *Vibration Problems in Engineering*, 5th ed., Wiley, Hoboken, NJ, **1990**.

[123] D. H. Litwhiler, 'A custom vibration test fixture using a subwoofer', *Proceedings of the 2011 IAJC-ASEE International Conference* **2011**.

[124] F. Xu, R. A. Wolf, T. Yoshimura, S. Trolier-McKinstry in Proceedings. 11th International Symposium on Electrets, IEEE, **2002**, pp. 386–396.

[125] R. Xu, S.-G. Kim, 'Figures of merits of piezoelectric materials in energy harvesters', *PowerMEMS* **2012**, 464–467.

[126] I. Kanno, H. Kotera, K. Wasa, 'Measurement of transverse piezoelectric properties of PZT thin films', *Sensors and Actuators A: Physical* **2003**, *107*, 68–74.

[127] J. Rödel et al., 'Perspective on the development of lead-free piezoceramics', *Journal of the American Ceramic Society* **2009**, *92*, 1153–1177.

[128] E. Cross, 'Lead-free at last', *Nuclear Medicine Communications* **2011**, *32*, 666–668.

[129] Institut National de Recherche et de Sécurité (INRS), 2-Méthoxyéthanol (fiche toxicologique n°103), **2014**, http://www.inrs.fr/publications/bdd/fichetox/fiche.html?refINRS=FICHETOX_103.

[130] S. C. Sumner, D. B. Stedman, D. O. Clarke, F. Welsch, T. R. Fennell, 'Characterization of urinary metabolites from [1,2,methoxy-^{13}C]-2-methoxyethanol in mice using ^{13}C nuclear magnetic resonance spectroscopy', *Chemical Research in Toxicology* **1992**, *5*, 553–560.

[131] Institut National de Recherche et de Sécurité (INRS), 2-Éthoxyéthanol (fiche toxicologique n°58), **2014**, http://www.inrs.fr/publications/bdd/fichetox/fiche.html?refINRS=FICHETOX_58.

[132] Institut National de Recherche et de Sécurité (INRS), 1-Méthoxy-2-propanol et son acétate (fiche toxicologique n°221), **2010**, http://www.inrs.fr/publications/bdd/fichetox/fiche.html?refINRS=FICHETOX_221.

[133] D. B. G. Williams, M. Lawton, 'Drying of organic solvents: quantitative evaluation of the efficiency of several desiccants', *Journal of Organic Chemistry* **2010**, *75*, 8351–8354.

[134] A. G. Emslie, F. T. Bonner, L. G. Peck, 'Flow of a viscous liquid on a rotating disk', *Journal of Applied Physics* **1958**, *29*, 858–862.

[135] T. W. Dekleva, J. M. Hayes, L. E. Cross, G. L. Geoffroy, 'Sol-gel processing of lead titanate in 2-methoxyethanol: investigations into the nature of the prehydrolyzed solutions', *Journal of the American Ceramic Society* **1988**, *71*, 280–282.

[136] P. Muralt, 'Texture control and seeded nucleation of nanosize structures of ferroelectric thin films', *Journal of Applied Physics* **2006**, *100*, 051605.

[137] S.-Y. Chen, 'Texture evolution and electrical properties of oriented PZT thin films', *Materials Chemistry and Physics* **1996**, *45*, 159–162.

[138] A. Matavž, J. Kovač, M. Cekada, B. Malič, V. Bobnar, 'Enhanced electrical response in ferroelectric thin film capacitors with inkjet-printed $LaNiO_3$ electrodes', *Applied Physics Letters* **2018**, *113*, 012904.

[139] H. N. Al-Shareef, K. R. Bellur, A. I. Kingon, O. Auciello, 'Influence of platinum interlayers on the electrical properties of RuO_2/$Pb(Zr_{0.53}Ti_{0.47})O_3$/$RuO_2$ capacitor heterostructures', *Applied Physics Letters* **1995**, *66*, 239–241.

[140] L. Pintilie, I. Vrejoiu, D. Hesse, M. Alexe, 'The influence of the top-contact metal on the ferroelectric properties of epitaxial ferroelectric $Pb(Zr_{0.2}Ti_{0.8})O_3$ thin films', *Journal of Applied Physics* **2008**, *104*, 114101.

[141] D. P. Vijay, S. B. Desu, 'Electrodes for $PbZr_xTi_{1-x}O_3$ ferroelectric thin films', *Journal of The Electrochemical Society* **1993**, *140*, 2640–2645.

[142] N. Godard, S. Glinšek, E. Defay, 'Inkjet-printed silver as alternative top electrode for lead zirconate titanate thin films', *Journal of Alloys and Compounds* **2019**, *783*, 801–805.

[143] G. Vandevenne et al., 'A study on the thermal sintering process of silver nanoparticle inkjet inks to achieve smooth and highly conducting silver layers', *Physica Status Solidi A* **2016**, *213*, 1403–1409.

[144] F. Chen, R. Schafranek, W. Wu, A. Klein, 'Formation and modification of Schottky barriers at the PZT/Pt interface', *Journal of Physics D: Applied Physics* **2009**, *42*, 215302.

[145] K. Prume, P. Muralt, F. Calame, T. Schmitz-Kempen, S. Tiedke, 'Piezoelectric thin films: evaluation of electrical and electromechanical characteristics for MEMS devices', *IEEE Transactions on Ultrasonics Ferroelectrics and Frequency Control* **2007**, *54*, 8–14.

[146] N. Godard et al., '1-mW vibration energy harvester based on cantilever with printed polymer multilayers', *Cell Reports Physical Science* **2020**, 100068.

[147] X. Ma, A. Wilson, C. D. Rahn, S. Trolier-McKinstry, 'Efficient energy harvesting using piezoelectric compliant mechanisms: theory and experiment', *Journal of Vibration and Acoustics* **2016**, *138*, 021005.

[148] J. Kymissis, C. Kendall, J. Paradiso, N. Gershenfeld in Digest of Papers. Second International Symposium on Wearable Computers, **1998**, pp. 132–139.

[149] X. Yuan et al., 'The large piezoelectricity and high power density of a 3D-printed multilayer copolymer in a rugby ball-structured mechanical energy harvester', *Energy & Environmental Science* **2020**, *13*, 152–161.

[150] M. Bohlén, K. Bolton, 'Conformational studies of poly(vinylidene fluoride), poly(trifluoroethylene) and poly(vinylidene fluoride-co-trifluoroethylene) using density functional theory', *Physical Chemistry Chemical Physics* **2014**, *16*, 12929.

[151] P. Lhéritier, S. Noël, N. Vaxelaire, F. Domingues Dos Santos, E. Defay, 'Actuation efficiency of polyvinylidene fluoride-based co- and ter-polymers', *Polymer* **2018**, *156*, 270–275.

[152] Z. Yang, J. Zu, J. Luo, Y. Peng, 'Modeling and parametric study of a force-amplified compressive-mode piezoelectric energy harvester', *Journal of Intelligent Material Systems and Structures* **2017**, *28*, 357–366.

[153] Q. He, T. Jiang, 'Complementary multi-mode low-frequency vibration energy harvesting with chiral piezoelectric structure', *Applied Physics Letters* **2017**, *110*.

[154] T. Ricart et al. in 2011 IEEE International Ultrasonics Symposium, IEEE, **2011**, pp. 1928–1931.

[155] M. Lallart, P.-J. Cottinet, L. Lebrun, B. Guiffard, D. Guyomar, 'Evaluation of energy harvesting performance of electrostrictive polymer and carbon-filled terpolymer composites', *Journal of Applied Physics* **2010**, *108*, 034901.

[156] M. Wang, R. Zuo, S. Qi, L. Liu, 'Synthesis and characterization of sol–gel derived $(Ba, Ca)(Ti, Zr)O_3$ nanoparticles', *Journal of Materials Science: Materials in Electronics* **2012**, *23*, 753–757.

[157] S. Roundy, P. K. Wright, 'A piezoelectric vibration based generator for wireless electronics', *Smart Materials and Structures* **2004**, *13*, 1131–1142.

[158] G. Tang et al., 'A piezoelectric micro generator worked at low frequency and high acceleration based on PZT and phosphor bronze bonding', *Scientific Reports* **2016**, *6*, 38798.

[159] X. Dai, Y. Wen, P. Li, J. Yang, G. Zhang, 'Modeling, characterization and fabrication of vibration energy harvester using Terfenol-D/PZT/Terfenol-D composite transducer', *Sensors and Actuators A: Physical* **2009**, *156*, 350–358.

[160] J. Liang, W.-H. Liao in Active and Passive Smart Structures and Integrated Systems 2010, *Vol. 7643*, **2010**, 76430K.

[161] L. Gu, 'Low-frequency piezoelectric energy harvesting prototype suitable for the MEMS implementation', *Microelectronics Journal* **2011**, *42*, 277–282.

[162] L. Tang, Y. Yang, 'A nonlinear piezoelectric energy harvester with magnetic oscillator', *Applied Physics Letters* **2012**, *101*, 094102.

[163] K. A. Singh, R. Kumar, R. J. Weber, 'A broadband bistable piezoelectric energy harvester with nonlinear high-power extraction', *IEEE Transactions on Power Electronics* **2015**, *30*, 6763–6774.

[164] Z. Yang, J. Zu, 'Comparison of PZN-PT, PMN-PT single crystals and PZT ceramic for vibration energy harvesting', *Energy Conversion and Management* **2016**, *122*, 321–329.

[165] Z. Yi et al., 'High performance bimorph piezoelectric MEMS harvester via bulk PZT thick films on thin beryllium-bronze substrate', *Applied Physics Letters* **2017**, *111*.

[166] Z. Gui, L. Li, S. Gao, X. Zhang, 'Low-temperature sintering of lead-based piezoelectric ceramics', *Journal of the American Ceramic Society* **1989**, *72*, 486–491.

[167] W. Wang, T. Yang, X. Chen, X. Yao, 'Vibration energy harvesting using a piezoelectric circular diaphragm array', *IEEE Transactions on Ultrasonics Ferroelectrics and Frequency Control* **2012**, *59*, 2022–2026.

[168] F. Bernard, F. Casset, J. S. Danel, C. Chappaz, S. Basrour, 'Characterization of a smartphone size haptic rendering system based on thin-film AlN actuators on glass substrates', *Journal of Micromechanics and Microengineering* **2016**, *26*, 084007.

[169] R. Nigon, T. M. Raeder, P. Muralt, 'Characterization methodology for lead zirconate titanate thin films with interdigitated electrode structures', *Journal of Applied Physics* **2017**, *121*, 204101.

[170] A. Gibaud, 'Specular reflectivity from smooth and rough surfaces' in *X-ray and Neutron Reflectivity: Principles and Applications*, Springer, Berlin, Heidelberg, **2007**, pp. 87–120.

[171] A. Mazzalai, D. Balma, N. Chidambaram, R. Matloub, P. Muralt, 'Characterization and fatigue of the converse piezoelectric effect in PZT films for MEMS applications', *Journal of Microelectromechanical Systems* **2015**, *24*, 831–838.

[172] K. Prume, S. Tiedke, T. Schmitz-Kempen, 'Double-beam and four-point', *Mikroniek* **2010**, *50*, 31–35.